Scaling and Kinematics of Daytime Slope Flow Systems

by

Christian Reuten

Diplomphysiker, University of Goettingen, 1993

A THESIS SUBMITTED IN PARTIAL FULFILLMENT OF
THE REQUIREMENTS FOR THE DEGREE OF

DOCTOR OF PHILOSOPHY

in

THE FACULTY OF GRADUATE STUDIES

(Atmospheric Science)

THE UNIVERSITY OF BRITISH COLUMBIA

March 2006

Abstract

Flows up heated slopes are an elementary component of thermally-driven flows in complex terrain and play a fundamental role in the transport of air pollutants. Our understanding of upslope flows is still incomplete because of the difficulty of carrying out field measurements in complex terrain, the sensitivity of upslope flows to external disturbances, and the difficulty of resolving topographic details in numerical models.

In this dissertation I study upslope flows by combining field observations and water-tank experiments. Field observations at a 19° slope showed strong upslope flows of 4 m s^{-1} in the lower half of the backscatter boundary layer (BBL), determined from lidar scans of aerosol backscatter. A return flow in the upper half of the BBL nearly compensated the upslope volume transport which suggests a trapping of air pollutants in a closed slope flow circulation.

I built a bottom-heated water tank with a 19° slope between a plain and a plateau and, using time-dependent scaling, I develop mathematical idealisations of the water tank and the field site. Field and tank observations of non-dimensional thermal boundary layer (TBL) depth agree within 20%. An analysis of the data with probability theory demonstrates that non-dimensional upslope flow velocities in atmosphere and water tank have significantly different functional dependencies on the governing parameters. I demonstrate that the tank flows are fluid-dynamically smooth and explain the similarity violation by a fluid-dynamic feedback: in the water tank, roughness length strongly decreases with increasing upslope flow velocity; by contrast the atmospheric flows were fluid-dynamically rough and roughness length was approximately constant.

Flows in the water tank show a persistent eddy with near-surface flows in downslope direction over the plain adjacent to the slope. I argue that the eddy is a result of a TBL depression in the lower part of the slope caused by upslope-flow advection of dense fluid. Water-tank experiments suggest that the eddy can cause strongly rising motion over a valley centre for a ratio of about three between valley width and ridge height.

In experiments with a plateau length exceeding roughly half the ridge height, independent plain-plateau and upslope flow circulations developed. The upslope flow layer in the water

tank agreed with the TBL; the return flow returned dye originally injected over the plain in an elevated layer above the TBL and underneath the plain-plateau flow. When the dye concentrations in TBL and elevated layer became sufficiently similar both layers appeared as one deep BBL.

As heating continued two regime changes occurred. First, the TBL merged with the elevated layer, and the upslope flow formed one large circulation with the plain-plateau flow. In a subsequent regime change, the TBL merged with a new elevated layer formed by the large circulation. Upslope flows in the atmosphere are likely to exhibit regime changes at multiple scales. Conditions conducive to re-entrainment of air pollutants are: symmetric topography; weak stratification and larger-scale flows; strong sensible surface heat flux; low ridge height; short plateau; sensible surface heat flux decrements over the slope; and abrupt slope-angle decrements.

Table of Contents

List of Figures

List of Tables

List of Symbols

Special Notations:

$'$	Suffix denoting turbulent perturbations
a	Subscript denoting atmospheric quantities
b	Subscript denoting background quantities
w	Subscript denoting water-tank quantities
(j)	Superscript denoting the jth hypothesis (when using probability theory)
δ	Prefix denoting finite differences
Δ	Prefix denoting non-turbulent perturbations of background quantities; denoting step length in summation

Latin Symbols:

A	Entrainment coefficient, Q_{top}/Q_H
$A_{h,w}$ $\left[m^2\right]$	Horizontal cross-sectional inner area of the water tank
A_w $\left[m^2\right]$	Inner surface area of the water-tank bottom
b_c $\left[m\,s^{-2}\right]$	Characteristic buoyancy in Chen et al. (1996)
c	Constant coefficient or correction factor
d	Julian day
d $[m]$	Characteristic depth in gravity current
d_i $[?]$	Individual datum
D	Statement on the data (when using probability theory)
D_w $[m]$	Water depth over the plain in the tank
$\overline{D_w}$ $[m]$	Mean water depth in the tank
E $[K\,m]$	Kinematic thermal-energy / heat density
E $\left[kg_{\text{water vapor}}\,m^{-3}s^{-1}\right]$	Water vapour created during phase change
Fr_i	Internal Froude number
g $\left[m\,s^{-2}\right]$	Gravitational acceleration
g_s $\left[m\,s^{-2}\right]$	Reduced buoyancy scale
Gr	Grashof number
h $[m]$	CBL depth
h_p $[m]$	CBL depth predicted for zero entrainment ($A = 0$)
H	Hypothesis (when using probability theory for hypothesis testing)

$H \quad [m]$	Ridge height
$H_f \quad [m]$	Total height of the fluid right above the gravity-current front
I	Statement on background information (when using probability theory)
$I_{eff} \quad [A]$	Effective (measured) current through heaters
lg	Briggs logarithm (to base 10), i.e. $\lg = \log_{10}$
ln	Natural logarithm (to base e), i.e. $\ln = \log_e$
$L \quad [m]$	Horizontal length of the slope
$L_b \quad [m]$	Length of the plain in the water tank
$L_D \quad [m]$	Diagonal length of the slope
$L_p \quad [m]$	Latent heat associated with phase change
$L_t \quad [m]$	Length of the plateau in the water tank
$m \quad [?]$	Slope of linear fit curve (units dependent on particular data)
$m \quad [kg]$	Mass
$M \quad \left[m\,s^{-1}\right]$	Kinematic mass flux
$\vec{m}$	Negative normalised insolation vector (unit vector pointing towards the sun)
$n \quad [m]$	Slope-normal coordinate in rotated coordinate system
$\vec{n}$	Slope surface normal vector (unit vector perpendicular to slope surface)
$N \quad \left[s^{-1}\right]$	Buoyancy frequency
$p \quad \left[kg\,m^{-1}\,s^{-2}\right]$	Pressure
$p(H\|I)$	Conditional probability that H is true, given that I is true
$P_w \quad [W]$	(Electrical) power supplied to heaters underneath the tank bottom
Pr	Prandtl number
$q \quad \left[K\,m^3\right]$	Kinematic thermal energy / heat
$\tilde{q} \quad [J]$	Dynamic thermal energy / heat
$Q^* \quad \left[K\,m\,s^{-1}\right]$	Kinematic net radiative surface heat flux / power density
$Q_E \quad \left[K\,m\,s^{-1}\right]$	Kinematic latent heat flux / power density
$Q_G \quad \left[K\,m\,s^{-1}\right]$	Kinematic molecular conductive flux / power density into the ground
$Q_H \quad \left[K\,m\,s^{-1}\right]$	Kinematic net sensible surface heat flux / power density
$Q_L^* \quad \left[K\,m\,s^{-1}\right]$	Kinematic longwave radiative surface heat flux / power density
$Q_{\max} \quad \left[K\,m\,s^{-1}\right]$	Maximum kinematic net sensible surface heat flux / power density
$Q_{top} \quad \left[K\,m\,s^{-1}\right]$	Kinematic heat flux added to CBL by entrainment at the top

$\widetilde{Q}$ $\left[J\,m^{-2}\right]$	Dynamic thermal-energy/heat density
$\widetilde{Q}_H$ $\left[W\,m^{-2}\right]$	Dynamic net sensible surface heat flux / power density
$\widetilde{Q}^*$ $\left[W\,m^{-2}\right]$	Dynamic net radiative surface heat flux / power density
r	Ratio of observed and predicted CBL depth, H_s/H_p
Ra	Rayleigh number
Re	Reynolds number
Ri_o	Overall Richardson number
Ro	Rossby number
s $[m]$	Slope-parallel coordinate in rotated coordinate system
t $[s]$	Time
t_d $[s]$	Time to maximum heating (diurnal heating time scale)
t_p $[s]$	Time of onset of sea breeze propagation at the coastline (relative to the beginning of positive heat flux)
t_t $[s]$	Time to transition to sea breeze at a location inland (relative to onset time t_p at the coastline)
t_{UTC} $[h]$	Time in hours UTC
T $[K]$	Temperature
T_0 $[K]$	Surface (screen) temperature
T_s $[K]$	CBL temperature scale
T_V $[K]$	Virtual temperature
U $\left[m\,s^{-1}\right]$	x component of velocity
U_0 $\left[m\,s^{-1}\right]$	Predicted fictitious maximum upslope flow velocity at surface
U_1, U_2, U_3 $\left[m\,s^{-1}\right]$	x, y, z component of velocity, respectively
U_{Chen} $\left[m\,s^{-1}\right]$	Maximum upslope flow velocity from Chen hypothesis
U_e $\left[m\,s^{-1}\right]$	Expected true maximum upslope flow velocity after application of no-slip condition at the surface
$U_{\exp}$ $\left[m\,s^{-1}\right]$	Expected maximum upslope flow velocity
U_{fit} $\left[m\,s^{-1}\right]$	Fitted maximum upslope flow velocity
U_{fric} $\left[m\,s^{-1}\right]$	Maximum upslope flow velocity from friction hypothesis
U_{Grav} $\left[m\,s^{-1}\right]$	Predicted nose velocity in gravity-current flow
U_{Hunt} $\left[m\,s^{-1}\right]$	Maximum upslope flow velocity from Hunt hypothesis
U_M $\left[m\,s^{-1}\right]$	Vertically-averaged (mean) upslope flow velocity
$U_{\max}$ $\left[m\,s^{-1}\right]$	Predicted maximum upslope flow velocity

U_{obs} $\left[m\,s^{-1}\right]$	Observed upslope flow velocity
U_p $\left[m\,s^{-1}\right]$	Propagation speed of sea breeze (sum of sea breeze and synoptic wind speed)
U_s $\left[m\,s^{-1}\right]$	Slope-parallel component of velocity
U_S $\left[m\,s^{-1}\right]$	Characteristic velocity scale
U_{Schu} $\left[m\,s^{-1}\right]$	Maximum upslope flow velocity from Schumann hypothesis
V $\left[m\,s^{-1}\right]$	y component of velocity
V $\left[m^3\right]$	Volume
V_{eff} $\left[V\right]$	Effective (measured) voltage of AC power supply
W $\left[m\,s^{-1}\right]$	z component of velocity
W_n $\left[m\,s^{-1}\right]$	Slope-normal component of velocity
W_w $\left[m\right]$	Interior width of the water tank
x_1, x_2, x_3 $\left[m\right]$	x, y, z component of location, respectively
x $\left[m\right]$	x coordinate in Cartesian coordinate system; distance inland from the coastline
$X = \{x_1,...,x_n\}$	Generic place holder for a set of data x_i, $i=1,...,n$
y $\left[m\right]$	y coordinate in Cartesian coordinate system and cross-slope coordinate in slope coordinate system
z $\left[m\right]$	z coordinate (height) in Cartesian coordinate system

Greek Symbols:

$\alpha_{0,w}$ $\left[m^3\,kg^{-1}\right]$	Specific volume at water surface
$\alpha_{D,w}$ $\left[m^3\,kg^{-1}\right]$	Specific volume difference between top and bottom of water
$\alpha_{s,w}$ $\left[m^3\,kg^{-1}\right]$	CBL mean specific volume increment in water tank
β $\left[K^{-1}\right]$	Coefficient of volumetric expansion
γ_a $\left[K\,m^{-1}\right]$	Environmental lapse rate for potential temperature in atmosphere
γ_w $\left[m^2\,kg^{-1}\right]$	Environmental lapse rate for specific volume in water tank
δ_{ij}	Kronecker delta
ε_{ijk}	Epsilon tensor
θ_a $\left[K\right]$	Potential temperature in the atmosphere
$\theta_{s,a}$ $\left[K\right]$	CBL mean potential temperature increment in the atmosphere
θ_V $\left[K\right]$	Virtual potential temperature

κ $\left[m^2\,s^{-1}\right]$	Kinematic molecular thermal diffusivity
μ $\left[kg\,m^{-1}\,s^{-1}\right]$	Dynamic viscosity
ν $\left[m^2\,s^{-1}\right]$	Kinematic molecular viscosity
Π_i	i^{th} Pi group
ρ $\left[kg\,m^{-3}\right]$	Density
τ_{ij} $\left[kg\,m^{-1}\,s^{-2}\right]$	Viscous stress tensor
φ $[°]$	Slope angle
Ω_i $\left[s^{-1}\right]$	i^{th} component of angular velocity of the Earth's rotation

List of Constants

This is a list of parameters that I assumed constant in the thesis to simplify calculations or to make a problem solvable. The values are collected from and cross-checked between Glickman (2000), Gobrecht (1974), Kuchling (1979), Serway and Beichner (2000), Stull (1988), Stull (2000), Weast (1978-79).

$\alpha_{0,w} = 1/998.23\ m^3\ kg^{-1}$	Specific volume of freshwater at 20°C
$\beta_a = 0.003674\ K^{-1}$	Coefficient of thermal expansion of air 20°C
$\beta_w = 2.6\times10^{-4}\ K^{-1}$	Coefficient of thermal expansion of freshwater 25°C
$C_a = 1006\ J\ kg^{-1}K^{-1}$	Specific heat of dry air at sea level at 20°C
$C_w = 4179.6\ J\ kg^{-1}K^{-1}$	Specific heat of water at 25°C
$D_s = 1.5\times10^{-9}\ m^2\ s^{-1}$	Diffusivity of NaCl salt at molarities 0.01-0.1
$\Gamma_d = 9.8\times10^{-3}\ K\ m^{-1}$	Dry adiabatic lapse rate
$g = 9.8\ m\ s^{-2}$	Gravitational acceleration at sea level at mid-latitudes
$\kappa_a = 2.11\times10^{-5}\ m^2\ s^{-1}$	Kinematic molecular thermal diffusivity of dry air at sea
$\kappa_w = 1.45\times10^{-7}\ m^2\ s^{-1}$	Kinematic molecular thermal diffusivity of water at 25°C
$L_f = 0.334\times10^6\ J\ kg^{-1}$	Latent heat of freezing (energy released during freezing)
$L_s = -2.83\times10^6\ J\ kg^{-1}$	Latent heat of sublimation (energy required for sublimation)
$L_v = -2.50\times10^6\ J\ kg^{-1}$	Latent heat of vaporization (energy required for vaporization)
$\nu_a = 1.52\times10^{-5}\ m^2\ s^{-1}$	Kinematic molecular viscosity of dry air at sea level pressure at 20°C
$\nu_w = 8.9\times10^{-7}\ m^2\ s^{-1}$	Kinematic molecular viscosity of water at 25°C ($\approx \pm10\%$ for $\mp5°C$)
$R = 287.053\ J\ K^{-1}\ kg^{-1}$	Gas constant for dry air
$\rho_a = 1.204\ kg\ m^{-3}$	Density of dry air at sea level pressure and 20°C
$\rho_w = 997.0\ kg\ m^{-3}$	Density of freshwater at 25°C
$\rho_a \cdot C_a = 1211 \frac{Wm^{-2}}{Kms^{-1}}$	Heat capacity of dry air at 20°C
$\rho_w \cdot C_w = 4.167\times10^6 \frac{Wm^{-2}}{Kms^{-1}}$	Heat capacity of freshwater at 25°C

List of Abbreviations

2-D	Two-dimensional
3-D	Three-dimensional
AI	Atmospheric idealisation
AMS	American Meteorological Society
BBL	Backscatter Boundary Layer
CBL	Convective Boundary Layer
CCW	Counter clockwise
CFCAS	Canadian Foundation for Climate and Atmospheric Sciences
CW	Clockwise
GVRD	Greater Vancouver Regional District
LES	Large-Eddy Simulation
LFV	Lower Fraser Valley
LST	Local standard time
lidar	light detection and ranging
MSL	(Above) Mean Sea Level
ND	Non-dimensional
NSERC	Natural Sciences and Engineering Research Council of Canada
PDF	Probability density function
PDT	Pacific Daylight Time
PIV	Particle image velocimetry
PM	Particulate matter
RASCAL	Rapid Acquisition SCanning Aerosol Lidar
RHI	Range height indicator
sodar	sound detection and ranging
TBL	Thermal boundary layer
TKE	Turbulent kinetic energy
WTI	Water-tank idealisation

Preface

Parts of this dissertation were published in Reuten et al. (2005). Section 1.3 "Review of Previous Investigations" is an extension of the literature review written by my. Section 2.1 "Experimental Layout and Methods" is basically unchanged. Dr. Kevin Strawbridge contributed the paragraph on the lidar. Paul Bovis wrote the synoptic weather analysis and obtained from Michel Jean at the Canadian Meteorological Center the original analysis charts, on which I based Figure 2.2. Furthermore, he provided the inset to Figure 1.1. Paul Jance helped me generate the topographic map in Figure 1.1 and Dr. Pascal Haegeli created the topographic map of Figure 2.1. Sections 2.2 "Observations of Closed Slope Flow Systems versus Mountain Venting" and section 2.3 "Discussion and Conclusions" were originally written by me and for this dissertation extended by additional analyses and a link to the remainder of the thesis. Dr. Kevin Strawbridge contributed the lidar scans in Figure 2.14 and Figure 2.4 and all backscatter boundary layer height data used in this dissertation. Paul Bovis pre-processed the tethersonde data, and provided final temperature, moisture, and wind data in Microsoft Excel format. I pre-processed the sodar data, carried out all further data analysis, and created the remaining figures.

Acknowledgements

First I would like to express my gratitude to my thesis supervisors Douw Steyn and Susan Allen for their financial and intellectual support. Beyond the dissertation research Douw Steyn has been an invaluable mentor in my professional growth and very supportive of my volunteer activities at UBC. Susan Allen has spent endless hours with me pondering over technical challenges with the water tank and many of the interesting questions that surfaced during the research.

I am grateful to Lorne Whitehead for his co-supervision and financial support at the beginning of my dissertation. In particular I appreciate his understanding and encouragement when I decided to "follow my heart" and change the thesis topic. I am indebted to the members of my Ph.D. committee, Roland Stull and Han van Dop, for providing very important feedback on my progress and the thesis manuscript. I also greatly appreciated Noboru Yonemitsu's help and inspiring discussions.

I wish to thank Greg Lawrence for providing the laboratory space for the water tank and sharing computer resources and instrumentation. The water tank was built in the workshop in the Department of Civil Engineering at UBC: Bill Leung built the mechanical parts and Scott Jackson the electrical and electronic components. Workshop supervisor Harald Schrempp generously allocated workshop time for the "fish-tank project", and his experience was of tremendous help particularly during the design stage. I thank Ian Chan for endless shared hours in the laboratory for re-designing and re-building the tank, re-writing parts of MatPIV, and running experiments, which often needed more than two hands.

Funding support for this study was provided by grants from NSERC and CFCAS to Douw Steyn and Susan Allen and also by Environment Canada under the Pacific 2001 project. I would like to thank Kevin Strawbridge and Paul Bovis (Environment Canada) for their collaboration in Reuten et al. (2005). Permissions for the setup of field instrumentation were granted by the Greater Vancouver Regional District (GVRD) and the City of Port Coquitlam. Al Percival (GVRD), Mr. Bernie Buttner (GVRD), and Mr. Geoff Yip (City of Port Coquitlam) were of great help for the setup of instrumentation and on-site support.

Several people have contributed to the dissertation in various ways. Phil Gregory in the Department of Physics and Astronomy at UBC taught me the use of probability theory to analyse data. Michel Jean (Canadian Meteorological Center) provided the synoptic analysis charts on which Figure 2.2 was based. Paul Jance and Pascal Haegeli in the Department of Geography at UBC helped me create Figure 1.1 and Figure 2.1. Furthermore, I wish to acknowledge all those people, whose names I forgot to mention here but who may have contributed to this dissertation by sharing their ideas and opinions.

Finally, in many respects having a dad or husband, who pursues a Ph.D., is different from having one, who works on a regular job. I would like to thank my children Serena and Sebastian and my wife Shan for putting up with the less pleasurable differences.

1 Introduction

1.1 Research Motivation, Goal, and Questions

The Lower Fraser Valley (LFV), British Columbia, Canada is characterised by a shallow maritime boundary layer, a valley geometry that narrows towards the interior, steep slopes rising over 1000 m above the adjacent plain, and tributary valleys (Figure 1.1). The LFV shares some of these characteristics with other places like Los Angeles, Santiago, and Athens, all notorious for their air-pollution problems.

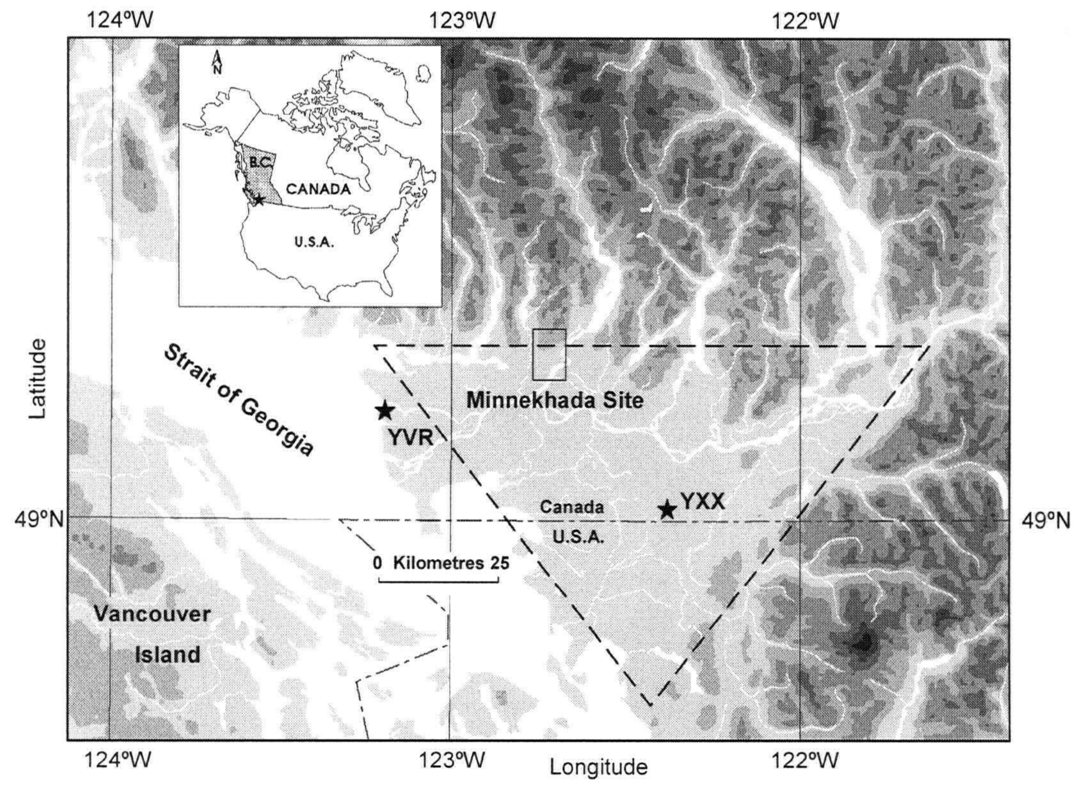

Figure 1.1: Map of the Lower Fraser Valley (LFV), Canada.
Shown are the locations of Vancouver International Airport (YVR), Abbotsford Airport (YXX), and site of slope flow observations in Minnekhada Park (black rectangle). White areas are water surfaces; shades of grey indicate contour intervals of 0-500 m, 500-1000 m, etc. The dashed triangle approximates the shape of the LFV. The black star in the inset shows the location of the LFV within British Columbia (B.C.) and Canada. (Based on Fig. 1 in Reuten et al., 2005)

In the case of the LFV the main source of air pollution is traffic near the coast at the Strait of Georgia. During summer under fair-weather conditions, ozone precursors and particulate matter are carried downwind toward the interior into rural areas where ozone levels reach a maximum (Steyn et al., 1997), significantly impairing the relatively large portion of the population that is performing physical work outdoors (Brauer and Brook, 1997).

Upslope flows play a particularly important role in the dispersion of air pollution at places like Vancouver, Los Angeles and Mexico City. In Whiteman's (2000) overview of air pollution dispersion in mountainous terrain it is assumed that upslope flows vent air pollutants out of the boundary layer into the free atmosphere. I will demonstrate in this thesis that this is not always the case, that air pollution can be trapped or recirculated within the boundary layer. Some investigators have come across the possibility of air-pollution recirculation without paying attention to it while most investigators have either not observed it or simply excluded the possibility in their models.

The possibility of a recirculation challenges the simple concept of an upslope flow filling the convective boundary layer (CBL) over a heated slope and opens up an array of questions. It is the goal of this dissertation to provide new insights into the kinematics of daytime slope flow systems by addressing these questions: Is the boundary layer over a heated slope identical to the CBL over flat terrain or does it have a more complicated structure? How do upslope and return flow relate to the boundary-layer structure? Is there a continuous transition between the two extremes of recirculation and venting or are there two distinct regimes? What are the determining parameters?

The simple conceptual model presented in section 1.2 below is fairly representative of our current understanding of upslope flows; yet, it does not answer any of these questions. In section 1.3 I will review previous investigations against the questions. After 160 years of research on upslope flows our understanding is still incomplete. The approach I have taken to answer those questions above is laid out in section 1.4.

1.2 The Basic Mechanism of Upslope Flows

During fair-weather conditions mountain slopes often exhibit upslope flows of air during the day and downslope flows during the night. The following high-level explanation for upslope flows is based on Atkinson (1981) (Figure 1.2).

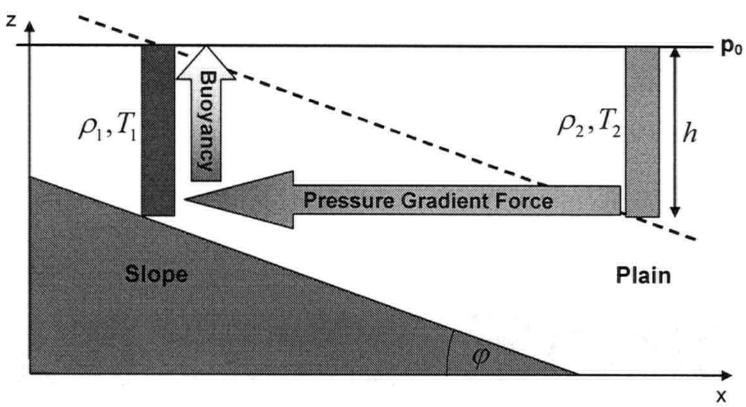

Figure 1.2: High-level diagram of the mechanism of upslope flows (adapted from Atkinson, 1981). *φ is the slope angle, ρ_1, T_1 and ρ_2, T_2 denote the density and temperature of the warmer and colder air parcel, respectively, and p_0 is the pressure of a reference level shown as the solid line. The dashed line marks the upper limit of the heated layer; 'Slope' and 'Plain' denote slope and plain region, respectively.*

During the day a column of air of depth h directly above the slope's heated surface within the heated layer of potential temperature T_1 has a lower density ρ_1 than a column of air over the plain which is based at the same height above sea level and has the same depth h, because the latter is further away from the heated surface. If the latter air column has mean potential temperature T_2 and mean density ρ_2 the warmer air column has a buoyancy deficit of $g(T_2 - T_1)/T_2$. An air parcel at the base of the heated column is at first displaced infinitesimally upward like a thermal over flat terrain because the slope surface acts as a barrier. After this step the parcel still has a buoyancy deficit relative to the unheated column of air over the plain to the right but has a buoyancy excess relative to the adjacent warmer parcel to the left and will therefore be displaced toward the slope surface. The two steps can be interpreted as the combined action of a vertical buoyancy force and a horizontal pressure gradient force which drives the air upslope.

This simple conceptual model of upslope flows applies to air and water (when potential temperature is replaced by specific volume) and to laminar and turbulent flows. It therefore does not answer two central questions of this dissertation, which are specific to convectively driven upslope flows: What is the structure of the boundary layer over heated slopes? And what relationship does the upslope flow system have to the boundary layer? Water-tank experiments reported in this dissertation will provide answers to both questions.

1.3 Review of Previous Investigations

Wenger (1923) pointed out that Bjerknes's circulation theorem requires a closed slope flow circulation in which a return flow compensates for the upslope mass transport (Figure 1.3, A). Previous observations only partly supported this theorem. Daytime slope flow systems often exhibited upslope flow adjacent to the slope with return flow above, but the return flow was often too weak to balance the upslope mass transport. There are two likely causes for that. Firstly, larger-scale winds like valley winds, sea breezes, and in particular synoptic winds are often much stronger than the upslope winds and strongly upset the mass balance (Figure 1.3, B). Secondly, real mountains are practically never symmetric; but asymmetries, like stronger heating on the lee side of the investigated mountain, lead to net fluxes into or out of the domain boundary and violate the mass balance requirement (Figure 1.3, C).

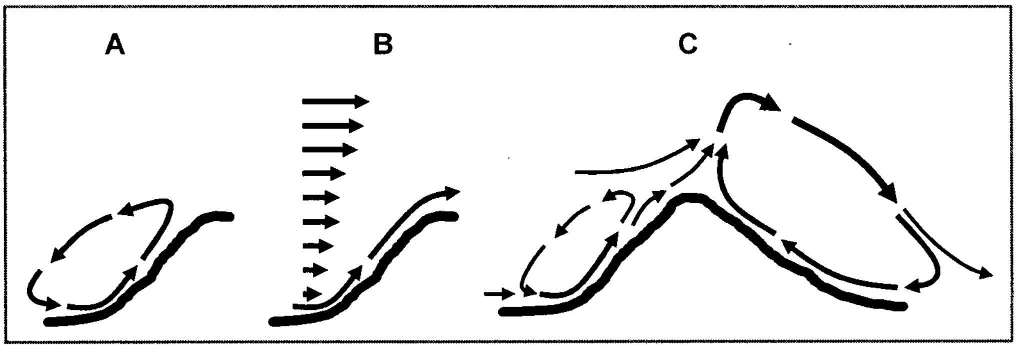

Figure 1.3: Scenarios of upslope flow systems.
Closed upslope flow system with mass balance (A), larger-scale flow superimposed on upslope flow system (B), and partially coupled upslope flow systems (C).

The literature on upslope flows in relation to CBL is spread over many decades and can be categorised according to the relationship between CBL and upslope flows. The older literature lacks direct measurements of the CBL so that in some cases I had to estimate or indirectly infer the CBL depth. I will separate cases with the return flow above the CBL from those with the return flow within the CBL. The former cases are often associated with mountain venting, i.e. upslope winds transporting air pollutants out of the CBL into the free atmosphere. In the latter cases, air pollutants can remain trapped in the CBL, a scenario widely ignored before we reported evidence from our observations in Reuten et al. (2002a, 2002b, 2005).

1.3.1 Return Flow Above the CBL or No Return Flow

Wenger (1923) cited observations of upslope winds on Teneriffa showing return flows at about 1500 m, well above the top of a maritime boundary layer of typically less than 1000 m. The observations reported by Mendonca (1969) exhibited no return flow within the CBL, although strong ridge-top winds were opposing the upslope flow. Orographic clouds directly above the upslope flow suggested that the upslope flows filled the entire CBL. Banta (1984) observed upslope flows in the morning filling the entire shallow CBL underneath a near-neutral residual layer topped by a stable layer. Before the CBL could penetrate the residual layer, the upslope flow disappeared under the influence of larger-scale winds. It is not possible to judge if and how much return flows above the CBL contributed to the strength of the ridge-top winds.

In water-tank studies of diurnal heating and cooling cycles at a ridge, Mitsumoto (1989) observed upslope flows filling the entire CBL and return flows and further layers of alternating flows occurring above the top of the CBL.

The large-eddy simulation (LES) performed by Schumann (1990) (see also Vergeiner, 1991) revealed upslope flows filling the modelled CBL and generally weak return flows occurring above the top of the CBL. Schumann's LES is in good agreement with the first analytical upslope flow model developed by Prandtl (1942). Because of the importance of the Prandtl model and the open question on the assumptions in the model, I derive the Prandtl model rigorously from first principles in Appendix A.

Prandtl's (1942) analytical solution for upslope flows over an infinite slope shows a very weak return flow above the upslope flow. The return flow can be within or above the CBL depending on the choice of eddy-transfer coefficients, which are unspecified in Prandtl's model.

An extension of the stationary Prandtl model by assuming sinusoidally varying surface temperatures leads to the Prandtl solution of temperature difference and upslope velocity, which now vary sinusoidally in phase with the surface forcing (Defant, 1949). Thus the return flow is also weak for this special non-stationary case.

A major limitation of the models by Prandtl and Defant is the assumption of an infinitely long slope, which does not permit a topographic length scale. Furthermore Bjerknes's circulation theorem cannot be applied because it requires a finite path of integration around the slope flow system. Egger (1981) took Defant's approach one step further by restricting the temperature increase to a finite length over a very long but finite slope with periodic boundary conditions, thus enforcing a mass transport balance. While the upslope flow profile is very similar to the one in the Prandtl model, the return flow is stronger and much deeper. The return flow velocity of 2 m s^{-1}, however, is much smaller than the upslope velocity of 7 m s^{-1}. The relation of the slope flow system to the CBL is complicated. The upslope flow layer has approximately constant thickness along the slope. If the isopleth of 0 degrees temperature deviations from the background is identified as the top of the CBL then the latter is approximately horizontal. Near the bottom of the heated area the upslope flow fills only about half of the CBL, and the return flow reaches far beyond the CBL top. At the top of the heated area the upslope flow fills the entire CBL.

Kondo (1984) provided additional insight into the analytical model used by Egger (1981) for an infinite slope with only a finite section being heated. Kondo pointed out that the model represents a heat island-upslope flow interaction. For $\varphi = 0°$ slope angle, the system represents a heat island with two convection cells. When tilted at an angle $\varphi > 0°$ up to a critical angle the heat island flow persists, now interacting with a slope flow. Above the critical angle there is only one convection cell and the slope wind is "Prandtl-like", with only weak return flows occurring above the CBL. Defining the CBL depth H_s as the thermal boundary layer depth for $\varphi = 0°$, Kondo showed that the critical angle is the one for which the CBL depth equals half of the height of the heated segment over the slope, $H_R/2$, or $H_R/H_s = 2$.

Numerical models for long shallow slopes with adjacent plain and plateau (Ye et al., 1987) show a remarkable feature, which was reported by de Wekker (2002): Over the plain right before the slope the CBL is deeper than further way from the slope, while it is much shallower over the bottom part of the slope. Ye et al. chose the boundary conditions such that upslope flow and CBL had to coincide, excluding the possibility of a critical slope angle or ridge height relative to the CBL depth. The same restriction applies to the analytical models by Petkovsek (1982) and Segal et al. (1987). Petkovsek's analytical model is based on quasi-balanced pressure gradient, buoyancy, and friction. Upslope flow layer depth and evolution were specified and the return flow neglected. Segal et al. (1987) performed a circulation evaluation assuming that the top of the CBL separates the upslope flow from the return flow.

When the constant eddy viscosity in the Prandtl model is replaced by a one-and-a-half order closure for the turbulent fluxes of momentum and heat (Brehm, 1986), upslope flow depth and velocity maximum become smaller but the return flow above the CBL remains weak. Non-linear surface forcing (Ingel', 2000) resulted in modifications to Prandtl's solution for the bottom part of the slope flow system but not for the return flow.

In contrast to the observations and models reviewed in this section we observed strong return flows underneath the CBL top during the Pacific 2001 Air Quality Field Study. This possibility is also supported by evidence in previous studies which I review next.

1.3.2 Return Flow Below the CBL

Slope flow circulations over the side walls in a Vermont valley (43°N) showed velocity profiles with equally strong upslope and return flows (Davidson, 1963). Measurements were taken over a 19° east facing slope with a ridge height of about 670 m at 0840-1010 LST on August 14. Synoptic winds of about 2 m s^{-1} were opposing the upslope flow. Shape, strength (1.25-1.75 m s^{-1}), and depth (approximately 150 m) of upslope flow and return flow were remarkably similar to our observations in the Lower Fraser Valley at a similar time of day reported in chapter 2. The CBL depth during Davidson's observations is not known, but the solar elevation angle over the slope in the Vermont valley was greater than over the slope at Minnekhada Park. If the land-surface characteristics were similar the CBL in the Vermont Valley was deeper than the 350-600 m in the LFV. This suggests that Davidson observed upslope flows and strong return flows within the CBL.

Over an 11° east-north-east facing slope with a ridge height of approximately 900 m, Wooldridge and McIntyre (1986) observed upslope flows up to 475 m and return flows between 475 and 800 m above the slope. The authors estimated the CBL depth at more than 1000 m. Synoptic winds were weak from the north.

Kuwagata and Kondo (1989) analysed eleven sets of data, from measurements of slope flow systems taken at six different sites. Ten data sets exhibited upslope flows filling the entire CBL and often exceeding it. Over the 9° west facing slope at Azuma Takayu, however, the upslope flow was only 100 m in a CBL of depth 180 m. The authors did not provide information on synoptic wind, ridge height, and return flow.

Over a 10° west-north-west facing slope with a ridge height of 1000 m in the Rhine Valley near Strasbourg, France, the upslope flow usually filled the entire CBL (Koßmann and Fiedler, 2000). In the early afternoon on September 16, 1992, however, measurements showed a CBL approximately twice as deep (850 m) as the upslope flow layer and weak winds with unsteady direction in the upper half of the CBL. In this case, west-north-westerly synoptic winds of 5-10 m s^{-1} opposed the return flow.

Orville (1964) developed a two-dimensional numerical model of a triangular mountain ridge with a height of 1 km and a slope angle of 45°. Initially, excess potential temperature and vorticity showed upslope flows filling the entire thermal boundary layer, but after 60 minutes the thermal boundary layer (TBL) depth exceeded the ridge height and a return flow occurred within the TBL. After 96 minutes, the upslope flow occupied only half the depth of the TBL and a fairly strong return flow occupied the upper half of the TBL.

As mentioned in the previous section, the analytical model by Kondo (1984) predicts a two-cell convection up to a ridge height-CBL depth ratio of $H_R/H_s = 2$. In a three-dimensional numerical model run over a 0.6° slope of ridge height 625 m Kondo (1984) found an upslope flow of approximately 600 m depth and an even deeper, slightly weaker return flow. The author estimated a CBL depth of 2100 m from his analytical model, suggesting that two-cell convection is associated with return flows within the CBL.

When the bottom surface of a tilted stratified water tank was uniformly heated, Deardorff and Willis (1987) observed upslope flows and return flows within the mixed layer, but the authors did not further investigate this situation because "in order that there be a net mean flow within the mixed layer in the upslope direction, extra heating coils were added at the upslope wall to simulate more closely cases of atmospheric interest."

A water-tank model of diurnal heating and cooling cycles over a symmetric triangular mountain showed closed circulation cells within the CBL for some parameter settings, which appear to coincide with a ridge height-CBL depth ratio of $H_R/H_s < 0.6-0.7$ (Chen et al., 1996).

The analytical model by Vergeiner (1982) based on an energy argument predicts the possibility of closed slope flow circulations within the CBL, in agreement with Vergeiner's personal communications with motor glider pilots. Partly based on Vergeiner's model, Haiden's (1990) analytical model also permits closed slope flow circulations within the CBL. However, the relationship between return flow and CBL must be specified and cannot be derived from the models.

The observational, numerical, experimental, and analytical studies that I reviewed in this section demonstrate that upslope flows under most circumstances fill the entire CBL, and that return flows are either weak or non-existent. However, there is also evidence scattered over many decades of research for upslope flow systems exhibiting strong return flows within the CBL. In this dissertation I add more evidence for the latter case and an explanation of the phenomenon by the combined use of field observations, physical scale modeling, and analytical studies.

1.4 Research Approach and Outline of Thesis

In the atmospheric science we have four tools available to investigate a question: field observations, physical scale modeling, analytical studies, and numerical modeling (Figure 1.4). In this dissertation I will make use of the first three tools to investigate the questions posed in section 1.1 on page 1.

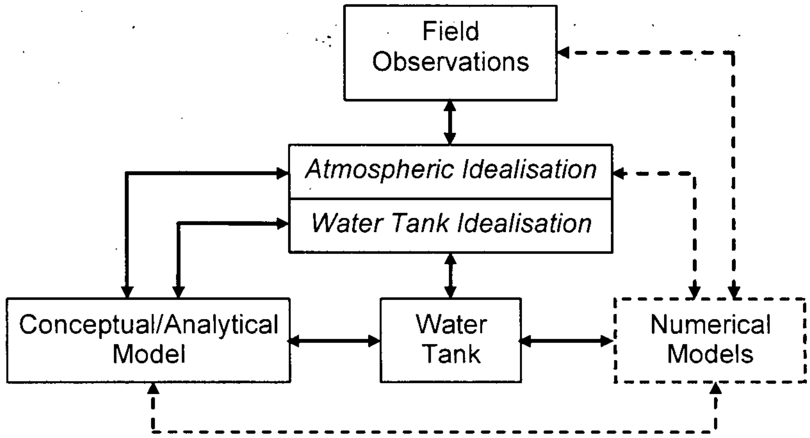

Figure 1.4: Schematics of research approach.
Solid lines and boxes are covered in this thesis; dashed lines and boxes are suggestions for future research and collaborations. The atmospheric idealisation (AI) is a mathematical model of the real conditions at the field site; the water-tank idealisation (WTI) is a mathematical model of the real water tank and a small scale version of the AI using water rather than air as the fluid.

This dissertation contains three major chapters. In chapter 2, I present the field observations of upslope flows during the Pacific 2001 Air Quality Field Study. In chapter 3, I introduce and scale atmospheric idealisations (AI) and water-tank idealisations (WTI) and test the scaling against the field observations. Chapter 4 is devoted to water-tank observations and a simple conceptual model of the observations. Water-tank (Figure 1.5) and conceptual model are both over simplifications of the true topography at the field site. They link to the field observations indirectly via AI and WTI, which are idealised representations of field and water-tank observations. The underlying assumption is that the observed phenomena are independent of particular details at the field site.

In chapter 5 I will conclude the main part of the thesis with a discussion of the interrelationships between observations, water-tank experiments, and the conceptual model and draw general conclusions. Originally I had planned to cover numerical modeling in my thesis research but when I started running the first water-tank experiments I realised that the experiments would generate a wealth of data and information, more than needed to fill a dissertation. A number of researchers suggested collaborations to compare water-tank results with meso-scale model runs and large-eddy simulations (LES). These and other suggestions for future research are also included in chapter 5. The appendices cover a derivation of the

Prandtl model from first principles (Appendix A), and additional material on scaling (Appendix B) and water tank (Appendix C).

In July 2001 I was sitting in a hot little pump house in Minnekhada Park watching over the laptop that controlled the nearby Doppler sodar. With little else to do I looked at the sodar data in a spreadsheet and found a strong return flow, which was clearly within the CBL that Paul Bovis with a tethersonde and Kevin Strawbridge with a lidar were observing at the same time. Being new in the field it took weeks before I learnt that this was something "exciting"; indeed it was and has fascinated me ever since. I started off by asking one question: Under which conditions do upslope flow systems exhibit closed circulations within the CBL? In the course of my research the question itself proved imprecise and I formulated and addressed the research questions given in section 1.1 on page 1. Many more questions remain for future research.

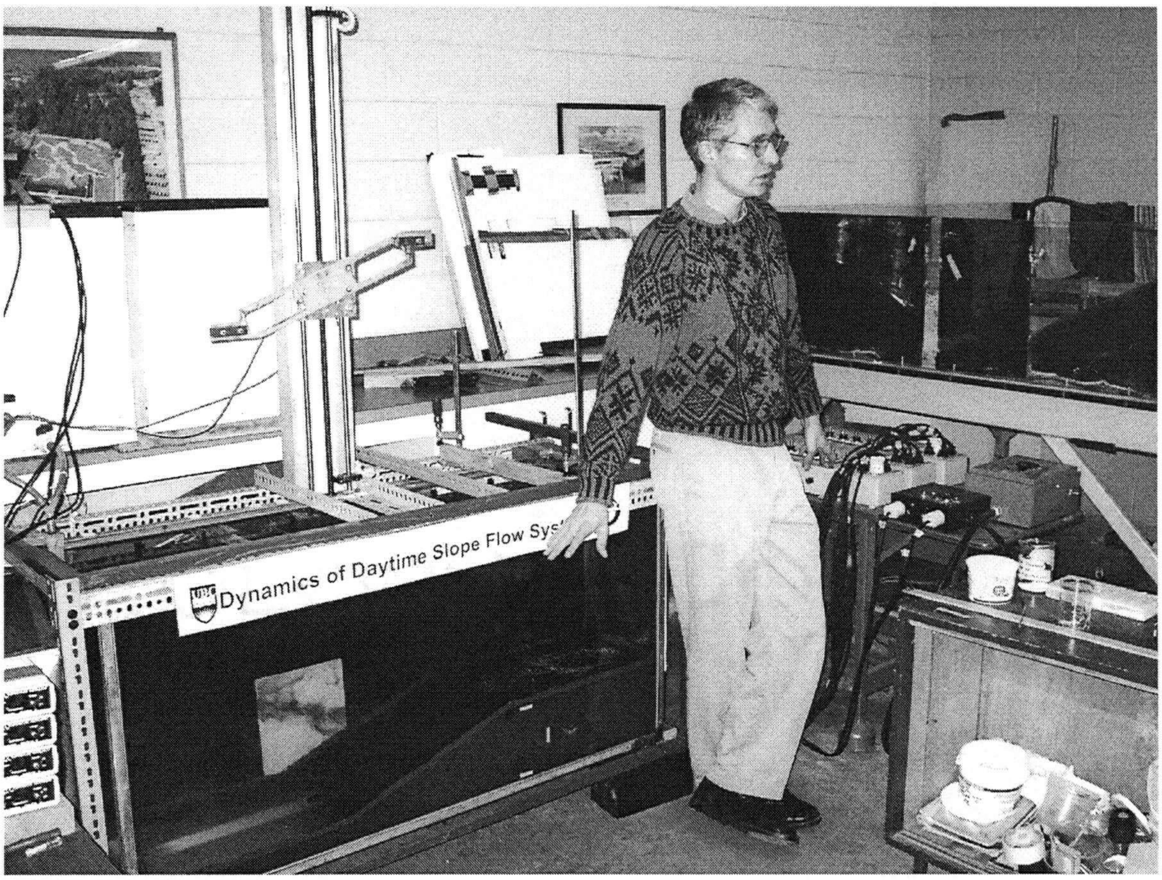

Figure 1.5: Photograph of the water tank.
Heater controls are shown on the right and two-tank filling system in the left background. Technical details are provided in Appendix C.

2 Field Observations during Pacific 2001

The observations of upslope flow systems in a satellite study to the Pacific 2001 Air Quality Field Study (Reuten et al., 2005) are the basis and motivation of my thesis research and are the starting point of this dissertation. Section 2.1 provides information on the measurement site and topography, synoptic weather, and instrumentation. In section 2.2, I present the observations of July 25-26, 2001. In section 2.3 I discuss the results and draw conclusions.

2.1 Experimental Layout and Methods

As a satellite study of the Pacific 2001 Air Quality Field Study (Li, 2004), we took measurements of the convective boundary layer (CBL) and of daytime slope flow systems near the foot of a steep slope. The goal was to investigate the relationship between slope flow systems and the CBL, and the compensation of mass transport in upslope flows. In this section I will introduce the location and topography of the upslope flow study, the synoptic weather situation during our observations, and the instrumentation.

2.1.1 Location, Topography, and Period of Observations

The Lower Fraser Valley (LFV) is nearly flat, mostly lower than 100 m above mean sea level (MSL), and has an approximately triangular shape narrowing from about 100 km width at the Strait of Georgia in the west to about 2 km approximately 90 km inland to the east (Figure 1.1 above). It is bounded by the Coast Mountain Ranges to the north and the Cascade Ranges to the south-east, which have heights of about 2000 m and 1000 m MSL, respectively. Tributary valleys interrupt the mountain range barriers. The Strait of Georgia causes diurnal cycles of sea-land breezes during fair weather conditions in summer (Steyn and Faulkner, 1986). Slope flow characteristics were measured at Minnekhada Park, shown by the rectangle in Figure 1.1.

Figure 2.1 shows the local topography at the Minnekhada site and the location of the deployed instruments. The dashed line indicates the direction of the steepest slope as seen from the sodar. The slope angle is approximately 19° and the ridge height about 760 m MSL. The slope is covered with dense mixed deciduous and coniferous forest. The adjacent plain is predominantly agricultural, grassland, and water surfaces, all within a few metres MSL.

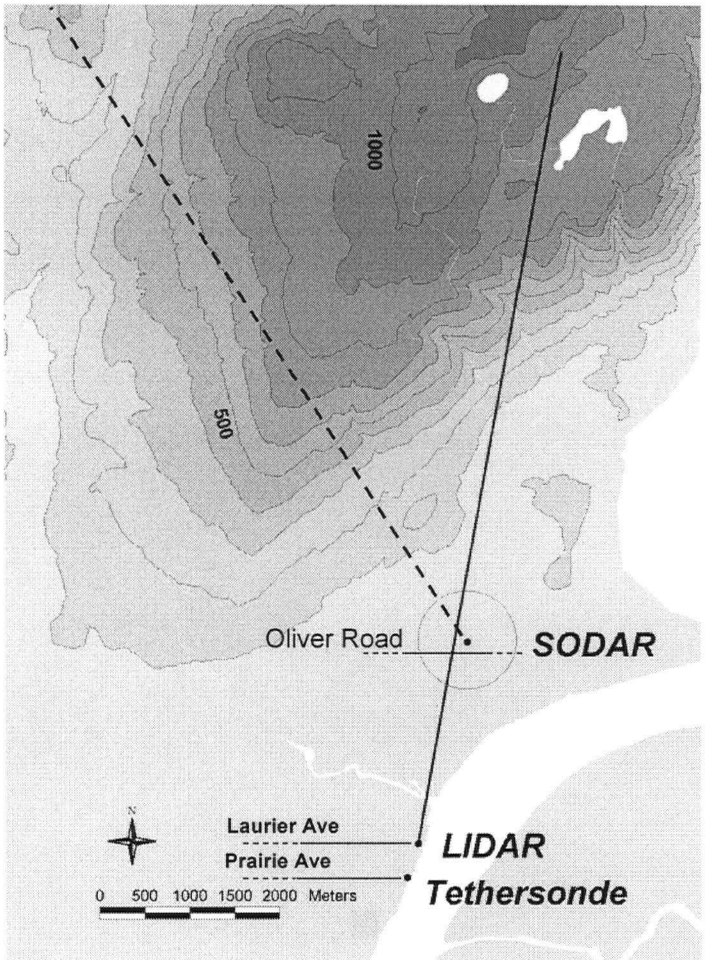

Figure 2.1: Contour plot of Minnekhada Park (see Figure 1.1).

Numbers are heights MSL in metres. Contours are shown every 100 m, darker shades of grey representing higher altitudes. White areas are water surfaces. Also shown are the locations of the tethersonde, lidar, and sodar. The line running north-north-east from the lidar shows the direction of the elevation scans, the line running north-north-west from the sodar indicates the approximate line of steepest ascent up the slope, and the circle centred at the sodar indicates the area at the mean maximum height of the CBL from which the pulse beams are backscattered. (Based on Fig. 2 in Reuten et al., 2005)

Sufficiently complete data on days with suitable weather conditions are available and reported here for the morning hours of July 25, 2001 and the entire daytime of July 26, 2001. For time of day I use Pacific Daylight Time (PDT). At the measurement site on July 25-26, 2001, local solar noon occurred at 1317 PDT, sunrise and sunset at approximately 0534 PDT and 2100 PDT, respectively.

2.1.2 Synoptic Weather

The synoptic conditions on July 25-26, 2001 were dominated by an extensive high-pressure system centred over the Eastern Pacific with a weaker high-pressure system centred over the central British Columbia (BC) interior (Figure 2.2). Synoptic surface winds were approximately 2.5 m s^{-1} roughly from the west.

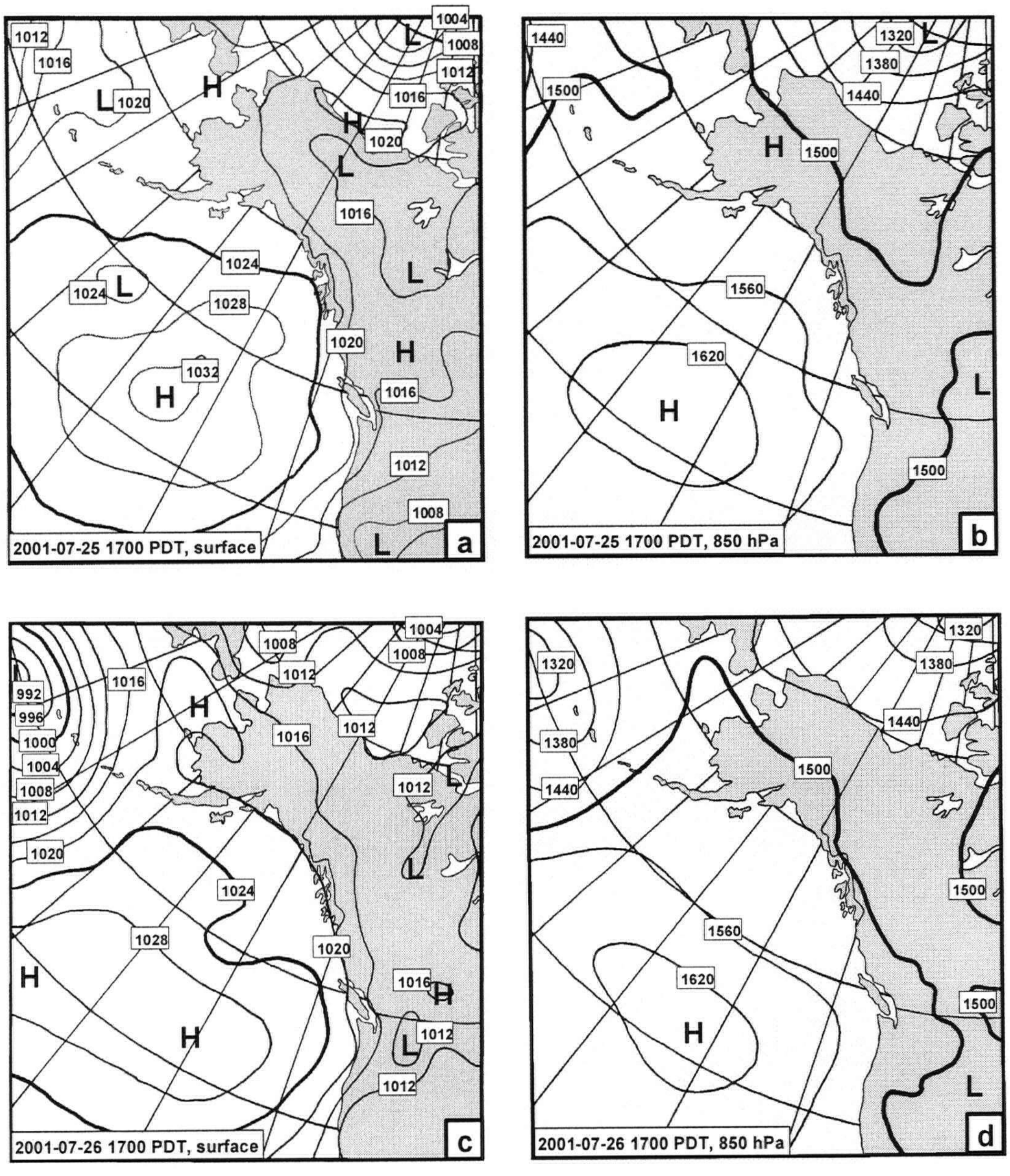

Figure 2.2: Synoptic charts for July 25 (a and b) and July 26 (c and d), 2001, at 1700 PDT.
The charts are based on CMC (Canadian Meteorological Centre) analyses. Contour lines on surface charts a *and* c *are sea-level pressure in hPa; contour lines on 850-hPa charts* b *and* d *are geopotential height in m. (Based on Fig. 4 in Reuten et al., 2005)*

Similar conditions prevailed at the 850-hPa level with light westerly winds of 2.5-5 m s^{-1}. The 850-hPa level is approximately 700 m above the mountain top.

Synoptic conditions on July 26 were similar to those on the previous day. A comparison of Figure 2.2a and Figure 2.2c shows that the high-pressure system centred over the Eastern Pacific had moved slightly farther eastward, as did the high-pressure system centred over BC. The weak low-pressure system over northern California had moved northward into eastern Washington. Westerly surface winds were approximately 2.5 m s^{-1}.

The 850-hPa chart for July 26 (Figure 2.2d) shows that light westerly winds prevailed due to a weak geopotential gradient. The high-pressure system had moved eastward and was centred over the Eastern Pacific west of Oregon.

2.1.3 Instrumentation

During the field study I operated a Scintec FAS 64 Doppler sodar to take vertical profile measurements of the 3 wind components with a vertical range of 20-1000 m. This allowed me to investigate the flow structure in the entire CBL, which reached a maximum depth of approximately 1000 m. The manufacturer-specified accuracies are 0.1-0.3 m s^{-1} for horizontal wind speed, 0.03-0.1 m s^{-1} for vertical wind speed, and 2-3° for wind direction at wind speeds >2 m s^{-1}. The thickness of the resolved vertical layers in our parameter settings was 50 m at heights 110-310 m and 30 m at all other heights between 20 and 1000 m. Each averaging cycle lasted approximately 20 minutes. The airflow components were determined by integrating all backscatter spectra over the entire 20-minute cycle. Due to the remoteness of the Minnekhada site and because no obstacles were near the sodar's beam, background noise or echo corrections were not necessary. I used the entire available pulse frequency range of 1650-2750 Hz. To optimise the signal-to-noise ratio (SNR), I operated the sodar in full multi-beam mode, i.e. one pulse sent vertically and one simultaneous pulse pair sent at 29° and 22° from the vertical for each of the four directions east, west, north, and south. The circle around the sodar location in Figure 2.1 indicates the horizontal spread of the pulse beams at the mean maximum CBL height. During daytime, high SNR occurred throughout the entire CBL. Above the entrainment zone the SNR was mostly low, a known effect which has been used by other investigators (e.g. Neff, 1990) to estimate the height of the CBL. Because the effect was inconsistent in our observations I did not use the SNR to determine CBL height. Sodar measurements were continuous except for approximately 1 minute of system integration at the end of each averaging cycle and manual adjustments of parameter settings a few times each day, which typically caused interruptions of a few minutes.

At a nearby site on the adjacent plain (Figure 2.1) Kevin Strawbridge operated a RASCAL (Rapid Acquisition SCanning Aerosol Lidar) to measure the backscatter of particulate matter (see Strawbridge and Snyder, 2004). Lidar data were obtained over a 12-km range at a resolution of 3 m along the beam axis and a scan speed of 0.2° per second. Each RHI (range height indicator) scan took about 5.5 minutes to acquire and covered an elevation range from 3° to 70° above the horizon. RHI scans were performed continuously at four different azimuth angles, every fourth scan passing over the sodar (solid line in Figure 2.1).

Paul Bovis flew a tethered balloon near the lidar with a standard meteorological package (AIR IT53 AH) to measure temperature, wind speed, wind direction, and specific humidity. For the two time periods presented here, the morning of July 25 and the daytime of July 26, 2001, I used a total of 3 ascents and 16 descents. About one half of all flights took approximately 15-20 minutes per ascent or descent with a vertical resolution of roughly 10 m. The remaining flights carried additional instrumentation so that each ascent or descent took approximately 30-40 minutes and the vertical resolution was roughly 5 m. The maximum height of most flights exceeded 1000 m MSL.

2.2 Observations of Closed Slope Flow Systems versus Mountain Venting

The results are presented in three steps. In the first step I show how I used the lidar data to establish the top of the CBL based on the agreement between the lidar backscatter boundary layer (BBL) and the thermal boundary layer (TBL). Lidar RHI scans intersected the beam range of the sodar at a height from 130 m to 1000 m MSL. Dr. Kevin Strawbridge used the algorithm detailed in Strawbridge and Snyder (2004) to determine the top of the BBL, which can be identified as a highly scattering, i.e. aerosol-rich, layer. After smoothing the raw backscatter data, the algorithm determines the height of the largest gradient in the backscatter profile around a first threshold estimate of the BBL depth. To verify the algorithm I visually estimated from lidar scans instantaneous values of the mixed layer depth z_i, which ranged from approximately the bottom to the top of the entrainment layer. The time or horizontal averages $\overline{z_i}$ are a measure for the mean mixed-layer depth at the midway point of the entrainment zone and agree well with the output of the algorithm.

When available and of sufficient quality I used my surface temperature measurements at the sodar site and vertical potential temperature profiles from Paul Bovis's tethersonde flights to determine the TBL depth as the neutral buoyancy height of near-surface air parcels (parcel method). In some cases this alone was inconclusive and I consulted vertical profiles of relative humidity (RH) to verify where RH dropped quickly and compared with an earlier or later tethersonde flight.

Even over flat terrain there will be some disagreement between BBL and TBL depth when determined as explained above. This is not of great concern for the investigation in this dissertation. As long as the fairly large error bars overlap I will assume that BBL and TBL depths are equally representative measures of the CBL depth. Of interest are only discrepancies, which are clearly identifiable as layering of one boundary-layer characteristics within the other, for example a thermal layering within the BBL.

The second section shows the vertical wind profiles I obtained with the Doppler sodar at the foot of the mountain slope. In the third section I present estimates of the mass transport over the slope. The final section contains an analysis of larger scale flows (synoptic winds, sea breeze, and valley flows) and their potential impact on the slope flow observations.

2.2.1 Convective Boundary Layer Height

When I compared the TBL and BBL a number of problems arose, exemplified by Figure 2.3 and Figure 2.4. Firstly, the horizontal position of the tethersonde is at -500 m relative to the lidar, and the lidar never scanned over the tethersonde position. From Figure 2.3 it is apparent that the BBL depth does not remain constant over the slope, a phenomenon that has been demonstrated by previous investigators such as Vogel et al. (1987) and de Wekker (1997). Our observations confirm previous observations that the BBL follows the underlying topography early in the day but becomes more horizontal as the BBL grows deeper. As a measure for the BBL height I averaged the minimum and maximum BBL heights over the 0 to 2500 m range of the lidar RHI scans for July 25. Over this horizontal range the BBL height is over flat ground, since the slope is more than 2500 m from the lidar. The BBL height determined with this method was in good agreement with point measurements of the BBL height above the sodar. For July 26 I therefore used the point measurements to simplify the analysis.

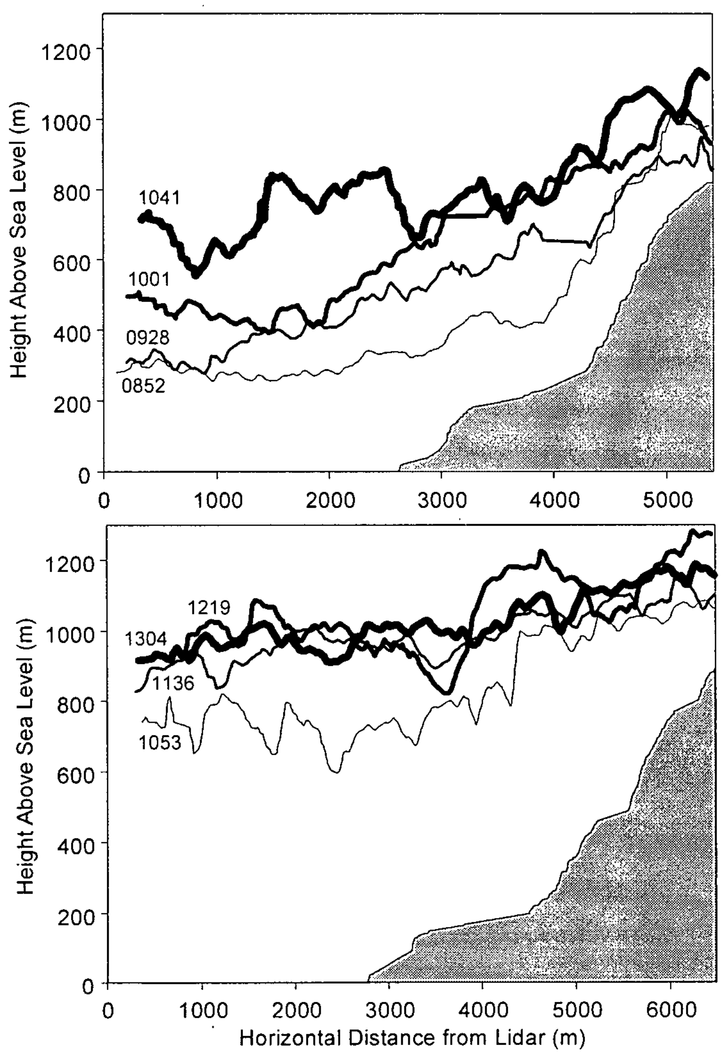

Figure 2.3: BBL depth above MSL at different times on July 25, 2001.
The four curves in the upper panel represent with increasing line width the BBL depth for 0852, 0928, 1001, and 1041 PDT, respectively. Similarly the lower panel shows BBL depth at 1053, 1136, 1219, and 1304 PDT. I smoothed the data with a 21-point uniform moving average, corresponding to averaging over a horizontal range of approximately 60m. The grey area shows the topography. Notice the slight differences in topography between the two panels due to different scanning angles. (Based on Fig. 6 in Reuten et al., 2005)

Secondly, it proved very difficult to determine TBL heights from the tethersonde data because of large variations in moisture and temperature measurements and an ambiguous entrainment zone at the top of the CBL, which contains a mixture of CBL air and free tropospheric air. In many cases I could only succeed by interpolating between those tethersonde profiles where the TBL heights were clearly expressed. I supplemented the tethersonde data by using surface temperature measurements, which I took irregularly at the sodar site, to determine the neutral buoyancy height of surface air parcels.

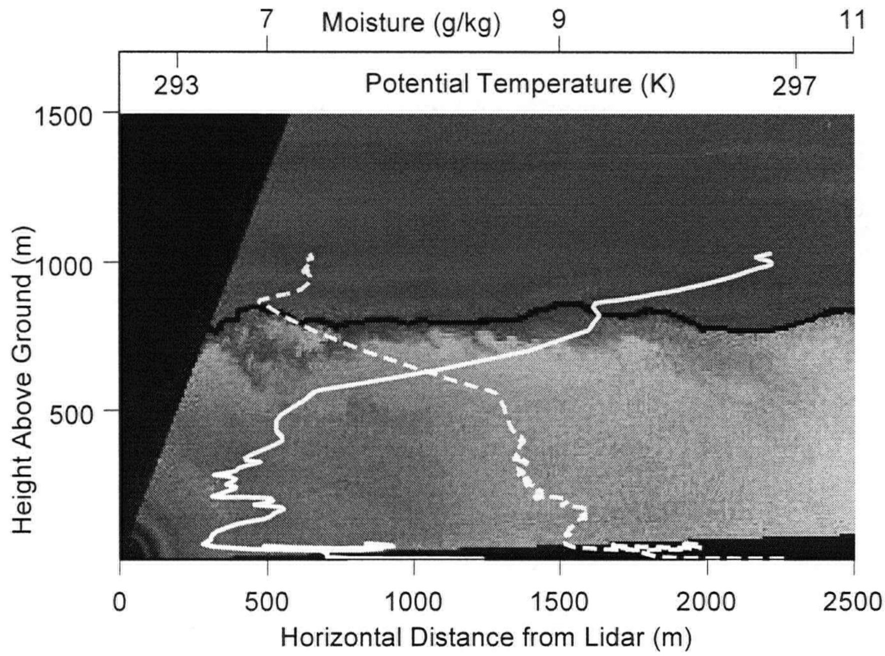

Figure 2.4: Tethersonde profiles superimposed on a RASCAL RHI scan.
The white solid line shows potential temperature and the white dashed line shows specific humidity measured with a tethersonde on July 26, 2001 from 1314-1355 PDT. The RASCAL RHI scan was taken on July 26, 2001 at 1350-1353 PDT. Lighter shades of grey correspond to greater aerosol loading. The bold dark line at the top of the light grey aerosol layer indicates the top of the BBL. The tethersonde profiles were smoothed by application of a seven point, binomially weighted moving average. (Based on Fig. 5 in Reuten et al., 2005)

It is possible that the advective processes over the slope affected the vertical profiles of potential temperature and moisture even as far as 3500 m away from the slope, making it more difficult to interpret the data. For example, a tilting of the potential temperature profile from the vertical within the TBL similar to the one in Figure 2.4 was anticipated by Prandtl in 1942 and demonstrated by Schumann (1990) in his large-eddy simulation. The potential temperature profile in Figure 2.4 was determined from an ascent sounding and the tilting could be the result of non-stationarity during the time it takes the tethersonde to rise; that this was not the cause is demonstrated by the same tilting seen in the descent sounding immediately following the one in Figure 2.4 (Figure 2.5).

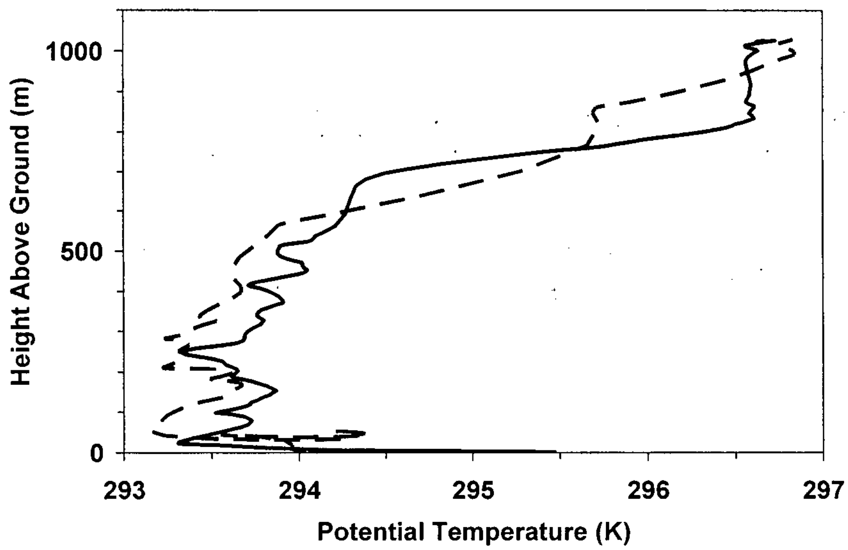

Figure 2.5: Potential temperature profile determined from tethersonde ascent and descent.
Potential temperature soundings on July 26, 2001 (smoothed by application of a seven point, binomially weighted moving average) determined from a tethersonde ascent from 1314-1355 PDT (dashed line, same as solid line in Figure 2.4) and a descent from 1355-1431 PDT (solid line).

Thirdly, lidar scans required only a few minutes while the tethersonde flights typically took 40 minutes. During the morning hours the boundary layer height changed greatly within 40 minutes. In the afternoon, on the other hand, the boundary layer height remained fairly constant in time but often exceeded the maximum elevation of the tethersonde flights. The increase of moisture with height above 800 m (Figure 2.4) is unlikely to be a measurement error. It could be that a return flow advected air of higher moisture content horizontally from above the mountain plateau onto the adjacent plain. I will revisit this point in the next section.

Despite the difficulties in determining the TBL, Figure 2.6 shows good agreement between the TBL and the BBL. Because of this agreement I decided to make use of the more abundant and precise lidar data to establish the relationship between the slope flow system and the CBL, and I equated the CBL with the BBL.

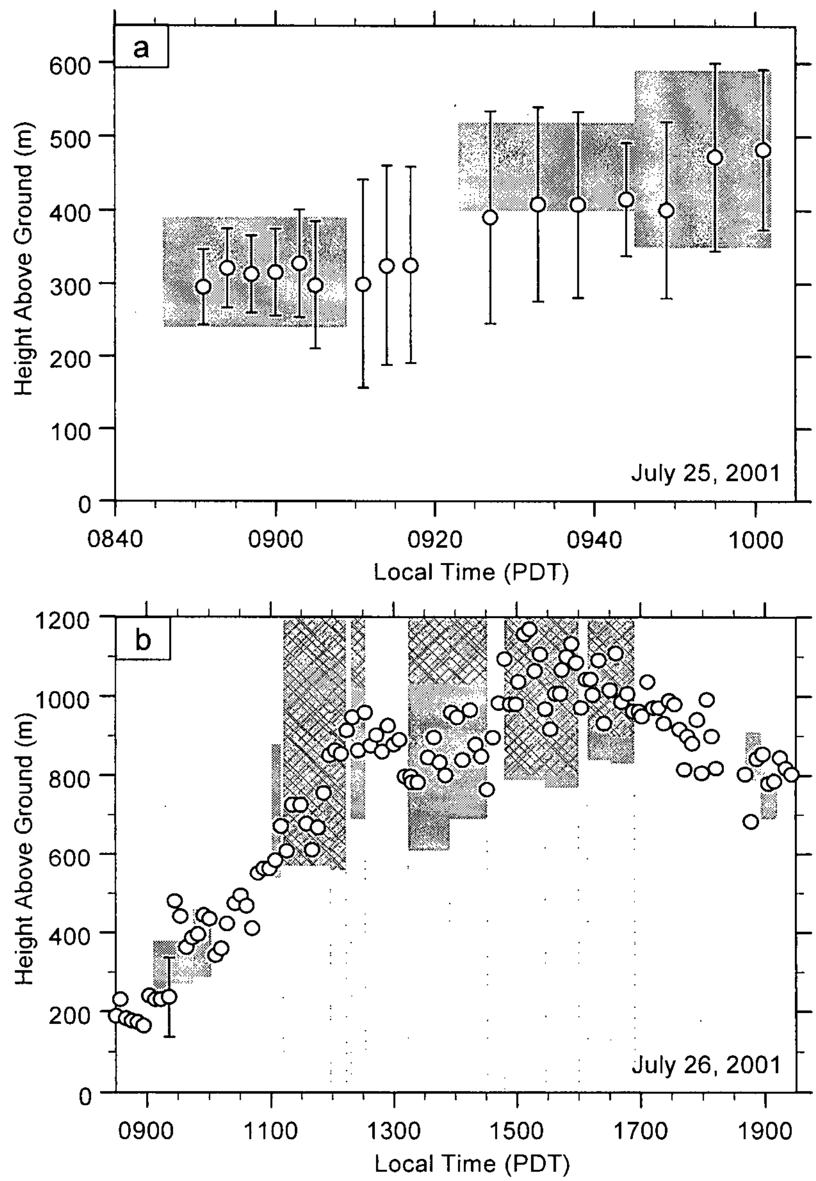

Figure 2.6: Time development of the entrainment zone of the TBL and the BBL on July 25 (a) and July 26 (b), 2001.

Grey areas show the entrainment zone of the TBL, open circles show the BBL, and the error bars show the maximum range of overshooting thermals and entrainment of the BBL. For July 26, I showed the error bar at only one of the open circles to avoid overloading the figure. Note the difference of time and height scale between (a) and (b). In the morning of both days, I could determine the lower and upper limit of the entrainment zone. However, after 1100 PDT on July 26, the top and sometimes also the bottom of the entrainment zone exceeded the maximum elevation of the tethersonde flights. In these cases, the grey area shows the range from the bottom of the entrainment zone to the maximum flight elevation, while the cross-hashed areas extend from the maximum flight elevation to the upper limit of the scale. The maximum flight elevations of the tethersonde ranged from less than 600 m to more than 1000 m. (Based on Fig. 7 in Reuten et al., 2005)

2.2.2 Slope Flow System versus Convective Boundary Layer

In this section I relate sodar measurements of wind speed to CBL estimates from lidar measurements at the foot of the mountain slope.

Figure 2.7 shows a time-height section of the horizontal along-slope components of the wind velocity over a 4-hour morning period on July 25, 2001. After 0850 PDT, an upslope wind gradually strengthened to about 3-5 m s^{-1} as it grew to a depth of approximately 500 m by late morning. During the same period, a return flow of approximately equal strength and depth was observed above the upslope flow layer. Initially the return flow occurred above the CBL, but when the CBL had reached a depth of about 500 m at 0930 PDT, the return flow occurred within the CBL, and the depth of upslope flow layer and the return flow layer aloft were each approximately half the depth of the CBL. The CBL stopped growing at about 1130 PDT and maintained a depth of about 1000 m until observations ended at 1230 PDT.

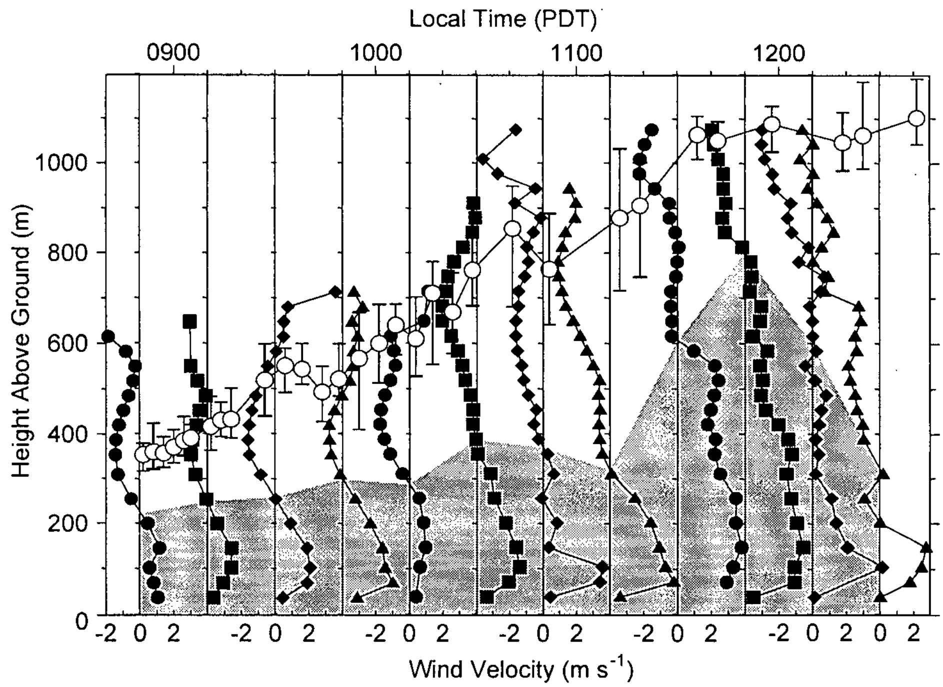

Figure 2.7: Time-height section of the along-slope component of the horizontal wind vectors above the Doppler sodar for July 25, 2001.

Positive values (grey shading) are upslope flows, negative values are return flows. Inner tick marks on the horizontal axis show 1 m s^{-1} intervals. Open circles show the CBL depths as determined from lidar measurements. The error bars show the range of overshooting thermals and entrainment within the horizontal range of the scanning cone of the sodar (circle in Figure 2.1). (Based on Fig. 8 in Reuten et al., 2005)

On July 26 (Figure 2.8) observations are less conclusive. A comparison with Figure 2.7 shows that both CBL and upslope flow grew more slowly. It took until about 1500 PDT for the CBL to reach its maximum depth of about 1100 m. At 1050 PDT a return flow started, at first above the CBL and then, after 1110 PDT, within the CBL. The CBL depth at that time was about 600 m, slightly more than the 500 m on July 25, when the return flow occurred underneath the CBL top.

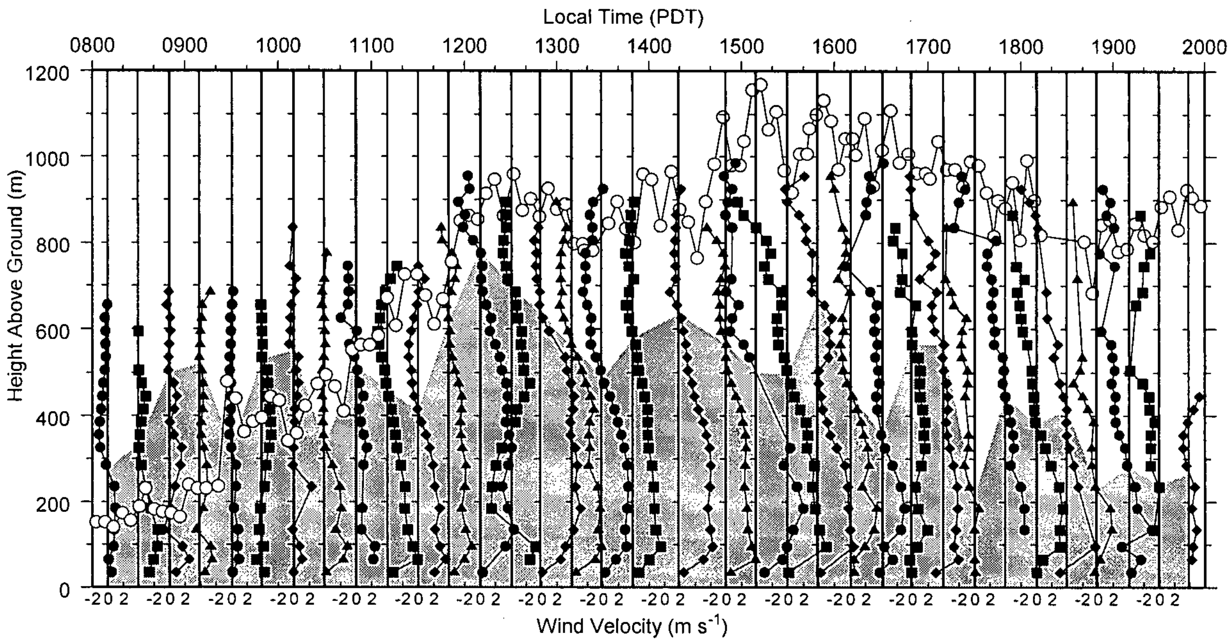

Figure 2.8: As Figure 2.7 but for July 26, 2001, and without error bars.
(Based on Fig. 9 in Reuten et al., 2005)

A direct comparison of the top of the upslope flow and the return flow with the top of the CBL for both days is shown in Figure 2.9. For July 25, the top of the upslope flow scatters around the dashed line indicating half the height of the CBL. The top of the return flow scatters along the solid line indicating the height of the top of the CBL. For July 26, morning measurements initially show the top of upslope and return flow both exceeding the CBL depth. From late morning until evening the situation is comparable to that of the morning of July 25.

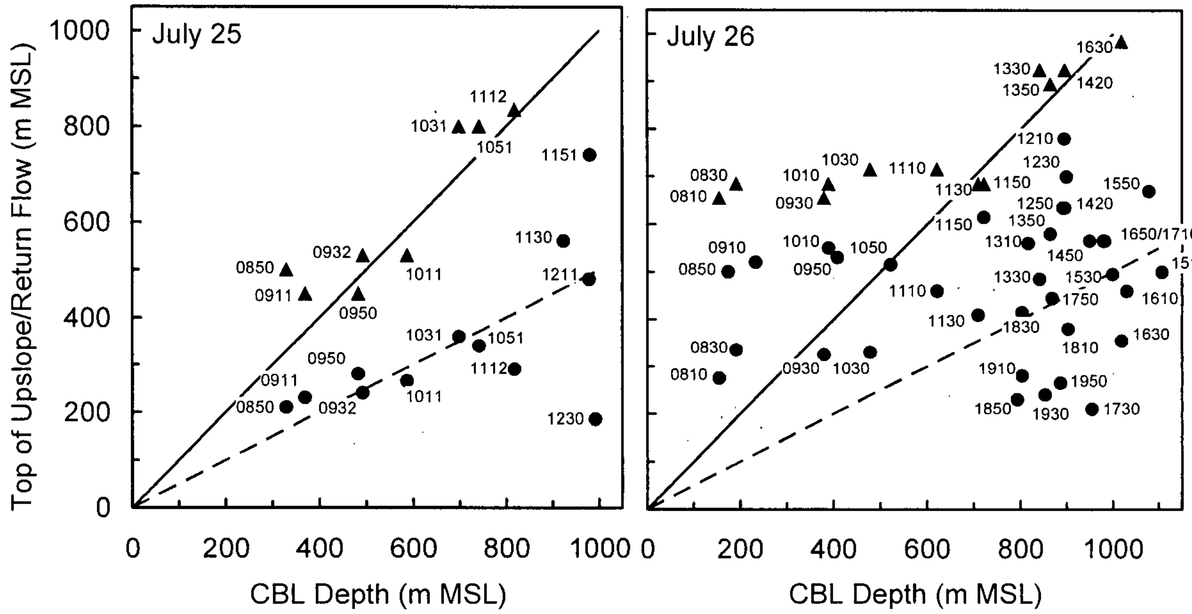

Figure 2.9: Comparison of upslope flow and return flow depths with CBL depth.
Top of the upslope flow (circles) and the return flow (triangles) plotted versus CBL depth for July 25 (left) and July 26, 2001 (right). The time (in PDT) of each measurement is shown next to the data points. Data for the top of the return flow are missing usually when the value exceeded the 1000-m vertical range of the Doppler sodar and in some cases because of a weak sodar signal above the CBL. The dashed and solid line represent half of and the full CBL height, respectively. (Based on Fig. 10 in Reuten et al., 2005)

2.2.3 Volume Transport

The volume transport in the along-slope direction per lateral distance across the slope is given by

$$\int_0^{H_s} U(z)\,dz \approx \sum_{j=1}^{n} U(z_j)\,\Delta z_j \qquad (2.1)$$

where $U(z)$ is the upslope flow velocity at height z and H_s is the CBL depth. I divided the CBL into n layers, where the j^{th} layer has a depth of Δz_j. $U(z_j)$ is the average slope wind component in the j^{th} layer.

For July 25, the volume transport appears unbalanced and unsteady over short periods of time (Figure 2.10). However, averaged over the entire morning period, the volume transport of the downslope flow (446 $m^2\ s^{-1}$) balanced 89% of the volume transport of the upslope flow

($502\ m^2\ s^{-1}$). The discrepancy of $56\ m^2\ s^{-1}$ is within the range of uncertainties in the data. No volume transport is shown for July 26 because it is obvious from Figure 2.8 that the volume transport of upslope and return flow was unbalanced.

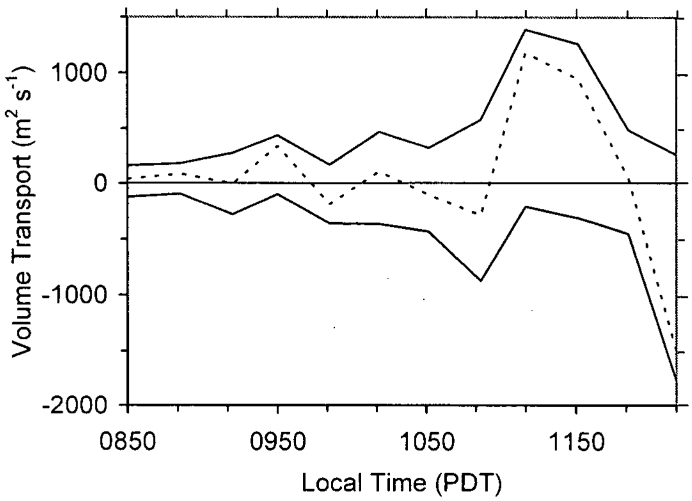

Figure 2.10: Along-slope Volume transport for the morning of July 25, 2001.
The upper solid curve shows upslope volume transport (positive) and the lower solid curve downslope volume transport (negative). The dashed line represents the sum of both. (Based on Fig. 11 in Reuten et al., 2005)

2.2.4 Impact of Larger-Scale Wind Systems

One hypothesis for the recirculation observed on July 25 is advection of larger-scale flows into the slope flow system. Referring back to Figure 1.1 there were three larger-scale wind systems that could modify the daytime slope flow system: synoptic-scale winds, sea breeze, and valley winds, which I will explain first individually in the following sections before discussing their impact on the slope flow system in the discussion section.

Synoptic Winds

The 850-hPa charts for July 25-26, 2001, and the nearest three soundings in Quillayute, Port Hardy, and Kelowna showed westerly to north-westerly winds of 2.5-5 $m\ s^{-1}$ at about 1500 m MSL. The surface charts and the few available sodar measurements above the surface layer for night-time and early morning indicate west-south-westerly CBL winds of roughly $2\ m\ s^{-1}$.

Above 500 m both sodar and tethersonde showed a change of wind direction from southerly to westerly winds with increasing altitude early in the night from July 25 to July 26, in approximate agreement with synoptic weather charts. Hourly wind measurements at Vancouver International Airport (YVR) and Abbotsford Airport (YXX) indicate west-north-westerly synoptic surface winds as will be shown in the following section on the sea breeze. The discrepancies between the different data may be due to differences in forced channelling of the synoptic flow.

Sea Breeze

From Figure 1.1 one expects a westerly sea breeze at the measurement site in Minnekhada Park. Figure 2.11 shows hourly measurements of wind direction, wind speed, temperature and relative humidity for July 25-26 for YVR and YXX. YVR is located right at the east coast of the Strait of Georgia. YXX lies approximately 30 km inland from the ocean to the south-west, which is similar to Minnekhada Park's 35-km distance from the ocean to the west. Both airports are sufficiently far away from the mountains enclosing the LFV to rule out any slope and valley flows at these two locations.

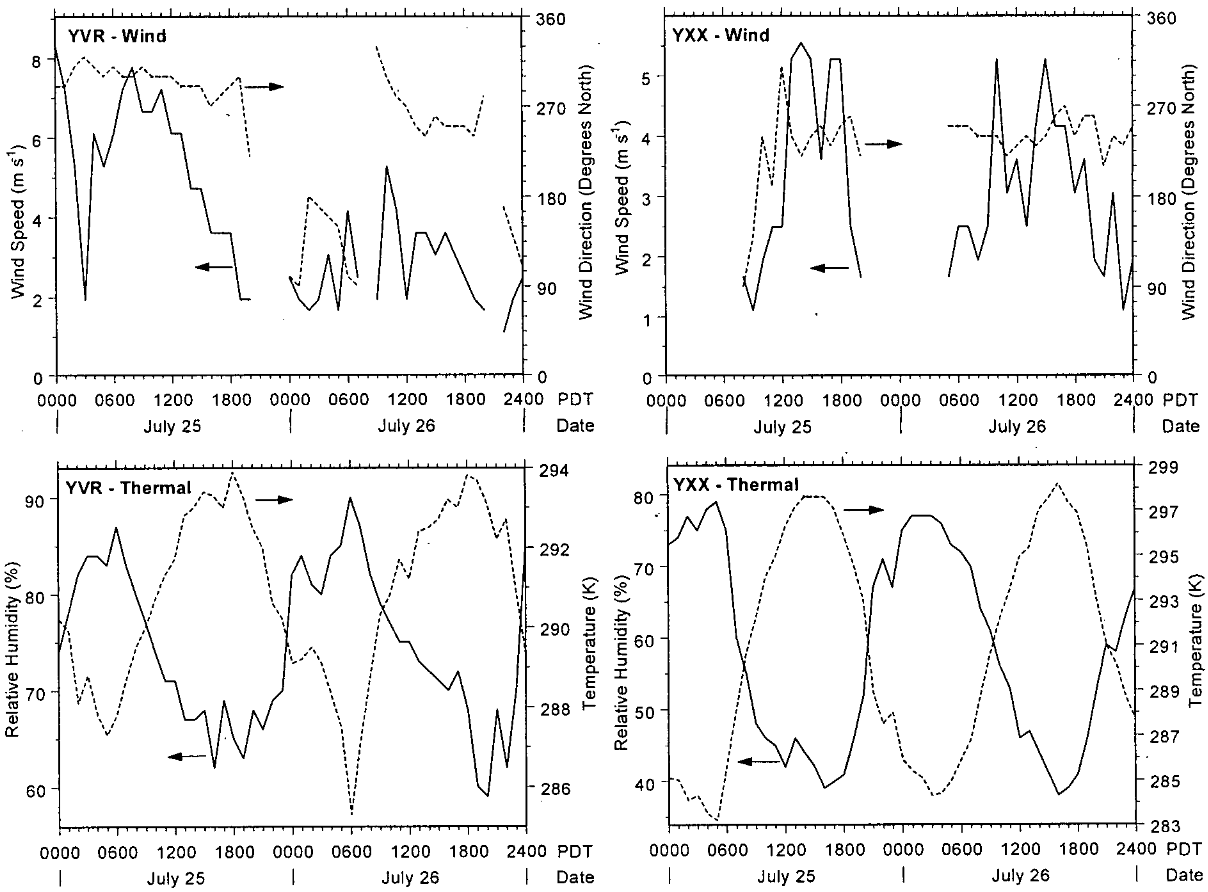

Figure 2.11: Hourly measurements of wind speed, wind direction, relative humidity, and temperature at Vancouver International Airport (YVR) and Abbotsford Airport (YXX) for July 25-26, 2001.

'YVR-Wind' and 'YXX-Wind' show wind speed (solid curves, left vertical axes) and wind direction (dashed curves, right vertical axes). 'YVR-Thermal' and 'YXX-Thermal' show relative humidity (solid curves, left vertical axes) and temperature (dashed curves, right vertical axes). Gaps are missing data. (Based on Fig. 12 in Reuten et al., 2005)

Because there was an onshore synoptic wind, I could not see a sea breeze front in the data and had to look for a time period of transition to an observable sea breeze. The data from YVR in the night and early morning of July 25 show west-north-westerly synoptic wind with no indication of a land breeze. At about noon on July 25, the wind started shifting to the expected westerly sea breeze direction. This minor shift was accompanied by a very weak temperature decrease and relative humidity increase between 1100 and 1200 PDT, while wind speed decreased from about 7 m s^{-1} in the late morning to about 2 m s^{-1} in the evening. Data for YVR on the following day were easier to interpret. In the late evening of July 25, winds shifted to the south-easterly land breeze direction. The land breeze ceased between 0700 and

0900 PDT on July 26 and was temporarily replaced by a north-westerly wind. Toward noon, the direction changed slowly to the westerly sea breeze direction with a wind speed of approximately 4 m s^{-1}. The temperature and relative humidity data for YVR on July 26 partly support this picture. Between 1100 and 1200 PDT, temperature briefly dropped while relative humidity remained constant. Surprisingly, the strongest signals for a sea breeze in the temperature and relative humidity data occur between 1600 and 1700 PDT on both July 25 and 26, 2001. Unfortunately, the wind data provide inconsistent information on the sea breeze.

In contrast to YVR, YXX further inland showed a decaying weak easterly land breeze between 0700 and 0900 PDT on July 25. A slightly stronger north-westerly synoptic wind of about 2.5 m s^{-1} replaced the land breeze until about noon. Between 1200 and 1400 PDT winds adjusted to the south-westerly sea breeze direction at YXX with speeds of about 5 m s^{-1}. At average wind speeds of 5-7 m s^{-1} between YVR and YXX the sea breeze must have started about 1.5 hours earlier in YVR than in YXX, which is in good agreement with the identification of a sea breeze transition between 1100 and 1200 PDT at YVR. Wind data for YXX on July 26 did not clearly show evidence of a transition to sea breeze. An increase of relative humidity and a brief slowing down of the daytime temperature increase between 1200 and 1300 PDT, however, suggest an air mass change associated with a sea breeze initiation, in reasonable agreement with the transition time at YVR.

In conclusion, I estimate the time of a transition to sea breeze for our measurement site at Minnekhada Park at approximately 1200-1300 PDT on both days, July 25-26. The direction of the sea breeze was westerly with strengths of approximately 5 m s^{-1} and 3 m s^{-1} on July 25 and 26, respectively, based on the assumption of a west-north-westerly synoptic wind of about 2 m s^{-1} at the two airport stations. These observations are in good agreement with the sea breeze climatology of the LFV in Steyn and Faulkner (1986).

Valley Winds

Up-valley winds were expected to start several hours after the onset of the upslope flow and fill the entire CBL (Whiteman, 2000). The local topography at Minnekhada Park (see Figure 1.1 and Figure 2.1) suggests that up-valley winds should come from the south-west. Since the wind measurements were made at the edge of the valley mouth it is not clear to what degree valley winds were noticeable. I will discuss this further in section 2.3.

2.3 Discussion and Conclusions

On the first day of observations, July 25, 2001, we observed daytime slope flow systems with a two-layer structure. The bottom half of the CBL was filled with strong upslope flows, while the upper half of the CBL was filled with an equally strong return flow (Figure 2.7-Figure 2.9). Individual 20-minute intervals of wind measurements differed strongly from each other. However, the time-averaged mass transport for the entire morning of July 25 showed an approximate balance between upslope flow and return flow within the CBL. The mass balance and the lidar scans, which did not show any venting of air pollutants out of the CBL, suggest a closed slope flow circulation, which trapped air pollutants within the CBL. In the following sections I discuss three hypotheses for the trapping.

2.3.1 Hypothesis 1: Impact by Larger-Scale Flow Systems

The insets in Figure 2.12 and Figure 2.13 show the direction of the larger-scale wind systems. Both days showed a complex interplay of slope wind systems and larger-scale flows. As with previous analyses the data for July 25 are easier to interpret than for July 26. Only near the surface does the horizontal wind vector indicate pure upslope winds until approximately noon, when most likely an up-valley wind started steering the horizontal wind vectors clockwise (Whiteman, 2000). This influence of the up-valley wind started later at lower altitudes within the upslope flow layer. Above the upslope flow layer, winds were approximately westerly. This cannot be a sea breeze, because the sea breeze started only after 1200 PDT (section 2.2.4).

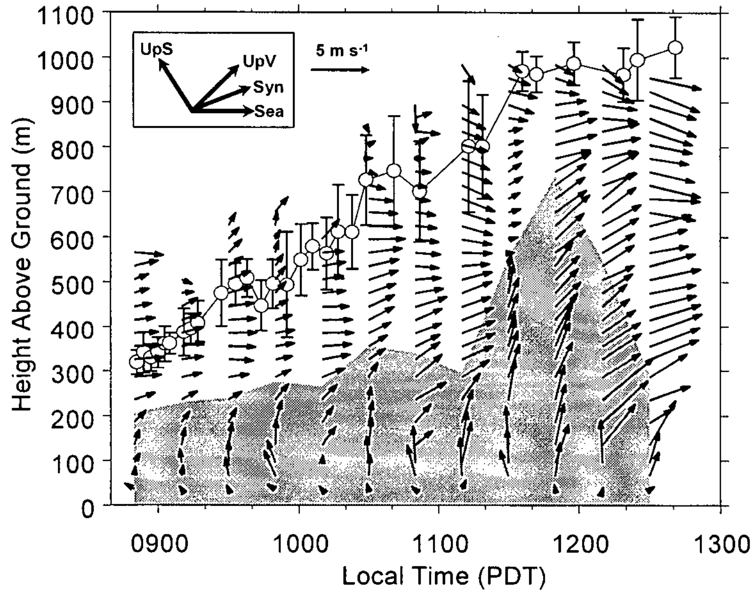

Figure 2.12: Time-height sections of the horizontal wind vector above the Doppler sodar for the morning of July 25, 2001.

Open circles with error bars represent the CBL depth as determined from the lidar scans above the sodar (also shown in Figure 2.7) and grey areas represent upslope flow. Inset shows the expected directions of upslope flow (UpS), up-valley flow (UpV), synoptic wind (Syn), and sea breeze (Sea). North is up. Also compare with Figure 1.1 and Figure 2.1. Notice that upslope and up-valley flows are not exactly perpendicular because the slope is at the mouth of the valley. (Based on Fig. 13 in Reuten et al., 2005)

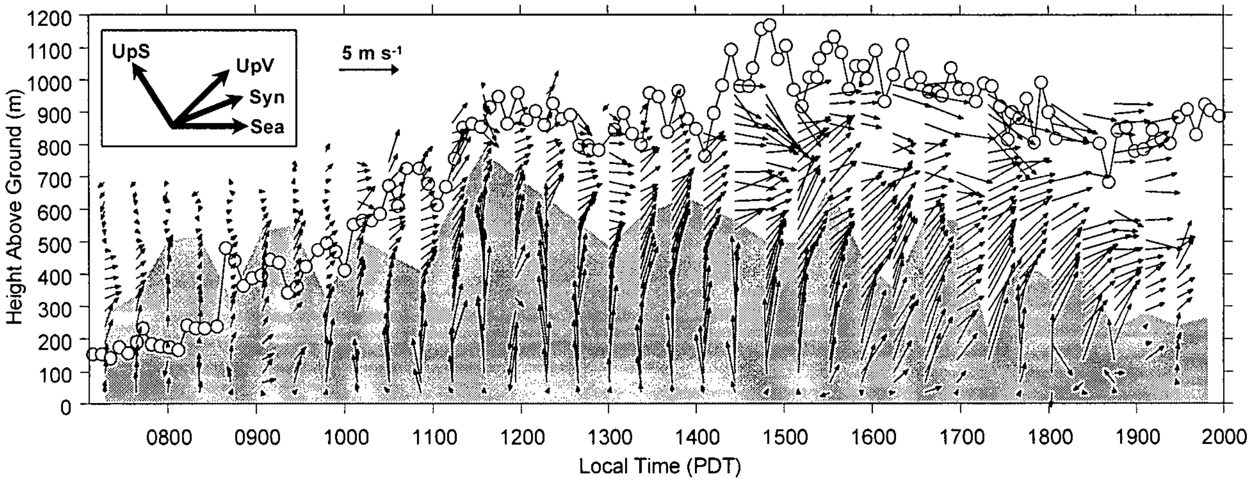

Figure 2.13: As Figure 2.12 but for July 26, 2001.

(Based on Fig. 14 in Reuten et al., 2005)

I cannot give a conclusive explanation for the observed wind directions but suspect a superposition of the synoptic wind with an upslope flow in the bottom part of the CBL and with a return flow in the upper part of the CBL. Any northerly synoptic wind on the order of 1 m s^{-1} could have caused a measurable net mass transport in the return flow direction. During the morning hours an up-valley flow is added to the wind system, which slowly penetrates downwards from the centre of the CBL. In the afternoon (see Figure 2.13) the wind system seems dominated by the up-valley wind, without a strong contribution from the sea breeze.

On July 26, 2001, we also observed return flows within the CBL, but they occurred much later in the day and did not balance the upslope flows. It is likely that venting of air pollutants occurred earlier on that day. Figure 2.14 shows a short and thin layer of strong aerosol backscatter over the ridge top about 6 km north of the lidar site on July 25 at 1047 PDT (upper panel). In contrast, the lower panel shows a longer and much deeper layer of strong aerosol backscatter moving over the ridge top on July 26 at a similar time in the morning. Also notice layers of strong aerosol backscatter and smooth appearance moving south toward the lidar from above the ridge top on both days. These layers are merging with the deep CBL on July 25 while they are clearly separated from the much shallower CBL on July 26.

These observations challenge the explanation that synoptic winds alone caused the trapping on July 25 because synoptic winds were of similar strength and direction on both days. The main difference between the two days was the growth of the CBL, which was slower on the second day, caused by stronger background stratification and probably large-scale subsidence. This suggests that the internal dynamics of the slope flow system played at least a partial role in the observed trapping.

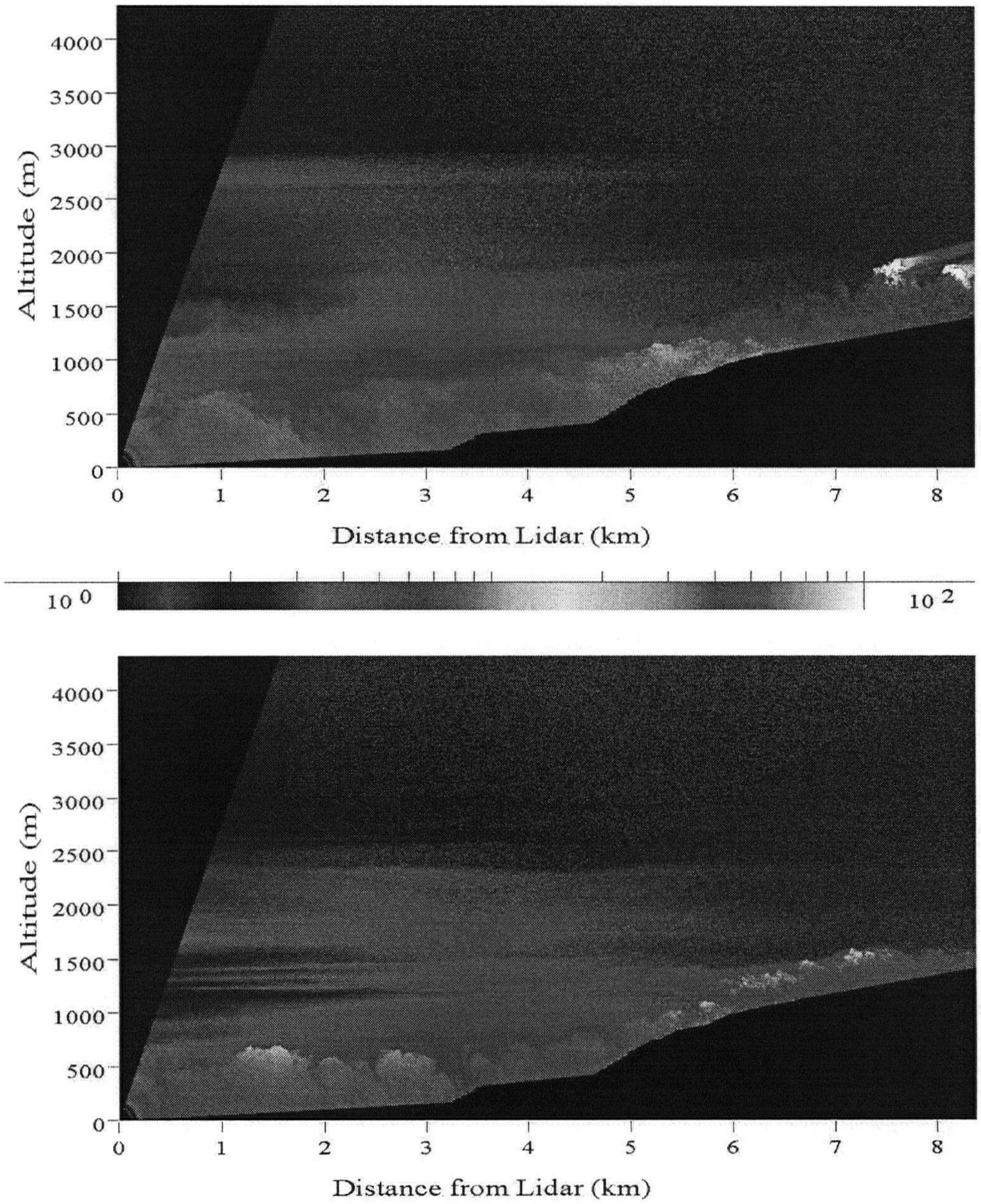

Figure 2.14: RASCAL RHI scans for July 25, 1047 PDT (top) and July 26, 1053 PDT (bottom).
The black areas represent the mountain slope as determined by the scanning lidar "ground" returns. The CBL can be identified visually as the turbulent layer of elevated particulate matter concentrations up to approximately 1000m (top) and 500m (bottom). Cumulus clouds are present on July 25 about 8km from the lidar at an altitude of approximately 1700m. The logarithmic grey scale represents the relative backscatter ratio at 1064nm (lighter shades represent high aerosol concentrations; darker shades represent low aerosol concentrations). (Based on Fig. 15 in Reuten et al., 2005)

2.3.2 Hypothesis 2: Internal Dynamics of Slope Flow System

In this hypothesis a return flow occurs within the CBL under particular conditions as part of the internal dynamics of the slope flow system. For example, Chen et al. (1996) found in their water-tank experiments for a two-dimensional ridge that the flow properties depended only on a non-dimensional (ND) quantity G_c, the ratio of ridge height and CBL depth far from the slope. Their results suggest that closed slope flow circulations within the CBL occur when G_c is below a critical value of $G_c \approx 0.6 - 0.7$. This value differs greatly from our observed values for July 25, $G_c \approx 2.6$, and July 26, $G_c \approx 1.4$. The possible reasons for the differences will be revisited in chapter 4 after the scaling.

2.3.3 Hypothesis 3: Thermal Boundary Layer and Backscatter Boundary Layer are Different

This hypothesis includes the possibility that the BBL may be composed of sub-layers, for example a CBL in contact with the heated ground and an elevated mixed layer separated from the underlying CBL by a temperature jump. In such a scenario, the upslope flow fills the ground-based CBL and the return flow recirculates pollutants in the downslope direction within the elevated mixed layer. To test this hypothesis a detailed analysis of vertical variations of aerosol concentrations within the BBL and a comparison with the TBL structure would be required. Unfortunately, the uncertainties in the tethersonde observations did not allow me to determine the internal structure of the TBL. In chapter 3, I will revisit the hypothesis in the context of physical scale modeling, which permits detailed measurements of the BBL and the TBL.

2.3.4 Conclusions

The review of previous studies in section 1.3 showed that in most cases return flows either did not occur or were rather weak and occurred above the CBL. Kuwagata and Kondo (1989) gathered information from several field studies and summarized the relation of the upslope flow depth to the CBL depth in their Fig. 4. All measurements of the top of the upslope flow, except for the one at Azuma Takayu, scattered near the diagonal representing the top of the CBL. In comparison, Figure 2.9 in this thesis showed upslope flow depths scattering near the dashed line representing half the depth of the CBL, providing more evidence that strong return flows can occur within the CBL.

We performed the measurements during fair-weather conditions. Under these conditions, predominantly westerly synoptic winds and the sea breeze advect air pollution, generated mainly near the coastline, towards the east (Steyn and Faulkner, 1986). During the advection, photochemical processes generate high concentrations of ozone. The fate of primary and secondary pollutants is of particular importance in the suburban and rural areas east of the main source area of pollution where a high percentage of the population works outdoors. Most previous observations at other locations showed upslope flows filling the entire CBL. As a consequence, air pollutants were vented into the free atmosphere above the mountain ridge. In contrast, our observations on July 25, 2001, suggest that air pollutants can remain trapped in closed slope flow circulations.

I speculate that these observations are at least partially internal to the dynamics of the slope flow system, albeit supported by synoptic winds opposing the upslope flow. It is impossible with our field data to test the hypothesis that the TBL and the BBL are different or that the TBL exhibits a more complex structure over steep slopes than over flat terrain. For the remainder of this thesis I will investigate this hypothesis with the help of water-tank experiments. In chapter 3 I will develop the scaling that will allow me to draw comparisons between field and water-tank observations (chapter 4).

3 Scaling and Idealisations

3.1 Introduction

Scaling has been used for hundreds of years as a powerful tool in applied mathematics and engineering and is often interpreted differently by different investigators (Barenblatt, 2003). The central goal of scaling in this thesis goes back to Tolman's (1914) principle of similitude requiring that two universes of different scales are exactly similar. Tolman postulated the principle "as a temporary criterion for the correctness of physical theories", hence as a screening tool[1]. Generalising Tolman' (1914) work, Buckingham (1914) developed the formalism of dimensional analysis, which is well explained in Barenblatt (2003) and which I will follow in this chapter.

I strongly emphasize here what this scaling is *not* meant to be: Often, scaling is used to estimate the relative magnitude of terms in the governing equations. Smaller terms are neglected and the governing equations may then be easier to solve numerically or analytically. Based on this use of scaling and often limited to steady state, previous investigators achieved an order-of-magnitude agreement between atmospheric and water-tank observations.

By contrast, I set a more stringent goal: to use the water tank as a *quantitative* scale model of the atmospheric upslope flows observed in Minnekhada Park. This goal is closely linked to Tolman's principle of similitude if we interpret the atmosphere and the water tank as two different universes. Major improvements over previous investigations are necessary to achieve this goal. Firstly, a clear concept map needs to be developed to connect mathematical models with real physical systems (water tank and atmosphere). Secondly, I will need to apply scaling as dimensional analysis using the Buckingham Pi theorem to determine the non-dimensional

[1] As an interesting digression into modern physics, Dr. Han van Dop pointed out to me that the combination of fundamental constants in our universe is probably scale invariant and therefore violates Tolman's principle of similitude.

governing parameters. Thirdly, time dependence needs to be explicitly included in the analysis.

To develop the concept map, recall the schematics of my research approach (Figure 1.4 on page 10). The goal is to establish a quantitative link between observations in the atmosphere and in the water tank by means of scaling. This requires the introduction of two mathematical idealisations, one each for the atmosphere and the water tank, which I will call the 'atmospheric idealisation' (AI) and the 'water-tank idealisation' (WTI), (Figure 3.1). In the context of scaling, these idealisations are models, a term which I will avoid in this context because of its sometimes confusing and inconsistent usage. For example in 'numerical model' the separation between the mathematical idealisation and the physical, i.e. numerical, experiment is not possible and in 'physical scale model' it is not clear if one means the mathematical model of the experimental apparatus or the physical apparatus itself. AI and WTI and their independent variables are introduced in section 3.2.

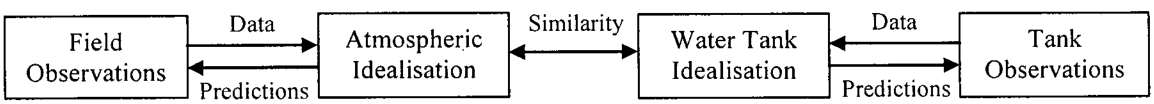

Figure 3.1: Concept map of the scaling.
Scaling has to be carried out between each pair of neighbouring boxes. Field and tank observations provide data to develop atmospheric and water-tank idealisations, respectively. In return, the two idealisations can be used to predict other quantities in the real atmosphere and water tank. Central is the similarity *over many orders of magnitude between atmospheric idealisation and water-tank idealisation.*

With regards to the second improvement, the use of dimensional analysis, the concept map Figure 3.1 clearly shows that three steps are required to carry out the scaling: first between real atmosphere and AI (section 3.3.1), second between real water tank and WTI (section 3.3.2), and finally by requiring similarity in the bulk behaviour of AI and WTI (section 3.3.3).

From AI and additional assumptions, hypotheses on dependent quantities can be derived and tested with field observations (section 3.4). Requiring similarity between AI and WTI, I will derive from the WTI testable hypotheses or predictions for water-tank experiments (section 3.5), which will be checked in chapter 4.

The third improvement is dropping the assumption of steady state. Surface heating in the atmosphere is roughly sinusoidal with time, while heating of the tank bottom is constant. I account for this difference in surface heating in the scaling, but this raises the issue of a common reference time in AI and WTI, which will be addressed in section 3.6. Appendix B contains additional material on scaling.

In this chapter, quantities specific to the atmosphere will be distinguished by a subscript 'a' from water-tank specific quantities, which will carry subscript 'w'. If a quantity applies generally to atmosphere and water tank the subscript will be dropped.

My hope was to achieve similarity between the two systems within the uncertainty of the field observations (about 20%) at any given point in time in the interval from the beginning of positive heat flux to maximum heat flux – not, however, simultaneously at every point in time. This would have allowed the use of tank experiments to quantitatively model field observations reported in the previous chapter. Water-tank experiments are repeatable and permit more measurements than field studies to investigate, for example, the hypothesis that thermal boundary layer and backscatter boundary layer are different (section 2.3.3). This goal was not fully achieved, the primary reasons being the complexity of the atmospheric flow, great uncertainties and insufficient range in atmospheric upslope flow velocity measurements, and violation of the scaling laws caused by molecular effects in the water tank. These reasons will be discussed in this and the following chapter.

3.2 Atmospheric and Water-Tank Idealisations

The topography of the AI is infinite in cross-slope direction and consists of an infinite periodic array of plains at mean sea level (MSL) with half length

$$L_{b,a} = 2400\, m \tag{3.1}$$

and plateaus at

$$H_a = 760\, m\ MSL \tag{3.2}$$

with half length

$$L_{t,a} = 2400\, m \tag{3.3}$$

separated by slopes with a horizontal length of

$$L_a = 2207\,m \tag{3.4}$$

(Figure 3.2, A).

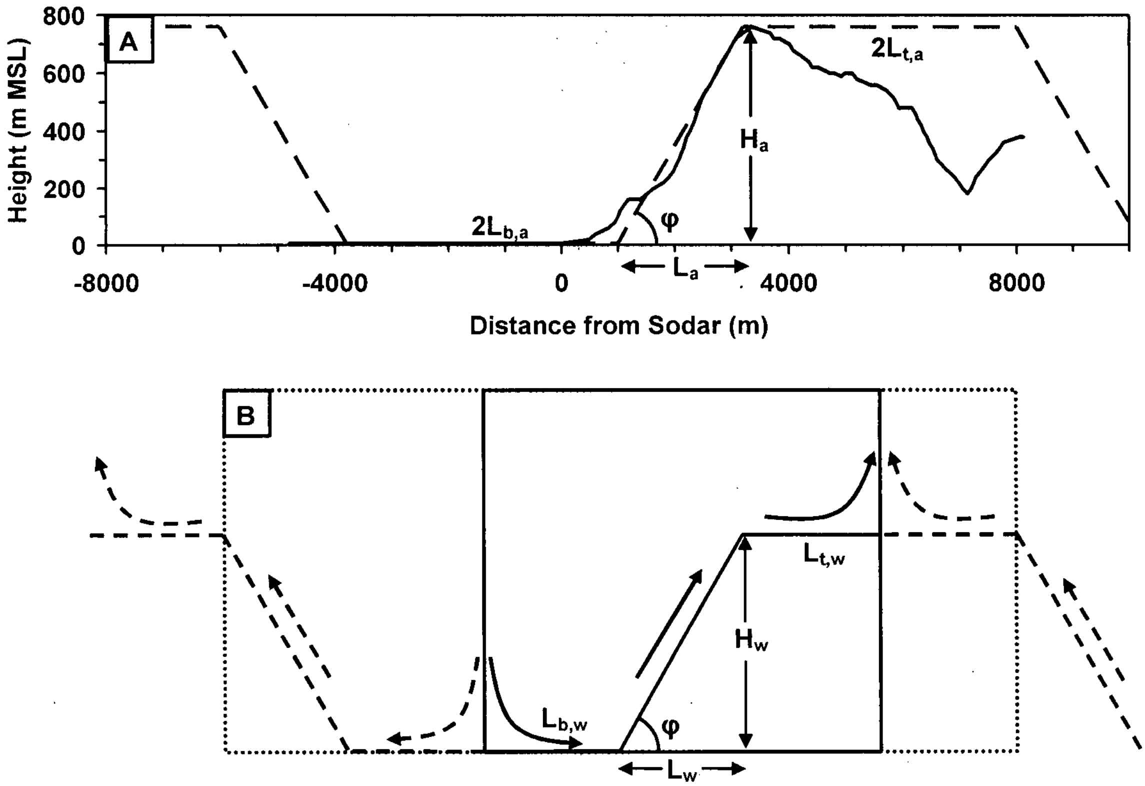

Figure 3.2: Topography at the field site and atmospheric and water-tank idealisations.
A: The solid line shows the vertical cross-section of the slope at Minnekhada Park as seen from the sodar in the direction of the steepest slope (dashed line in Figure 2.1 on page 13). The dashed line represents the idealised periodic topography. B: The solid box encloses the water-tank domain. The end walls impose a mirror symmetry shown by a schematic flow pattern within the tank (solid arrows) and the imaginary mirrored flow outside the tank (dashed arrows). For comparison, the dotted box encloses the domain to be used with numerical models with wrap-around symmetry. Notice that horizontal and vertical axes do not have the same scale.

In the corresponding WTI,

$$L_{b,w} = L_{t,w} = 0.470\,m\,, \tag{3.5}$$

$$H_w = 0.149\,m\,, \text{ and} \tag{3.6}$$

$$L_w = 0.433\,m \tag{3.7}$$

(Figure 3.2. B). The tank width is

$$W_w = 0.431m. \tag{3.8}$$

Notice the underlying assumption that in both AI and WTI, the slope angle $\varphi = 19°$, i.e. the aspect ratio $L_w/H_w = 2.90$. In other words, horizontal and vertical lengths scale identically between AI and WTI. I will briefly return to this assumption in section 3.3. $L_{b,w}$ and $L_{t,w}$ are constraints originating from the finite dimensions of the tank. The tank's end walls impose the symmetry indicated by the schematic flow patterns inside and outside of the water-tank domain (Mitsumoto, 1989), if heat loss and additional friction between end wall and fluid is negligible (a mirror or even-parity symmetry) (Figure 3.2. B). I chose $L_{b,a}$ and $L_{t,a}$ in (3.1) and (3.3) such that AI and WTI are geometrically similar, i.e.

$$\frac{L_{b,a}}{H_a} = \frac{L_{b,w}}{H_w} \text{ and} \tag{3.9}$$

$$\frac{L_{t,a}}{H_a} = \frac{L_{t,w}}{H_w}. \tag{3.10}$$

The dotted box in Figure 3.2 shows the corresponding domain in numerical models like large-eddy simulation (LES) with wrap-around symmetry, in which any fluid leaving on the domain's left boundary re-enters on the right boundary. Notice that the numerical model domain is exactly twice as long as the water-tank domain.

In the AI the air is assumed dry and linearly stably stratified at the beginning of positive net sensible surface heat flux, i.e. the environmental lapse rate

$$\gamma_a \equiv \frac{d\theta_a}{dz_a} = const > 0, \tag{3.11}$$

where θ_a is the atmospheric background potential temperature. In the water tank the background stratification is established by decreasing salt concentration with height. A convenient measure of stable stratification is specific volume α_w, which is the inverse of density ρ_w and increases with height in the water tank as does potential temperature in the atmosphere:

$$\alpha_w \equiv \frac{1}{\rho_w} = \frac{\delta V_w}{\delta m_w}, \tag{3.12}$$

where δV_w is the volume and δm_w the mass of a small test parcel. I define the background environmental lapse rate in the water tank as the vertical gradient of background specific volume α_w, i.e.

$$\gamma_w \equiv \frac{d\alpha_w}{dz_w} = \frac{\alpha_{D,w}}{D_w} = const > 0\,, \tag{3.13}$$

where $\alpha_{D,w}$ is the specific volume difference over the water depth

$$D_w = 0.580\,m\,. \tag{3.14}$$

Notice that γ_a and γ_w have different units, $K\,m^{-1}$ and $m^2\,kg^{-1}$, respectively.

Steyn (1998) used the buoyancy parameter g/T_a, where T_a is the near surface background temperature, as an external parameter for his sea breeze scaling, which is also likely to be an important parameter in upslope flows. Here I will use the more general form

$$g\beta_a = 0.036\,m\,s^{-2}K^{-1}, \tag{3.15}$$

where

$$\beta \equiv \frac{1}{V}\frac{dV}{dT} \tag{3.16}$$

is the coefficient of thermal expansion. If the fluid is an ideal gas, a good approximation for air, (3.15) is identical to g/T_a, because for constant pressure p_a, the ideal gas law,

$$p_a V_a = m_a R T_a, \tag{3.17}$$

(m_a is the mass of the air of volume V_a, R is the gas constant, and T_a is the temperature) implies

$$p_a \frac{dV_a}{dT_a} = m_a R \quad \Leftrightarrow \quad \frac{1}{V_a}\frac{dV_a}{dT_a} = \frac{m_a R}{p_a V_a} \quad \Leftrightarrow \quad \beta_a = \frac{1}{T_a}\,. \tag{3.18}$$

This relationship does not hold for water so that one has to use

$$g\beta_w \approx 2.59\times 10^{-3}\,m\,s^{-2}K^{-1}. \tag{3.19}$$

Notice that β_w depends on temperature. I use the value at 25°C, $\beta_w = 2.6\times10^{-4} K^{-1}$, which is approximately in the middle of the typical experimental temperature range between 20°C ($\beta_w = 2.1\times10^{-4} K^{-1}$) and 30°C ($\beta_w = 3.0\times10^{-4} K^{-1}$). The choice of the product $g\beta$ rather than individual g and β as governing parameters is equivalent to making the Boussinesq approximation, in which density differences caused by temperature variations are neglected everywhere but in the buoyancy term (Barenblatt, 2003).

The background environmental lapse rate for the water tank, γ_w in (3.13), introduces the fundamental dimensional unit of mass, kg. It is possible to eliminate the units of mass by replacing γ_α with the buoyancy frequency (Brunt-Väisälä frequency) as an independent parameter, which is defined in the atmosphere as

$$N_a \equiv \left(g\beta_a \frac{d\theta_a}{dz_a} \right)^{1/2} = \left(g\beta_a\gamma_a \right)^{1/2}. \tag{3.20}$$

and in the water tank as

$$N_w = \left(\frac{g}{\alpha_{0,w}} \frac{d\alpha_w}{dz_w} \right)^{1/2} = \left(\frac{g}{\alpha_{0,w}} \gamma_w \right)^{1/2}, \tag{3.21}$$

where $\alpha_{0,w} = 1/998.23\ m^3\,kg^{-1} \approx 1.0018\times10^{-3}\ m^3\,kg^{-1}$. This replacement is common in geophysical fluid dynamics because it transforms the governing equations for atmospheric and oceanic flows into the same form.

When requiring similarity between AI and WTI, advection and subsidence external to the slope system and the Coriolis force must be neglected due to technical limitations of the water tank. I will revisit these assumptions as part of the discussions on discrepancies between atmospheric and water-tank observations.

In the AI, surface roughness and heating are assumed homogeneous with sinusoidal sensible surface heat flux, i.e.

$$Q_{H,a}(t_a) = Q_{\max,a} \cdot \sin\left(\frac{\pi}{2} \frac{t_a}{t_{d,a}} \right), \tag{3.22}$$

where $Q_{\max,a}$ is the maximum sensible heat flux value, $t_{d,a}$ is the diurnal heating time scale, defined as the time from the beginning of positive surface heat flux to the maximum value, and $t_a \in \left[0, t_{d,a}\right]$ is an atmospheric reference time scale. Because we did not measure heat flux at Minnekhada Park, I extract representative values for $Q_{\max,a}$ and $t_{d,a}$ from an ensemble average of heat flux measurements taken on individual days in the interval from July 17 - August 26 over the years 1983-1986 (see Figure 8 in Steyn, 1998). The beginning of positive surface heat flux was approximately 0800 PDT, the maximum heat flux of $\widetilde{Q}_{\max,a} \approx 350\,Wm^{-2}$, or in kinematic units

$$Q_{\max,a} \approx 0.289\,K\,m\,s^{-1}, \tag{3.23}$$

was reached at approximately 1545 PDT. With this the diurnal heating time scale becomes

$$t_{d,a} \approx 7.75\,h = 27{,}900\,s, \tag{3.24}$$

which is identical to the time difference from sunrise to solar noon on July 25. I define the beginning of positive heat flux at 0800 PDT as the origin of time so that $t_{d,a}$ corresponds to 1545 PDT. Recall from the introduction to this chapter that time dependence is explicitly included so that the scaling applies to arbitrary atmospheric reference times $t_a \in \left[0, t_{d,a}\right]$. With respect to heat flux this implies that two quantities are of physical importance: the instantaneous heat flux, $Q_{H,a}$ in (3.22), because it drives convection, and the time-integrated heat flux, which is the total supplied energy per surface area or energy density and determines the CBL depth. For the AI this is

$$E_a \equiv t_a \cdot \overline{Q_{H,a}(t)}^{0,t_a} = t_a \cdot \frac{1}{t_a}\int_0^{t_a} Q_{H,a}(t)\,dt = \int_0^{t_a} Q_{\max,a} \cdot \sin\left(\frac{\pi}{2}\frac{t}{t_{d,a}}\right)dt \quad \Rightarrow$$

$$E_a = Q_{\max,a} t_{d,a} \cdot \frac{2}{\pi}\left[1 - \cos\left(\frac{\pi}{2}\frac{t_a}{t_{d,a}}\right)\right]. \tag{3.25}$$

In the water tank, the surface heat flux remains constant during each experiment, typically:

$$Q_{H,w} \approx 1.85 \times 10^{-3}\,K\,m\,s^{-1}. \tag{3.26}$$

With this the energy density in the water tank becomes

$$E_w = \overline{Q_{H,w}}^{0,t_w} t_w = Q_{H,w} t_w , \tag{3.27}$$

where t_w is the water-tank reference time.

The detailed specification of sensible surface heat flux is a major extension of previous scaling approaches. The assumption of a *constant* atmospheric heat flux would be a substantial simplification, because similarity of atmospheric and tank surface heat flux would automatically imply similarity between energy densities. The assumption, however, contradicts evidence that upslope flow systems depend on both instantaneous and integrated heat flux. For example, a wide-held view going back at least to Jelinek (1937) is that upslope flows cease as soon as insolation is interrupted, e.g. by cumulus clouds, evidence for a strong dependence on instantaneous heat flux. On the other hand, CBL depth, which determines the upslope flow layer depth, is primarily a function of total supplied energy. The error associated with the assumption of constant heat flux is far greater than the targeted 20 %. For example, during the morning in the atmosphere heat flux increases approximately linearly and total supplied energy is only half of the value it would be if heat flux had been constant at the instantaneous value. The time dependence of the scaling in this chapter will be further discussed in section 3.6.

To complete the description of AI and WTI I will need the molecular parameters, kinematic viscosities,

$$\begin{aligned} \nu_a &= 1.52 \times 10^{-5}\, m^2\, s^{-1} \\ \nu_w &= 8.9 \times 10^{-7}\, m^2\, s^{-1}, \end{aligned} \tag{3.28}$$

and thermal diffusivities,

$$\begin{aligned} \kappa_a &= 2.11 \times 10^{-5}\, m^2\, s^{-1} \\ \kappa_w &= 1.45 \times 10^{-7}\, m^2\, s^{-1}. \end{aligned} \tag{3.29}$$

The independent parameters for AI and WTI are summarised in Table 3.1.

Name	Variable	Fundamental Units	AI	WTI
Ridge height	H	m	$760\,m$	$0.149\,m$
Instantaneous heat flux	Q_H	$K\,m\,s^{-1}$	dependent on time of day $\left(0-0.289\,K\,m\,s^{-1}\right)$	controllable $\left(1.5-3.7\times10^{-3}\,K\,m\,s^{-1}\right)$
Background buoyancy frequency	N	s^{-1}	dependent on day $\left(14.9-16.2\times10^{-3}\,s^{-1}\right)$	controllable $\left(\sim 0.1-1.5\,s^{-1}\right)$
Horizontal slope length	L	m	$2207\,m$	$0.433\,m$
Energy density	E	$K\,m$	dependent on time of day $\left(0-5130\,K\,m\right)$	controllable $\left(\sim 0-6\,K\,m\right)$
Buoyancy parameter	$g\beta$	$m\,s^{-2}K^{-1}$	$0.036\,m\,s^{-2}K^{-1}$	$2.59\times10^{-3}\,m\,s^{-2}K^{-1}$
Kinematic viscosity	ν	$m^2\,s^{-1}$	$1.52\times10^{-5}\,m^2\,s^{-1}$	$8.9\times10^{-7}\,m^2\,s^{-1}$
Thermal diffusivity	κ	$m^2\,s^{-1}$	$2.11\times10^{-5}\,m^2\,s^{-1}$	$1.45\times10^{-7}\,m^2\,s^{-1}$.
Half length of plain	L_b	m	$2400\,m$	$0.470\,m$
Half length of plateau	L_t	m	$2400\,m$	$0.470\,m$
Tank width	W_w	m	-	$0.431\,m$
Water depth over the plain	D_w	m	-	$0.580\,m$

Table 3.1: Independent parameters in atmospheric idealisation (AI) and water-tank idealisation (WTI). The distinguishing subscript 'a' for AI and 'w' for WTI has to be added correspondingly; tank width and water depth are shown with subscript 'w' because they only apply to WTI.

3.3 Buckingham Pi Analysis

3.3.1 Pi Groups in the Atmospheric Idealisation

Table 3.1 above lists $n=10$ independent parameters for the AI, H_a, $Q_{H,a}$, N_a, L_a, E_a, $g\beta_a$, ν_a, κ_a, $L_{b,a}$, and $L_{t,a}$, which use $k=3$ fundamental units (K, m, s). According to the Buckingham Pi Theorem (Buckingham, 1914) I need $k=3$ independent key parameters to form $n-k=7$ dimensionless Pi groups. I choose the first three parameters, $H_a\,[m]$, $Q_{H,a}\,\left[K\,m\,s^{-1}\right]$, and $N_a\,\left[s^{-1}\right]$. These are independent: Any combination of H_a and $Q_{H,a}$

contains the unit K and therefore cannot be used to non-dimensionalise N_a, which does not contain K. With the same argument, N_a and $Q_{H,a}$ cannot be used to non-dimensionalise H_a. Finally, because neither N_a nor H_a contain unit K, they cannot be used to non-dimensionalise $Q_{H,a}$. The Pi groups are formed by non-dimensionalising the remaining seven variables L_a, E_a, $g\beta_a$, ν_a, κ_a, $L_{b,a}$, and $L_{t,a}$ with appropriate combinations of the key variables.

The horizontal slope length L_a is divided by H_a to form the first Pi group,

$$\Pi_1 \equiv \frac{L_a}{H_a} = \frac{L_w}{H_w} = 2.90, \tag{3.30}$$

the aspect ratio, which I assumed to be equal for AI and WTI in the discussion of (3.7). The energy density E_a is non-dimensionalised by,

$$\Pi_{2,a} \equiv E_a \cdot \frac{N_a}{Q_{H,a}}, \tag{3.31}$$

and the buoyancy parameter $g\beta_a$ by,

$$\Pi_{3,a} \equiv g\beta_a \cdot \frac{Q_{H,a}}{H_a^2 N_a^3}. \tag{3.32}$$

Two more Pi groups can be formed to describe molecular effects,

$$\Pi_{4,a} \equiv \nu_a \cdot \frac{1}{H_a^2 N_a} \text{ and} \tag{3.33}$$

$$\Pi_{5,a} \equiv \kappa_a \cdot \frac{1}{H_a^2 N_a}. \tag{3.34}$$

Finally, from half lengths of plain and plateau and the requirement of geometric similarity between AI and WTI, (3.9) and (3.10), I can define two Pi groups:

$$\Pi_6 \equiv \frac{L_{b,a}}{H_a} = \frac{L_{b,w}}{H_w} \approx 3.15 \text{ and} \tag{3.35}$$

$$\Pi_7 \equiv \frac{L_{t,a}}{H_a} = \frac{L_{t,w}}{H_w} \approx 3.15 . \tag{3.36}$$

3.3.2 Pi Groups in the Water-Tank Idealisation

The Pi groups specific to the AI readily translate into Pi groups for the WTI:

$$\Pi_{2,w} \equiv E_w \cdot \frac{N_w}{Q_{H,w}}, \tag{3.37}$$

$$\Pi_{3,w} \equiv g\beta_w \cdot \frac{Q_{H,w}}{H_w^{\,2} N_w^{\,3}}, \tag{3.38}$$

$$\Pi_{4,w} \equiv \nu_w \cdot \frac{1}{H_w^{\,2} N_w}, \tag{3.39}$$

$$\Pi_{5,w} \equiv \kappa_w \cdot \frac{1}{H_w^{\,2} N_w}. \tag{3.40}$$

In the WTI there are two additional independent parameters, tank width W_w and water depth D_w. Because the number of fundamental units, $k = 3$, is the same as in the AI (Table 3.1, page 44), two additional Pi groups are required to completely describe the WTI,

$$\Pi_{8,w} \equiv \frac{W_w}{H_w} \approx 2.89 \text{ and} \tag{3.41}$$

$$\Pi_{9,w} \equiv \frac{D_w}{H_w} \approx 3.89 . \tag{3.42}$$

The nine Pi groups fall into four categories (Table 3.2). I propose that the core category, Π_1 to Π_3, guarantees similarity between AI and WTI for bulk flow features that are independent of the fine details of the flow. For the AI, I will define these to be flow features occurring at the scales of our field measurements, i.e. roughly at time scales of $O(\geq 10\,\text{min})$, horizontal length scales of $O(\geq 100\,m)$, and vertical length scales of $O(\geq 20\,m)$. The second category, Π_4 and Π_5, concerns molecular properties, which are covered in Appendix B.6. The assumption is that the bulk flow features are not affected by Π_4 and Π_5, at least if critical inequalities are met. The third category, Π_6 and Π_7, is a consequence of the finite length of the water tank, which imposes the symmetry restriction on the AI (Figure 3.2, page 38). In this chapter I will assume that Π_6 and Π_7 are large enough for the flow to be independent of the particular values. In section 4.3 I will investigate the impact of the end walls when the value of the Pi groups is reduced. The fourth category are the water tank-specific Pi groups, Π_8 and Π_9. I assume that both are asymptotically large enough to neglect the impact of the side walls and the finite depth of the water, respectively.

Category	Description	AI	WTI
Core	Aspect ratio	$\Pi_1 = \frac{L_a}{H_a}$	
	ND energy density	$\Pi_{2,a} = E_a \cdot \frac{N_a}{Q_{H,a}}$	$\Pi_{2,w} = E_w \cdot \frac{N_w}{Q_{H,w}}$
	ND buoyancy parameter	$\Pi_{3,a} = g\beta_a \cdot \frac{Q_{H,a}}{H_a^2 N_a^3}$	$\Pi_{3,w} = g\beta_w \cdot \frac{Q_{H,w}}{H_w^2 N_w^3}$
Molecular	ND viscosity	$\Pi_{4,a} = \nu_a \cdot \frac{1}{H_a^2 N_a}$	$\Pi_{4,w} = \nu_w \cdot \frac{1}{H_w^2 N_w}$
	ND thermal diffusivity	$\Pi_{5,a} = \kappa_a \cdot \frac{1}{H_a^2 N_a}$	$\Pi_{5,w} = \kappa_w \cdot \frac{1}{H_w^2 N_w}$
Longitudinal boundary conditions	ND half length of plain	$\Pi_6 = \frac{L_{b,a}}{H_a} = \frac{L_{b,w}}{H_w}$	
	ND half length of plateau	$\Pi_7 = \frac{L_{t,a}}{H_a} = \frac{L_{t,w}}{H_w}$	
Water-tank specific	ND tank width	-	$\Pi_{8,w} = \frac{W_w}{H_w}$
	ND water depth over plain	-	$\Pi_{9,w} = \frac{D_w}{H_w}$

Table 3.2: Summary of Pi groups in atmospheric idealisation (AI) and water-tank idealisation (WTI). The Pi groups in the core category are critical for similarity of bulk properties in AI and WTI. The molecular category is assumed negligible. The category of longitudinal boundary conditions is equal for both idealisations by definition. The two water tank-specific Pi groups are assumed asymptotically large enough to be neglected. Quantities that are equal for AI and WTI do not carry a distinguishing subscript.

Now that the Pi groups of AI and WTI are determined, the central link in the concept map (Figure 3.1 on page 36) can be completed by requiring similarity between the two idealisations.

3.3.3 Similarity between Atmospheric and Water-Tank Idealisations

According to the explanations in the previous section, I expect similarity of the bulk features in AI and WTI if the three core Pi groups Π_1 to Π_3 are equal for AI and WTI, i.e.

$$\Pi_2 \equiv \Pi_{2,a} = \Pi_{2,w} \text{ and} \tag{3.43}$$

$$\Pi_3 \equiv \Pi_{3,a} = \Pi_{3,w}. \tag{3.44}$$

We see here that the assumption that the aspect ratio Π_1 is equal for AI and WTI arises from the similarity requirement.

If $\Pi_{2,a}$ and $\Pi_{3,a}$ for the AI are given from field observation, parameters in the WTI are constrained by:

$$E_w \cdot \frac{N_w}{Q_{H,w}} = t_w \cdot N_w = \Pi_{2,a} \text{ and} \tag{3.45}$$

$$g\beta_w \cdot \frac{Q_{H,w}}{H_w^{\ 2} N_w^{\ 3}} = \Pi_{3,a}, \tag{3.46}$$

where I simplified (3.45) by substituting $E_w = Q_{H,w} t_w$ from (3.27).

Practically, when designing water-tank experiments to represent atmospheric observations, one needs to revert back to dimensional quantities. It is not *a priori* obvious that it is possible to meet the similarity requirements technically, because some of the independent dimensional parameters are fixed and cannot be manipulated. For example, if one required similarity of all flow *details*, the ratio of molecular viscosity to thermal diffusivity (the Prandtl number, see Appendix B.6) would have to be equal for air and water which is technically impossible.

Of the original set of twelve independent quantities of the WTI, H_w, $Q_{H,w}$, N_w, L_w, E_w, $g\beta_w$, ν_w, κ_w, $L_{b,w}$, $L_{t,w}$, W_w, and D_w (Table 3.1, page 44), the last six quantities, ν_w, κ_w,

$L_{b,w}$, $L_{t,w}$, W_w, and D_w, are not affected by requiring similarity of bulk flow features. The first six independent parameters, H_w, $Q_{H,w}$, N_w, L_w, E_w, and $g\beta_w$, constitute the core category. Of these, ridge height H_w, horizontal slope length L_w, and buoyancy parameter $g\beta_w$ are fixed quantities that cannot be manipulated. The remaining *three* parameters, $Q_{H,w}$, N_w, and E_w, are constrained by *two* equations, (3.45) and (3.46), so that *one* quantity remains independent. Time can be measured more directly than energy density, so it is advantageous to use $E_w = Q_{H,w}t_w$ (3.27) to replace $Q_{H,w}$, N_w, and E_w by the new set $Q_{H,w}$, N_w, and t_w. The (constant) instantaneous net heat flux into the water, $Q_{H,w}$, has the narrowest range of controllability; for technical reasons the electrical power supplied for the heating of the tank can only be varied within 40-100% of the total fixed output of the electrical power outlet. Therefore I keep $Q_{H,w}$ as an independent variable and constrain N_w and t_w via (3.45) and (3.46):

$$t_w = \Pi_2\left(g\beta_w \frac{Q_{H,w}}{H_w^{\;2}\Pi_3}\right)^{-1/3} \quad \text{and} \tag{3.47}$$

$$N_w = \left(g\beta_w \frac{Q_{H,w}}{H_w^{\;2}\Pi_3}\right)^{1/3} \tag{3.48}$$

Table 3.3 provides a comparison between the independent parameters before and after applying the similarity constraints.

Categories	Name	Symbol	Before Scaling	After Scaling
Core	Ridge height	H_w	$0.149\,m$	
	Instantaneous heat flux	$Q_{H,w}$	controllable	
	Background buoyancy frequency	N_w	controllable	$\left(g\beta_w \frac{Q_{H,w}}{H_w{}^2\Pi_3}\right)^{1/3}$
	Horizontal slope length	L_w	$0.433\,m$	
	Water-tank reference time	t_w	controllable	$\Pi_2\left(g\beta_w \frac{Q_{H,w}}{H_w{}^2\Pi_3}\right)^{-1/3}$
	Buoyancy parameter	$g\beta_w$	$2.59\times10^{-3}\,m\,s^{-1}\,K^{-1}$	
Molecular	Kinematic viscosity	ν_w	$8.9\times10^{-7}\,m^2\,s^{-1}$	
	Thermal diffusivity	κ_w	$1.45\times10^{-7}\,m^2\,s^{-1}$	
Longitudinal boundary conditions	Half length of plain	$L_{b,w}$	$0.470\,m$	
	Half length of plateau	$L_{t,w}$	$0.470\,m$	
Water-tank specific	Tank width	W_w	$0.431\,m$	
	Water depth over the plain	D_w	$0.580\,m$	

Table 3.3: Independent water-tank quantities before and after applying the scaling and similarity constraints. Before scaling, $Q_{H,w}$, N_w, and t_w are controllable, all other quantities are fixed. After scaling, $Q_{H,w}$ remains controllable, N_w and t_w become dependent quantities. Categories are the same as in Table 3.2.

The next step is to derive from the independent parameters hypotheses on quantities that we measured at Minnekhada Park, and compare the derived hypotheses against field observations. This will require further assumptions about the flow in AI and WTI.

3.4 Hypotheses for the Atmosphere

Testable hypotheses can be derived for both field and water-tank observations from the independent parameters in Table 3.1 and Table 3.3 and further assumptions about the flow. This will be done in three steps, each corresponding to the three subsections in section 3.3 and the three interfaces in the concept map (Figure 3.1, page 36).

In the first step (this section) I will discuss hypotheses for three quantities, which we measured in the atmosphere: CBL depth, CBL mean potential temperature, and upslope flow velocity. Here I use the term 'hypothesis' with a broad meaning, as a quantitative and *qualitative* statement on a parameter. Therefore, I will not carry out formal statistical hypotheses tests but compare the hypotheses with field observations.

In the second step, I will discuss hypotheses on CBL depth, CBL mean specific volume, and upslope velocity in the water tank (section 3.5). In chapter 4 I will compare these hypotheses with water-tank experiments.

The flows in AI and WTI progress along different time lines that are not linear to each other, because of the different time development of surface heat flux in the two idealisations. In the two steps explained above, the quantities are expressed in terms of an atmospheric reference time (time of day in PDT) and a water-tank reference time (duration of heating in s). The third step is to find the relationship between atmospheric and water-tank reference time and express the quantities of AI and WTI as functions of a common reference time (section 3.6). This last step completes the scaling and permits a direct comparison between atmospheric and water-tank observations.

Verification of the hypotheses would strongly support the scaling developed in this chapter and complete the entire link from field observations to tank observations in the concept map (Figure 3.1, page 36). The failure to fully verify the hypotheses provides additional insight into the real physical systems.

3.4.1 CBL Depth and Potential Temperature

The independent parameters of the AI listed in Table 3.1 (page 44) are based on field observations during Pacific 2001. More field data are available: the CBL depth h_a; the difference of average CBL potential temperature and the idealised surface potential temperature under the assumption of a linear background stratification, $\theta_{s,a}$, which I will call 'CBL mean potential temperature increment' (Figure 3.3); and the upslope flow velocity U_a. I will now derive h_a and $\theta_{s,a}$ from the independent parameters of the AI and compare the values with the field observations.

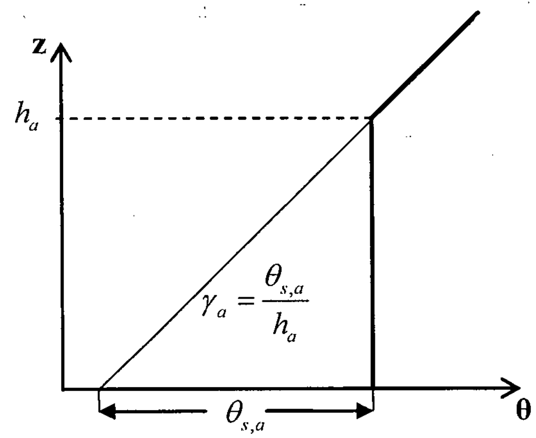

Figure 3.3: Diagram of quantities in an encroachment model of the CBL in the atmospheric idealisation. The CBL depth at time t_a is h_a, $\theta_{s,a}$ is the corresponding CBL mean potential temperature increment, and γ_a is the background environmental lapse rate before the start of positive net surface heat flux.

To determine $\theta_{s,a}$ and h_a, I represent the CBL by an encroachment model over flat terrain (Lilly, 1968), (Figure 3.3). It neglects the surface layer and assumes an entrainment coefficient of $A = 0$ in Carson's (1973) more general entrainment model. Previous field observations and water-tank experiments have shown that $A > 0$ (e.g. van Dop et al., 2005)[2]. The weaker the stratification the greater the value of A (Carson, 1973) and the more will the CBL depth be underestimated by the simple encroachment model. For similarity between atmospheric and water-tank observations this is not a concern. At this point, we will simply keep the expected underestimation in mind. Nevertheless, the entrainment model is a desirable improvement for future research because its difficulty is its merit: The entrainment coefficient is a function of internal advection in the upslope flow system and potentially key to developing a better upslope flow velocity hypothesis than I will offer in this dissertation.

If I neglect conversion of heat into kinetic energy, then the kinematic energy density is simply the triangular area between linear background stratification and CBL profile in Figure 3.3, i.e.

$$E_a = \frac{\theta_{s,a} \cdot h_a}{2}. \tag{3.49}$$

[2] The entrainment coefficient A is potentially different for atmosphere and water tank (e.g. Plate, 1998), but as long as the difference is small, AI and WTI remain approximately similar.

Furthermore, from Figure 3.3,

$$\theta_{s,a} = \gamma_a h_a. \tag{3.50}$$

Together with (3.25) and (3.20), the last two equations give

$$h_a = \left(\frac{2E_a}{\gamma_a}\right)^{1/2} = \frac{(2g\beta_a E_a)^{1/2}}{N_a} = \left\{\frac{g\beta_a}{N_a^2} \cdot Q_{\max,a}\, t_{d,a} \cdot \frac{4}{\pi}\left[1-\cos\left(\frac{\pi}{2}\frac{t_a}{t_{d,a}}\right)\right]\right\}^{1/2} \text{ and} \tag{3.51}$$

$$\theta_{s,a} = (2E_a \gamma_a)^{1/2} = N_a \frac{(2E_a)^{1/2}}{g\beta_a} = \left\{\frac{N_a^2}{g\beta_a} \cdot Q_{\max,a}\, t_{d,a} \cdot \frac{4}{\pi}\left[1-\cos\left(\frac{\pi}{2}\frac{t_a}{t_{d,a}}\right)\right]\right\}^{1/2}. \tag{3.52}$$

Although these expressions look fairly complicated, CBL depth and mean potential temperature increment are approximately linear in time t_a, because applying the second-order Taylor expansion $\cos x \approx 1 - x^2/2$, one finds that within an error of 12% for $t_a \in \left[0, t_{d,a}\right]$,

$$h_a \approx \left(\frac{\pi}{2}\frac{g\beta_a Q_{\max,a}}{N_a^2 t_{d,a}}\right)^{1/2} \cdot t_a \text{ and} \tag{3.53}$$

$$\theta_{s,a} \approx \left(\frac{\pi}{2}\frac{N_a^2 Q_{\max,a}}{g\beta_a t_{d,a}}\right)^{1/2} \cdot t_a. \tag{3.54}$$

These equations can only hold until the onset of a sea breeze approximately between 1200 and 1300 PDT (section 2.2.4). One can estimate the impact of the sea breeze on the growth of the CBL by assuming that the sea breeze replaces the CBL by a convective thermal internal boundary layer (TIBL). Garratt (1994, eqn. 6.86) derived the depth of the convective TIBL $h_{t,a}$ over a homogeneous surface for sinusoidally varying net sensible surface heat flux. He assumed constant sea breeze propagation speed $U_{p,a}$ and a location x so far from the coastline that the time $t_{t,a} = x/U_{p,a}$ to sea breeze transition is at least one hour later than the sea breeze propagation onset time $t_{p,a}$ at the coastline (to achieve an "equilibrium" convective TIBL depth "far" inland). I will show below that this condition is met at the field site at Minnekhada Park. I modify Garratt's formula by using the duration from zero to maximum net sensible surface heat flux, $t_{d,a} = 7.75$ hours, rather than one quarter of the day length, and neglect entrainment at the top of the convective TIBL:

$$h_{t,a} \approx \left\{ \frac{g\beta_a}{N_a^2} \cdot Q_{\max,a} t_{d,a} \cdot \frac{4}{\pi} \left[\cos\left(\frac{2}{\pi} \frac{t_{p,a}}{t_{d,a}} \right) - \cos\left(\frac{2}{\pi} \frac{t_{p,a} + t_{t,a}}{t_{d,a}} \right) \right] \right\}^{1/2} \tag{3.55}$$

and via (3.50) for the mean potential temperature increment within the convective TIBL:

$$\theta_{t,a} \approx \left\{ \frac{N_a^2}{g\beta_a} \cdot Q_{\max,a} t_{d,a} \cdot \frac{4}{\pi} \left[\cos\left(\frac{2}{\pi} \frac{t_{p,a}}{t_{d,a}} \right) - \cos\left(\frac{2}{\pi} \frac{t_{p,a} + t_{t,a}}{t_{d,a}} \right) \right] \right\}^{1/2} . \tag{3.56}$$

Formulation and Verification of the Hypothesis on CBL Mean Potential Temperature Increment

I can now formulate the hypothesis for the development of the CBL mean potential temperature increment at the tethersonde site over the plain far from the slope (Figure 2.1, page 13).

Hypothesis:

The expected value of the CBL mean potential temperature increment in the atmosphere over the plain far from the slope as a function of atmospheric reference time t_a is given by

$$\theta_{s,a}(t_a) = \left\{ \frac{N_a^2}{g\beta_a} \cdot Q_{\max,a}\, t_{d,a} \cdot \frac{4}{\pi} \left[1 - \cos\left(\frac{\pi}{2} \frac{t_a}{t_{d,a}} \right) \right] \right\}^{1/2} .$$

Early in the heating cycle, this is a good approximation to the observations. Between 1200 and 1300 PDT, the CBL at the field site is replaced by a convective TIBL of cooler marine air, briefly decreasing the convective TIBL mean potential temperature increment to

$$\theta_{t,a} \approx \left\{ \frac{N_a^2}{g\beta_a} \cdot Q_{\max,a} t_{d,a} \cdot \frac{4}{\pi} \left[\cos\left(\frac{2}{\pi} \frac{t_{p,a}}{t_{d,a}} \right) - \cos\left(\frac{2}{\pi} \frac{t_{p,a} + t_{t,a}}{t_{d,a}} \right) \right] \right\}^{1/2} .$$

Once the sea breeze is established, the convective TIBL mean potential temperature increment rises again. ■

To verify this hypothesis, I averaged the background buoyancy frequency above the CBL over several early morning tethersonde flights. For the two field days I determined

$$N_a = \begin{cases} (14.9 \pm 0.2) \times 10^{-3} s^{-1} \text{ on July 25} \\ (16.2 \pm 0.6) \times 10^{-3} s^{-1} \text{ on July 26.} \end{cases} \tag{3.57}$$

The increase of stability from July 25 to July 26 is in line with a further increase to $N_a = (19.3 \pm 0.3) \times 10^{-3} s^{-1}$ on July 27. The diurnal heating time scale was practically the same on both days, (3.24). Because of the absence of heat flux measurements and because it was sunny and dry for nine days I assume that the sensible surface heat flux was the same on both days, (3.23).

Only few measurements of the CBL mean potential temperature increment $\theta_{s,a}$ are available. The agreement with the predicted curves is within the uncertainty, although the prediction seems to overestimate the observations for July 26 (Figure 3.4). I included manual measurements of surface temperatures at the sodar site and station measurements from Pitt Meadows Airport, 6 km south of the tethersonde site. The surface measurements demonstrate that the error bars for the tethersonde measurements are considerably smaller than the temperature difference between CBL and surface layer. With only very few data available I did not succeed in deriving CBL mean potential temperature from station measurements by using radix-layer similarity equations (Santoso and Stull, 1998 and 2001). Other similarity equations usually require the fitting of more parameters and are unlikely to give better results.

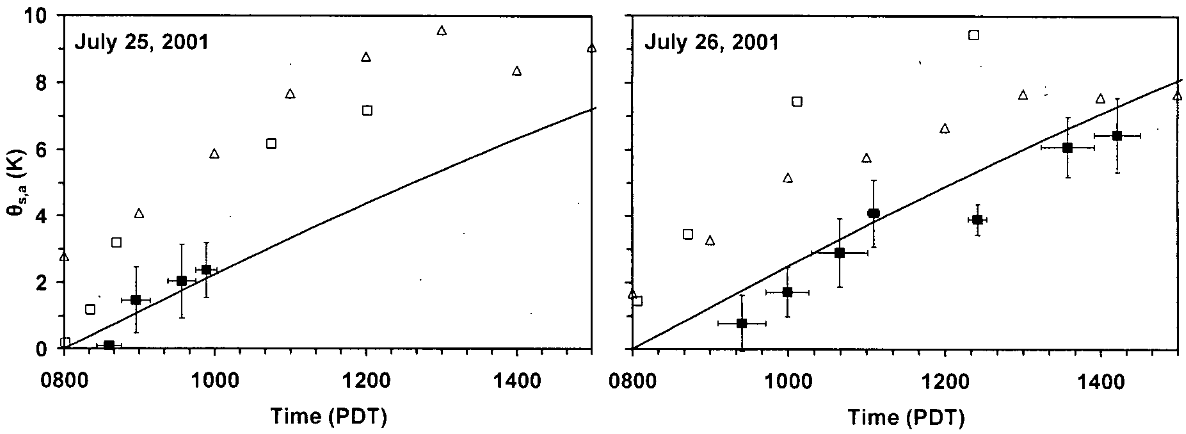

Figure 3.4: Comparison of field observations and AI predictions of CBL mean potential temperature increment. Left graph is for July 25, right graph for July 26, 2001. Axes have the same scale. The solid lines are the hypothesis predictions based on (3.52) and the data discussed in the text, solid squares with error bars denote tethersonde measurements of CBL mean potential temperature over the plain. Horizontal error bars are flight duration, and vertical error bars span the range of temperatures observed in the CBL. Open squares are manual surface measurements of temperature at the sodar site and open triangles are hourly automated temperature measurements at Environment Canada's surface station in Pitt Meadows approximately 6 km south of the tethersonde site (from www.climate.weatheroffice.ec.gc.ca).

Between 1100 and 1220 PDT on July 26 the CBL mean potential temperature drops from an expected 5-6 K (roughly estimated from predicted value and extrapolated from earlier measurements) to 3.9 K and then rises again, as hypothesised probably because of the beginning sea breeze. To compare the temperature drop with the prediction, I can extract for July 26, 2001, the following values (section 2.2.4). The beginning of the sea breeze propagation at the coastline (near YVR) at 1130 PDT, i.e.

$$t_{p,a} \approx 3.5\, hours = 12{,}600\, s \tag{3.58}$$

after the beginning of positive net sensible surface heat flux at 0800 PDT; the distance of Minnekhada Park from the coastline,

$$x \approx 35{,}000\, m\,; \tag{3.59}$$

the speed of sea breeze propagation as the sum of sea breeze speed (3 m s^{-1}) and synoptic wind speed (2 m s^{-1}),

$$U_{p,a} \approx 5\, m\, s^{-1}\,. \tag{3.60}$$

The transition time to sea breeze after the beginning of the sea breeze propagation at the coastline at Minnekhada Park is then

$$t_{t,a} = \frac{x}{U_{p,a}} \approx 7{,}000\, s\,, \tag{3.61}$$

or approximately 1330 PDT. Substituting (3.15), (3.23), (3.24), and (3.57) into (3.52) gives the CBL mean potential temperature increment right before the onset of the sea breeze at 1330 PDT,

$$\theta_a \approx 6.4\, K\,. \tag{3.62}$$

Using (3.15), (3.23), (3.24), (3.57), (3.58), and (3.61) in (3.56) gives the predicted convective TIBL mean potential temperature increment at the onset time of the sea breeze

$$\theta_{t,a} \approx 4.8\, K\,. \tag{3.63}$$

Hence one can roughly expect a temperature drop of 1.6 K at 1330 PDT. Tethersonde observations on July 26 show the expected temperature drop, but the onset time before 1230 PDT (approximately in line with the conclusions in section 2.2.4.), is more than an hour too early. Station data show the expected temperature drop at the expected time. On July 25, station data from 1100-1300 PDT give an extrapolated surface temperature increment of 10-10.5 K for 1400 PDT compared to an observed value of 8.4 K (Figure 3.4). A similar extrapolation on July 26 gives 8.5-9 K versus observed 7.6 K. It is possible that the sea breeze arrived later in the surface layer than in the mixed layer above because of surface friction. Moreover, the discrepancy between the onset time at the tethersonde site and the Pitt Meadows surface station could be an uncertainty caused by the complicated coastline of the Lower Fraser Valley.

Overall the few available data reasonably support the hypothesis on the CBL mean potential temperature increment despite the simplifying assumptions.

Formulation and Verification of the Hypothesis on CBL Depth

Next I formulate a hypothesis for the CBL depth at the tethersonde site over the plain far from the foot of the slope (Figure 2.1, page 13). A quantitative estimate of the CBL depth is given by (3.51). Recall from page 52 that entrainment should be fairly small because of the strong background stratification. Equation (3.55) gives an estimate of the depth of the TIBL after the onset of the sea breeze. In summary:

Hypothesis:

The expected value of the CBL depth in the atmosphere over the plain far from the slope as a function of atmospheric reference time t_a is given by

$$h_a(t_a)=\left\{\frac{g\beta_a}{N_a^2}\cdot Q_{\max,a}\,t_{d,a}\cdot\frac{4}{\pi}\left[1-\cos\left(\frac{\pi}{2}\frac{t_a}{t_{d,a}}\right)\right]\right\}^{1/2}.$$

This formula underestimates the observed values, but only slightly because the background stratification is fairly strong and entrainment is weak. Between 1200 and 1300 PDT, the CBL at the field site is replaced by a convective TIBL of cooler marine air, briefly reducing the CBL depth to

$$h_{t,a}\approx\left\{\frac{g\beta_a}{N_a^2}\cdot Q_{\max,a}t_{d,a}\cdot\frac{4}{\pi}\left[\cos\left(\frac{2}{\pi}\frac{t_{p,a}}{t_{d,a}}\right)-\cos\left(\frac{2}{\pi}\frac{t_{p,a}+t_{t,a}}{t_{d,a}}\right)\right]\right\}^{1/2}.$$

Once the sea breeze is established the convective TIBL depth rises again. ■

The CBL depth h_a has to be determined from the thermal structure over the plain where the local slope presumably does not affect the CBL. The few tethersonde measurements of the thermal boundary layer (TBL) depth are in reasonable agreement with the predictions for July 25 (Figure 3.5) and slightly exceed predictions for the morning of July 26 as expected for an entrainment coefficient of $A>0$.

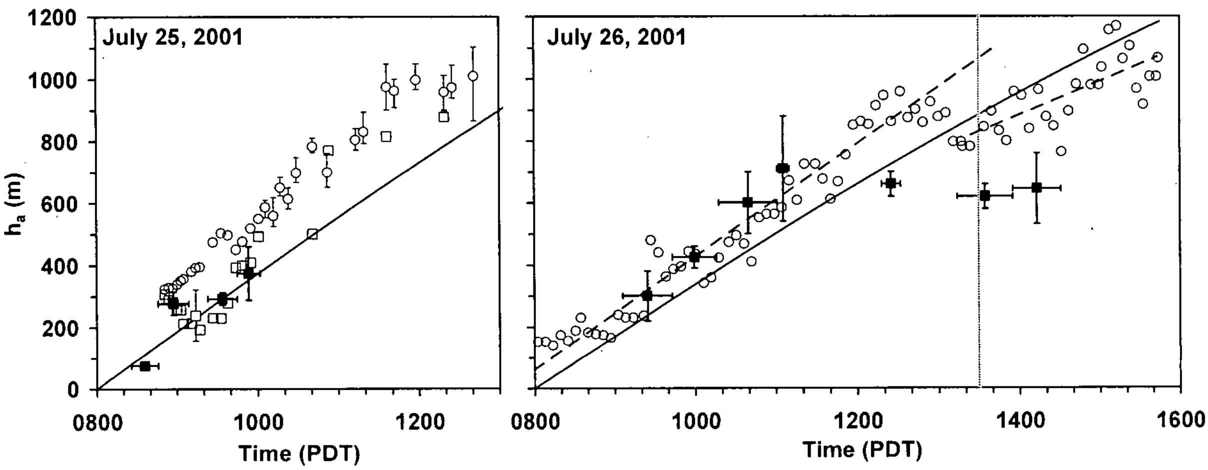

Figure 3.5: Comparison of field observations and AI predictions of CBL depth.
Left graph is for July 25, right graph for July 26, 2001. Axes have the same scale. The solid line is the hypothesis prediction based on (3.51). The data are a synopsis of CBL information retrieved from Figure 2.3 to Figure 2.8. Solid squares with error bars denote tethersonde measurements of thermal boundary layer depth over the plain. Horizontal error bars are flight duration, and vertical error bars represent the uncertainty in the neutral buoyancy height. Open squares show the backscatter boundary layer (BBL) as determined from lidar measurements extrapolated to the tethersonde site (data only available for July 25); a representative uncertainty from the extrapolation is shown once by a vertical error bar at 0915 PDT. Open circles are lidar measurements of the BBL above the sodar. Variations of this height over the horizontal beam spread of the sodar signal are shown as vertical error bars only on July 25 after 1000 PDT. The graph for July 26 includes two individual linear best fit curves for 0800-1230 PDT and 1320-1540 PDT (dashed lines). The thin vertical line indicates the approximate time of transition to sea breeze as determined from station data.

On July 25, TBL and BBL depth over the plain agreed well as was demonstrated above (Figure 2.6, page 21). I do not have data to determine the BBL depth over the tethersonde site for July 26, but will assume here that the two agree. In the afternoon of July 26, TBL depth over the tethersonde site does not agree well with the BBL depth over the *sodar* site. This is a potentially interesting point, which I will revisit in chapter 4, with the support of water-tank data.

On both days, the backscatter boundary layer (BBL) at the foot of the slope grew fairly linearly throughout the morning until the sea breeze slowed down the growth just before 1200 PDT on July 25 and at about 1230 PDT on July 26, in agreement with the hypothesis. As already pointed out above in the discussion on potential temperature, the transition to sea breeze predicted from station data occurred between 1300 and 1400 PDT, approximately one hour later than estimated from tethersonde observations. For July 26, with (3.15), (3.23), (3.24), (3.57), (3.58), and (3.61) substituted into (3.55), the predicted convective TIBL depth over the plain at the beginning of the sea breeze at 1330 PDT is

$$h_{t,a} \approx 659\, m\,, \tag{3.64}$$

a drop of about 220 m from the CBL depth of

$$h_a \approx 880\, m \tag{3.65}$$

right before the sea breeze at 1330 PDT.

Given the agreement between TBL and BBL depth, the predicted drop in boundary-layer depth can best be compared with the abundant lidar data at the sodar site. These data indicate a transition to sea breeze between 1230 and 1320 PDT. Recall from (3.53), that the CBL depth is approximately linear in time in the morning. A linear regression for 0800-1230 PDT gives

$$h_a = \left(0.051 \pm 0.002\right) m\, s^{-1} \times t_a + \left(60 \pm 20\right) m \tag{3.66}$$

with an adjusted R^2 of 0.94. A linear approximation for afternoon data from 1320-1540 PDT is very crude (R^2 = 0.46), but suffices here to gain an estimate of the drop in boundary-layer depth at 1330 PDT:

$$h_a = \left(0.030 \pm 0.006\right) m\, s^{-1} \times t_a + \left(240 \pm 150\right) m\,. \tag{3.67}$$

For 1330 PDT, (3.66) and (3.67) give a drop of $\Delta h_a = 1066\, m - 829\, m = 237\, m$ in boundary-layer depth, in good agreement with the expected drop of 220 m.

Overall, the hypothesis on the CBL depth is supported by the field observations.

3.4.2 Upslope Flow Velocity

So far, the quantities h_a and $\theta_{s,a}$ were considered for convection over a homogeneous horizontal surface (the plain), for which the encroachment model seems a reasonable approximation. The third quantity, for which I have field observations over the plain near the foot of the slope, the upslope flow velocity U_a, requires further assumptions.

The approaches taken in the literature to derive upslope flow velocities can roughly be divided into those trying to address the complexity of real slopes (e.g. Vergeiner, 1982, and Vergeiner and Dreiseitl, 1987) and those dealing with idealisations (e.g. Egger, 1981; Brehm, 1986; Haiden, 1990; and Schumann, 1990). The exchange of ideas between Vergeiner and Schumann in Vergeiner (1991) demonstrates the existing gap between the two approaches. Clearly, the work in this dissertation belongs to the latter category. It is my hope, however, to narrow this gap. The field observations at Minnekhada Park come closer to idealisations than many previous observations with regards to constant angle and two-dimensionality of the slope, homogeneous surface properties, linear background stratification, and negligible larger-scale flows. Furthermore, water-tank experiments in this thesis add 'physical reality' that critics may miss in numerical models.

I now introduce five hypotheses of upslope flow velocity extracted from the literature and compare them with our field observations. Appendix B.1 contains the derivations and detailed discussions of these hypotheses.

Upslope Flow Velocity Hypotheses

In Appendix B.1, I discussed several upslope flow hypotheses by different authors. Because the hypotheses do not agree well with observations I generalised these allowing for an unknown constant parameter in all but one hypothesis. The goal here is to compare the different hypotheses with each other in the first step. In the second step I will carry out an empirical analysis on all available morning observations on July 25 and 26 to derive a best-fit hypothesis. Afternoon observations on July 26 will not be included in the analysis because of likely modifications by sea breeze and up-valley flow.

Empirical Analysis of Non-dimensional Upslope Flow Velocity

The scaling analysis in this chapter substantially reduces the effort needed to find functional relationships between upslope flow velocity and potentially physically relevant quantities. Because the aspect ratio $\Pi_1 = L_a/H_a$ is fixed, the ND maximum upslope flow velocity is only a function of Π_2 and Π_3 (Appendix B.2). I want to make use of the data to find a monomial relationship for the atmosphere,

$$U_{\max,a}^{*} \equiv \frac{U_{\max,a}}{H_a N_a} = f_U\left(\Pi_{2,a}, \Pi_{3,a}\right) = c_a \cdot \Pi_{2,a}^{\ m_1} \cdot \Pi_{3,a}^{\ m_2}, \tag{3.68}$$

where $\Pi_1 = L_a / H_a$ is included in the constant c_a and

$$\Pi_{2,a} = E_a \cdot \frac{N_a}{Q_{H,a}},$$

$$\Pi_{3,a} = g\beta_a \cdot \frac{Q_{H,a}}{H_a^{\ 2} N_a^{\ 3}}.$$

The hypotheses in ND form to be studied are given by (B.59)-(B.63), which I repeat here for the atmosphere:

$$U_{Hunt,a}^{*} = c_{Hunt,a} \cdot \Pi_{2,a}^{\ 1/6} \cdot \Pi_{3,a}^{\ 1/2} \text{ (Hunt)}, \tag{3.69}$$

$$U_{Chen,a}^{*} = c_{Chen,a} \cdot 2^{1/2} \cdot \Pi_{2,a}^{\ 1/2} \cdot \Pi_{3,a}^{\ 1/2} \text{ (Chen)}, \tag{3.70}$$

$$U_{fric,a}^{*} = 0.322 \cdot 2^{1/2} \cdot \Pi_{2,a}^{\ 1/2} \cdot \Pi_{3,a}^{\ 1/2} \text{ (friction)}, \tag{3.71}$$

$$U_{Grav,a}^{*} = c_{Grav,a} \cdot \Pi_{2,a}^{\ 1/4} \cdot \Pi_{3,a}^{\ 1/4} \text{ (gravity current)}, \tag{3.72}$$

$$U_{Schu,a}^{*} = c_{Schu,a} \cdot \Pi_{3,a}^{\ 1/2} \text{ (Schumann)}. \tag{3.73}$$

At this stage of the investigation, the factors $c_{Hunt,a}$, $c_{Chen,a}$, $c_{Grav,a}$, and $c_{Schu,a}$ are expected to be constant, which may include a dependence on the aspect ratio Π_1, because Π_1 is constant in all atmospheric observations.

In Appendix B.2 I carry out a conventional statistical analysis, which shows that the uncertainty of m_1 and m_2 in (3.68) is very large. Here I will demonstrate the use of probability theory as extended logic to determine probability distributions for c_a, m_1, and m_2 and to compare different hypothesis. I begin with the hypothesis comparison, for which I will determine the probability distribution for the coefficients c_a in an intermediate step.

Estimation of the Hypotheses Coefficients Using Probability Theory

The basic question I ask from the data is: What are the relative probabilities of the hypotheses (3.69)-(3.73) for the upslope flow velocity given the field observations of maximum upslope flow velocities at Minnekhada Park on the morning of July 25 and 26, 2001? I define the following statements or propositions. Notice that I change the notation from (3.69)-(3.73) to one with running indices and mostly drop the subscript 'a' to reduce the number of subscripts.

- I = "The maximum value in the vertical profile of upslope flow velocity at the foot of Minnekhada Park was measured every 20 minutes from 0850-1230 PDT on July 25 and 0810-1210 PDT on July 26, 2001. Maximum upslope flow velocity was non-dimensionalised by dividing by ridge height $H_a = 760\,m$ and buoyancy frequency $N_a = 0.0149\,s^{-1}$ on July 25 and $N_a = 0.0162\,s^{-1}$ on July 26. It is assumed that the ND maximum upslope flow velocity can be expressed as a monomial plus independent, identically distributed Gaussian background noise of unknown but equal standard deviation." (Background information)

- D = "The observed $n = 24$ data were $d_i = \ldots$, where $i = 1,\ldots,n$" (Statement on the data)

- $H^{(1)}$ = "The ideal data are described by $f^{(1)}{}_i = U_{Hunt,a}{}^* = c^{(1)} \cdot \Pi_{2,i}{}^{1/6} \cdot \Pi_{3,i}{}^{1/2}$, $i = 1,\ldots,n$" (Hunt hypothesis)

- $H^{(2)}$ = "The ideal data are described by $f^{(2)}{}_i = U_{Chen,a}{}^* = c^{(2)} \cdot 2^{1/2} \cdot \Pi_{2,i}{}^{1/2} \cdot \Pi_{3,i}{}^{1/2}$, $i = 1,\ldots,n$" (Chen hypothesis)

- $H^{(3)}$ = "The ideal data are described by $f^{(3)}{}_i = U_{Grav,a}{}^* = c^{(3)} \cdot \Pi_{2,i}{}^{1/4} \cdot \Pi_{3,i}{}^{1/4}$, $i = 1,\ldots,n$" (gravity-current hypothesis)

- $H^{(4)}$ = "The ideal data are described by $f^{(4)}{}_i = U_{Schu,a}{}^* = c^{(4)} \cdot \Pi_{3,i}{}^{1/2}$, $i = 1,\ldots,n$" (Schumann hypothesis)

- $H^{(5)}$ = "The ideal data are described by $f^{(5)}{}_i = U_{fric,a}{}^* = 0.322 \cdot 2^{1/2} \cdot \Pi_{2,i}{}^{1/2} \cdot \Pi_{3,i}{}^{1/2}$, $i = 1,\ldots,n$" (friction hypothesis)

In all hypotheses the ideal data are of the form $f^{(j)}{}_i = c^{(j)} \cdot \left(2^{1/2}\right) \cdot \Pi_{2,i}{}^{m_1^{(j)}} \cdot \Pi_{3,i}{}^{m_2^{(j)}}$, where $m_1^{(j)}$ and $m_2^{(j)}$ are given, the constant coefficients $c^{(1)}$ to $c^{(4)}$ are for now assumed unknown, and $c^{(5)} = 0.322$ is given.

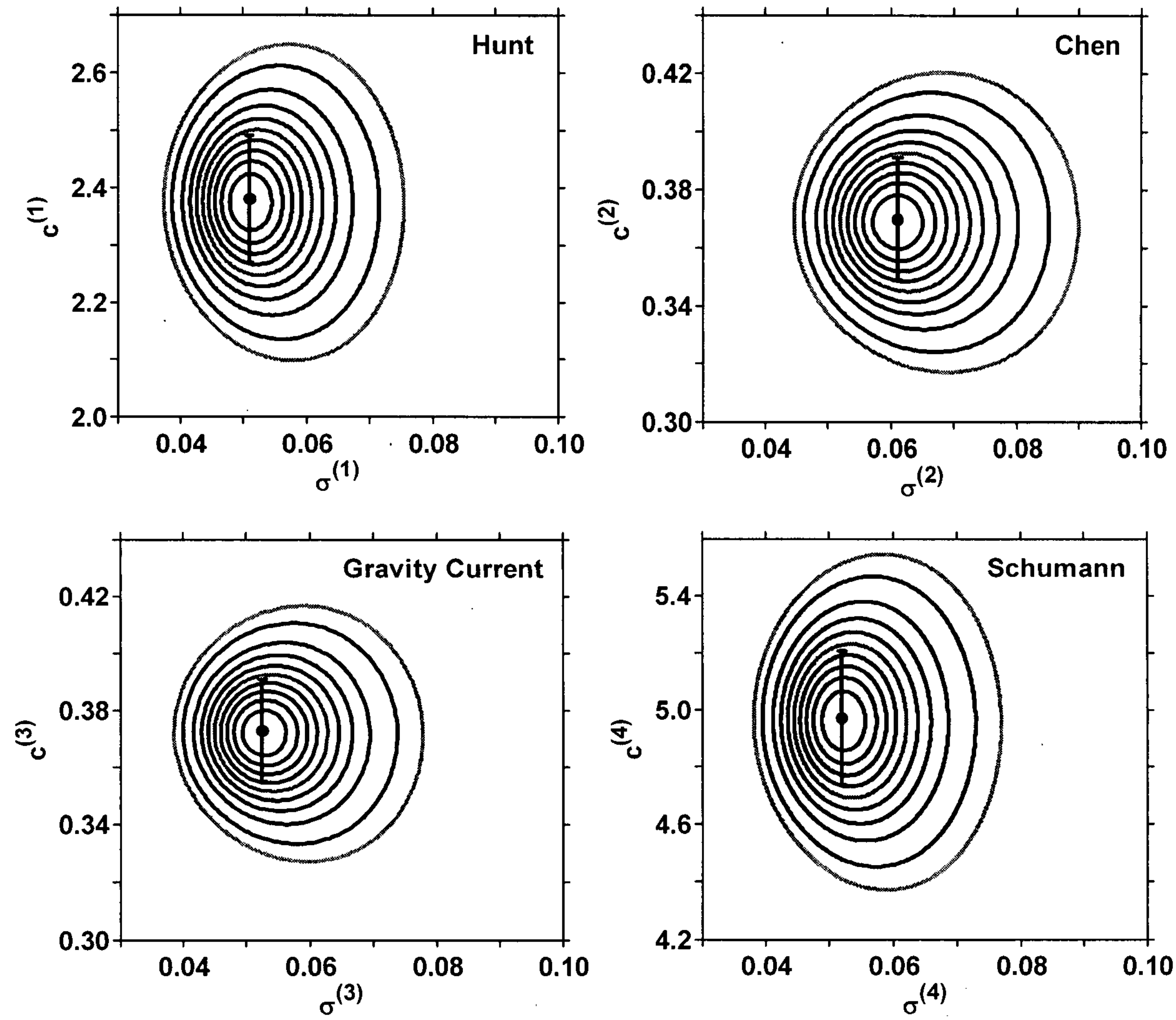

Figure 3.6: Joint probability distribution of unknown constant factor and standard deviation of background noise for different upslope flow velocity hypotheses.

All probability distributions are normalised to a maximum value of 1. Contour lines are shown for 0.05 (outer line) and from 0.1 to 0.9 in steps of 0.1. Notice that the scale for the standard deviations is equal in all four panels, but the scale for the constant factors is different. The linear least-square best fit values of the constant factors $c^{(1)}$ to $c^{(4)}$ are shown as data points with one standard deviation.

In Appendix B.3, I derive the equation for the joint probability distribution of the constant factors $c^{(1)}$ to $c^{(4)}$ and the standard deviations of the Gaussian background noise, $\sigma^{(1)}$ to $\sigma^{(4)}$,

$$p\left(c^{(j)},\sigma^{(j)}\middle|D,H^{(j)},I\right)\propto\frac{1}{c^{(j)}\left(\sigma^{(j)}\right)^{n+1}}\exp\left[-\frac{1}{\left(\sigma^{(j)}\right)^{2}}\sum_{i=1}^{n}\left(d_i-c^{(j)}{}_k\cdot\Pi_{2,i}{}^{m_1^{(j)}}\cdot\Pi_{3,i}{}^{m_2^{(j)}}\right)^{2}\right]. \quad (3.74)$$

The joint probability distributions (3.74) agree very well with the constant factors and their standard deviations, (B.85)-(B.88), determined from linear regression (Figure 3.6).

All probability distributions show the same asymmetry relative to $\sigma^{(j)}$. This suggests that some systematic bias must be present. The assumption of Gaussian noise was therefore not the best and more conservative than necessary if one could quantify the asymmetry. Changes in the internal flow structure, which are not accounted for in the simple hypotheses $H^{(1)}$ to $H^{(4)}$, could be responsible for the bias, but I lack additional information to investigate this further.

Figure 3.6 also confirms that $c^{(j)}$ and $\sigma^{(j)}$ are independent of each other because the principle axes of the (distorted) ellipses are parallel to the Cartesian coordinates (for more information see Gregory, 2005).

Finally, the Chen hypothesis shows a larger standard deviation than the other three hypotheses, and the probability distribution of the constant coefficient for the Chen hypothesis shows a wider spread than for the gravity-current hypothesis. This agrees with the result of the hypothesis comparison, which I will carry out in the next subsection.

It is of interest to compare the results of Figure 3.6 and (B.89), (B.90), and (B.92), i.e.

$$U_{Hunt,a}^* = 2.4\Pi_2^{1/6} \cdot \Pi_3^{1/2}, \tag{3.75}$$

$$U_{Chen,a}^* = 0.37 \cdot 2^{1/2}\Pi_2^{1/2} \cdot \Pi_3^{1/2}, \tag{3.76}$$

$$U_{Schu,a}^* = 5.0\Pi_3^{1/2}, \tag{3.77}$$

with the hypotheses originally suggested by the authors. For Hunt et al. (2003) from (B.11),

$$7.72\Pi_2^{1/6} \cdot \Pi_3^{1/2}, \tag{3.78}$$

for Chen et al. (1996) from (B.28), where I corrected for a missing $2^{1/2}$,

$$1 \cdot 2^{1/2}\Pi_2^{1/2} \cdot \Pi_3^{1/2}, \tag{3.79}$$

and for Schumann (1990) from (B.53),

$$2.1\Pi_3^{\frac{1}{2}}. \tag{3.80}$$

It is obvious that the original hypotheses (3.78)-(3.80) do not agree with observations within my target of 20 %, but all three hypotheses agree with the order-of-magnitude of the more accurate hypotheses (3.75)-(3.77).

Hypothesis Comparison Using Probability Theory

Summation over the joint probability distributions in Figure 3.6 and normalisation gives the relative probabilities for $H^{(1)}$ to $H^{(4)}$. In Appendix B.3, I show how the inclusion of the friction hypothesis $H^{(5)}$ penalises $H^{(1)}$ to $H^{(4)}$ for their additional unknown constant factor. This is called an 'Occam's penalty', a quantification of Occam's intuitive argument that simpler hypotheses are to be preferred over more complex hypotheses unless the data warrant the latter. The relative probabilities are given by (B.122),

$$p\left(H^{(j)}\middle|D,I\right) \propto \frac{\Delta c}{\ln\left(c_H/c_L\right)} \sum_{c_k=c_L}^{c_H} \sum_{\sigma_l=\sigma_L}^{\sigma_H} \frac{1}{c_k \sigma_l^{\,n+1}} \exp\left[-\frac{\sum_{i=1}^{n}\left(d_i - c_k \cdot \Pi_{2,i}^{\;m_1^{(j)}} \cdot \Pi_{3,i}^{\;m_2^{(j)}}\right)^2}{2\sigma_l^{\,2}}\right] \tag{3.81}$$

for $j = 1,\ldots 4$, and (B.123),

$$p\left(H^{(5)}\middle|D,I\right) \propto \sum_{\sigma_l=\sigma_L}^{\sigma_H} \frac{1}{\sigma_l^{\,n+1}} \exp\left[-\frac{\sum_{i=1}^{n}\left(d_i - 0.322\,\Pi_{2,i}^{\;\frac{1}{2}} \cdot \Pi_{3,i}^{\;\frac{1}{2}}\right)^2}{2\sigma_l^{\,2}}\right]. \tag{3.82}$$

The choice of priors has been much debated in the literature (e.g. Jaynes, 2003), but for the purpose of this thesis is suffices to choose realistically wide and equal prior ranges of $c^{(j)}$ and $\sigma^{(j)}$ for all hypotheses. With my particular choice, $c_H = 0.2$ and $c_L = 6.2$, the probabilities for $H^{(1)}$ to $H^{(4)}$ are reduced by the Occam's penalty

$$1/\ln\left(c_H/c_L\right) \approx 0.29. \tag{3.83}$$

Computation of (3.81) and (3.82) and normalisation according to (B.98) gives

$$p\left(H^{(1)}\middle|D,I\right) = 0.460 \text{ (Hunt)}, \tag{3.84}$$

$$p\left(H^{(2)}\middle|D,I\right)=0.008 \text{ (Chen)}, \tag{3.85}$$

$$p\left(H^{(5)}\middle|D,I\right)=0.015 \text{ (friction)}, \tag{3.86}$$

$$p\left(H^{(3)}\middle|D,I\right)=0.224 \text{ (gravity current)}, \tag{3.87}$$

$$p\left(H^{(4)}\middle|D,I\right)=0.293 \text{ (Schumann)}. \tag{3.88}$$

The Hunt hypothesis is the most probable, and the gravity-current and Schumann hypotheses are also very probable. The Chen and friction hypotheses have such a low probabilities that they are practically rejected by the field data. Although the Chen hypothesis agrees better with the data than the friction hypothesis (Figure Appendix VII), its probability is lower due to the Occam's penalty.

The progress made in the analysis so far emphasises the importance of the steps I have taken in the scaling. Previous investigators developed upslope flow hypotheses, which gave an order-of-magnitude agreement with "typical" values in the atmosphere. I applied dimensional analysis in an attempt to develop a mathematical model that agrees with the observations within 20 %. Inclusion of the time dependence of heating enabled me to compare the model with observations at different times. Individual data may agree or disagree accidentally with the hypothesis. For example, the friction hypothesis agreed well with the observation of the test case, (B.46), but Figure Appendix VII (page 199) clearly showed that the friction hypothesis compared poorly with observations at other times. Probability theory adds an important strength to the analysis here: The result of a conventional statistical analysis in Figure Appendix VII shows that the other four hypotheses perform better than the friction hypothesis; but only with a quantitative Occam's penalty in probability theory it was possible to show that the data justify the unknown coefficients in the Hunt, gravity-current, and Schumann hypotheses. Similarly, probability theory tells us that in the Chen hypothesis the unknown coefficient $c_{Chen,a}$ is not supported by the data because the Occam's penalty more than offsets the improved agreement by fitting the hypothesis to the data.

I will now take one more step in the application of probability theory and demonstrate a much more powerful way of comparing the hypotheses with the field data than Figure Appendix VI (page 198).

The Joint Probability Distribution of m_1 ***and*** m_2

I want to calculate the joint probability distribution of the exponents m_1 and m_2 in (3.68), given the data and background information and using probability theory as extended logic. As before for the probabilities of the four hypotheses the procedure is straightforward, however, substantial algebraic manipulations are required to make a brute-force computation of the joint probability distribution feasible (Appendix B.2). These lead to (B.136), which I reproduce here:

$$p\left(m_1, m_2 \middle| D, I\right) \propto \sum_{k=0}^{k_H} \left[\sum_{i=1}^{n} \left(d_i - c_L \cdot 10^{k/n_s} \cdot \Pi_{2,i}{}^{m_1} \cdot \Pi_{3,i}{}^{m_2} \right)^2 \right]^{-n/2}, \tag{3.89}$$

where $k_H = n_s \cdot \log_{10} \frac{c_H}{c_L}$ and n_s is the number of steps per order of magnitude in the range of c from c_L to c_H. The LHS is the conditional joint probability distribution of the two unknown parameters given the same background information I and proposition on the data D as before.

The probability distribution, normalized such that the maximum value is one, is shown in Figure 3.7, A. The almost 45°-angle of the two principle axes of the ellipse relative to the Cartesian axes and the large ratio between major and minor axes indicate a strong correlation between m_1 and m_2 (Gregory, 2005). The reason for the correlation is that both $\Pi_{2,a}$ and $\Pi_{3,a}$ depend on time t_a. In Appendix B.2 I demonstrate that $\Pi_{3,a}{}' = \Pi_{3,a}/\Pi_{2;a}$ depends only weakly on t_a so that $\Pi_{2,a}$ and $\Pi_{3,a}{}'$ are only weakly correlated. The normalised joint probability distribution for m_1 and m_2 in the hypothesis $U_{\max,a}{}^* = c \cdot \Pi_{2,a}{}^{m_1} \cdot \left(\Pi_{3,a}{}'\right)^{m_2}$ confirms this only weak correlation by showing only slightly tilted principle axes (Figure 3.7, B).

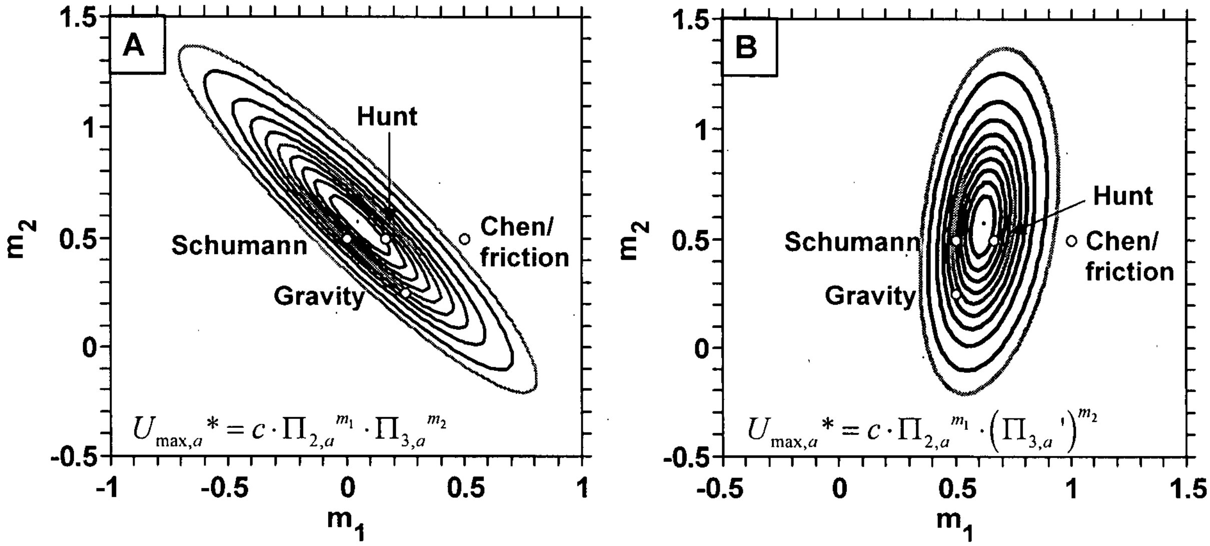

Figure 3.7: Joint probability distribution $p(m_1, m_2 | D, I)$ of the exponents in upslope flow velocity hypothesis for the atmosphere.

I assumed an upslope flow hypothesis of form $U_{\max,a}{}^* = c \cdot \Pi_{2,a}{}^{m_1} \cdot \Pi_{3,a}{}^{m_2}$ (A) and $U_{\max,a}{}^* = c \cdot \Pi_{2,a}{}^{m_1} \cdot (\Pi_{3,a}{}')^{m_2}$ (B) for the field data on July 25 and 26 until 1230 PDT and determined the joint probability distribution $p(m_1, m_2 | D, I)$ of the exponents m_1 and m_2 by marginalising over the unknown factor c and assuming normally-distributed background noise. The joint probability distribution is normalised such that the maximum value is 1. Contour lines are shown for 0.05 (outer line) and from 0.1 to 0.9 in steps of 0.1. Included are the positions (circles) of the upslope flow velocity hypotheses discussed in the main text.

If one adds the four hypotheses $H^{(1)}$ - $H^{(4)}$ to Figure 3.7, it is easy to see that the Hunt hypothesis is close to the mode and that the gravity-current and Schumann hypotheses also have high probability, while the Chen and friction hypotheses are outside of the 0.05 contour line.

In Lieu of Formulating a Hypothesis on Upslope Flow Velocity

Rather than attempt to formulate a hypothesis on the maximum upslope flow velocity I briefly summarise the results of this section and Appendix B.1. I discussed three derivations of upslope flow velocity hypotheses in the literature (Hunt et al., 2003; Chen et al., 1996; Schumann, 1990). None of these hypotheses agreed within 20 % with field observations at 1200 PDT on July 25. Based on these hypotheses I developed four generalisations with tuneable coefficients, the 'Hunt', 'Chen', 'gravity-current', and 'Schumann hypotheses'. Based on the Prandtl (1942) profile and the derivation in Chen et al. (1996), I developed a 'friction hypothesis' with fixed coefficient, which agreed well with the observations at 1200 PDT on July 25. A hypothesis comparison using probability theory reveals that, after fitting the coefficients, the Chen and friction hypotheses are much less likely than the other three hypotheses.

It was not possible to empirically derive a sufficiently concrete hypothesis for the ND upslope flow velocity as a function of the two Pi groups $\Pi_{2,a}$ and $\Pi_{3,a}$. In the atmosphere, $\Pi_{2,a}$ and $\Pi_{3,a}$ are closely coupled via atmospheric reference time t_a. I replaced $\Pi_{3,a}$ by a new Pi group $\Pi_{3,a}' = \Pi_{3,a}/\Pi_{2,a}$, which is only weakly dependent on t_a and therefore $\Pi_{2,a}$. The uncertainty in the dependence of ND maximum upslope flow velocity $U_{\max,a}*$ on $\Pi_{3,a}'$ is very large because the field data from Minnekhada Park cover only a narrow range. An informative representation of the field data is given by Figure 3.7, which confirms the result of the hypothesis comparison: Hunt, gravity-current, and Schumann hypotheses all have reasonably high probabilities above 0.4 because of the large uncertainty in the exponents of $\Pi_{2,a}$ and $\Pi_{3,a}$, while the Chen and friction hypotheses are outside of the 0.05 probability contour line.

This completes the discussion of hypotheses for the field observations. I now derive the water-tank hypotheses, which will be tested later in section 4.3.

3.5 Hypotheses for the Water Tank

In this section I derive testable hypotheses for the water-tank experiments, which will be covered in chapter 4, for the CBL depth over the plain h_w, the CBL specific volume increment $\alpha_{s,w}$, and the maximum upslope flow velocity $U_{\max,w}$.

3.5.1 CBL Depth

To calculate the CBL depth over the plain in the water tank, h_w, note that the ND CBL depth $h* = h/H = \left(2\Pi_2\Pi_3\right)^{1/2}$ must be equal for both WTI and AI, i.e.

$$\frac{h_a}{H_a} = \frac{h_w}{H_w} = \left(2\Pi_2\Pi_3\right)^{1/2}. \tag{3.90}$$

Solving for h_w and substituting Π_2 and Π_3 from (3.45) and (3.46) gives

$$h_w = \frac{\left(2g\beta_w Q_{H,w} t_w\right)^{1/2}}{N_w}. \tag{3.91}$$

Using this last equation and the hypothesis on CBL depth in the AI (page 58), I can formulate the corresponding WTI hypothesis.

Hypothesis:

The expected value of the CBL depth in the water tank over the plain as a function of water-tank reference time t_w is given by

$$h_w\left(t_w\right) = \frac{\left(2g\beta_w Q_{H,w} t_w\right)^{1/2}}{N_w}.$$

This formula underestimates the observed values, but only slightly because background stratification is fairly strong and entrainment is weak. ■

3.5.2 CBL Specific Volume

For the water tank, the CBL encroachment model equivalent to Figure 3.3 (page 52) is shown in Figure 3.8.

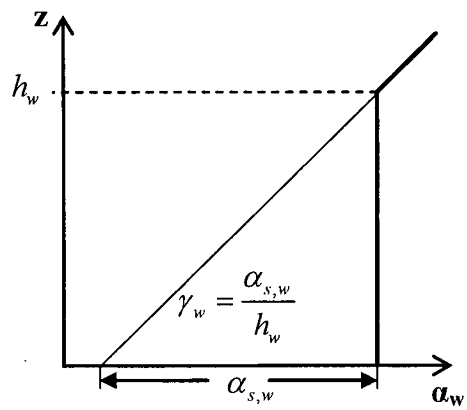

Figure 3.8: Diagram of quantities in an encroachment model of the CBL in the WTI.

h_w is the CBL depth at the water-tank reference time t_w, α_w is the corresponding CBL mean specific volume increment, and γ_w is the background stratification before the start of the experiment.

The CBL specific volume increment $\alpha_{s,w}$ is, using (3.21) and (3.91),

$$\alpha_{s,w}(t_w) = \gamma_w h_w = \frac{\alpha_{0,w}}{g} N_w^{\ 2} h_w = \frac{\alpha_{0,w}}{g} N_w \left(2g\beta_w Q_{H,w} t_w\right)^{1/2}. \tag{3.92}$$

With this, the hypothesis for the CBL mean specific volume increment in the WTI becomes:

Hypothesis:

The expected value of the CBL mean specific volume increment in the water tank at the foot of the slope as a function of water-tank reference time t_w is given by

$$\alpha_{s,w}(t_w) = \frac{\alpha_{0,w}}{g} N_w \left(2g\beta_w Q_{H,w} t_w\right)^{1/2}. \ \blacksquare$$

3.5.3 Upslope Flow Velocity

Finally I derive a hypothesis for the maximum upslope flow velocity $U_{\max,w}$. Because of the required similarity between AI and WTI, (B.58) in Appendix B.2, (B.65) also applies to the WTI, i.e.

$$U_{\max,w}{}^* \equiv \frac{U_{\max,w}}{H_w N_w} = (5 \pm 17) \cdot \Pi_{2,w}{}^{\pm 0.3} \Pi_{3,w}{}^{(0.6 \pm 0.3)}. \tag{3.93}$$

The dimensional form follows from (3.45) and (3.46),

$$U_{\max,w}(t_w) = (5 \pm 17) \cdot H_w N_w \cdot (t_w \cdot N_w)^{\pm 0.3} \left(\frac{g\beta_w Q_{H,w}}{H_w^{\ 2} N_w^{\ 3}}\right)^{(0.6 \pm 0.3)}. \tag{3.94}$$

The reader can easily verify that the use of (B.76) instead of (B.65) above leads to the same result.

Hypothesis:

The maximum value in the vertical profile of ND upslope flow velocity in the water tank over the plain near the foot of the slope as a function of laboratory time t_w is

$$U_{\max,w}{}^* \equiv \frac{U_{\max,w}}{H_w N_w} = (5 \pm 17) \cdot \Pi_{2,w}{}^{\pm 0.3} \Pi_{3,w}{}^{(0.6 \pm 0.3)}.$$

The vertical profiles of along-slope velocities are expected to show return flows like the field observations at Minnekhada Park. ■

3.6 The Relation Between Atmospheric and Water-Tank Reference Time

So far, all hypotheses expressed atmospheric quantities in atmospheric reference time and water-tank quantities in water-tank reference time. The similarity constraints $\Pi_{2,a} = \Pi_{2,w}$, (3.43), and $\Pi_{3,a} = \Pi_{3,w}$, (3.44), entered the derivation of each of the quantities h_w, $\alpha_{s,w}$, and $U_{\max,w}$ either directly or through t_w and N_w in (3.47) and (3.48). The testing of the hypotheses involving these three quantities at all water-tank reference times t_w in the next chapter therefore is a powerful test of similarity. However, similarity between AI and WTI can only be achieved at one instant in time because of the different time dependence of the surface heat flux.

Heating in the atmosphere was assumed to be approximately sinusoidal while it is constant in the water tank. That immediately implies that instantaneous heat flux and energy density, which is time-integrated heat flux, grow differently in atmosphere and water tank. Similarity is possible only at one instant in time for any given experimental setup. To see that recall (3.22), (3.32), (3.44), and (3.48):

$$Q_{H,a}\left(t_{a,sim}\right) = Q_{\max,a} \cdot \sin\left(\frac{\pi}{2}\frac{t_{a,sim}}{t_{d,a}}\right),$$

$$\Pi_3 = \Pi_{3,a} = g\beta_a \cdot \frac{Q_{H,a}}{H_a^{\ 2} N_a^{\ 3}}, \text{ and}$$

$$N_w = \left(g\beta_w \frac{Q_{H,w}}{H_w^{\ 2}\Pi_3}\right)^{1/3},$$

where $t_{a,sim}$ denotes the instant in time, at which to achieve similarity between AI and WTI. Substituting the first into the second and the second into the third equation gives

$$N_w = N_a \left[\frac{\beta_a}{\beta_w} \frac{H_w^{\ 2}}{H_a^{\ 2}} \frac{Q_{\max,a}}{Q_{H,w}} \sin\left(\frac{\pi}{2} \frac{t_{a,sim}}{t_{d,a}} \right) \right]^{-1/3} . \tag{3.95}$$

For a water-tank experiment with given $Q_{H,w}$ and field observations with given $Q_{\max,a}$, $t_{d,a}$, and N_a, all quantities on the right-hand side of (3.95) are given and the buoyancy frequency of the WTI, N_w, is fully determined. This value needs to be chosen before the experiment (Figure 3.9), which can achieve similarity only at $t_a = t_{a,sim}$. To achieve similarity for another instant in time on the same day another experiment with another N_w needs to be carried out.

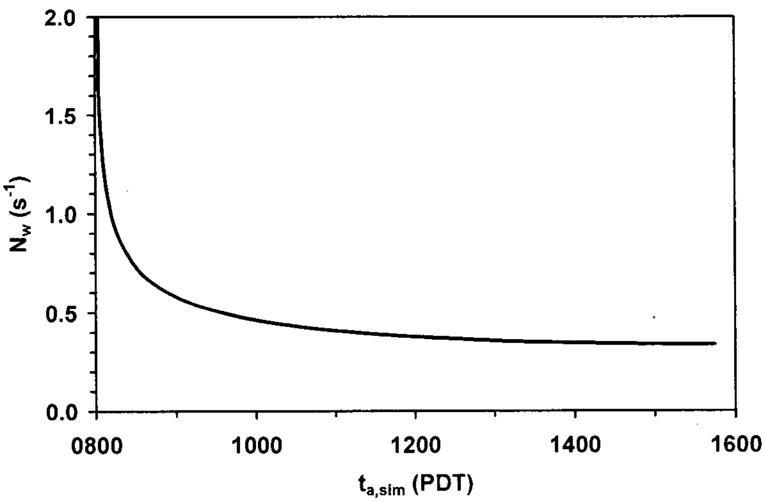

Figure 3.9: Water-tank buoyancy frequency N_w required to achieve similarity of the tank experiment with the atmosphere at atmospheric reference time $t_{a,sim}$.

The graph shows the buoyancy frequency N_w to be prepared at the beginning of a water-tank experiment to achieve similarity with atmospheric observations at an instant in time, $t_{a,sim}$, for the following parameter settings: $Q_{H,w} = 1.85 \times 10^{-3}\ K\ m\ s^{-1}$, $Q_{\max,a} \approx 0.289\ K\ m\ s^{-1}$, $t_{d,a} \approx 27{,}900\ s$, $N_a \approx 0.0149\ s^{-1}$, and all other values as in Table 3.1 on page 44.

At this time I have not made use, yet, of the similarity requirement $\Pi_{2,w} = \Pi_{2,a}$, which gives

$$t_w = \frac{N_a}{N_w} \cdot t_{d,a} \cdot \frac{2}{\pi} \frac{1-\cos\left(\frac{\pi}{2}\frac{t_a}{t_{d,a}}\right)}{\sin\left(\frac{\pi}{2}\frac{t_a}{t_{d,a}}\right)}. \tag{3.96}$$

If one chooses an atmospheric reference time $t_{a,sim}$ to achieve similarity, then (3.95) substituted into (3.96) gives the corresponding water-tank reference time

$$t_{w,sim} = t_{d,a} \frac{2}{\pi} \left[\frac{\beta_a}{\beta_w} \frac{H_w^{\ 2}}{H_a^{\ 2}} \frac{Q_{\max,a}}{Q_{H,w}} \right]^{1/3} \left[\sin\left(\frac{\pi}{2}\frac{t_{a,sim}}{t_{d,a}}\right) \right]^{-2/3} \left[1-\cos\left(\frac{\pi}{2}\frac{t_{a,sim}}{t_{d,a}}\right) \right]. \tag{3.97}$$

For example, for the parameter settings in the test case, 1200 PDT in the atmosphere corresponds to about 5 minutes in the water tank. Equation (3.97) must not be used without including the constraint in (3.95). I can try to achieve similarity at another atmospheric reference time, and (3.97) will give me the corresponding water-tank reference time. Similarity cannot be achieved in the same experiment, however, because (3.95) tells us that the experiment should have started with a different background buoyancy frequency N_w.

An important corollary can be derived by reversing (3.95):

$$N_a = N_w \left[\frac{\beta_a}{\beta_w} \frac{H_w^{\ 2}}{H_a^{\ 2}} \frac{Q_{\max,a}}{Q_{H,w}} \sin\left(\frac{\pi}{2}\frac{t_a}{t_{d,a}}\right) \right]^{1/3}. \tag{3.98}$$

The same experiment with initial background buoyancy frequency $N_w = 0.3785\,s^{-1}$ can be used to check similarity with atmospheric observations for a buoyancy frequency $N_a = 0.0149\,s^{-1}$ (July 25) at $t_a = 14,400\,s$ (1200 PDT) and for $N_a = 0.0162\,s^{-1}$ (July 26) at $t_a = 21,018\,s$ (1350 PDT) (dashed lines in Figure 3.10). I will use this corollary in section 4.4.

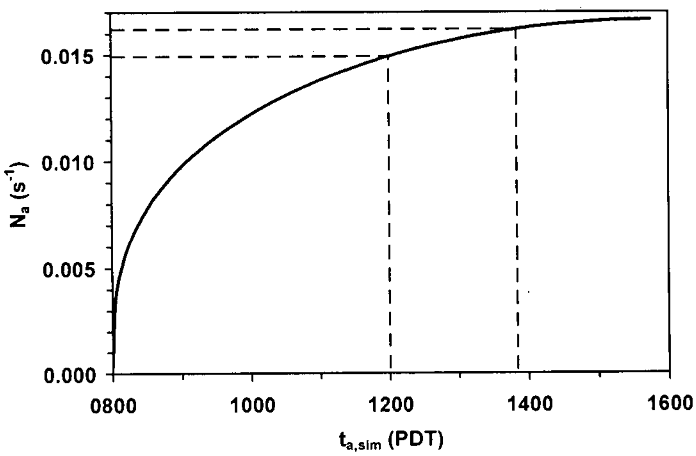

Figure 3.10: Relationship between atmospheric background buoyancy frequency N_a and time of similarity $t_{a,sim}$ for a given water-tank experiment.

The graph demonstrates how one experimental setup with $Q_{H,w} = 1.85\times10^{-3}\ K\ m\ s^{-1}$ and $N_w = 0.3785\ s^{-1}$ can be used to check similarity between water-tank and field observations at two different days with different atmospheric background buoyancy frequencies. The horizontal dashed lines mark background conditions on July 25 and 26, 2001. The vertical dashed lines show the corresponding time of day at which the atmosphere was similar to the water tank. The respective water-tank reference times can be computed from (3.97). Parameter settings were $Q_{\max,a} \approx 0.289\ K\ m\ s^{-1}$, $t_{d,a} \approx 27{,}900\ s$, and all other values as in Table 3.1 on page 44.

That any given water-tank experiment can achieve similarity with the atmosphere only at one point in time is not a substantial drawback. The three quantities that are of interest for a comparison between atmosphere and water tank are CBL depth, CBL mean potential temperature or specific volume increment, and upslope flow velocity. One can test similarity for each of these three quantities individually.

Non-dimensional CBL depths (3.90) for AI and WTI become, using (3.51) and (3.91),

$$h_a^*(t_a) \equiv \frac{h_a}{H_a} = \frac{1}{H_a N_a}\left\{2g\beta_a Q_{\max,a}\, t_{d,a}\cdot\frac{2}{\pi}\left[1-\cos\left(\frac{\pi}{2}\frac{t_a}{t_{d,a}}\right)\right]\right\}^{1/2} \quad \text{and} \tag{3.99}$$

$$h_w^*(t_w) \equiv \frac{h_w}{H_w} = \frac{1}{H_w N_w}\left(2g\beta_w Q_{H,w} t_w\right)^{1/2}. \tag{3.100}$$

There is a one-to-one relationship between the two ND CBL depths so that $h_a^*(t_a)$ can be mapped onto $h_w^*(t_w)$ by expressing t_a in terms of t_w by requiring $h_a^*(t_a) = h_w^*(t_w)$,

$$t_a = t_{d,a}\frac{2}{\pi}\arccos\left[1-\left(\frac{H_aN_a}{H_wN_w}\right)^2\frac{\beta_wQ_{H,w}t_w}{\beta_aQ_{\max,a}\,t_{d,a}}\frac{\pi}{2}\right] \tag{3.101}$$

and vice versa,

$$t_w = t_{d,a}\cdot\frac{2}{\pi}\left(\frac{H_wN_w}{H_aN_a}\right)^2\frac{\beta_aQ_{\max,a}}{\beta_wQ_{H,w}}\left[1-\cos\left(\frac{\pi}{2}\frac{t_a}{t_{d,a}}\right)\right]. \tag{3.102}$$

This permits a similarity test of ND CBL depth between atmosphere and water-tank against a common reference time at any point in time. The same holds true for CBL mean potential temperature and specific volume increment as I will show next.

To directly compare the tethersonde observations of Figure 3.4 (page 56) with tank observations in the next chapter, I convert the former by substituting (3.50) and (3.92) into (3.20) and (3.21), which gives

$$h_a{}^* = \frac{h_a}{H_a} = g\beta_a\frac{\theta_{s,a}}{H_aN_a{}^2}, \tag{3.103}$$

$$h_w{}^* = \frac{h_w}{H_w} = \frac{g}{\alpha_{0,w}}\frac{\alpha_{s,w}}{H_wN_w{}^2}. \tag{3.104}$$

Requiring similarity, i.e. $h_a{}^* = h_w{}^*$, I get

$$\alpha_{s,w} = \alpha_{0,w}\beta_a\frac{H_wN_w{}^2}{H_aN_a{}^2}\theta_{s,a} \tag{3.105}$$

and for the uncertainties

$$\sigma_\alpha = \alpha_{0,w}\beta_a\frac{H_wN_w{}^2}{H_aN_a{}^2}\sigma_\theta. \tag{3.106}$$

For the conversion from atmospheric to tank reference time I use (3.102), and for the uncertainties $\sigma_{t_w} = \partial t_w/\partial t_a\big|_{t_a=\bar{t}_a}\cdot\sigma_{t_a}$, i.e.

$$\sigma_{t_w} = \left(\frac{H_wN_w}{H_aN_a}\right)^2\frac{\beta_aQ_{\max,a}}{\beta_wQ_{H,w}}\sin\left(\frac{\pi}{2}\frac{\bar{t}_a}{t_{d,a}}\right)\cdot\sigma_{t_a} \tag{3.107}$$

where the over bar denotes the mean value.

Both for CBL depth and CBL mean potential temperature/specific volume increment I only required similarity of the product $\Pi_2 \cdot \Pi_3$, (3.90), but not separately for Π_2 and Π_3, leaving me with one degree of freedom and the ability to compare for example atmospheric with water-tank observations against a common prediction $h_a^*(t_w) = h_w^*(t_w)$ for different values of t_w (section 4.3.2). This works in the same way for the Chen, friction, and gravity-current hypotheses for upslope flow velocity, because they contain only the product $\Pi_2 \cdot \Pi_3$. For the Hunt and Schumann hypotheses, the additional constraint (3.95) applies.

3.7 Summary and Conclusions

In this chapter I have demonstrated that comparing field observations with water-tank experiments requires establishing a scaling chain from field observations via an atmospheric idealisation and a water-tank idealisation to water-tank experiments (Figure 3.1, page 36). The three links between these four elements of the chain required three separate scaling steps. Previous scaling investigations have not made this distinction and focused on achieving an order-of-magnitude agreement between atmospheric observations and physical scale models or numerical models.

Using the scaling chain I derived hypotheses for atmospheric CBL depth and mean potential temperature increment and compared them with field observations. The hypotheses were based on an encroachment model of convection over a flat horizontal homogeneous plain. The hypotheses showed quantitative agreement with the field observations within about 20%. I qualitatively accounted for features of the real atmosphere that violated the assumptions. For upslope flow velocity I could not empirically derive an upslope flow velocity hypothesis from the field data because of a lack of range in the data and large uncertainties in the field measurements. A comparison of field observations with upslope flow velocity hypotheses derived from the literature remained inconclusive. These hypotheses require a fitting to observations, with the exception of the 'friction' hypothesis, which is not well-supported by the data.

I used scaling, the atmospheric hypotheses on CBL depth and temperature, and analyses of atmospheric upslope flow velocities, to formulate testable hypotheses for the water tank, which will be tested in the next chapter.

Unlike in previous upslope flow scalings, I accounted for time dependence by including both instantaneous and integrated heat flux in the scaling. This, for the first time, permits a direct comparison of field, numerical model, and water-tank observations for different time dependences of the heating and without the assumption of a steady state. I demonstrated that different development of atmospheric and water-tank surface heat flux restricts simultaneous similarity of *all* quantities to one designated point in time, but that *individual* quantities can be compared at all times using an appropriate mapping between atmospheric and water-tank reference time.

In Appendix B the reader can find more information on the scaling. Details on the upslope flow velocity hypotheses considered in this chapter are presented in Appendix B.1. In Appendix B.2 I provide more information on empirical analysis, and in Appendix B.3 I give an introduction to the use of probability theory as extended logic for hypothesis comparison and parameter estimation. The spreadsheet in Appendix B.4 proved invaluable during the development phase of the scaling presented in this chapter. In Appendix B.5 I share the strategy that I used in the 'art' of developing the scaling. There are a number of non-dimensional quantities that typically occur as critical parameters in scaling analyses, for example the Reynolds number. In Appendix B.6 I show how the most common ND quantities relate to the Pi groups that I identified in the scaling analysis.

4 Physical Scale Modeling

4.1 Introduction

In chapter 2, I presented the field observations, which formed the starting point of my thesis research. The scaling in chapter 3 plays a central role by investigating the possibility to reproduce atmospheric observations in a water tank and to draw conclusion for atmospheric behaviour by studying water-tank experiments. Much was promised in those two chapters to be investigated in this chapter on physical scale modeling, i.e. water-tank experiments. This chapter is organised as follows. Section 4.2 deals with the basic aspects of the experimental layout and methods. The interested reader can find technical details in Appendix C. The scaling hypotheses for the water tank are tested in section 4.3, followed by a discussion of flow characteristics and regimes in section 4.4. In section 4.5 I will discuss the results, in particular investigate the core questions posed at the beginning of this dissertation, and draw conclusions.

The experimental work presented in this chapter complements and extends beyond three previous physical scale modeling studies, which have been mentioned in previous chapters. Deardorff and Willis (1987) tilted a flat bottom tank to a 10° angle to study turbulence in a baroclinic mixed layer. They applied steady and spatially homogeneous heat flux through the tank bottom. Deardorff and Willis filled the bottom layer with water of constant temperature capped by a temperature-stratified layer and only studied short periods of almost steady state, i.e. only slow growth of the mixed layer into the stratified layer aloft. In this experimental design the authors observed a return flow almost entirely contained within the mixed layer. "To simulate more closely cases of atmospheric interest" Deardorff and Willis added extra heating coils at the upslope wall forcing strong venting at the upslope wall and return flow mostly above the mixed layer. Deardorff and Willis measured turbulent and mean 3-D velocities (but not the lowest 2 cm or 5% of the mixed layer depth) and density (via temperature).

Mitsumoto (1989) modelled a 30° slope with a wall at the ridge and a plain adjacent to the slope. He used linearly temperature-stratified freshwater and supplied spatially homogeneous heat flux from underneath, which he varied approximately sinusoidally to model diurnal cycles of heating and cooling in the atmosphere. Mitsumoto did not investigate inhomogeneous heating. He took measurements of 2-D mean velocities, apparently down to the tank bottom, and density (temperature).

Chen et al. (1996) modelled triangular ridges with 14° and 27° slope angles and long adjacent plains. The working fluid was linearly salt-stratified water. Chen et al. injected water of sinusoidally-varying temperature into the ridge region underneath the tank bottom and removed the water underneath the plains at the far end walls, which lead to inhomogeneous heat flux of an unknown gradient towards the ridge during the heating period. The authors measured 2-D mean velocities but did not provide accurate measurements of upslope velocities, because they could not measure close enough to the surface. Probably because of the difficulty of measuring the density of heated saltwater, the authors reported only surface temperatures.

The design of the water-tank experiments described in this thesis overcomes some of the limitations of the investigations discussed above. I can control the initial linear background stratification over a wide range ($\sim 0.1-1.5\,s^{-1}$) with good accuracy. Heat flux is well-known and controllable within $1.5-3.7\times10^{-3}\,K\,m\,s^{-1}$, but kept steady during each experiment, and can be homogeneous or inhomogeneous with reasonable flexibility. Length of plain and plateau next to the slope, which is fixed at 19°, can be varied by inserting removable end walls. Measurements of 2-D turbulent and mean velocities and up to three separate vertical profiles of density (via temperature and salt concentration) are possible with good spatial and temporal resolution, permitting detailed studies of the time development of the flow field and CBL depth and structure. The inability to measure velocities within 7 mm above the tank surface is not a major restriction because the vertical profiles captured the maximum velocity in most cases.

4.2 Experimental Layout and Methods

In this section I provide a summary of the experimental layout and methods of the water tank. Details are provided in Appendix C.

The water tank (Figure 4.1) was designed and built as a physical scale model of the idealised atmosphere shown in Figure 3.2 on page 38.

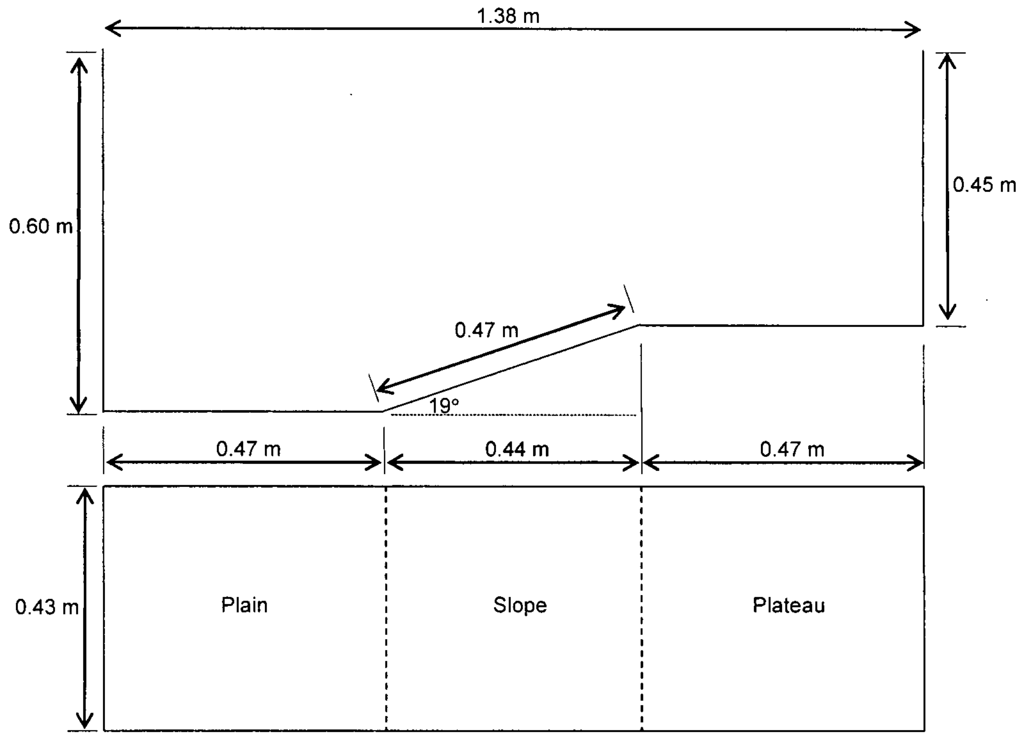

Figure 4.1: Schematic of the water tank.
Scale is approximately 1:10. Top: vertical cross-section. Bottom: plan view.

Side walls and end walls of the tank are glass and the tank bottom is a stainless steel sheet. Walls and bottom are encased in a stainless steel frame, which can be levelled with adjustable bolts. Convection is triggered in the tank by heating the bottom steel sheet from below with strip heaters.

The field observations show a fairly linear stratification through most of the bottom 1000 m of the atmosphere, except very near the surface. Linear stratification has the additional advantage of tractable calculations for growth of the convective boundary layer and other quantities. The goal was therefore to start water-tank experiments with linear density stratification. This was achieved by decreasing salt concentration with height using a two-bucket method (Fortuin, 1960), which I modified to account for the bottom topography.

When performing experiments in a water tank, the data to extract for comparison with field observations or numerical models are specific volume (which is the inverse of density and the quantity that compares directly with potential temperature in the atmosphere), tracer dispersion, and velocities.

The specific volume of the heated saltwater was determined by measuring salt concentration and temperature with Conductivity & Temperature (CT) sensors. Before or after each experiment the sensors had to be calibrated. I used three CT probes simultaneously, which were attached to the beam of a vertical profiler. Measurements were taken repeatedly in descents from above the CBL top to within a few millimetres above the tank bottom.

To gain qualitative and partially quantitative information on the layering and the dynamics of the flow in the tank I performed experiments with dyes injected just before the start of the experiment.

Velocities in the water tank were measured using particle image velocimetry (PIV). The water flow was visualised with submerged neutrally-buoyant particles illuminated by a bright light source. Particles were produced across a range of densities so that neutral-buoyancy heights were fairly homogeneously spread across the depth of the water tank (see Appendix C.9 for more information). The motion was video taped and the velocity of the flow determined from the change of location of individual particles and the elapsed time between different video frames.

4.3 Testing the Scaling Hypotheses

Before using the water tank to draw conclusions on trapping versus venting mechanisms in daytime upslope flow systems I need to test the scaling hypotheses for observable quantities in the water tank. As a test case I choose the water-tank settings to achieve similarity with the atmospheric test case at 1200 PDT on July 25, 2001, (B.1)-(B.6); from Table Appendix I on page 211,

$$t_w = 301\,s \text{ (water-tank reference time),} \quad (4.1)$$

$$N_w \approx 0.379\,s^{-1} \text{ (background buoyancy frequency), and} \quad (4.2)$$

$$Q_{H,w} = 1.85\times10^{-3}\,K\,m\,s^{-1} \text{ (surface heat flux).} \quad (4.3)$$

4.3.1 CBL Depth

I repeat here the hypothesis for the CBL depth in the water tank (page 72):

Hypothesis:

The expected value of the CBL depth in the water tank over the plain as a function of water-tank reference time t_w is given by

$$h_w(t_w) = \frac{\left(2g\beta_w Q_{H,w} t_w\right)^{1/2}}{N_w}.$$

This formula underestimates the observed values, but only slightly because background stratification is fairly strong and entrainment is weak. ■

The CBL development over the plain is more complicated than hypothesised (Figure 4.2). I only highlight the dominant mechanisms here and present a more detailed discussion in section 4.4.

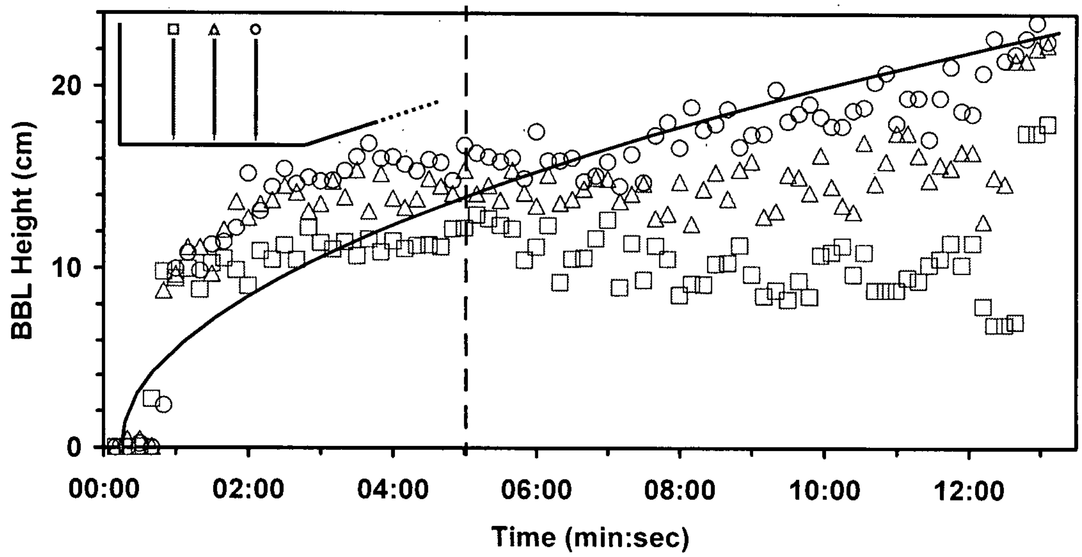

Figure 4.2: CBL growth over the plain.
Water-tank observations of the CBL depth over the plain from the left end wall (see inset): 14 cm (squares), 24 cm (triangles), and 34 cm (circles). CBL depth was determined every ten seconds from still images (until about 10:00) and video frames (after 10:00) as the depth of a layer of dispersed dye originally injected over the tank bottom. The solid curve shows the predictions for the CBL growth over flat terrain for a heat flux of $Q_{H,w} = 1.85\times10^{-3}\ K\,m\,s^{-1}$ *and a buoyancy frequency of* $N_w = 0.379\,s^{-1}$. *At* $t_w \approx 5\,\mathrm{min}$ *(dashed vertical line) similarity conditions are met with the field data at 1200 PDT on July 25, 2001 (*$N_a = 0.0149\,s^{-1}$, $Q_{\max,a} = 0.289\ K\,m\,s^{-1}$*).*

The upslope flow circulation has indirect impact on the flow over the entire plain. Flow characteristics change, affecting different locations over the plain differently. Eventually, after passing through two regime changes, approximately at 07:00 and 13:00, the CBL over the plain, with the exception of the region close to the left end wall, agrees well with predictions.

The field site does not have the horizontal limitation of the atmospheric idealisation (AI), (Figure 3.1, page 36). In AI and water tank idealisation (WTI), the ND length of the plain, (3.35),

$$\Pi_6 \equiv \frac{L_{b,a}}{H_a} = \frac{L_{b,w}}{H_w} \approx 3.15, \tag{4.4}$$

permits the development of two circulations over the plain (section 4.4). Therefore I do not expect the left end wall to have a substantial impact on the flow near the slope base in the water tank, and the finite value of Π_6 should not limit similarity between water tank and atmosphere. Next I will compare atmospheric CBL observations with water-tank observations and predictions.

As discussed in section 3.6, by mapping atmospheric reference time onto water-tank reference time (3.102), similarity between atmospheric and water-tank ND CBL depth $h^* = h/H$ can be tested at any instant in time. The location 13 cm from the slope (solid circles in Figure 4.2) is approximately comparable with the sodar location at Minnekhada Park (Figure 2.1, page 13). As a measure of CBL depth I use the BBL depth, determined in the atmosphere from lidar aerosol backscatter scans and in the water tank from images of dye concentrations. Between 00:45 and 04:00 water-tank reference time, atmospheric observations of BBL depth at the sodar site agreed very well with tank observations 13 cm from the slope (Figure 4.3). The last lidar observations after 04:00, corresponding to atmospheric reference times of 1136-1241 PDT, are roughly 20% higher than water-tank observations. In the water tank the BBL began growing faster again after a merging of the BBL with an elevated plain-plateau circulation with high dye concentrations at 07:00 (the first regime change, see section 4.4.2). In the atmosphere the merger possibly occurred earlier. Reasons for that could be faster velocities in the atmosphere (section 4.3.3) and a deeper BBL at the beginning of positive heat flux, which is obvious from early lidar observations in Figure 4.3. Unfortunately, atmospheric observations are not available to check the agreement with tank observations after the regime change in the tank.

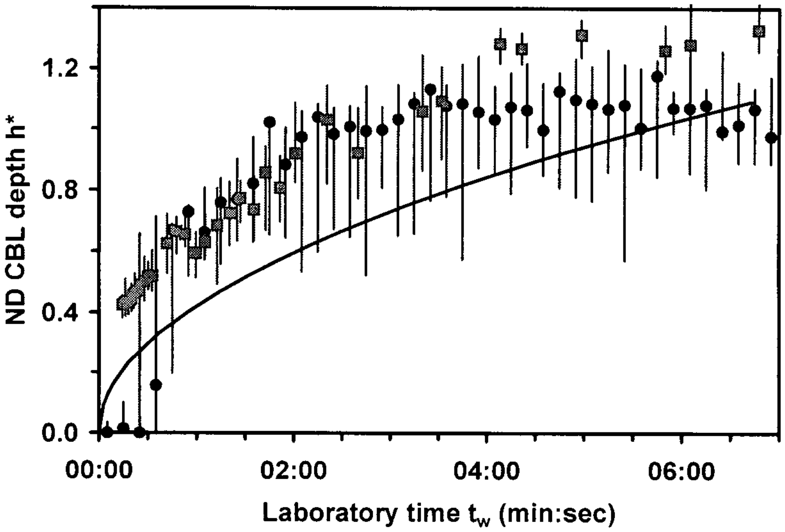

Figure 4.3: Non-dimensional CBL depth comparison of field and tank observations.

Non-dimensional BBL depth $h_a^* = h_a / H_a$ from lidar observations over the sodar site (red squares) and $h_w^* = h_w / H_w$ from dye experiment in the water tank 13 cm from the slope, corresponding approximately to the sodar location (blue circles). Atmospheric reference time t_a was converted into laboratory reference times t_w by using (3.102). Error bars indicate minimum and maximum BBL depths within the horizontal beam range of the sodar at the approximate BBL top for the lidar and the similar range for the water tank. Predictions for flat terrain without entrainment are shown as the black solid line.

Notice that the large lower error bars for tank observations is caused by a BBL depression within the horizontal range corresponding to the sodar's beam spread, which was not observed by the lidar.

In conclusion, observations in water tank and atmosphere showed similarity of ND CBL depth roughly within the goal of 20%, and for a long duration the agreement was much better. By contrast, atmospheric and tank observations of BBL depth over the plain near the slope agreed poorly with predictions of CBL depth far from the slope due to flow characteristics discussed in section 4.4.

4.3.2 CBL Specific Volume

The hypothesis on CBL mean specific volume increment in the water tank is (page 73):

Hypothesis:

The expected value of the CBL mean specific volume increment in the water tank at the foot of the slope as a function of water-tank reference time t_w is given by

$$\alpha_{s,w}(t_w) = \frac{\alpha_{0,w}}{g} N_w \left(2g\beta_w Q_{H,w} t_w\right)^{1/2}. \ \blacksquare$$

The specific volume increment is, under the assumption of a constant specific volume lapse rate γ_w and a simple encroachment model, directly related to the CBL depth via $\alpha_{s,w} = \gamma_w h_w$. As for the CBL depth this simple hypothesis predicts specific volume increments that show discrepancies with tank observations.

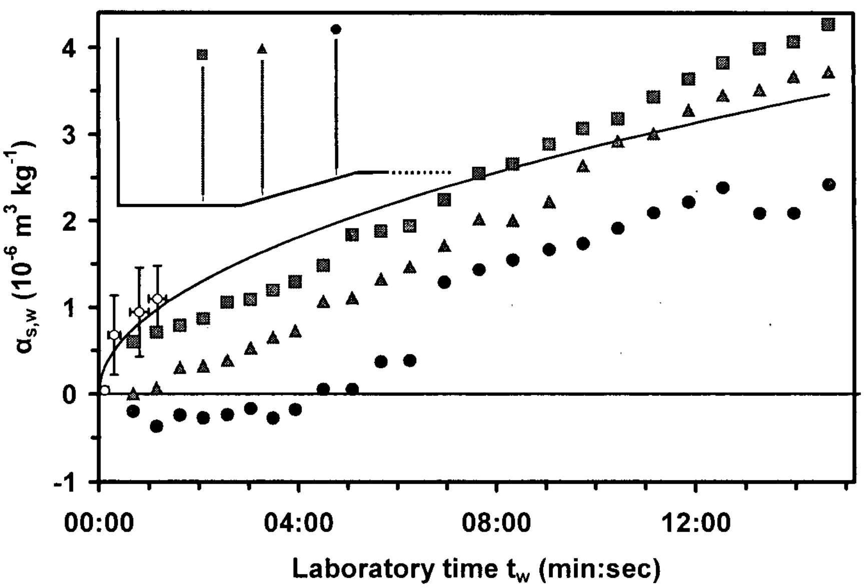

Figure 4.4: Comparison of field and tank observations of CBL mean specific volume increment $\alpha_{s,w}$. Water-tank settings as in Figure 4.2 ($Q_{H,w} = 1.85\times10^{-3}\ K\,m\,s^{-1}$, $N_w = 0.379\,s^{-1}$). Three vertical profiles were acquired synchronously at the locations indicated in the inset: over the plain 15 cm from the slope (red squares), over the slope 9 cm from the bottom (green triangles), and over the slope 9 cm from the top (blue circles). For each of the three locations, CBL mean specific volume increments were determined relative to the initial values right at the surface of each location. Black open circles with error bars are the tethersonde observations of Figure 3.4 (page 56) converted into specific volume and laboratory time. The black solid curve shows the time series expected from the formula in the hypothesis.

I ran a water-tank experiment for settings (4.2)-(4.3) and measured vertical profiles of specific volume at three different locations (Figure 4.4, inset). Initially, the observed CBL mean specific volume increments were lower than predicted. After seven minutes the observed values over the *plain* (Figure 4.4, red squares) began to exceed the predicted values, a consequence of a regime change at 07:00. Included in the graph are the tethersonde observations of Figure 3.4 (page 56), converted to specific volume and water-tank reference time using (3.102) and (3.105)-(3.107) (open black circles in Figure 4.4). The atmospheric time series is so short and the error bars are so large that the comparison with predictions and water-tank observations remains inconclusive.

The predicted CBL mean specific volume increment far from the slope is proportional to the square root of laboratory reference time, $\sqrt{t_w}$, but increments observed in the tank are proportional to t_w, for example

$$\alpha_{s,w} = 4.57\times10^{-9}\frac{m^3}{s\cdot kg}\times t_w + 0.3325\times10^{-6}\frac{m^3}{kg}, \tag{4.5}$$

with an r-squared value of 0.996 over the plain near the slope (Figure 4.4, red squares). Over the lower part of the slope (green triangles) the r-squared value is 0.993, and over the upper part of the slope (blue circles) it is 0.928. This provides evidence that different processes determine the time development of the CBL mean specific volume increment over flat terrain and near a heated slope. I will show now that the proportionality to t_w agrees with the observation that the CBL depth remains constant at $h_w \approx H_w$ from 02:00 until 07:00 (Figure 4.3, page 88).

From (3.27),

$$dE_w = Q_{H,w}dt_w, \tag{4.6}$$

from (3.16) and (3.12),

$$dT_w = \frac{1}{\alpha_{0,w}\beta_w}d\alpha_{s,w}, \tag{4.7}$$

and from the First Law of Thermodynamics the energy density in kinematic units is

$$dE_w = \frac{1}{A_w}\frac{m_w C_w}{\rho_w C_w} dT_w = \frac{V_w}{A_w} dT_w, \qquad (4.8)$$

where A_w is the bottom surface area through which heat flux is supplied, m_w and V_w are mass and volume of the heated water, ρ_w and C_w are density and specific heat of water, and dT_w is the infinitesimal temperature increase. Substituting (4.7) into (4.8) gives

$$dE_w = \frac{V_w}{A_w}\frac{1}{\alpha_{0,w}\beta_w} d\alpha_{s,w}. \qquad (4.9)$$

Finally, a comparison with (4.6) yields

$$\frac{d\alpha_{s,w}}{dt_w} = \alpha_{0,w}\beta_w \frac{A_w}{V_w} Q_{H,w}. \qquad (4.10)$$

Taking the time derivative of (4.5) and comparing with the last equation gives

$$h_{eff,w} = \frac{\alpha_{0,w}\beta_w Q_{H,w}}{4.57\times 10^{-9} m^3 s^{-1} kg^{-1}} = 0.105\, m \qquad (4.11)$$

where $h_{eff,w}$ is the effective mean depth of the heated volume $V_w = h_{eff,w} A_w$. The total volume between tank bottom and ridge height over plain and slope is

$$V_w = \frac{3}{4} H_w A_w = 0.112\, m \times A_w, \qquad (4.12)$$

where A_w is the total bottom area of plain and slope, and the effective mean depth $h_{eff,w} = 0.112\, m$ is in good agreement with (4.11).

I will show in section 4.4.2 that a regime change occurs at about 07:00, but Figure 4.4 (page 89) demonstrates that the linear relationship between $\alpha_{s,w}$ and t_w persists after the regime change. More measurements and a closer look at the detailed structure of the CBL, in particular after 07:00, will be required in future research to explain the surprisingly accurate linear relationship between $\alpha_{s,w}$ and t_w.

4.3.3 Upslope Flow Velocity

In section 3.5.3 the hypothesis for the maximum upslope flow velocity in water-tank experiments was derived from the field observations:

Hypothesis:

The maximum value in the vertical profile of ND upslope flow velocity in the water tank over the plain near the foot of the slope as a function of laboratory time t_w is

$$U_{\max,w}^* \equiv \frac{U_{\max,w}}{H_w N_w} = (5 \pm 17) \cdot \Pi_{2,w}^{\pm 0.3} \Pi_{3,w}^{(0.6 \pm 0.3)}.$$

The vertical profiles of along-slope velocities are expected to show return flows like the field observations at Minnekhada Park. ■

Even before a detailed analysis of water-tank experiments it is obvious that similarity with field observations cannot be reached: From field observations of maximum upslope flow velocity $U_{obs,a} \approx (3.8 \pm 0.3)\, m\, s^{-1}$, (B.7), at 1200 PDT on July 25, 2001, and the required similarity between AI and WTI, (B.58), follows an expected maximum upslope flow velocity in the water tank of

$$U_{exp,w} = \frac{H_w N_w}{H_a N_a} U_{obs,a} = (1.9 \pm 0.2)\, cm\, s^{-1}, \tag{4.13}$$

where I used the values from Table Appendix I on page 211.[3]

In the same water-tank experiment as in Figure 4.4, at the expected time of similarity, $t_w = 301\, s$ from (4.1), I observed maximum horizontal velocities of $(0.6 \pm 0.1)\, cm\, s^{-1}$ (averaged over 20 s and the bottom 20 cm of the slope), clearly much lower than the expected value (Figure 4.5). Even more unexpectedly, at locations that approximately correspond to the sodar site at Minnekhada Park ($x = -15$ to $-5\, cm$), horizontal velocities near the tank bottom were negative, in full agreement with Mitsumoto's (1989) experimental results. Furthermore,

[3] I will express water-tank velocities in units of $cm\, s^{-1}$, which are more convenient and intuitive than $m\, s^{-1}$.

none of the profiles shows a strong return flow. A more detailed discussion will follow in section 4.4.

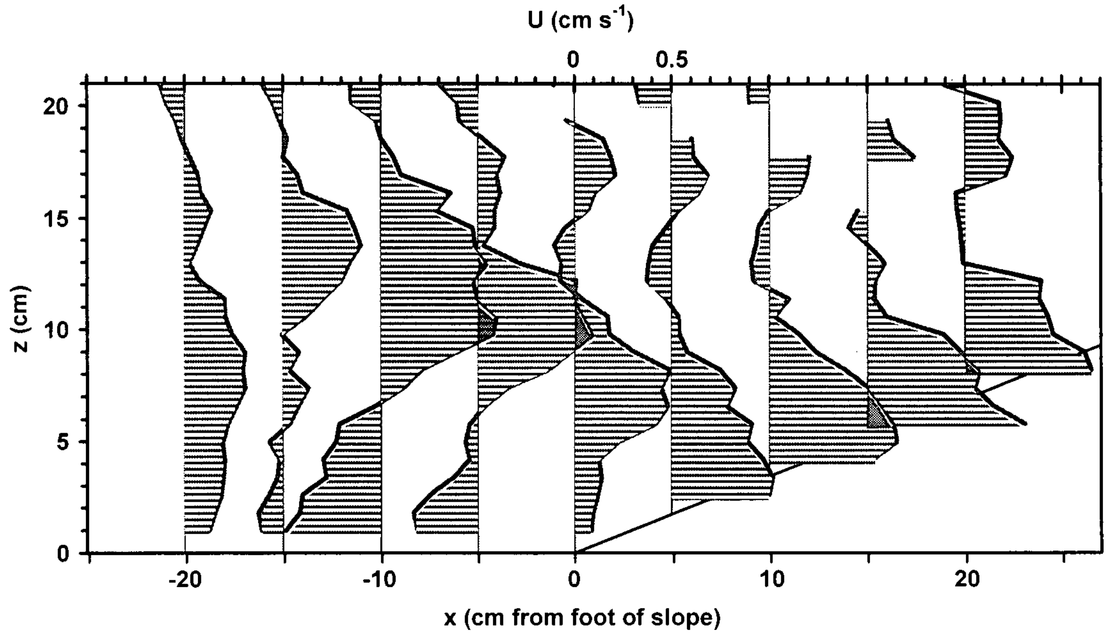

Figure 4.5: Vertical profiles of the (plain-parallel) x-component of velocities in the water tank. The graph shows a domain of the water tank about 50 cm wide (lower x-axis) and 20 cm high. The tilted black line is the surface of the slope. Vertical profiles of horizontal velocities are shown every 5 cm at the locations indicated by the corresponding thin vertical straight lines. The difference between profiles and vertical lines is a measure for the velocity. Its scale is shown on the upper x-axis (with exemplary values for the profile over the foot of the slope), the distance between minor tick marks corresponding to 0.1 cm s^{-1}. Flows to the right have a positive difference. The experiment was the same as in Figure 4.4. Velocities are time-averaged over 100 individual profiles between 300 and 320 s after the beginning of positive heat flux. Each profile is spatially averaged over three adjacent vertical profiles spanning a horizontal range of approximately 1.5 cm. Interruptions in the profiles are caused by a lack of data.

Empirical Analysis Using Probability Theory

In the same way as for the atmosphere in section 3.4.2, I will now use probability theory to carry out a hypothesis comparison and to determine an empirical relationship between $U_{\max,w}$ and $\Pi_{2,w}$, $\Pi_{3,w}$. The reader can find a conventional statistical analysis in Appendix C.11. I will focus on the mid-point of the slope, where typically the largest values of maximum upslope flow velocity occur and the vertical profiles of upslope flow velocity agree qualitatively with those observed in the field (Figure Appendix III, page 182).

Of the 16 particle experiments, which Ian Chan and I ran, six were suitable for analysing vertical profiles of horizontal velocities over the midpoint of the slope (Table 4.1). These experiments cover a wide range of $\Pi_{3,w}$ and differ substantially in geometry and the spatial distribution of heat flux at the slope surface. It is not *a priori* obvious that these differences permit an empirical analysis with small uncertainties.

Name	$N_w\left(s^{-1}\right)$	$\overline{Q}_{H,w}$ $\left(10^{-3} Kms^{-1}\right)$	$\Pi_{3,w}$	$L_{b,w}(m)$	$L_{t,w}(m)$	$Q_{H,w}$ details $\left(10^{-3} K\, m\, s^{-1}\right)$ Plain	Slope	Plateau
WT1	0.567	1.85	0.00117	0.470	0.470	1.85	1.85	1.85
WT2	0.379	1.85	0.00406	0.470	0.470	1.85	1.85	1.85
SP	0.379	1.85	0.00406	0.225	0.470	1.85	1.85	1.85
TR1	0.379	2.68	0.00588	0.470	0	1.48	1.67-3.70	-
TR2	0.342	3.15	0.00903	0.470	0	1.48/ 2.04	2.59-3.70	-
WT3	0.374	2.96	0.00649	0.470	0.470	1.85	2.96	1.85

Table 4.1: Overview of water-tank experiments used for upslope flow velocities analyses. Experiments are named according to their geometry as WT ('Whole Tank'), SP ('Short Plain'), and TR ('Triangular Ridge'), followed by a number to distinguish those with equal geometry. The next three columns show background buoyancy N_w, average surface heat flux over the slope only, $\overline{Q}_{H,w}$, and the resultant $\Pi_{3,w}$. The columns $L_{b,w}$ and $L_{t,w}$ show the length of plain and plateau, respectively. I inserted a removable end wall over the plain in SP and at the ridge top in TR1 and TR2. The last three columns show details of the heat flux supplied to the tank. In TR1 the heat flux at the slope surface increased with height in twelve increments from 1.67 *to* $3.70\times10^{-3}\, K\, m\, s^{-1}$. *In TR2, the slope surface heat flux increased from* 2.59 *to* $3.70\times10^{-3}\, K\, m\, s^{-1}$, *and the surface heat flux in left and right half of the plain was* 1.48 *and* $2.04\times10^{-3}\, K\, m\, s^{-1}$, *respectively.*

In analogy to (3.69)-(3.73), the hypotheses for ND maximum upslope flow velocity are

$$U_{Hunt,w}* = c_{Hunt,w}\cdot\Pi_{2,w}^{1/6}\cdot\Pi_{3,w}^{1/2} \text{ (Hunt),} \tag{4.14}$$

$$U_{Chen,w}* = c_{Chen,w}\cdot 2^{1/2}\cdot\Pi_{2,w}^{1/2}\cdot\Pi_{3,w}^{1/2} \text{ (Chen),} \tag{4.15}$$

$$U_{fric,w}* = 0.322\cdot 2^{1/2}\cdot\Pi_{2,w}^{1/2}\cdot\Pi_{3,w}^{1/2} \text{ (friction),} \tag{4.16}$$

$$U_{Grav,w}* = c_{Grav,w} \cdot \Pi_{2,w}^{1/4} \cdot \Pi_{3,w}^{1/4} \text{ (gravity current)}, \tag{4.17}$$

$$U_{Schu,w}* = c_{Schu,w} \cdot \Pi_{3,w}^{1/2} \text{ (Schumann)}, \tag{4.18}$$

where the constant factors $c_{Hunt,w}$, $c_{Chen,w}$, $c_{Grav,w}$, and $c_{Schu,w}$ contain the dependence on Π_1.

Estimation of the Hypotheses Coefficients Using Probability Theory

As for the atmosphere, I will change the notation in (4.14)-(4.18) to use indices and drop the subscript 'w' for the remainder of this section when the context is clear. I define the following propositions.

- I = "The maximum value in the vertical profile of horizontal velocities over the midpoint of the slope in the water tank was determined from the median of 100 individual profiles over 20-second intervals for a total duration of 12 to 17 minutes for the six experiments shown in Table 4.1. Maximum upslope flow velocity was non-dimensionalised by dividing by ridge height $H_w = 0.149\,m$ and the buoyancy frequencies N_w shown in Table 4.1. It is assumed that the ND maximum upslope flow velocity can be expressed as a monomial plus independent, identically distributed Gaussian background noise of unknown but equal standard deviation." (Background information)

- D = "The observed $n = 253$ data were $d_i = \ldots$, where $i = 1,\ldots,n$" (Statement on the data)

- $H^{(1)}$ = "The ideal data are described by $f^{(1)}{}_i = U_{Hunt,w}* = c^{(1)} \cdot \Pi_{2,i}^{1/6} \cdot \Pi_{3,i}^{1/2}$, $i = 1,\ldots,n$" (Hunt hypothesis)

- $H^{(2)}$ = "The ideal data are described by $f^{(2)}{}_i = U_{Chen,w}* = c^{(2)} \cdot 2^{1/2} \cdot \Pi_{2,i}^{1/2} \cdot \Pi_{3,i}^{1/2}$, $i = 1,\ldots,n$" (Chen hypothesis)

- $H^{(3)}$ = "The ideal data are described by $f^{(3)}{}_i = U_{Grav,w}* = c^{(3)} \cdot \Pi_{2,i}^{1/4} \cdot \Pi_{3,i}^{1/4}$, $i = 1,\ldots,n$" (gravity-current hypothesis)

- $H^{(4)}$ = "The ideal data are described by $f^{(4)}{}_i = U_{Schu,w}{}^* = c^{(4)} \cdot \Pi_{3,i}{}^{1/2}$, $i = 1,\ldots,n$." (Schumann hypothesis)

- $H^{(5)}$ = "The ideal data are described by $f^{(5)}{}_i = U_{fric,w}{}^* = 0.322 \cdot 2^{1/2} \cdot \Pi_{2,i}{}^{1/2} \cdot \Pi_{3,i}{}^{1/2}$, $i = 1,\ldots,n$" (friction hypothesis)

In all hypotheses the ideal data are of the form $f^{(j)}{}_i = c^{(j)} \cdot \left(2^{1/2}\right) \cdot \Pi_{2,i}{}^{m_1^{(j)}} \cdot \Pi_{3,i}{}^{m_2^{(j)}}$, where $m_1{}^{(j)}$, $m_2{}^{(j)}$, and $c^{(5)} = 0.322$ is given. The coefficients $c^{(1)}$ to $c^{(4)}$ for the water tank (Figure 4.6) are significantly lower than those for the atmosphere (Figure 3.6, page 65). This result suggests that the molecular Pi groups Π_4 and Π_5 have to be included in the upslope flow velocity hypotheses to achieve similarity. Since Π_4 and Π_5 are fixed, similarity cannot be achieved practically, but even theoretically their inclusion alone cannot achieve similarity as I will show next.

The Joint Probability Distribution of m_1 and m_2

The joint probability distribution of m_1 and m_2 is in excellent agreement with the conventional statistical analysis, (C.13), including the tilt for positive correlation (Figure 4.7, A). The uncertainty for the water-tank data is much smaller than for the atmospheric data (Figure 4.7, B); the two joint probability distributions are different with a probability greater than 0.99.

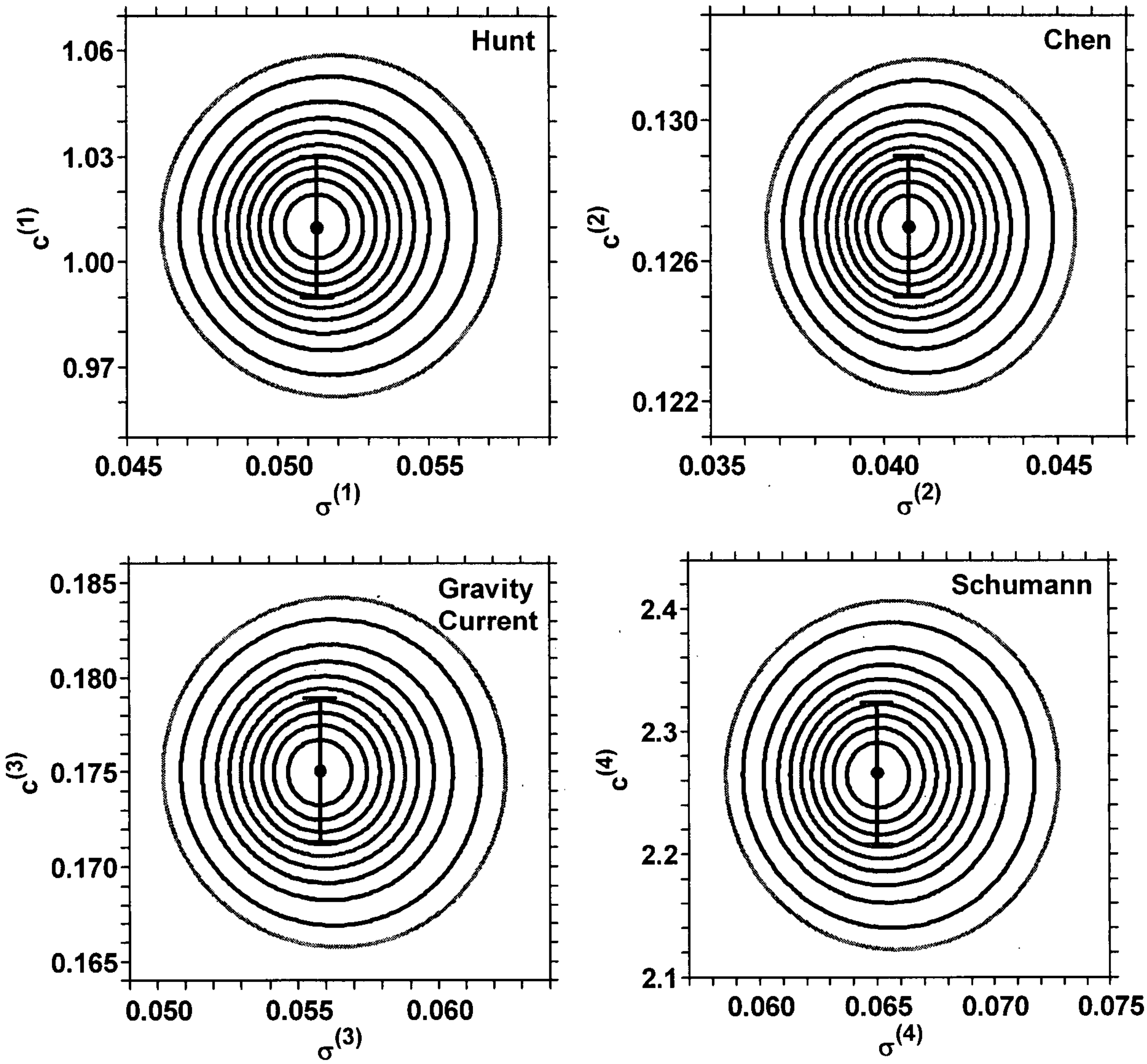

Figure 4.6: Joint probability distribution of unknown constant factor and standard deviation of background noise for different upslope flow velocity hypotheses in the water tank.

Same as Figure 3.6 (page 65) but for the water-tank experiments listed in Table 4.1 (page 94). All probability distributions are normalised to a maximum value of 1. Contour lines are shown for 0.05 (outer line) and from 0.1 to 0.9 in steps of 0.1. Notice that the scale for the standard deviations and the constant factors is different. The linear least-square best fit values of the constant factors $c^{(1)}$ to $c^{(4)}$ and their standard deviations are shown as data points with error bars.

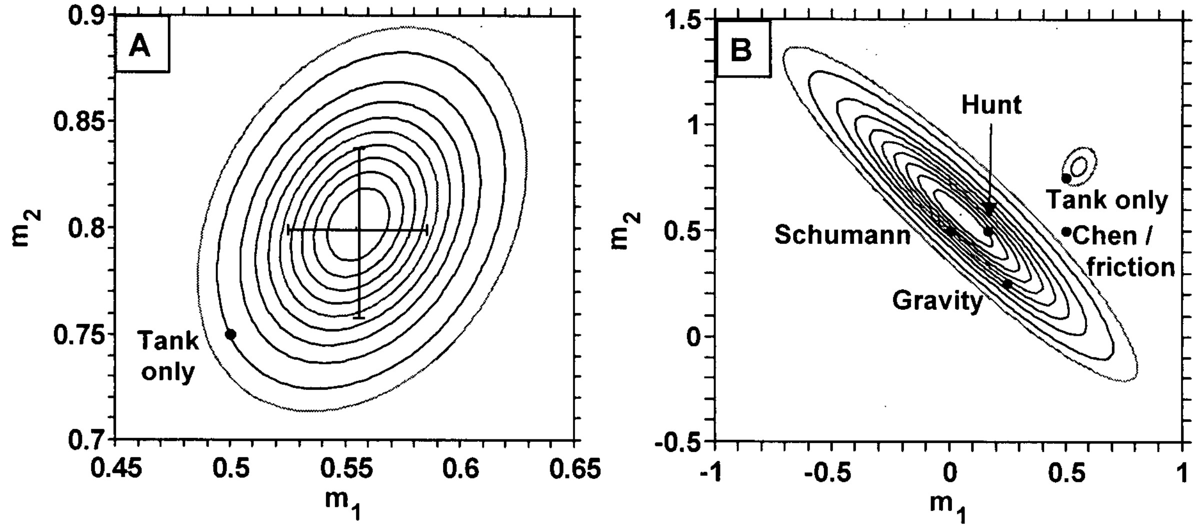

Figure 4.7: Joint probability distribution $p(m_1, m_2 | D, I)$ of the exponents in upslope flow velocity hypothesis for the water tank and comparison with atmosphere, plotted using two different scales.
A: I determined the joint probability distribution $p(m_1, m_2 | D, I)$ of the exponents m_1 and m_2 in an upslope flow hypothesis of form $U_{\max,w}{*} = c \cdot \Pi_{2,w}^{m_1} \cdot \Pi_{3,w}^{m_2}$ for the water-tank data in Table 4.1 (page 94) by marginalising over the unknown factor c and assuming normally-distributed background noise. The joint probability distribution is normalised such that the maximum value is 1. Contour lines are shown for 0.05 (outer line) and from 0.1 to 0.9 in steps of 0.1. The error bars cross at the mean values of m_1 and m_2, determined from nonlinear regression, and show the standard errors of estimate. 'Tank only' data point denotes $(m_1, m_2) = (1/2, 3/4)$, which is the pair of simple rational numbers that is closest to the mode. B: Synthesis of Figure 3.7 (page 70) for the atmosphere and left graph (A) for the water tank. Contours for the atmosphere are the same as in A, but for the water tank only the 0.05 (outer line) and 0.5 (inner) contour lines are shown. The labelled data points represent upslope flow velocity hypotheses discussed in the text.

The hypotheses $H^{(1)}$ - $H^{(5)}$ lie far outside the 0.05-probability contour line and their predictions cannot agree with tank observations even if the coefficients $c^{(j)}$ are adjusted. Of all the pairs (m_1, m_2) with simple rational entries (i.e. numerators and denominators 2, 3, or 4), the pair $(1/2, 3/4)$ is closest to the mode $(0.55, 0.80)$ lying on the 0.1-probability contour line. Although this is still a fairly low probability, a 'tank-only hypothesis' of form $U_{Tank,w}{*} = c_{Tank,w} \cdot 2^{1/2} \Pi_{2,w}^{1/2} \cdot \Pi_{3,w}^{3/4}$ is far superior to the Hunt hypothesis

$U_{Hunt,w}* = c_{Hunt,w} \cdot \Pi_{2,w}^{\frac{1}{6}} \cdot \Pi_{3,w}^{\frac{1}{2}}$, which is the most probable hypothesis for the atmosphere (Figure 4.8).

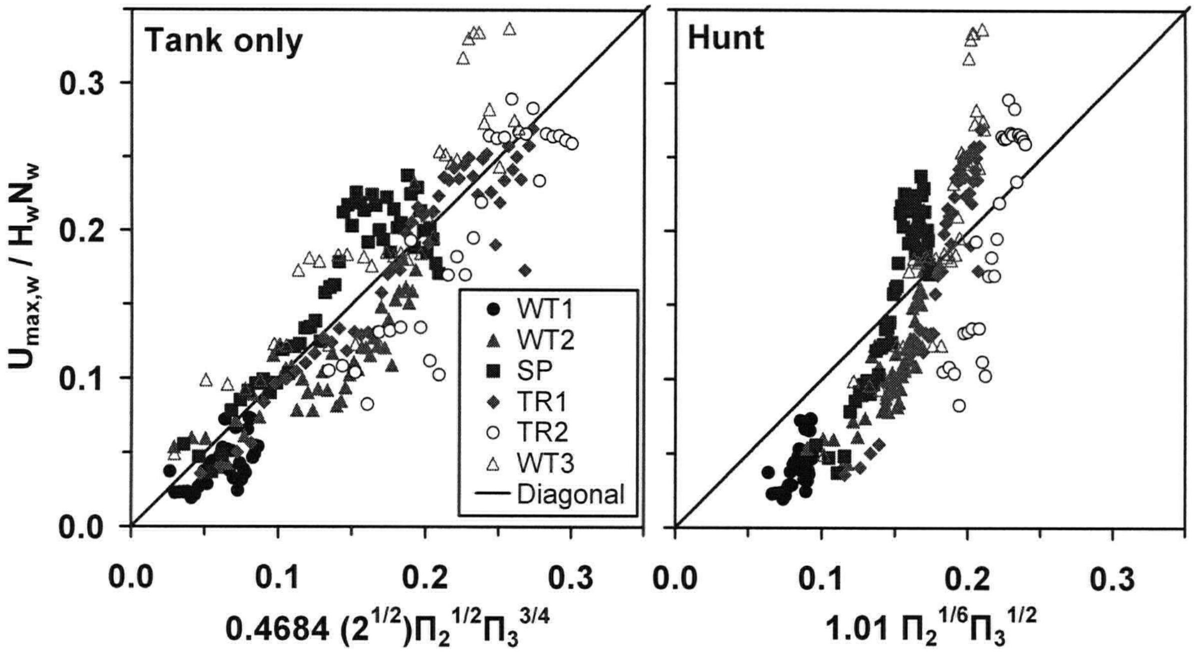

Figure 4.8: Comparison of fitted upslope flow velocity hypotheses with tank observations in ND form. ND maximum upslope flow velocities (ordinates) are shown for observations in water-tank experiments. The acronyms in the legend refer to Table 4.1 (page 94). Left graph shows the tank-only hypothesis and right graph the Hunt hypothesis, which was the best hypothesis for atmospheric observations. The constant factors were fitted. Ordinates and abscissae are of equal scale. Compare with Figure Appendix VI (page 198).

Inclusion of other Pi groups in coefficients $c^{(j)}$ in an equation of form $U* = c^{(j)}\,\Pi_2^{m_1}\,\Pi_3^{m_2}$ does not change the exponents m_1 and m_2 and therefore is insufficient to resolve the similarity violation. The only possibility to achieve similarity, at least theoretically, is the inclusion of an additional dependence of $c^{(j)}$ on Π_2 and Π_3. I will now discuss this further and gather evidence and ideas for future research to develop an upslope flow velocity hypothesis, which resolves the similarity violation.

4.3.4 Discussion of the Similarity Violation of Upslope Flow Velocity

Introduction

For maximum upslope flow velocity, similarity between atmosphere and water tank is violated under the assumption that Π_1, Π_2, and Π_3 are the only governing parameters. There are two aspects or problems to the similarity violation. Firstly, all hypotheses investigated in this dissertation require fitting of constant coefficients to the data, because the coefficients were either undetermined or badly determined from theory, but the values for atmospheric and tank observations differed significantly. For the test case maximum upslope flow velocities in the tank were only roughly 40 % of those in the atmosphere. Secondly, the functional dependence of ND upslope flow velocity on Π_2 and Π_3 is significantly different for atmosphere and water tank.

Explanations ruled out by Evidence

I used data from six water-tank experiments, which included substantial variations of plain and plateau length (Table 4.1, page 94). Nevertheless, the probability distribution of the exponents m_1 and m_2 in $U^* = c^{(j)}\,\Pi_2^{m_1}\,\Pi_3^{m_2}$ was very narrow for the tank observations and far from the probability distribution for the field observations (Figure 4.7, page 98). Therefore the ND lengths of plain and plateau, Π_6 and Π_7, are not significant within the accuracy of the data.

I did not test the dependence of ND upslope flow velocities on ND tank width, $\Pi_{8,w}$. Friction at the lateral side walls is certainly a negligible factor for upslope flow velocities near the slope centre, because early in the experiments the upslope flow of dye was as fast near the side walls as in the centre.

Another possible impact of lateral side walls is the suppression of horizontally mass-compensating flows; instead, return flows have to be established vertically up against gravity above the upslope flow. The unheated surface areas near the side walls may be too narrow to allow the mass balance. Although a comparable lateral confinement does not exist in the atmosphere, I observed flows in downslope direction above the upslope flow. If upslope flows were compensated horizontally the flow in downslope direction would be unexplained as would be all previous field observations of overshooting and venting of upslope flows over mountain ridges. If the slope at Minnekhada Park could not be considered approximately two-dimensional the alternative idealisation would be a slope of finite width in an otherwise flat landscape. In this geometry, however, lateral inflow of unheated air from the plain would impair upslope flows.

I did not consider ND water depth over the plain, $\Pi_{9,w}$, an important factor, because in all experiments the water surface was far above the top of the CBL. Like Mitsumoto (1989), I observed elevated layers of alternating flows above the plain-plateau flow. These were shallow, their velocities decreased substantially with height, and they never seemed to affect water near the top surface.

Another question related to the finite depth of the water tank is the role of energy dissipation by waves. I have no atmospheric or tank observations on waves, but I would expect more energy to be removed from the upslope flow system and dissipated in the atmosphere than in the confined water tank.

Three more quantities could possibly explain the similarity violation: the two molecular Pi groups, ND viscosity Π_4 and ND thermal diffusivity Π_5, and a ND surface roughness length, which I define as

$$\Pi_{10} \equiv z_0/H \qquad (4.19)$$

for both atmosphere and water tank, in line with the Buckingham Pi analysis in chapter 3. I first consider ND surface roughness length.

In his large-eddy simulations (LES), Schumann (1990) found

$$U_a{}^* \propto \Pi_{3,a}{}^{1/2} \cdot \Pi_{10,a}{}^{-0.033} \qquad (4.20)$$

for a slope angle of 10°. To cut the ND upslope flow velocity by half the ND roughness length has to increase by nine orders of magnitude! Because of the heterogeneous land-use near Minnekhada Park (Figure 4.9) it is difficult to estimate the momentum roughness length. It is more intuitive to compare heights of individual roughness elements, which at the field site ranged from metres for bushes, hedges, and buildings to tens of metres for tall trees. These roughness elements occurred individually, in rows, or as areas and heterogeneously distributed in an otherwise flat terrain within several square kilometres upwind of Minnekhada Park. The well-sanded and painted tank bottom lacks any roughness elements of more than a tenth of a millimetre, which is similar to half a metre in the atmosphere. Clearly, the tank bottom surface is comparatively smoother than the atmospheric counterpart.

Figure 4.9: Satellite view of Minnekhada Park field site.

The circles mark the locations of sodar (S), lidar (L), and tethersonde (T); compare with Figure 2.1, page 13. Satellite image retrieved from Google Maps at maps.google.ca on 2005-08-06.

Although roughness length cannot explain the similarity violation it may point to a potential resolution. In the following subsections I will consider the roles of ND viscosity and diffusivity of heat and the different functional dependence of ND maximum upslope flow velocity on Π_2 and Π_3.

Similarity Violation as a Result of Fluid-Dynamic Feedback

A closer look at viscosity tells us that upslope flows in the water tank are fluid-dynamically smooth, i.e. roughness elements are much smaller than the viscous sublayer. This turns out to be the likely cause for differences between upslope flow velocity in tank and atmosphere - not only in strength but also in the dependence on Π_2 and Π_3.

First, one needs to determine friction velocity, which will be one of the challenges for future development of an upslope flow velocity hypothesis that can reconcile tank and atmospheric observations. It is questionable if flat-terrain similarity theories, which were developed for externally imposed horizontal velocities, are applicable to sloping terrain with internally triggered upslope flow velocities. Here, for the purpose of gaining a *rough* estimate of friction velocity, I use convective transport theory (Santoso and Stull, 2001),

$$u_{*,a} = \left(C_{*D,a} w_{*,a} \Delta U_a\right)^{1/2} = \left(C_{*D,a} w_{*,a} U_{obs,a}\right)^{1/2} \approx 0.37 \frac{m}{s}, \tag{4.21}$$

where the momentum transport coefficient $C_{*D,a}$ is a function of surface roughness. I assumed a value of $C_{*D,a} = 0.02$, corresponding to surface properties at Lamont (Oklahoma) of BLX96 (see Santoso and Stull, 2001, for a description of the field site). Furthermore I used field data from Minnekhada Park at 1200 PDT on July 25, 2001: the estimated convective velocity scale was $w_{*,a} = 1.76\,m\,s^{-1}$ (Table Appendix I, page 211) and the observed maximum upslope flow velocity $\Delta U_a = U_{obs,a} = 3.8\,m\,s^{-1}$, (B.7). Santoso and Stull (2001) developed a similarity theory, in which the CBL is comprised of a radix layer, a uniform layer, and an entrainment layer. The radix layer contains the surface layer and is smoothly matched at the boundary with the uniform layer. Radix-layer theory was demonstrated to apply to hilly terrain. With $w_{*,a} = 1.76\,m\,s^{-1}$, (4.21), and the observed BBL depth $h_a \approx 1000\,m$, the radix-layer depth for momentum becomes

$$z_{RM,a} \approx \frac{1}{2}\left(\frac{u_{*,a}}{w_{*,a}}\right)^{3/4} h_a \approx 155\,m\,. \tag{4.22}$$

This value compares well with the height of observed maximum upslope flow velocity, roughly 125 m.

From similarity, (B.58), the friction velocity in the tank for the test case should be

$$u_{*,w} = u_{*,a}\frac{H_w N_w}{H_a N_a} \approx 0.18\frac{cm}{s}\,. \tag{4.23}$$

This value is conservatively high, because observed velocities in the tank are smaller than expected by similarity. The viscous sublayer is therefore likely thicker than (see equation 3.3 in Garratt, 1994)

$$\delta_w \approx \frac{5\nu_w}{u_{*,w}} \approx 2.5\,mm\,. \tag{4.24}$$

This is much greater than the height of roughness elements in the tank, and hence the flow in the water tank is fluid-dynamically smooth.

Because of fluid-dynamical smoothness, the roughness length in the water tank is not a function of distribution and size of roughness elements but of viscosity and friction velocity (equation 4.3 in Garratt, 1994), namely

$$z_{0,w} \approx \frac{0.11\nu_w}{u_{*,w}} \approx 0.054\,mm\,. \tag{4.25}$$

This value is approximately similar to a roughness length at Minnekhada Park of

$$z_{0,a} = \frac{H_a}{H_w} z_{0,w} = 0.28\,m\,, \tag{4.26}$$

roughly the value expected from local land-use.

Equation (4.25) implies a feedback mechanism, which can explain why ND maximum upslope flow velocity depends more strongly on Π_2 and Π_3 in the tank than in the atmosphere. As instantaneous sensible surface heat flux or integrated heat flux increase in the tank, upslope flow velocity and thus, (4.21), friction velocity increases. Therefore, (4.25), roughness length decreases permitting a further increase of upslope flow velocity. For the surface characteristics at Minnekhada Park, on the other hand, one would initially assume that roughness length is independent of friction velocity. I will next discuss how to quantify the fluid-dynamic feedback.

A Tentative Explanation of the Similarity Violation Using the Gravity-Current Hypothesis

Similarly to (4.21),

$$\frac{u_{*,w}}{H_w N_w} = \frac{1}{H_w N_w}\left(C_{*D,w} w_{*,w} U_w\right)^{1/2} = \left(C_{*D,w}\frac{w_{*,w}}{H_w N_w} U_w{}^*\right)^{1/2}. \tag{4.27}$$

With the definition of the convective velocity scale (B.9) for the water tank and (3.90) this gives

$$\frac{u_{*,w}}{H_w N_w} = \left(U_w{}^*\right)^{1/2} \cdot C_{*D,w}{}^{1/2} \cdot 2^{1/2} \cdot \Pi_{2,w}{}^{1/12} \cdot \Pi_{3,w}{}^{1/4}. \tag{4.28}$$

Next I substitute this result into (4.25) and (4.19) to get

$$\Pi_{10,w} = \frac{z_{0,w}}{H_w} \approx \frac{0.11 \nu_w}{H_w u_{*,w}} = 0.11 \Pi_{4,w}\left(U_w{}^*\right)^{-1/2} \cdot C_{*D,w}{}^{-1/2} \cdot 2^{-1/2} \cdot \Pi_{2,w}{}^{-1/12} \cdot \Pi_{3,w}{}^{-1/4}, \tag{4.29}$$

where I used the definition of $\Pi_{4,w}$ in (3.39).

The key step is now to include in each of the four upslope flow hypotheses discussed in section 4.3.3 a dependence on the ND roughness length $\Pi_{10,w}$. I first demonstrate this here for the gravity-current hypothesis, i.e.

$$U_w{}^* = \frac{c_1}{\Pi_{10,w}{}^A}\Pi_{2,w}{}^{1/4} \cdot \Pi_{3,w}{}^{1/4} \tag{4.30}$$

where $A > 0$ is in unknown exponent. Substituting (4.29) into (4.30) and solving for $U_w{}^*$,

$$U_w{}^* \approx c_1^{\frac{2}{2-A}} \cdot 0.11^{\frac{-2A}{2-A}} \cdot 2^{\frac{A}{6(2-A)}} \cdot C_{*D,w}{}^{\frac{2}{2-A}} \cdot \Pi_{4,w}{}^{\frac{-2A}{2-A}} \cdot \Pi_{2,w}{}^{\frac{A+3}{6(2-A)}} \cdot \Pi_{3,w}{}^{\frac{A+1}{2(2-A)}}. \tag{4.31}$$

Writing this in the form

$$U_w{}^* \equiv c_{2,w}(A) \cdot \Pi_{2,w}{}^{m_1(A)} \cdot \Pi_{3,w}{}^{m_2(A)}, \tag{4.32}$$

the pairs $\left(m_1(A), m_2(A)\right)$ are a parametric representation of the path shown in Figure 4.10, A.

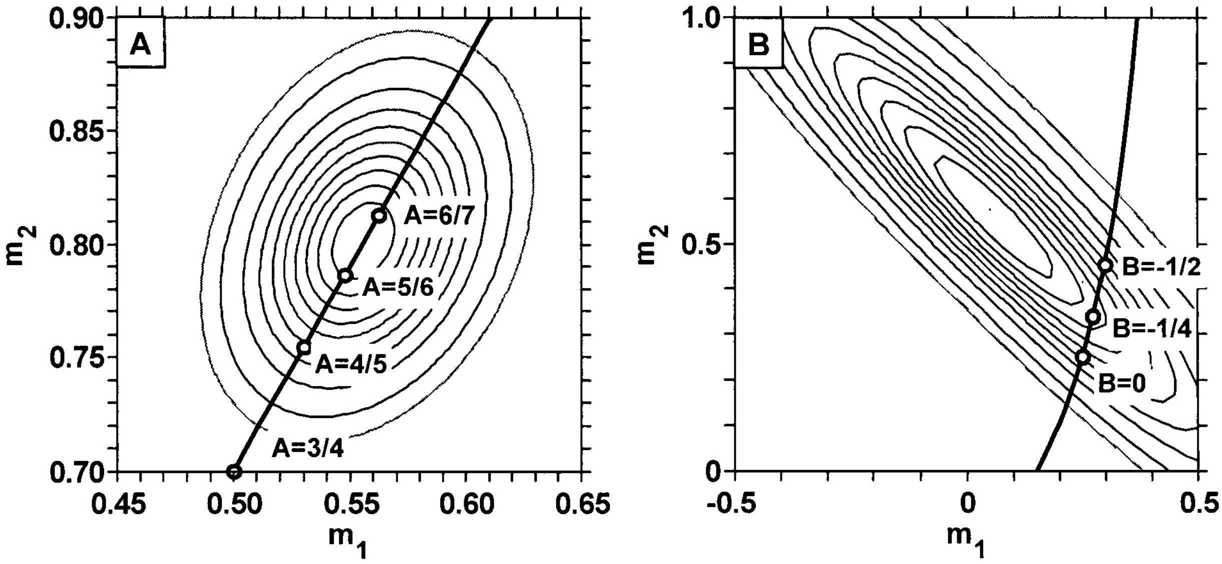

Figure 4.10: Parameter representations of exponents of roughness length in the gravity-current hypothesis.

A: Path of pairs $\left(m_1(A), m_2(A)\right)$ *in* $U_w{}^* \equiv c_2(A)\cdot \Pi_{2,w}{}^{m_1(A)}\cdot \Pi_{3,w}{}^{m_2(A)} = \dfrac{c_1}{\Pi_{10,w}{}^{A}}\Pi_{2,w}{}^{1/4}\cdot \Pi_{3,w}{}^{1/4}$ *superimposed on the joint probability distribution for tank observations (Figure 4.7, A, page 98).*

B: Path of pairs $\left(m_1(B), m_2(B)\right)$ *in* $U_a{}^* \equiv c_{3,a}(B)\cdot \Pi_{2,a}{}^{m_1(B)}\cdot \Pi_{3,a}{}^{m_2(B)} = \dfrac{c_1}{\Pi_{10,a}{}^{5/6}}\Pi_{2,a}{}^{1/4}\cdot \Pi_{3,a}{}^{1/4}$, *superimposed on the joint probability distribution for field observations (Figure 4.7; B, page 98).*

The path runs right through the mode of the joint probability distribution for m_1 and m_2 that I had determined from water-tank observations (Figure 4.7, A, page 98). Here I select a value for A empirically. Research should be carried out in the future to try to derive a value from first principles. Exemplary parameter values are shown in Figure 4.10, A. Of these, I choose for the following discussions $A = 5/6$. This is somewhat arbitrary, but for this value, $\left(m_1(A), m_2(A)\right)$ is close to the mode, and if one could succeed in deriving A from first principles, $A = 5/6$ would seem more likely than $A = 6/7$.

This shows that the gravity-current hypothesis agrees very accurately with water-tank observations if the ND roughness length with an exponent of $-A = -5/6$ is included in the coefficient, i.e.

$$U_w{}^* = \frac{c_1}{\Pi_{10,w}{}^{5/6}}\Pi_{2,w}{}^{1/4}\cdot\Pi_{3,w}{}^{1/4} = 25.4\cdot c_1{}^{12/7}\cdot C_{*D,w}{}^{5/7}\cdot\Pi_{4,w}{}^{-10/7}\cdot\Pi_{2,w}{}^{23/42}\cdot\Pi_{3,w}{}^{11/14}. \tag{4.33}$$

In the atmosphere, it is often assumed as a first estimate that the roughness length is independent of friction velocity, so that

$$U_a{}^* = \frac{c_1}{\Pi_{10,a}{}^{5/6}}\Pi_{2,a}{}^{1/4}\cdot\Pi_{3,a}{}^{1/4} = c_{3,a}\cdot\Pi_{2,a}{}^{1/4}\cdot\Pi_{3,a}{}^{1/4}, \tag{4.34}$$

where $c_{3,a}$ is a constant. I showed in Figure 4.7, B, page 98, that the gravity-current hypothesis with a constant coefficient agrees reasonably well with the field observations.

I take one more step to explore how a dependence of roughness length on friction velocity could alter the result for the atmosphere. Substituting

$$\Pi_{10,a} = c_{4,a}\left(\frac{u_{*,a}}{H_a N_a}\right)^B \tag{4.35}$$

with an unknown coefficient B into (4.34) gives

$$U_a{}^* \propto \Pi_{2,a}{}^{\frac{18-5B}{6(12+5B)}}\cdot\Pi_{3,a}{}^{\frac{6-5B}{2(12+5B)}} = \Pi_{2,a}{}^{m_1(B)}\cdot\Pi_{3,a}{}^{m_2(B)}. \tag{4.36}$$

The path of the pairs $(m_1(B), m_2(B))$ is shown in Figure 4.10, B. The pair with $B=0$ corresponds to the pair labelled 'Gravity' in Figure 4.7, B, page 98. Improvements to the assumption that roughness length is independent of friction velocity ($B=0$) are only possible for negative values with the best agreement with observations for $B\approx -1/4$.

The gravity-current hypothesis agrees so well with the very narrow joint probability distribution of m_1 and m_2 for the water-tank observations that it is hard to believe that this could be by chance. I repeated the same procedure as above for Hunt, Chen, and Schumann hypotheses, but the parameter paths were far outside of the 0.05 contour line. I also confirmed that upslope flow velocity increases with increasing ridge height: substituting the definitions of the Pi groups into (4.33) gives

$$U_w \propto H_w{}^{16/11}. \tag{4.37}$$

The dependence of the gravity-current hypothesis on roughness length as detailed here can only be tentative and guide in a search for underlying first principles. Future research will have to address several questions and challenges: Is convective transport theory, (4.27), applicable to smooth flows? Can we derive the unknown coefficients c_1 and $C_{*D,w}$ in (4.33) from first principles? Finally, $\Pi_{4,w} = \nu_w / H_w^2 N_w$ is not a constant for experiments with different N_w. With more tank data one could determine the probability density function of m_3 in an upslope flow hypothesis of form

$$U_w = c_w \cdot \Pi_{4,w}^{m_3} \cdot \Pi_{2,w}^{m_1} \cdot \Pi_{3,w}^{m_2} \tag{4.38}$$

and compare with $m_3 = -10/7$ in (4.33).

Equations (4.33) and (4.34) suggest a much stronger dependence of ND maximum upslope flow velocity U^* on ND roughness length Π_{10} than Schumann's (1990) LES experiments (4.20). A comparison with Schumann's results is difficult, however, and it is questionable to what extent Schumann's one-dimensional slope with the assumption of a steady state is applicable to our field and water-tank observations. I conclude the discussion of the similarity violation with another tentative approach to reconciling field and tank observations of upslope flow velocity.

A Tentative Explanation of the Similarity Violation Based on the Hunt Hypothesis

A hint at another important difference between tank and atmosphere comes from Hunt et al. (2003). The authors included in their derivation of upslope flow velocity the thermal roughness length z_{0T}, (B.8) and (B.10),

$$U_{M,a} \approx \frac{1}{k} \ln\left(\frac{-L_{*,a}}{z_{0,a}}\right) \left[\frac{h_{s,a}}{h_a} \frac{1}{k} \ln\left(\frac{-L_{*,a}}{z_{0T,a}}\right)\right]^{1/3} \left(\sin\varphi \cdot g\beta_a h_a Q_{H,a}\right)^{1/3}. \tag{4.39}$$

From Garratt's (1994) equation 4.8 follows

$$\ln \frac{z_0}{z_{0T}} = k\, B_H^{-1}, \tag{4.40}$$

where $k \approx 0.4$ is the von Kármán constant and B_H^{-1} is a function of surface characteristics and Prandtl number. Substituting Garratt's equation 4.13a, which applies to fluid-dynamically smooth surfaces as in the tank, into (4.40) gives

$$\ln \frac{z_{0,w}}{z_{0T,w}} = k\left(13.6\,\mathrm{Pr}_w^{2/3} - 12\right) \approx 13 \text{ (smooth, water tank).} \tag{4.41}$$

Note the sensitivity to Pr, e.g. with the Prandtl number Pr_a for air, $\ln\left(z_{0,a}/z_{0T,a}\right) \approx -0.47$. For surfaces with 'bluff element', which should be representative of Minnekhada Park, equation 4.14 in Garratt (1994) gives

$$\ln \frac{z_{0,a}}{z_{0T,a}} \approx k\left[7.3\left(\frac{u_{*,a} z_{0,a}}{\nu_a}\right)^{1/4} \mathrm{Pr}_a^{1/2} - 5\right] \approx 20 \text{ (rough, atmosphere).} \tag{4.42}$$

The ratio z_0/z_{0T} for atmosphere and water tank therefore differs by about three orders of magnitude. Therefore differences in surface properties and Prandtl number can lead to substantial differences in thermal roughness length.

I will conclude this section with a brief investigation of the impact of momentum and thermal roughness length on the Hunt hypothesis. Writing (4.39) in ND form,

$$c_{Hunt} = \frac{2^{1/2}}{k} \ln\left(\frac{-L_*}{z_0}\right)\left[\frac{h_s}{h}\frac{1}{k}\ln\left(\frac{-L_*}{z_{0T}}\right)\sin\varphi\right]^{1/3} \tag{4.43}$$

for the coefficients in (3.69) for atmosphere and (4.14) for water tank. The values determined from hypothesis fitting to atmospheric and tank observations were $c_{Hunt,a} = 2.4 \pm 0.1$, (B.85), and $c_{Hunt,w} = 1.01 \pm 0.02$ (Figure 4.6, page 97). Assuming

$$h_s \approx \frac{h}{10}, \tag{4.44}$$

and substituting the definition of the Monin-Obukhov length

$$L_* \equiv -\frac{u_*^3}{kg\beta Q_H}, \tag{4.45}$$

and (4.21), (4.23), (4.25), (4.26), (4.41), and (4.42) into (4.43) gives $c_{Hunt,a} \approx 20$ and $c_{Hunt,w} \approx 17$.

Given the coarse surface classification for Minnekhada Park and other uncertainties - without attempting here to quantify these – this difference of upslope flow velocities in tank and atmosphere is certainly not statistically significant. However, the hypothesis vastly overestimates observations, and therefore requires modifications. The main point here is to demonstrate that differences in surface properties and Prandtl number can indeed lead to differences in maximum upslope flow velocity. An improved hypothesis that agrees better with observations may depend more strongly on surface characteristics and Prandtl number.

4.3.5 Conclusions on the Similarity between Atmosphere and Water Tank

I have now arrived at the end of the scaling between atmospheric and water-tank observations and its test. Retracing the steps, I developed mathematical idealisations of atmosphere and water tank, imposed similarity requirements on both idealisations and verified the similarity between atmospheric and water-tank observations for CBL depth within the uncertainty of the observations (20%). I discovered that similarity between atmosphere and water tank cannot be achieved by only matching Π_1 to Π_3 and that upslope flow velocities in atmosphere and water tank have significantly different functional dependencies on Π_2 and Π_3 (Figure 4.7, B, page 98). Previous investigators lacked sufficiently accurate scalings and measurements to discover the similarity violation of upslope flow velocity in atmosphere and water tank, which will be a challenge for future research.

I have sketched two tentative approaches to explaining the similarity violation, one based only on (momentum) roughness length and another one based on momentum and thermal roughness length and Prandtl number. The approaches can reconcile atmospheric with tank observations by including additional Pi groups. For example for the gravity-current approach, one needs to include ND momentum roughness length and ND viscous sublayer depth. Technically, however, it would be very difficult to achieve similarity for both additional Pi groups. Roughness length in the water tank needs to be large enough for the flow to be fluid-dynamically rough, but that would require a tank at least one order of magnitude deeper than the tank I used for this research. The approach based on the Hunt hypothesis requires the introduction of ND momentum and thermal roughness lengths. This may be technically easier to achieve. Future research will have to reveal, which of the two approaches is more promising and if similarity can be achieved by including additional parameters.

I began this thesis with the hypothesis that under certain circumstances upslope flow systems may recirculate air pollutants within the CBL rather than vent pollutants into the free atmosphere (section 1.1). Field observations of such recirculation were presented in chapter 2. To understand the observations, the goal was to investigate the kinematics of daytime slope flow systems with a water-tank model of the field site. The similarity violation of upslope flow velocity in atmosphere and water tank raises the concern that it is not possible to draw conclusions from water-tank experiments for atmospheric observations. It is therefore important, before investigating the conditions that lead to recirculation of air pollutants in upslope flow systems, to study the flow characteristics in the water tank and compare with available atmospheric observations.

4.4 Flow Characteristics and Regimes

4.4.1 Flow Characteristics of the Test Case

The mean flow in the tank is well defined and its geometry remains unchanged for considerable periods of time. Changes of the flow geometry, which I call 'regime changes', are associated with substantial changes in velocity and specific-volume distribution.

In this section I will analyse a dye and a particle experiment ('WT2' in Table 4.1 on page 94), which were both run for the test case $N_w \approx 0.379\,s^{-1}$ (4.2) and $Q_{H,w} = 1.85\times10^{-3}\,K\,m\,s^{-1}$ (4.3) to achieve similarity between water tank at $t_w = 05:01$, (4.1) in units of minutes and seconds, and atmosphere at 1200 PDT on July 25, 2001 (Figure 4.11).

The backscatter boundary layer of high aerosol concentrations at the field site originated mostly from near-surface area sources in the Lower Fraser Valley. In the water tank, I initially released a thin layer of high dye concentrations over the plain, which I expect to be redistributed similarly to the aerosol layer in the atmosphere. Therefore, I will also call this layer in the water tank 'backscatter boundary layer' (BBL).

Figure 4.11 (next two pages): Modelling Pacific 2001 in the water tank.

All graphs in this figure are based on a dye and a particle experiment (abbreviated as 'dye' and 'particle'), both with $Q_{H,w} = 1.85 \times 10^{-3}\ K\ m\ s^{-1}$ *and* $N_w = 0.379\ s^{-1}$ *to achieve similarity at 05:01 (min:sec) with atmospheric observations at 1200 PDT on July 25, 2001 ('WT2' in Table 4.1, page 94).*

First page, A (dye): Same as Figure 4.2 (page 86). B (particle): Same as Figure 4.4 (page 89). The inset shows the positions where measurements of CBL depth (open symbols, A) and mean specific volume increment (filled symbols, B) were taken. The white rectangle encloses the field where the velocity measurements of D on the second page were taken. C (dye): Movie frames extracted at the four times indicated in A and B by dashed vertical lines. The dye (Uranine) was originally released as a sub-millimetre thin layer over the entire plain and is illuminated from the left.

Second page, D (particle): Two-dimensional velocity fields corresponding to the four movie frames in C, time averaged over 20-second periods (100 individual fields) approximately centred at the indicated time of each graph. Red and green curves are vertical profiles of specific volume (in arbitrary units) measured approximately during the averaging period of the velocity fields $x = -15\ cm$ *to the left and* $x = 9\ cm$ *to the right of the foot of the slope (at the origin,* $x = 0\ cm$*). All length and velocity scales are identical in the four graphs. A representative velocity vector of length 1 cm* s^{-1} *is shown near the bottom right of each graph underneath the straight line indicating the slope surface.*

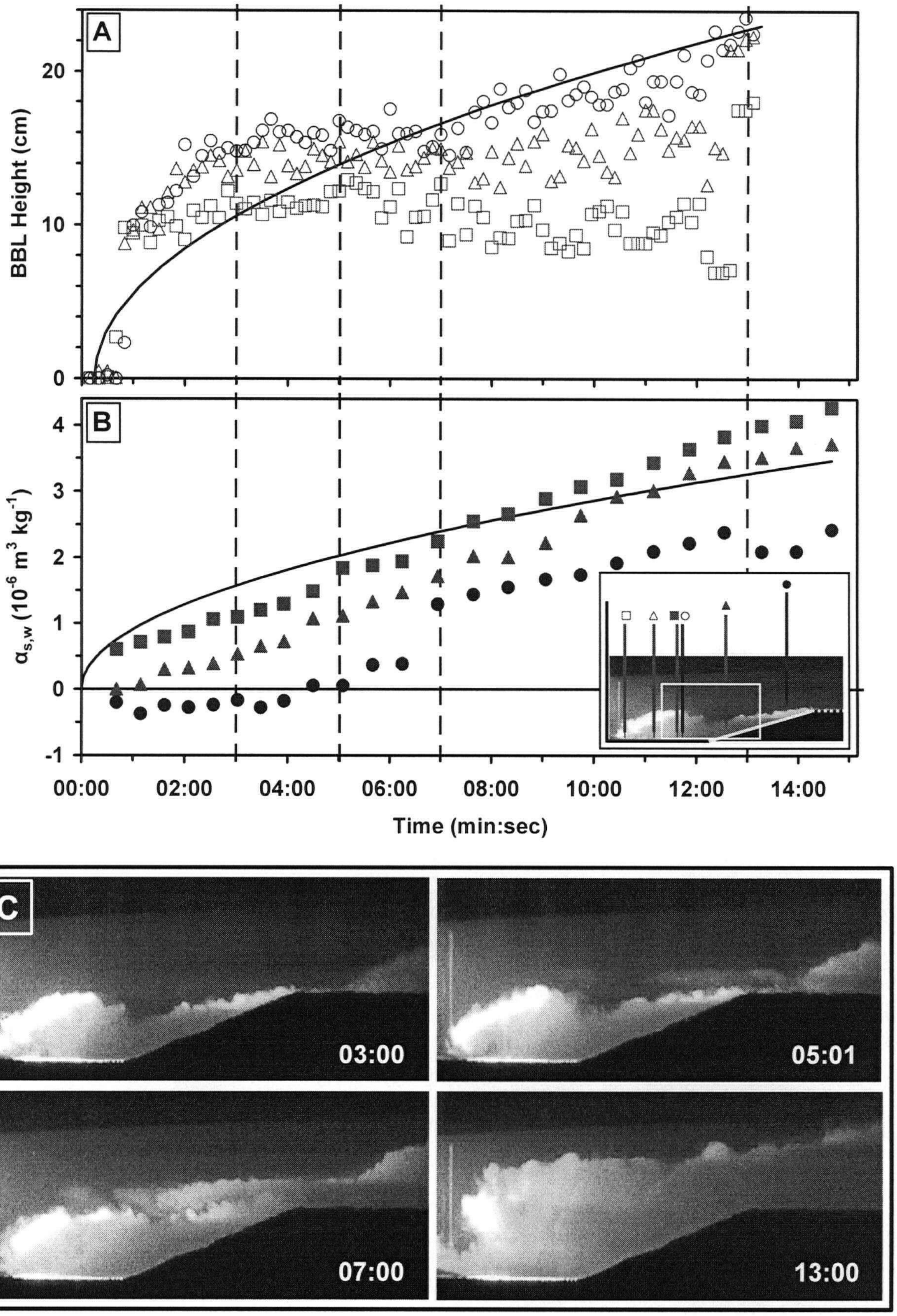
A
B
C
BBL Height (cm)
$\alpha_{s,w}$ (10^{-6} m^3 kg^{-1})
Time (min:sec)
00:00
02:00
04:00
06:00
08:00
10:00
12:00
14:00
03:00
05:01
07:00
13:00

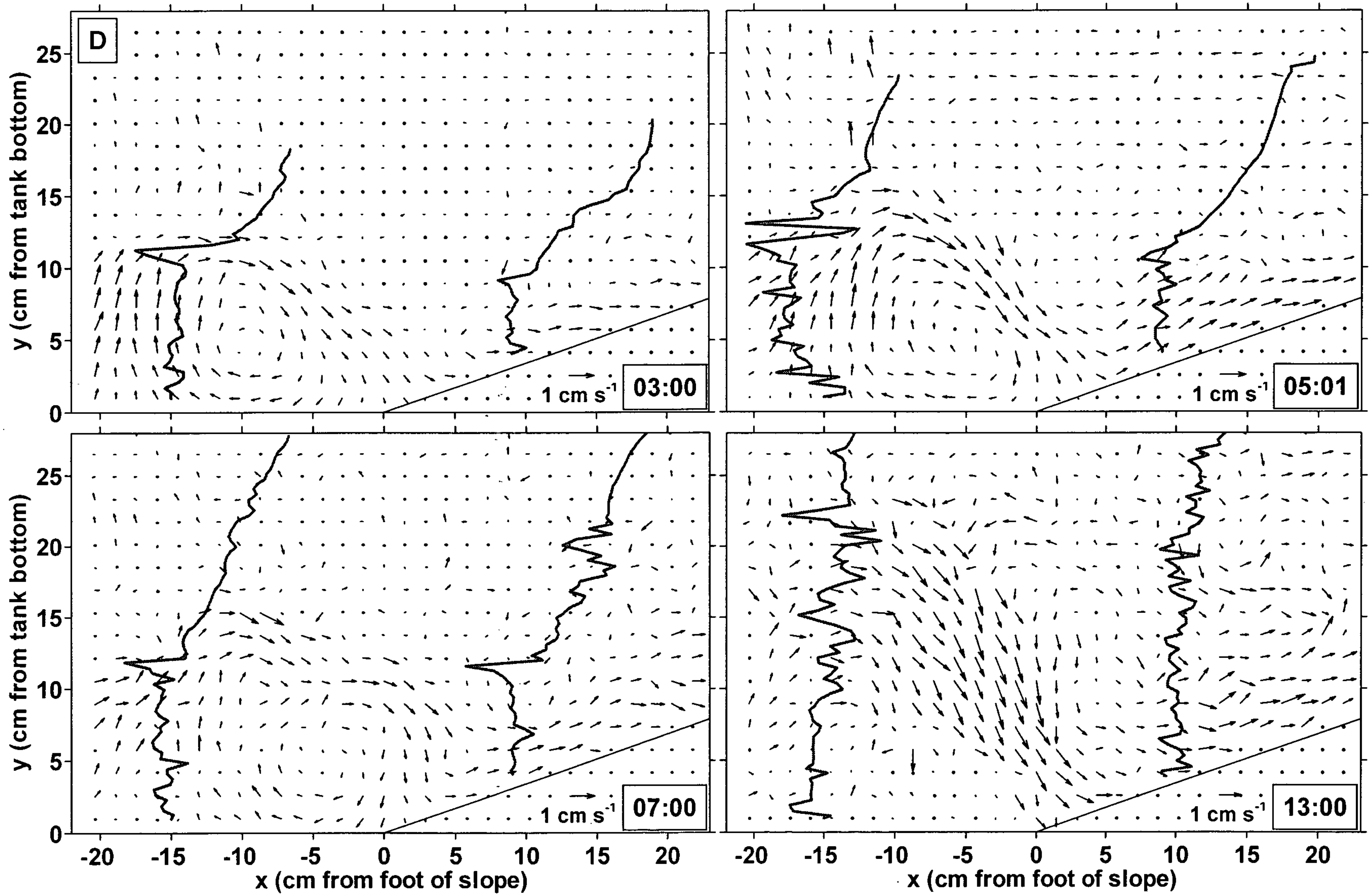
D
03:00
05:01
07:00
13:00
1 cm s^{-1}
y (cm from tank bottom)
x (cm from foot of slope)

I will study the flow characteristics at four water-tank reference times, 03:00, 05:01, 07:00, and 13:00. All four times correspond to realistic conditions in the atmosphere for the same maximum sensible surface heat flux as on July 25 (Table 4.2) but different background buoyancy frequencies.

Water Tank			Atmosphere		
$Q_{H,w}\left(K\,m\,s^{-1}\right)$	$N_w\left(s^{-1}\right)$	$t_w\,(\min:\sec)$	$t_a\,(PDT)$	$N_a\left(s^{-1}\right)$	$Q_{\max,a}\left(K\,m\,s^{-1}\right)$
1.85×10^{-3}	0.379	03:00	1045	0.0134	0.289
		05:01	1200	0.0149	
		07:00	1305	0.0158	
		13:00	1545	0.0166	

Table 4.2: Similarity between water-tank and atmospheric idealisation.

For one given water-tank experiment at four different points in time, similarity between water-tank and atmospheric idealisation can be achieved for a fixed maximum surface heat flux in the atmosphere at four different times of day and background buoyancy frequencies. The second point in time ($t_w = 05:01$) corresponds to the test case, July 25, 1200 PDT, and the third point roughly corresponds to July 26, 1305 PDT.

03:00 ('Mid-Morning')

This early time in the water tank experiment is similar to 1045 PDT ('mid-morning') in the atmosphere with a constant background buoyancy frequency of $N_a = 0.0134\,s^{-1}$ and a maximum heat flux of $Q_{\max,a} = 0.289\,K\,m\,s^{-1}$.

At 03:00 the BBL was much deeper over the plain than predicted (Figure 4.11, A), with the exception of the location nearest to the left end wall. The corresponding video frame (C) shows a bulge of high dye concentrations over the plain.

The two-dimensional (2-D) velocity field at 03:00 (D) reveals a strong clockwise(CW)-rotating eddy between plain midpoint and foot of the slope. To the left of the 2-D velocity field I could identify on the video a counter clockwise(CCW)-rotating eddy. A net fluid flow from this CCW-rotating eddy into the right CW-rotating eddy was compensated at the left end wall by inflow from above the BBL. This subsidence caused the suppression of BBL growth clearly evident at the left position (red open squares in A).

The bulge on the video frame for 03:00 (C) was caused by a thermal updraft over the plain at $x \approx -10$ to $-15\,cm$ from the foot of the slope and was a persistent feature for most of the experiment. As in chapter 2 I define the top of the thermal boundary layer (TBL) as the maximum height to which fluid parcels of high specific volume will rise or from where parcels of low specific volume will drop (parcel method). The apparently exaggeratedly sharp spikes of high or low specific volume in graph D were most likely caused by double diffusion and are not a major factor for the overall flow (Appendix C.4). They are, however, indicators of layer boundaries. For example, in the vertical profile of specific volume at $x = -15\,cm$ (red curve, 03:00, D) a sharp spike of very low specific volume is visible at the top of the TBL about 11 cm above the tank bottom.

The down-moving part of the CW-rotating eddy split up into a branch closing the eddy and a branch joining the upslope flow. The former branch caused a flow in the downslope direction over the plain near the slope as noted earlier in Figure 4.5 (page 93). Over the slope at $x = 9\,cm$, the TBL was only about 6 cm deep, in agreement with the BBL depth (not shown for this location in A, but can be estimated from the video frame, C). The upslope flow appears shallower than the TBL, but at this early stage of the experiment only few particles were visible at greater heights, so that data coverage was insufficient to determine the upslope flow depth. To the right of the BBL bulge over the plain, a BBL depression occurred over the slope approximately in the interval from $x = 0$ to $10\,cm$.

The video frame (C) shows that the BBL depth over the slope decreased approximately linearly to almost zero at the ridge. The upslope flow depth also decreases toward the ridge top which I inferred from the video of WT2 and other water tank experiments. Strongest upslope flow velocities in this and other experiments generally occurred at about $x = 20\,cm$, near the midpoint of the slope. Decreasing upslope flow depth and velocity from slope midpoint to ridge top imply decreasing mass flux, and incompressibility requires a compensating detrainment of fluid from the upslope flow.

If the upslope flow filled the entire TBL such a detrainment would have to occur vertically against gravity, because fluid from the upslope flow layer has a lower specific volume than the stratified fluid above, or laterally, adding a substantial three-dimensional (3-D) component to the overall flow. The videos support the former process and show no evidence for the latter process at 03:00. In Figure 4.11, C and D, there is only weak evidence for the former process, because there were not enough particles in the return flow region, and a very slow flow is difficult to extract from the data with MatPIV.

Strongest upslope flow velocities at 03:00 were about $0.5-0.6\,cm\,s^{-1}$ (D). At the ridge top a shallow plain-plateau flow of roughly the same strength dragged some of the dye along the plateau toward the right end wall (C). In the atmosphere this would be perceived as a venting of aerosols over the ridge top. Notice, however, that fluid, which was carried along the plain-plateau flow and hit and overshot at the right end wall, returned above the plain-plateau flow (C). Aerosols are initially vented out of the upslope flow system, but by joining the plain-plateau flow circulation they return at a later time above a growing CBL, where they are re-entrained if the CBL grows deep enough.

The CBL mean specific volume increments at 03:00 (B) were all lower than predicted, even negative over the slope near the ridge. The slope is a transient region: fluid of lower specific volume is advected into this region, while heated fluid of greater specific volume is advected into higher regions. Near the foot of the slope the fluid had only slightly lower specific volume; fluid advected into regions further up the slope had comparatively much lower specific volume. Over the slope near the ridge, the specific volume increments were negative, i.e. the specific volume was reduced below its initial surface value, because of overshooting due to the momentum the fluid gained up to approximately midpoint of the slope. This explains why the CBL was shallower over the higher slope regions than over the lower slope regions. This is obvious in all frames of Figure 4.11 and in the field data (Figure 2.14, on page 32).

05:01, the Time of Similarity with July 25 ('Noon')

This is the time of expected similarity of all bulk quantities with the atmosphere at 1200 PDT on July 25 ($N_a = 0.0149\,s^{-1}$ and $Q_{\max,a} = 0.289\,K\,m\,s^{-1}$).

Qualitatively, the flow characteristics remained unchanged from 03:00 to 05:01 (Figure 4.11, C and D). At 05:01, the average BBL, determined at the three locations over the plain in Figure 4.11 A, was in very good agreement with the predicted value. The BBL was weakly suppressed at the location nearest to the left end wall (open squares) and slightly deeper than predicted at the location of the bulge.

The velocity field at 05:01 shows some changes from the field at 03:00 (D). The CW-rotating eddy had moved roughly 3 cm closer to the slope (C and D) and the eddy's velocity had slightly increased. The BBL depression seems not to have moved. Near the left edge of the 2-D velocity field (D) clearly visible is the flow from the left CCW-rotating eddy into the CW-rotating eddy.

The vertical profile of specific volume at $x = -15\,cm$ (red curve, D) shows substantially more turbulence at 05:01 than at 03:00. The TBL depth, determined by the parcel method, is the same as the BBL depth (16 cm). Over the slope at $x = 9\,cm$, TBL depth (D), upslope flow depth (D), and BBL depth (C) are all about 8 cm. As before at 03:00, the BBL depth over the slope decreased approximately linearly to almost zero at the ridge (C). Notice, however, that closer to the slope base, at $x \approx 0 - 5\,cm$, the upslope flow depth was only about 7 cm (D) while the BBL was almost twice as deep (C). At this location in the upper half of the BBL velocities were weak with some return flow. The BBL depression was not as pronounced as at 03:00, probably because the weak compensating return flow had carried dye into the depression.

The strongest upslope flow velocities at 05:01 were about $0.6 - 0.8\,cm\,s^{-1}$ (D). Just above ridge height ($y \approx 16 - 19\,cm$, D) a shallow plain-plateau flow continued dragging some of the dye along the plateau toward the right end wall (C), where the layer of overshooting dye had grown a little deeper. The return flow of the plain-plateau flow is clearly visualised by dye that has propagated horizontally from the plateau to above the midpoint of the slope (C) and in the 2-D velocity field at $y \approx 22 - 25\,cm$ (D).

The CBL mean specific volume increments at 05:01 (B) are still lower than predicted, but not negative any longer.

07:00 ('Early Afternoon')

At 07:00, the water tank experiment should be similar to atmospheric conditions at 1305 PDT with a background buoyancy frequency of $N_a = 0.0158\,s^{-1}$ (more stable than on July 25, but slightly less stable than on July 26) and the same maximum heat flux as before ($Q_{\max,a} = 0.289\,K\,m\,s^{-1}$).

At 07:00, the flow characteristics began to change. The BBL depth had slightly decreased since 05:01 and dropped below the predicted values at all three locations over the plain (Figure 4.11, A). The specific volume increments had continued to increase approximately linearly in time over the plain and near the foot of the slope and jumped up rapidly over the slope near the ridge (B).

BBL bulge and depression had disappeared (C). Apart from the subsidence near the left end wall, the BBL top was horizontal over the plain and the bottom half of the slope. In the upper half of the slope the BBL of upslope flow system and plain-plateau flow system began to merge.

The specific volume profile at $x=-15\,cm$ (red curve, D) confirms that the TBL depth over the plain had decreased to roughly 13 cm. The profile over the slope at $x=9\,cm$ (green curve, D), however, shows a new feature: While the TBL depth (about 8 cm) had not changed since 05:01 the fluid layer above between $y\approx 12-22\,cm$ appears turbulent, although overall weakly stable.

The velocity field at 07:00 (D) still shows a bulge at $x\approx -10\,cm$ and a deep depression between $x\approx 5-10\,cm$ which disagrees with the BBL in the video frames (C). At this stage of the experiment, the dye has been substantially distributed throughout the tank, and the BBL characteristics are of limited value for inferences about instantaneous flow field and thermal structure.

In general, velocities in the tank were slightly lower at 07:00 than at 05:01 (D). At $x=9\,cm$ the upslope flow was shallow and a weak return flow occurred within the TBL. Within the shown velocity field the plain-plateau flow system had disappeared. The CW-rotating eddy had broadened a few centre metres into the slope region.

13:00 ('Time of Maximum Sensible Surface Heat Flux)

At 13:00, the water tank experiment is similar to atmospheric conditions at 1545 PDT, with a background buoyancy frequency of $N_a = 0.0166\,s^{-1}$, slightly higher than on July 26, the second day of the field study, but the same maximum heat flux $Q_{\max,a} = 0.289\,K\,m\,s^{-1}$.

At 13:00, the flow characteristics were very different from those at 07:00. At $x = -13\,cm$ the BBL depth had been growing as predicted (Figure 4.11, A, open circles), at $x = -23\,cm$ it had slightly increased until just before 13:00 when it rapidly jumped to the predicted value (open triangles). At $x = -33\,cm$ the BBL had been slightly decreasing until just before 13:00 (open squares), when it also jumped rapidly to within 80% of the predicted value. The reason for this behaviour was that subsidence at the left end wall became increasingly strong, but the area affected by subsidence also became increasingly confined, so that at the two locations $x = -23\,cm$ and $-33\,cm$ subsidence was eventually replaced by deep convection.

The CBL mean specific volume increments at all three locations had continued to increase approximately linearly in time (B) and at 13:00 slightly exceeded the predicted values over the plain and over the lower part of the slope. Over the upper part of the slope the specific volume increment remained well below the predicted values, indicating that upslope flows continued advecting fluid of lower specific volume into the upper slope region.

Upslope flows were strong (about 1 cm s^{-1}) and deep, but at 10-15 cm still shallower than the TBL, which at 13:00 agreed again with the BBL and had a depth of about 23 cm over the slope at $x = 9\,cm$ and about 26 cm over the plain at $x = -15\,cm$ (D). Of the CW-rotating eddy, the lower part of the rotation had disappeared, but the upper part still existed with down-moving velocities exceeding 1 cm s^{-1}. The eddy was contained within the TBL and BBL, and BBL bulge and depression had disappeared (C). At this time the top of the deep BBL showed no details of the underlying topography. The BBL top sloped approximately linearly from near the left end wall to the right end wall.

An analogue video looking down at the flow of an earlier experiment showed a flow front moving upslope initially across the entire width of the tank, although the heaters underneath the tank bottom do not permit heating the first few centimetres closest to the side walls (Figure Appendix XI, page 227). At this early stage, however, the upslope flow is mostly laminar, similar to the situation in Figure Appendix I (page 176), and heat supplied through the tank bottom enters the water through slow molecular diffusion. Because the heat conductivity of stainless steel is much greater than that of water, the tank bottom is fairly homogeneously heated all the way to the side walls. As time progresses the flow becomes more turbulent and transports heat more effectively into the water than molecular conduction transports heat along the stainless steel sheet. Therefore one would expect that less heat flux is supplied to the water near the side walls at a later time in the water tank experiments. Such a lateral heat flux inhomogeneity would favour upslope flows over the centre of the slope and return flows at the same height near the side walls. Indeed, the video reveals three-dimensional flow characteristics at 13:00. Particles near the side walls were out-of-focus and only weakly illuminated by stray light. It is difficult to separate them automatically from the background and apply MatPIV, but when watching the videos it is obvious to the human eye that particles near the side walls moved in the opposite direction of particles near the centre of the tank. Because not the entire flow in upslope direction can be compensated within the weakly heated narrow strip near the side wall, some of the flow moved against gravity at the right end wall and returned above the plain-plateau flow.

In atmospheric and water-tank idealisations I assumed a 2-D flow (section 3.2), but real atmospheric flows are always 3-D. In particular, the slope at Minnekhada Park is only a few kilometres wide (Figure 2.1, page 13), and the upslope flow may, at least partially, return laterally rather than vertically against gravity. Therefore atmospheric and water-tank observations may differ from their 2-D idealisations in the same manner so that the water tank remains a reasonably good model of the real atmosphere.

I will now show more observations on the layering that appeared over the slope at 07:00 (Figure 4.11, D) and on regime changes in the flow and then summarise the flow characteristics discussed in this section.

4.4.2 Layering and Regime Changes in the Test Case

In the test case at 07:00 the CBL mean specific volume increment rapidly increased over the slope near the ridge (solid blue circles, Figure 4.11, B). At the same time, BBL depth began to increase again over the plain near the midpoint and the slope (open green triangles and open blue circles, Figure 4.11, A).

These changes are closely related to the time development of vertical specific volume profiles (Figure 4.12). The profiles corresponding to the solid blue circles in Figure 4.11, B (page 113), at $x = 34\,cm$, are denoted as 'top' in Figure 4.12. At 04:22-04:39 they began to exhibit a three-layer structure. Lower and middle layer were unstable and neutral, respectively, and separated by a sharp spike at about ridge height caused by double diffusion (see Appendix C.4). The top layer was the stable background. Their mean specific volumes differed until lower and middle layer began to merge at 06:47-07:07. This implies that return flow of the upslope flow system and plain-plateau flow became indistinguishable and upslope and plain-plateau flow system merged.

Figure 4.12 (next page): Vertical specific volume profiles in test case WT2.
The three graphs correspond to the locations in Figure 4.11, B, (page 113): $x = -15\,cm$ (bottom), $x = 9\,cm$, (middle) and $x = 34\,cm$ (top). The difference between tick marks on the x-axis is $10^{-6} m^3 kg^{-1}$. The profiles are horizontally offset by $2 \times 10^{-6} m^3 kg^{-1}$ to avoid overlap. Time interval of each profile (bold lines) is shown alternately below and above profiles in minutes and seconds after the beginning of positive heat flux. Each profile is accompanied by the predicted specific volume profile (solid thin lines), the predicted initial background specific volume profile (dashed thin lines), and the CBL depth averaged over the time interval of the specific volume profiles (short horizontal bars), all relative to the plain. The specific volume is shown as the difference from the expected initial surface value over the plain.

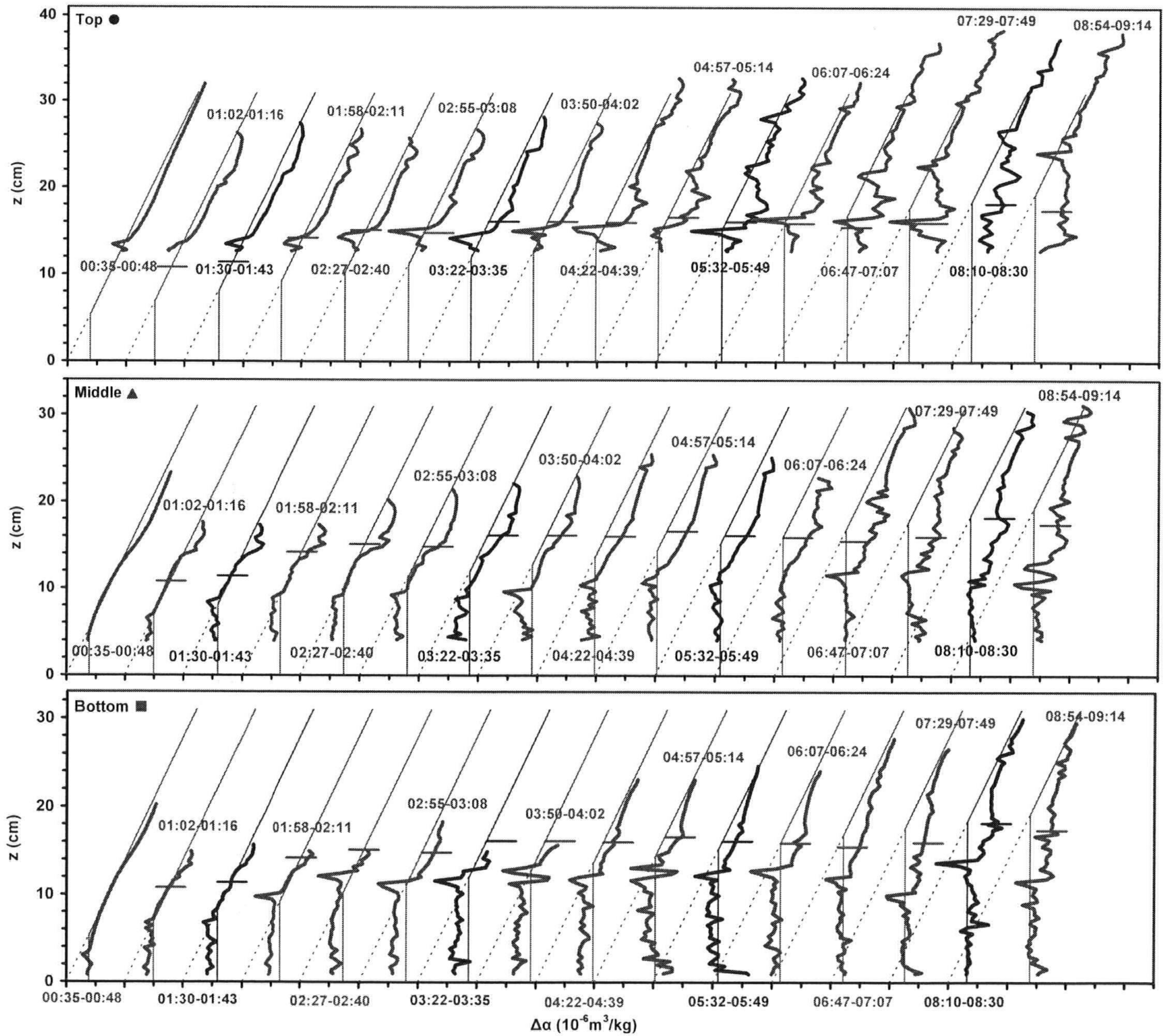
Top ●
Middle ▲
Bottom ■
z (cm)
Δα ($10^{-6}m^3/kg$)
00:35-00:48
01:02-01:16
01:30-01:43
01:58-02:11
02:27-02:40
02:55-03:08
03:22-03:35
03:50-04:02
04:22-04:39
04:57-05:14
05:32-05:49
06:07-06:24
06:47-07:07
07:29-07:49
08:10-08:30
08:54-09:14

At 06:47-07:07, a three-layer structure began to develop over the lower part of the slope at $x = 9\,cm$ (solid green triangles in Figure 4.11, B, page 113, and middle graph in Figure 4.12). The lower layer was well mixed, the middle layer had higher specific volume and a weaker stability than the original background, and the upper layer was stable background. TBL and BBL (Figure 4.11, C, 07:00, page 113) were both about 8 cm deep. The BBL depth over the plain at $x = -15\,cm$ is shown as a reference point in all three graphs in Figure 4.12. Comparison between $x = -15\,cm$ (bottom) and $x = -15\,cm$ (middle) at 06:47-07:07 shows that the TBL was slightly deeper over the plain than over the slope, in agreement with the BBL top (Figure 4.11, C, 07:00). Notice that TBL and BBL were measured at slightly different locations and as a result the TBL was systematically shallower than the BBL in the bottom graph in Figure 4.12.

The vertical specific volume profiles in the bottom graph also show a three-layer structure. Unlike over the slope near the ridge ($x = 34\,cm$), at $x = -15\,cm$ and $x = 9\,cm$ the two lower layers in the vertical profiles did not merge at 06:47-07:07, but much later (not shown in Figure 4.12). By 13:00 they had formed a well-mixed TBL of approximately 25 cm depth, in agreement with Figure 4.11, C, 13:00 (page 113). The BBL top was almost horizontal apart from the subsidence at the left end wall and some overshooting at the right end wall; no substantial amount of dye was carried into layers above the BBL. At this time, the average of the CBL mean specific volumes at the three locations over the slope was in very good agreement with the expected value (Figure 4.11, A, page 113).

Finally I return to the question if the simple encroachment model should be replaced by an entrainment model. Surprisingly, the vertical profiles of specific volume in Figure 4.12 do not show evidence of strong entrainment at the top of the TBL even in cases where the TBL is topped by a weakly stratified elevated layer. I do not know the reason but speculate that double-diffusive convection may be disturbing the build up of a strong inversion.

Before returning to the key questions of this dissertation raised in section 1.1, I discuss and summarise the results and draw conclusions.

4.4.3 Summary of the Test Case

The merging of layers in the vertical specific volume profiles corresponds to changes in flow characteristics. In the test case such regime changes occurred approximately at 07:00 and 13:00. Summarising the analysis in the last section and this section, flow characteristics at 03:00 and 05:01 were very similar. A CCW- and a CW-rotating eddy occurred over the plain, an upslope flow circulation occurred over the slope, and plain-plateau circulation occurred over slope and plateau. A large circulation filling the entire tank width was superimposed on top of the smaller circulations (Figure 4.13, A).

Figure 4.13 (next page): Sketch of flow characteristics in test case WT2.
A: Flow characteristics in experiment WT2 between 03:00 and 05:01, the time of expected similarity with the field observations at 1200 PDT on July 25, 2001, and B: flow characteristics at 07:00; dashed arrows denote small persistent circulations; solid arrows denote a large circulation, which appears superimposed on top of the smaller circulations. C: Side view of flow characteristics at 13:00, and D: plan view of C. Thin arrows show the compensating flows near the lateral side walls.

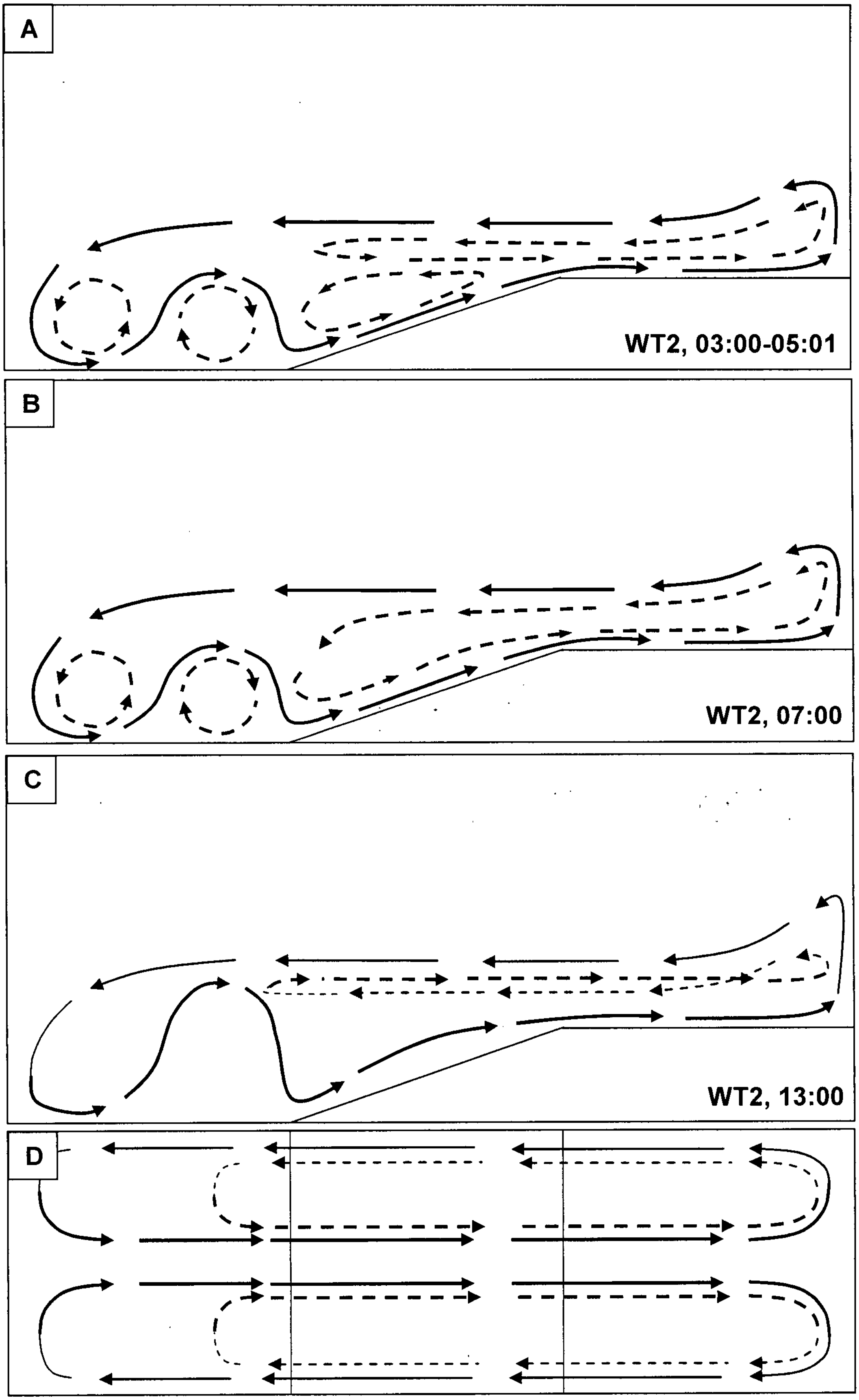
A
WT2, 03:00-05:01
B
WT2, 07:00
C
WT2, 13:00
D

The first regime change occurred at 07:00, when the upper part of upslope flow circulation and the bottom part of plain-plateau circulation cancelled each other and the two circulations merged to one large circulation reaching from the bottom of the slope to the right end wall (Figure 4.13, B).

Just before 13:00, the second regime change occurred. A deep BBL developed with a combined upslope and plain-plateau flow deeper than ridge height, where compensating flows occurred partially above the combined flow system and partially near the side walls. The eddies over the plain had disappeared, but the large circulation across the entire tank could still be identified (Figure 4.13, C).

4.4.4 Impact of the Left End Wall: Hypothesis on CBL Rising in a Valley Centre

It is widely accepted and demonstrated (Whiteman, 2000) that upslope flows over valley side walls cause compensating subsidence over the valley centre. But is that always the case? Water-tank experiment SP suggests that valleys with an aspect ratio of valley bottom width to ridge height of $2 \times 22.5\,cm : 14.9\,cm \approx 3:1$ could exhibit CBL rising over the valley centre[4] (Figure 4.14).

[4] Remember from section 3.2 that the end walls impose a mirror symmetry.

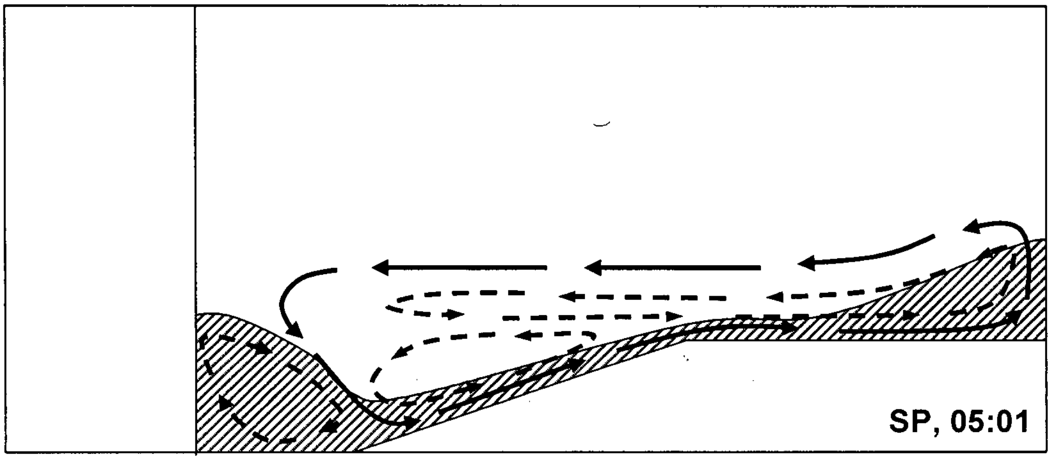

Figure 4.14: CBL rising over valley centre.
In particle experiment SP, conditions were identical to those in WT2 (Table 4.1, page 94) with the exception of an end wall inserted over the plain 22.5 cm from the slope (vertical line). Flow characteristics are sketched with dashed arrows (small circulations) and solid arrows (large superimposed circulation), determined from 2-D velocity fields. The hashed region is the estimated BBL.

Such CBL rising over the valley centre apparently was never reported. I did not test the sensitivity of this result on the aspect ratio. Possibly the aspect ratio must be achieved fairly accurately. Notice that the aspect ratio may be different for the real atmosphere where the CW-rotating eddy may occur further from the slope (see next subsection). Furthermore, measurements may simply not have been taken at the right locations. Unless the rising motion led to condensation it would not be noticed. Furthermore, inhomogeneous sensible surface heat flux and imperfect valley symmetry in the real atmosphere reduce the likelihood of strong rising motion. The search for CBL rising over valley centres in the atmosphere offers interesting future research opportunities.

Motivation for running experiment SP was the CW-rotating eddy over the plain next to the slope. If this location is similar to the location of the sodar at the field site (Figure 2.1, page 13) the flow in downslope direction near the surface (Figure 4.11, D, page 113) contradicts field observations (Figure 2.7, page 22). Mitsumoto (1989) had observed the same CW-rotating eddy in his water tank experiments. It persisted through complete cycles of diurnal heating and cooling and was independent of the length of the plain.

Nevertheless I ran SP to test the obvious explanation: if the large circulation sketched in Figure 4.13, A, (page 126) closes through subsidence at the left end wall (the 'valley centre') then this motion sets off a CCW-rotating eddy over the left half of the plain, which in turn triggers a CW-rotating eddy over the right half of the plain. By reducing the length of the plain in SP, I did not allow the existence of two eddies with a width-over-height ratio of about one. If subsidence caused the eddy motion, the only eddy over the plain in Figure 4.14 would be CCW rotating. By contrast, the observations sketched in Figure 4.14 show a CW-rotating eddy. The causal chain is therefore: the upslope flow causes a CW-rotating eddy, which in turn causes strongly rising motion at the valley centre for a short plain (Figure 4.14) or causes a CCW-rotating eddy closer to the valley centre for a longer plain. In the latter case, the CCW-rotating eddy causes the familiar subsidence near the valley centre (Figure 4.13, page 126). I will next look into the possible reasons for the existence of the CW-rotating eddy and discuss the consequences for similarity between water tank and atmosphere.

4.4.5 CBL Bulge and Depression near the Foot of the Slope

Lidar observations at the Minnekhada Park field site covering the entire morning of July 25 (Figure 2.3, page 18) did not show a BBL bulge and adjacent depression. A close look at the RASCAL RHI scan acquired at 1047 PDT on July 25 (Figure 2.14, page 32) indicates that the TBL depth, characterised by the turbulent appearance of the BBL, could have been substantially shallower between one and 2.5 km from the lidar. The second scan in Figure 2.14 and a few more scans I received from Dr. Strawbridge, however, do not support this interpretation.

There are several possible reasons for the lack of a BBL depression in our field observations. Without lateral boundaries even very light cross winds can advect aerosols laterally into the depression. Furthermore, the aerosol layer at the beginning of positive sensible surface heat flux was much deeper in the atmosphere than the water tank (note the difference of BBL depth in the first one and a half minutes of water-tank reference time in Figure 4.3 on page 88). Finally, atmospheric flows return the aerosols within the upslope flow circulation and fill the BBL depression much faster than the slower flows in the water tank.

De Wekker (2002) observed and numerically modeled CBL bulge and depression, but with a width of 5-10 km they were one order of magnitude larger than expected from similarity with the water tank experiment. He reported observations at Minnekhada Park in the mid-afternoon on August 4, 1993 acquired by a downward-looking airborne lidar. The south-north flight cut our direction of steepest slope at 32° (Figure 2.1, page 13) and looked much further up the mountain range to a ridge height of roughly 1200 m. Looking at this part of the slope and from this angle, the assumption of a 2-D slope does not hold at the scale of hundreds of metres but could be more reasonable at a scale of kilometres for the entire mountain range north of the Lower Fraser Valley (Figure 1.1, page 1). It is possible that de Wekker (2002) observed CBL bulge and depression that were triggered at these larger scales rather than the small slope at Minnekhada Park. Longer distances imply longer time scales and partially explain de Wekker's (2002) observation that the CBL depression strengthened with time.

De Wekker (2002) observed the CBL depression over the plain adjacent to the slope rather than directly over the foot of the slope as in Figure 4.11 C. If during our field study a smaller-scale CBL depression occurred also over the plain rather than the slope, the location of the Doppler sodar near the foot of the slope in Minnekhada Park was located underneath the CBL depression. In the water tank the CBL depression was located over the slope at $x \approx 5\,cm$ (Figure 4.11, D, 05:01, page 113). The corresponding vertical profile of horizontal longitudinal wind velocity (Figure 4.5, page 93) is in good qualitative agreement with our field observations (Figure Appendix III, page 182).

De Wekker (2002) did not report a CW-rotating eddy underneath the CBL bulge, because he had no field observations of the velocity field, and the spatial resolution of the meso-scale numerical model was probably insufficient to resolve the eddy motion. De Wekker (2002) concluded that the CBL depression is associated with increased heating within and above the CBL at the foot of the slope due to advection of warm air by the upslope flow system. Furthermore, he hypothesised that subsidence over the CBL depression is enhanced by horizontal wind divergence due to upslope flow acceleration at the foot of the slope. Mitsumoto (1989) speculated that the CW-rotating eddy was energetically economic. The water tank observations of the CW-rotating eddy suggest the following kinematic explanation of the CBL depression.

The upslope flow advects fluid of low specific volume upwards along the slope into regions of higher specific volume, thereby constantly reducing specific volume and inhibiting CBL growth in these regions. In contrast, advection over the plain does not have the same 'cooling' effect, and the CBL grows faster there than over the slope. This leads to the CBL depression sketched in Figure 4.15.

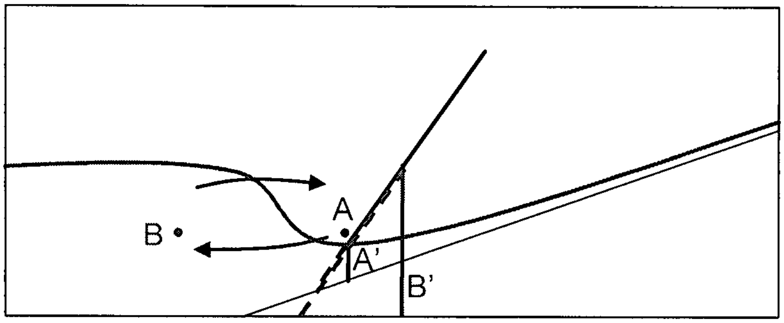

Figure 4.15: Mechanics of CBL depression and CW-rotating eddy.

Sketch of the CBL top (solid thick green curve) over plain and slope near the slope base. Underneath point A in the CBL depression the vertical specific volume profiles are sketched for: CBL at point A (solid thick blue vertical line, labelled with A'); CBL at point B (solid thick red vertical line, labelled with B'); background above the CBL (solid thick black tilted line); and the original background (dashed blue and red tilted lines). The fluid exchange triggered by horizontal specific volume variations is indicated by the two arrows.

The horizontal pressure gradient caused by horizontal specific volume differences between point A above the CBL depression and point B within the CBL bulge is comparable to a lock exchange with the denser fluid on the right at point A. In a static situation this would lead to a CW exchange flow as indicated by the arrows. In the dynamic situation this favours a CW motion over the plain where fluid is removed from high above the plain, moved downward left of the CBL depression, and advected up the slope. This enforcement of a CW rotation is so strong that it even eliminates subsidence near the valley centre for a case like in Figure 4.14 (page 129).

The other important component to a CW-rotating eddy next to the slope is the CCW-rotating upslope flow circulation, which favours CW-rotating flows in adjacent regions. The CCW-rotating plain-plateau circulation right above the upslope flow circulation is an exception that only persists as long as the two layers are clearly separated by a strong density gradient. This argument becomes particularly compelling in the following discussion.

4.4.6 Inhomogeneous Heating

Why did Chen et al. (1996) not observe the CW-rotating eddy over the plain adjacent to the slope? They used a triangular ridge and approximately sinusoidal cycles of diurnal heating and cooling like Mitsumoto (1989). One possible difference could be inhomogeneous heat flux because Chen et al. (1996) injected hot water underneath the ridge top, from where it flowed outward toward the end walls underneath the tank bottom. Strong venting over the ridge in Chen's et al. (1996) experiments provide evidence that there was a strong heat flux increase from end wall to ridge top. By contrast, Mitsumoto (1989) ensured homogeneous heat flux by individually controlling the water temperature from injection pipes underneath the slope.

To test if a positive heat flux gradient from left end wall to ridge top eliminates the CW-rotating eddy I ran experiment TR2 (Table 4.1, page 94). In TR2 heat flux increased by a factor of 2.5 from the left end wall to the removable end wall at the ridge top (Figure 4.16). Because the plateau was cut off from the rest of the tank with a removable end wall, there was no plain-plateau flow. The heat-flux gradient triggered long CCW-rotating circulations over plain and slope (dashed arrows) and increased the strength of the upslope flow, causing overshooting over the ridge top. One would expect that the two circulations would merge, but they remained separated by the large circulation, which formed a high arch between them (solid arrows).

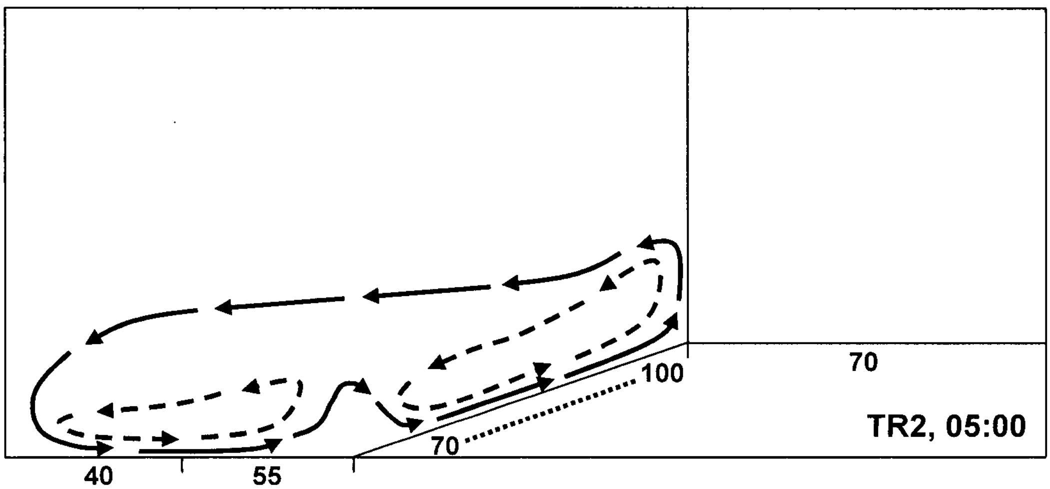

Figure 4.16: Flow characteristics for inhomogeneous heat flux.

This experiment (TR2) with a background buoyancy frequency of $N_w = 0.342\,s^{-1}$ *was designed to reproduce, at least qualitatively, tank observations by Chen et al. (1996), with their time of maximum heating corresponding roughly to 05:00 in this experiment. Distribution of heat flux underneath the tank bottom is indicated by the numbers, which are in % of the maximum value of* $3.7\times10^{-3}\ K\ m\ s^{-1}$ *right below the ridge top. Heat flux underneath the tank bottom increased in twelve increments from 70-100%. The plateau was separated from the rest of the tank by a removable end wall (vertical line). The arrows represent the circulations at 05:00.*

Chen et al. (1996) reported the large circulation but not the individual CCW-rotating circulations and the arch between them. The quality of the reproduction of their particle streak experiments in the publication is insufficient to confirm the existence of the smaller-scale flow features. At 74 cm Chen's et al. (1996) interrogation window was almost twice as wide as on my videos and therefore provided less spatial resolution. Also, the authors took particle streak photographs every 30 s which may not have given them enough time resolution to confidently identify the unexpected and unusual arch. Moreover, the authors could not analyse velocities near the surface and therefore may not have noticed the stagnant flow underneath the arch, which made it less likely to notice the arch itself. Finally, it is possible that the authors did not pay attention to this flow detail, because they mostly investigated the overall features of the large circulation.

4.5 Discussion and Conclusions

4.5.1 Conclusions on Flow Characteristics and Regimes

Given the open questions and issues raised so far: What can we infer about the atmosphere from water-tank experiments? There is one major difference between field and water-tank observations that cannot be reconciled: upslope flows are clearly stronger in the atmosphere than derived from similarity with water-tank experiments. Possibly, similarity of upslope flow velocity cannot be achieved with a tank of this small size. It is likely that the flow in the water tank needs to be fluid-dynamically rough, like in the atmosphere, to achieve a satisfactory agreement between ND upslope flow velocities in the two systems. But that implies that individual roughness elements would have to be at least of similar size as the viscous sub-layer depth (4.24) of roughly 2.5 mm in the water tank. To what extent that requires a higher ridge to match the ND roughness lengths remains an open question. According to the preliminary investigations in section 4.3.4 upslope flow velocity could depend strongly on ND roughness length $\Pi_{10,w}$, (4.33), therefore requiring a tank with a ridge height on the order of metres.

The kinematic explanation of CBL bulge and depression and CW-rotating eddy over the plain near the slope base holds for atmosphere and water tank. With a stronger upslope flow in the atmosphere the CBL depression should be even deeper and the eddy rotation faster. I discussed above that insufficient evidence of the eddy in field observations and numerical models does not preclude its existence.

The sodar's location in the plain near the base of the slope could not be identified with the similar location in the water tank. A constant 19° slope angle, however, is a crude approximation to the real slope with a slowly increasing angle near the slope base, nearby hills, and other slope variations (Figure 2.1, page 13, and Figure 3.2, page 38). It is therefore acceptable to compare the sodar location with a location over the slope near its base.

Similar CBL growth in atmosphere and water tank provides evidence that the two systems do not behave very differently. For the atmosphere we can expect faster transport of air pollutants and stronger overshooting over the ridge top due to greater inertia. A comparison of water-tank images with lidar scans roughly at the time of similarity shows good qualitative agreement (Figure 4.17). Overshooting over the ridge top is apparent on both lidar scans (C and D), well documented by cumulus clouds.

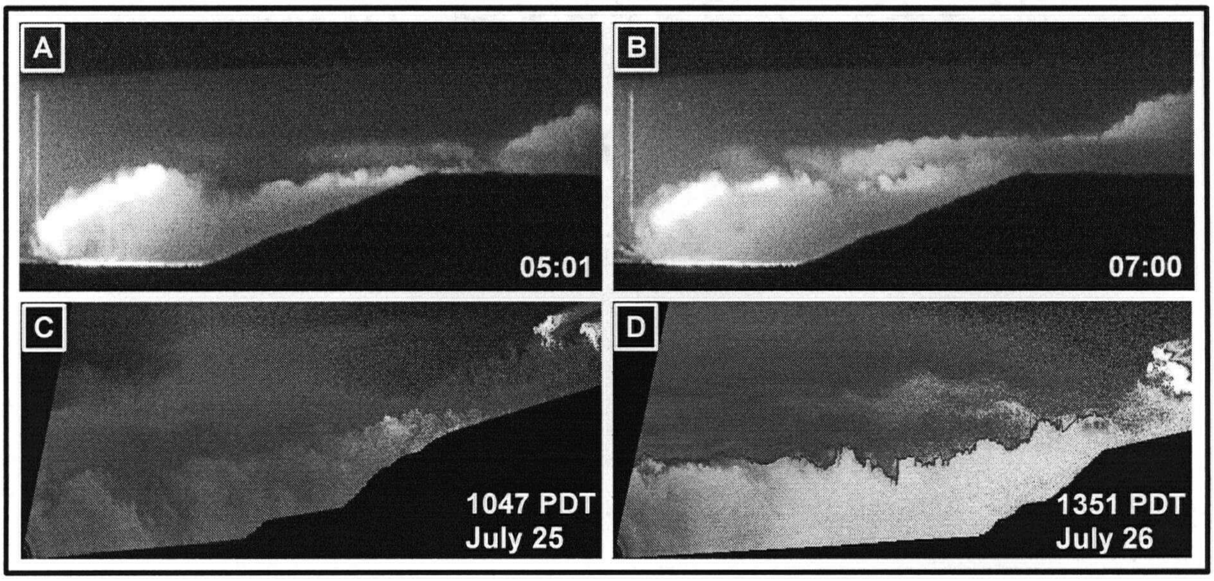

Figure 4.17: Comparison of water tank dye experiments with atmospheric RASCAL RHI scans.
Images A and B are dye experiments taken from Figure 4.11, C (page 113). Image C is the RASCAL RHI scan acquired at 1047 PDT on July 25, adapted from Figure 2.14 (page 32). RASCAL scan D was acquired at 1351 PDT on July 26 (courtesy of Dr. Kevin Strawbridge, Environment Canada). The purple line in D marks the BBL top determined with the algorithm in Strawbridge and Snyder (2004) and the bright white area on the right is caused by cumulus clouds. I adjusted the horizontal and vertical scales of the RASCAL scans to agree approximately with the scales represented by the water tank. In D, the topography looks different from C because the RASCAL RHI scan cut the slope at a smaller angle farther north of the sodar (see Figure 2.1, page 13).

At 1047 PDT on July 25, (C), aerosols were mostly returning in the laminar-looking layer at a height of about 1000 m right above the turbulent CBL. This layer had propagated much farther into the plain than the counterpart in the water tank (A), as expected from faster horizontal flows. Double-diffusive convection at the interface between plain-plateau flow and its return flow may also contribute to a slowing and eventual breakdown of the flow (Appendix C.4). From lidar scan C it is not clear if the aerosols are returning as part of the upslope flow or the plain-plateau circulation. In the atmospheric idealisation I assumed a heated plateau. An alternative assumption could be a triangular ridge, which I accomplished in the water tank by inserting a removable end wall at the ridge top (TR1 and TR2, Table 4.1, page 94). The flow caused by a triangular ridge (Figure 4.16, page133), is more likely to produce the aerosol distribution shown in Figure 4.17, C.

On July 26, background stratification was stronger. At 1351 PDT (D), the BBL was approximately as deep as on the previous day at 1047 PDT (C), in good agreement with the water-tank experiment (B). High aerosol concentrations above the BBL were at least partially caused by the return flow of the plain-plateau circulation, better seen from the lidar image acquired earlier at 1053 PDT on the same day (Figure 2.14 bottom, page 32). This supports the assumption of a heated plateau and implies that the elevated aerosol layer on July 25 (C) was also caused by the return flow of the plain-plateau circulation.

After these detailed comparisons between atmospheric and water-tank observations little doubt remains about qualitative and quantitative similarity, with the exception of upslope flow velocities. Any conclusions I can draw about flow characteristics from water-tank experiments are relevant to the atmosphere, which applies in particular to the key questions, which I posed at the beginning of this dissertation (section 1.1) and to which I can finally return: Is the boundary layer over a heated slope identical to the CBL over flat terrain or does it have a more complicated structure? How do upslope and return flow relate to the boundary-layer structure? Is there a continuous transition between the two extremes of recirculation and venting or are there two distinct regimes? What are the determining parameters?

4.5.2 Relation between Upslope Flow System and Atmospheric Boundary Layer

Clarification of Boundary-Layer Definitions and Terminology

In this dissertation I used two definitions of the CBL: the TBL determined from vertical profiles of specific volume/potential temperature using the parcel method and the BBL determined from images of dye concentrations and lidar aerosol-backscatter scans. Other definitions have been used by previous investigators, e.g. the Richardson number (e.g. de Wekker, 2002), which will typically give different results even over homogeneous flat terrain, because the entrainment zone does not have sharp boundaries with the uniform layer underneath and the free atmosphere above. This difference is not of concern here. The greater question was raised in section 1.1: Is the boundary layer over a heated slope identical to the CBL over flat terrain or does it have a more complicated structure?

To clarify terminology I distinguish the atmospheric boundary layer (ABL) from TBL and BBL and abandon the ambivalent term 'CBL'. It is common to "define the [atmospheric] boundary layer as the part of the troposphere that is directly influenced by the presence of the earth's surface, and responds to surface forcings with a timescale of about an hour or less" (Stull, 1988). Intuitively we seem to relax the requirement of such fast response for example in the case of the residual layer above a strongly stratified nocturnal boundary layer in the winter. Behind this is a sense of continuity of entrainment zone and capping inversion from one day to the next (Figure 1.7 in Stull, 1988), which suggests defining *the ABL as the part of the troposphere that exchanges temperature, tracers, or moisture with the earth's surface within one diurnal heating cycle*. This definition solves another problem of the traditional definition: venting of upslope flows over mountain ridges is very fast and can create elevated aerosol-rich layers within one hour. Such layers meet the traditional definition of ABL although they may remain above the entrainment zone for the entire day and therefore defy our intuitive understanding of the ABL. On the other hand, elevated layers that merge with the TBL within one diurnal heating cycle should be considered part of the ABL even before merging occurs.

Multi-Scale Layering

De Wekker (2002) drew a comprehensive conceptual picture of the ABL characteristics over complex terrain and clearly demonstrated that the BBL often substantially exceeds the TBL, in particular in the afternoon. In this dissertation I focused on upslope flows and minimised other potential influences like valley flows. Several kilometres from the slope, our field observations suggested that TBL and BBL were identical on the mornings of July 25 and July 26, when larger-scale flows were negligible (Figure 2.6, page 21). Near the slope the water tank experiments revealed complicated layering and regime changes. I will argue now that many of the complicated ABL features investigated by de Wekker (2002) are probably caused by 'multi-scale layering', a repetition of layering processes and regime changes at increasingly larger spatial and temporal scales.

The fastest of these processes is convection, which creates the TBL. Without horizontal inhomogeneities no other process could lead to further ABL structures. Over inhomogeneous flat terrain, for example at land-sea interfaces, layering can be expected but may be hard to observe; because the spatial and temporal scales driving such flows are typically large, elevated layers may not return within a diurnal cycle. By contrast, short steep slopes like at Minnekhada Park can drive upslope flows of several metres per second and force a compensating return flow over horizontal distances of only a few kilometres. In less than one hour aerosols transported from near the surface up the slope return in an elevated layer above the TBL.

Elevated layers tend to have intermediate characteristics: aerosol concentrations and stability between those in TBL and free atmosphere. The underlying TBL needs less surface heating to grow into a weakly stratified elevated layer than it would need to grow into the strongly stratified free atmosphere. In water-tank experiment WT2, the TBL began merging with the elevated layer at about 07:00, which I identified as a typical atmospheric early-afternoon case (Table 4.2, page 116). In the atmosphere the difference in aerosol concentrations between TBL and elevated layer is a complicated function of the day's history of emissions, advection, and entrainment. Before the merging of TBL and elevated layer their aerosol concentrations may become indistinguishable so that both layers appear as one deep BBL.

These arguments answer the second question that I posed at the beginning of this dissertation was: How do upslope and return flow relate to the boundary-layer structure? In the water-tank experiments the upslope flow layer agreed with the TBL at all times and the return flow built up a BBL deeper than the underlying TBL. This supports hypothesis 3 in section 2.3.3 stating that BBL and TBL were different for extended periods during our field observations.

I argued that the large CBL depressions investigated by de Wekker (2002) were the result of the same kinematics as in the water tank but at a scale that is similar to the Northshore Mountains as a whole rather than the smaller individual slope at Minnekhada Park. In the water tank I can clearly identify the repetitive multi-scale layering. Water-tank experiments with a heated plateau caused a plain-plateau flow circulation that removed dye-rich fluid from the upslope flow circulation at the ridge and returned it above the plain in the return flow part of the plain-plateau circulation. Upslope and plain-plateau flow circulation merged at approximately the same time as the TBL merged with the elevated layer. At this point the process of developing an elevated layer above the TBL was repeated at the larger-scale combined upslope plain-plateau flow circulation, until eventually the TBL merged with the new elevated layer at about 12:30 in the tank (similar to typical atmospheric settings just before the time of maximum heating, Table 4.2, page 116). By 13:00 the TBL had grown beyond the scale of the underlying topography, which could not provide further horizontal inhomogeneities to continue the multi-scale layering.

In many real atmospheric settings horizontal inhomogeneities are likely to continue at increasingly larger scales, and the multi-scale layering is only limited by the finite duration of the diurnal heating cycle. Furthermore, inhomogeneities often occur at more closely-spaced scales and are not restricted to upslope flows but may include along- and cross-valley flows, topographically-altered synoptic winds, and flows caused by land-use variations. Such closely-spaced discrete scales cause a de facto "continuum in topographic complexity and scale" (Whiteman, 1990). In this dissertation I have demonstrated that a water tank of sufficiently simple topography can clearly discriminate the steps in the multi-scale layering, which may be practically indistinguishable in the atmosphere. In the next section I will discuss the role atmospheric imperfections, i.e. deviations from the idealisations, play in the transport of air pollutants.

Governing Parameter for Regime Changes

Two of the questions I posed at the beginning of this dissertation still need an answer: Is there a continuous transition between the two extremes of recirculation and venting or are there two distinct regimes? What are the determining parameters? In chapters 1 and 2, I pointed out that Chen et al. (1996) identified as the critical parameter in their upslope flow scaling,

$$G_c \equiv \frac{H}{h} \equiv \frac{1}{h*} = HN(2g\beta E)^{-\frac{1}{2}} = (2\Pi_2\Pi_3)^{-\frac{1}{2}}, \tag{4.46}$$

where I used (3.51) and (3.90). Chen's et al. (1996) scaling is independent of instantaneous heat flux, because surface heating in their tank followed a similar time development as in the atmosphere. In (4.46), h and therefore E, Π_2 and Π_3 are the values at the time of maximum heating.

I can now capitalise on my scaling in chapter 3. As my water-tank experiments progress, each point in time is similar to a particular atmospheric parameter setting, and the time-dependent scaling allows me to fairly accurately determine the conditions during regime changes. Tank experiment WT2 showed a regime change at about 12:30, when the TBL merged with the elevated layer aloft (Figure 4.11, page 113). The expected TBL depth of $h_w \approx 22.5\,cm$ leads to

$$G_c \approx \frac{14.9\,cm}{22.5\,cm} \approx 0.66, \tag{4.47}$$

in excellent agreement with Figures 10 and 12 in Chen et al., 1996, which show substantially different time developments of the TBL over the plain far from the slope for $G_c \leq 0.6$ (small closed slope flow circulation within the TBL) and $G_c \geq 0.7$ (large slope flow circulation with venting over the ridge top and subsidence over the plain). These are two distinct regimes of recirculation versus venting, and the merging of TBL and elevated layer occurs so fast that it is essentially discontinuous.

Chen et al. (1996) used a triangular ridge in their water tank, while I used a plateau, which suggests that the regime change for $G_c \approx 0.66$ is independent of topography and that G_c, or in terms of the Pi groups in this dissertation, $\Pi_2 \cdot \Pi_3$ is the parameter that determines if elevated layers of high pollutant concentrations will be re-entrained into the underlying TBL during the diurnal cycle. However, the following comparison with field data shows that the good agreement in G_c may be incidental.

In section 2.3.2 I reported field observations of regime changes at $G_c \approx 2.6$ for July 25 before 0900 PDT, and $G_c \approx 1.4$ on July 26 between 1000 and 1030 PDT. These values differ substantially from the values in the water tank but also from each other. Regime changes at such large values of G_c did not occur in my water tank experiments. The first regime change in experiment WT2 occurred at about 07:00 when $G_c \approx 0.90$, which was less drastic than the regime change for $G_c \approx 0.66$ and outside the range of values investigated by Chen et al. (1996).

A possible explanation for the difference in G_c is that fast atmospheric upslope flow circulations create elevated layers much faster than the slower tank circulations. This is in line with the quick filling of the atmospheric BBL depression with aerosols. In the water tank a deep BBL builds up just before the merging of upslope flow and plain-plateau flow circulation. By then, h_w is fairly large and G_c smaller than in the atmosphere. This does not explain why the values of G_c differ on the two days on which a stronger stratification on July 26 was the only major difference. Besides G_c, another ND parameter that depends on background stratification N_w must be important for the occurrence of a regime change. This is not surprising because I identified two governing parameters for the similarity between atmosphere and water tank, Π_2 and Π_3. More experiments will have to be carried out and analysed in the future to determine the dependence of regime changes on Π_2 and Π_3.

Under many circumstances in the real atmosphere the growth of the TBL is practically a continuous multi-scale process and there are nearly continuous degrees of venting versus trapping of air pollutants, probably often hard to identify. This is certainly the case in the afternoon of July 26, when sea breeze and up-valley flow add to the complexity of the flow at Minnekhada Park. Even during the morning on both field days, small differences for example in soil moisture, plant transpiration, synoptic wind, subsidence, emissions, and initial conditions of aerosols in the early morning could lead to substantially different aerosol distributions and flow characteristics. This may be another reason for the great difference in G_c on the two field days.

Conclusions

The clarification of the terminology for ABL, TBL, and BBL in this discussion becomes critical for assessing air pollution exposure of populations in complex terrain. The definition of the ABL should comprise all layers that exchange air with the surface during the day. Together with in- and outflow by advection and venting, the ABL constitutes the atmospheric environment to which local population is exposed. Venting of air pollutants over mountain ridges is documented in many studies, some of which I reviewed in section 1.3. However, even in highly idealised scenarios like those discussed in this dissertation, the ultimate fate of pollutants depends on the questions: Will regime changes lead to re-entrainment of pollutants into the TBL before surface heating ceases? How many of these regime changes will occur? And how much air pollution will ultimately find its way back to the ground? I will conclude this chapter with a discussion of the transport of air pollutants under more realistic atmospheric conditions than assumed in the atmospheric idealisation.

4.5.3 Trapping versus Venting of Air Pollution

The water tank is an extreme simplification of the complexity of the real atmosphere. This even holds for nearly ideal conditions at Minnekhada Park during the morning of July 25, 2001. Nevertheless, the detailed investigations of the flows in the water tank and the comparison with field observations in this dissertation permit conclusions about atmospheric flows under typically less ideal conditions. In this section I discuss the consequences of the ideal conditions and different deviations from these conditions for the transport of air pollutants over a heated slope. This is partly a sequence of open-ended avenues, each of which points towards questions for future research.

The 'Perfect World'

The end walls of the water tank impose a mirrow symmetry (Figure 3.2, page 38). Therefore the water-tank and the atmospheric idealisation have perfect symmetry. Furthermore, both idealisations represent closed systems without larger-scale flows or net cross flows. Air pollution in such systems can only escape from the surface by transport into elevated layers that are not re-entrained during one diurnal cycle. As the discussion above demonstrates even this simple scenario is difficult to assess.

Asymmetries in Geometry or Sensible Surface Heat Flux

Asymmetries are usually beneficial for areas with high air pollution levels. A rough sketch of an asymmetric flow pattern is shown in Figure 1.3 C (page 4), where the area to the left of the ridge is less strongly heated than the area to the right. Air pollution on left side will be reduced because part of the upslope flow feeds into the strongly venting upslope flow on the east-facing side. This assumes that the mass loss over the mountain ridge is compensated by an inflow of less polluted air from the west. In the right area air pollution levels will increase if they were originally lower in the right area than in the left area and if the polluted elevated layer from the left is eventually entrained into the growing TBL.

Larger-scale Flows

The impact of larger-scale flows is so complex and subtle that I will only touch on a few ideas that will have to be addressed in future research. One has to distinguish between different types of larger-scale flows, strength, and direction.

A synoptic wind that is much stronger than the upslope flow will destroy it regardless of wind direction. If the synoptic wind is too weak to destroy the upslope flow its effect on slope flow transport depends mostly on its direction. The effect of a ridge-parallel synoptic wind on local air pollution primarily depends on upwind pollution levels. A synoptic wind in upslope flow direction, if strong enough, suppresses the return flow as sketched in Figure 1.3 B (page 4); air pollutants reaching the ridge top will be transported downwind away from the source area. In contrast, synoptic winds opposing upslope flows enhance return flows and the build-up of elevated layers, which may eventually be entrained into the TBL.

Up-valley flows and sea breezes affect upslope flows similar to the way synoptic winds do, but their particular characteristic is that they often reverse diurnally. For example, air pollutants carried offshore by the land breeze may return with the sea breeze during the day. Obviously a good understanding of the transport mechanisms of valley flows and sea-land breezes is needed to reliable predict upwind air pollution levels.

More complicated water-tank models could be designed in the future to study the impact of up-valley flows and sea breezes on upslope flow circulations and the consequences for air-pollution transport. Synoptic winds, however, may be technically too challenging, and numerical models may be the only alternative to field observations.

Sensible Surface Heat Flux

Stronger sensible surface heat flux is for example caused by less cloud cover, greater insolation angles, longer days, drier conditions, and smaller albedo. Such conditions favour a deeper TBL via (3.51) and (3.91), i.e. $h = (2g\beta E)^{1/2}/N$, increasing the chance of re-entraining air from polluted elevated layers.

The effect of sensible surface heat flux on the strength of upslope flows is important because stronger upslope flows are beneficial if air pollutants are partially removed at the ridge top. Moreover, stronger upslope flows may cause stronger venting and carry pollutants higher than weaker flows. From the definition of the Pi groups in Table 3.2 (page 47) I get

$$U \propto HN \cdot \left(\frac{EN}{Q_H}\right)^{m_1} \left(\frac{g\beta Q_H}{H^2 N^3}\right)^{m_2} \propto \left(\frac{E}{Q_H}\right)^{m_1} Q_H^{\ m_2} . \tag{4.48}$$

For the water tank with $E_w = Q_{H,w} t_w$, (3.27),

$$U_w \propto Q_{H,w}^{\ m_2} , \tag{4.49}$$

which increases with $Q_{H,w}$. In the atmosphere, I assume that sensible surface heat flux is sinusoidal and the increase in $Q_{H,a}$ caused by an increase in $Q_{\max,a}$. From (4.48) follows

$$U_a \propto Q_{\max,a}^{\ m_2} , \tag{4.50}$$

which increases with $Q_{\max,a}$.

Stronger sensible surface heat flux increases both upslope flow velocity and TBL growth, which partially offset each other. Probably the increase in TBL growth is a more important effect than the increase of upslope flow velocity, so that the net effect of stronger sensible surface heat flux is an increase of the re-entrainment of air pollutants.

Stratification

When background stratification is approximately linear, weaker stratification permits a stronger TBL growth than stronger stratification. Over flat terrain this increases the entrainment of free atmospheric air and the volume of air into which air pollutants are dispersed. Near heated slopes, however, weaker stratification implies a greater chance of entraining elevated layers into the TBL during the diurnal heating cycle, which offsets the benefits at least partially.

The situation is more complicated if the background stratification is not linear. A strong inversion, for example, may not be relevant if it breaks up during the day. If the TBL cannot penetrate the inversion the question remains to what extent the upslope flow circulation can build up elevated layers above the inversion.

The impact of stratification on upslope flow velocity is not clear. From the definition of the Pi groups in Table 3.2 (page 47) I get

$$U = c \cdot HN \cdot \Pi_2^{m_1} \Pi_3^{m_2} \propto c \cdot N^{1+m_1-3m_2}. \tag{4.51}$$

Notice that the unknown coefficient c may depend on N, for example by being dependent upon $\Pi_{4,w} \equiv \nu_w / H_w^2 N_w$. For the field observations a dependence of c_a on N_a does not seem likely, but the large uncertainties in m_1 and m_2 do not permit any conclusion about the sign of $1+m_1-3m_3$ in (4.51). For the water tank, it is obvious from Figure 4.7 (page 98) that $1+m_1-3m_3<0$, but without specifying the coefficient c_w no conclusion is possible on the dependence of U_w on N_w.

I conclude that weaker stratification implies a deeper TBL, but that it is not clear what impact weaker stratification has on upslope flow velocity. Most likely a deeper TBL dominates over the change in upslope flow velocity, and the net effect is increased re-entrainment of pollutants.

Ridge Height

For lower ridge heights, $G_c \equiv H/h$ is more likely to drop below critical values like 0.90 and 0.66, determined in the previous subsection, which increases trapping. Arguing physically, the ridge height determines the height of elevated layers. Lower ridge heights imply more trapping because the lower the elevated layers the more likely and faster they can be re-entrained by a growing TBL. Therefore, small hills are less likely to vent air pollutants than tall mountains.

The dependence of upslope flow velocity on ridge height can be determined again from Table 3.2 (page 47),

$$U \propto c \cdot H^{1-2m_2}. \tag{4.52}$$

Physical intuition tells us that upslope flow velocity should not increase with decreasing ridge height. This is a constraint on attempts to develop an upslope flow velocity hypothesis. The coefficient c may depend on $\Pi_{10} \equiv z_0/H_w$, $\Pi_4 \equiv \nu/H^2N$, or $\Pi_5 \equiv \kappa/H^2N$. Figure 4.7 (page 98) shows that $m_2 \approx 0.8$ for the water-tank data, so that $U_w \propto H_w^{-0.6}$. For U_w to increase with H_w, it cannot be a function of only the Prandtl number $\Pr_w \equiv \Pi_{4,w}/\Pi_{5,w}$, but must also decrease with $\Pi_{10,w}$, $\Pi_{4,w}$, or $\Pi_{5,w}$. For the atmosphere, c_a probably depends on $\Pi_{10,a}$, but not on $\Pi_{4,a}$ or $\Pi_{5,a}$.

I conclude that the increase of G_c with increasing ridge height increases the chance of re-entrainment of pollutants and, as in the case of stratification, I speculate that this increased chance is only partially offset by faster upslope flow velocities.

Length of Plateau

From the discussion in the previous section on the regime change at $G_c = 0.66$ it seems that this value is independent of the existence of a plateau. In contrast, $G_c = 0.90$ probably depends on the existence of a sufficiently long heated plateau, because it marked the regime change when upslope flow and plain-plateau flow circulation merged. If the plateau is too short it will not generate a plain-plateau flow. Even if Chen et al. (1996) had tested this value they would not have found a regime change, because their tank did not have a plateau. In his honour's thesis research Ian Chan observed a plain-plateau flow circulation in the tank only when the plateau was at least about 9 cm long, approximately 60% of the ridge height.

A sufficiently long plateau carries a substantial fraction of the air pollutants from the upslope flow beyond the ridge top. The longer the plateau the longer it will take for the plain-plateau circulation to return the air pollutant in an elevated layer into the slope region and the greater the chance of disturbances like synoptic flows to remove the elevated layer from the source region.

Sensible Surface Heat Flux Inhomogeneities over the Slope

Sensible surface heat flux inhomogeneities over the slope cause elevated layers at interfaces where the heat flux drops, but only if the variations occur at sufficiently large scales. I suspect that the required minimum length is roughly the same as that required for a plain-plateau flow circulation, i.e. roughly half the ridge height (see above). For example gaps between the strip heaters underneath the tank and variations in power of individual strip heaters do not appear to generate any layering. On the other hand, an early experiment in which the upper four strip heaters ($\sim 15\,cm$ length) did not have sufficient contact with the tank bottom led to a separation of the upslope flow into an elevated layer and a residual upslope flow (Figure 4.18).

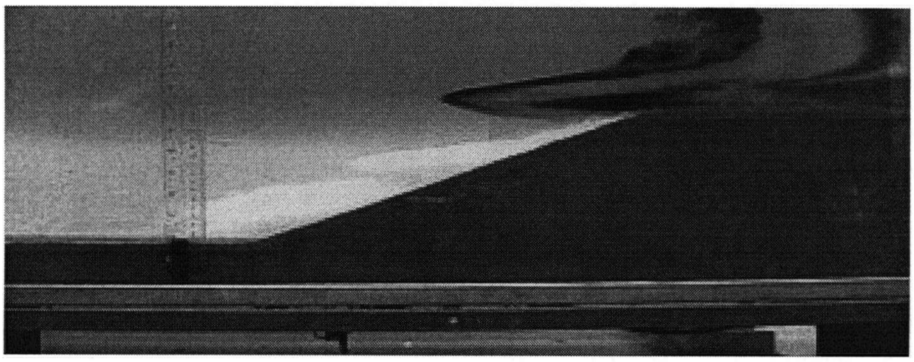

Figure 4.18: Video frame of mass flux break-up over the slope.

Video frame of an early experiment with a substantial surface heat flux increment in the upper third of the slope. At the time of this frame some of the yellow dye, which was originally released at the slope base, had been carried upslope. At about two-third of the total slope length the flow separated into an elevated layer intruding into the plain region and a residual upslope flow layer. I manipulated contrast and gamma value of the image so that the yellow dye stands out more clearly on a grey-scale reproduction of this figure.

Let M_1 denote the mass flux of the upslope flow just below the interface, where the heat flux is $Q_{H,1}$, and M_2 the mass flux of the residual upslope flow after the interface, where the heat flux is $Q_{H,2}$ (Figure 4.19). A first attempt at quantifying the mass-flux break-up is

$$\frac{M_2}{M_1} = \left(\frac{Q_{H,2}}{Q_{H,1}} \right)^a \tag{4.53}$$

where $a > 0$ could be determined from future experiments.

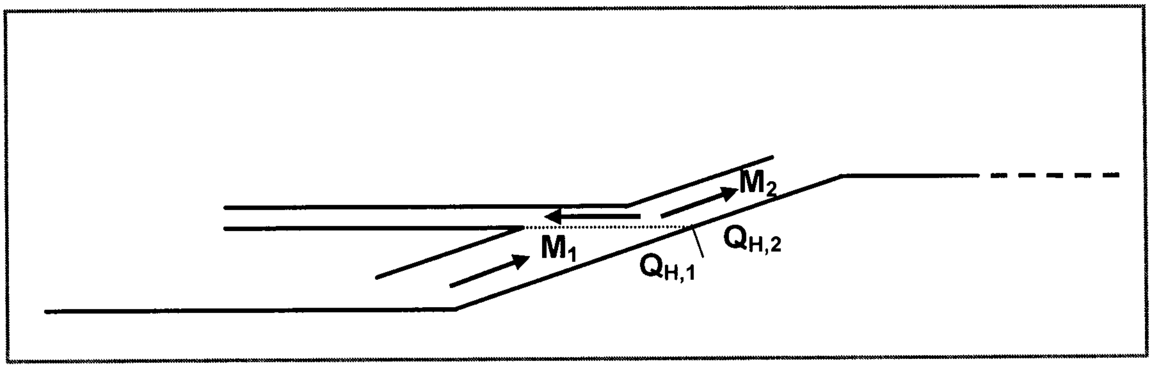

Figure 4.19: Schemata of mass flux break-up caused by a surface heat flux decrement.
Lower and upper surface heat fluxes are denoted by $Q_{H,1}$ and $Q_{H,2}$, respectively. Mass fluxes of upslope flow below the decrement and residual upslope flow above the decrement are denoted by M_1 and M_2.

Abrupt Changes in Slope Angle

Real slopes in the field do not have constant slope angles. Vergeiner (1982) pointed out that a sharp decrease of the slope angle, e.g. above a ledge, can lead to upslope flow separation and elevated layers (Figure 4.20). The phenomenon is analogous to a surface heat flux decrement and can be explained by upslope flow velocity hypotheses that predict a decrease of velocity with decreasing slope angle: mass continuity requires either flow separation above the ledge or a deeper upslope flow. The inertia of the upslope flow at the ledge favours flow separation and is also a likely trigger for thermals, which are preferentially released at ledges (Vergeiner, 1982).

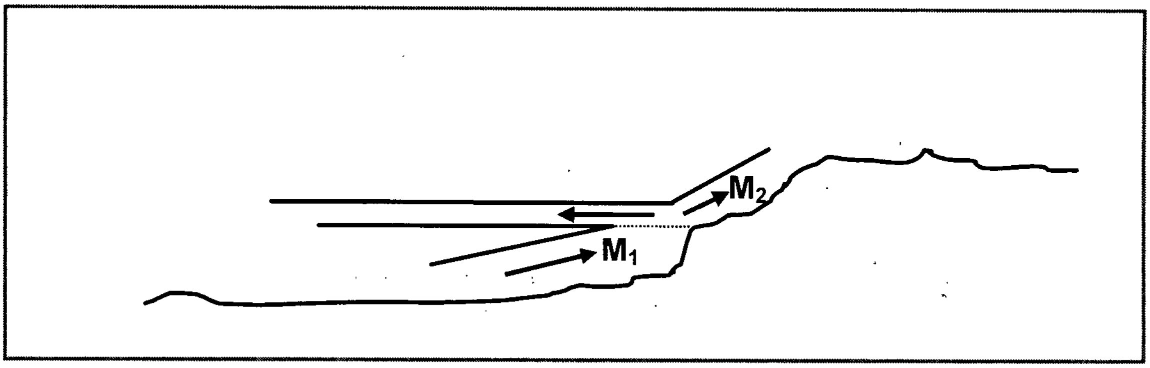

Figure 4.20: Schemata of mass-flux break-up caused by an abrupt slope-angle decrement. Similarly to Figure 4.19, mass fluxes of upslope flow below the ledge and residual upslope flow above the ledge are denoted by M_1 and M_2.

Summary of Conditions Conducive to Air-Pollution Trapping

Although the net effect of some of the atmospheric variations still requires more future research we can be fairly confident that the following conditions favour trapping of air pollution over heated mountain slopes:

- nearly symmetric geometry
- weak larger-scale flows
- weak stratification
- strong sensible surface heat flux
- low ridge height
- short or no plateau
- sensible surface heat flux decrement over a sufficiently large area over the slope
- abrupt slope-angle decrement over a sufficiently large area

This concludes the last main chapter of this dissertation. In the next chapter I summarise the findings of this dissertation, draw overall conclusions, and briefly outline future research questions.

5 Summary of Conclusions and Recommendations for Future Research

In section 4.5 I answered the four main questions, which I posed in section 1.1. Many new questions were raised throughout this dissertation. In this chapter I conclude the main part of this dissertation with a summary of the main conclusions and recommendations for future research.

5.1 Summary of Conclusions

The work in this thesis demonstrates the need to distinguish atmospheric boundary layer (ABL) from thermal boundary layer (TBL) and backscatter boundary layer (BBL). I suggested defining the ABL as the part of the troposphere that exchanges temperature, tracers, or moisture with the earth's surface within one diurnal heating cycle. I defined the TBL as the layer from the surface to the height at which air parcels rising from the heated surface are neutrally buoyant (parcel method). The BBL is the layer from the surface to the height where the backscatter of aerosols has the steepest gradient. Similar definitions of TBL and BBL apply to the water tank.

In our field observations BBL and TBL coincided *3.5 km from the slope*. The water tank experiments supported the hypothesis that BBL and TBL did not coincide *over the slope*. Based on the water-tank observations the field observations can be explained as follows. In an approximately closed upslope flow circulation aerosols were carried from surface sources up the slope and returned in an elevated layer above the TBL. Fairly soon after the beginning of positive surface sensible heat flux the lidar backscatter scans showed one deep BBL of indistinguishable aerosol concentrations in the TBL and in the elevated layer. So clarifying the view expressed in chapter 2, the upslope flow layer, which coincided with the TBL, occupied approximately the lower half and the return flow the upper half of the BBL.

In agreement with previous water-tank studies I observed a persistent eddy with near-surface flows in downslope direction over the plain adjacent to the slope. The eddy was accompanied by a TBL depression over the lower part of the slope, which has previously been observed in the atmosphere and in numerical models. Our vertical profiles of wind velocity at the sodar location in the plain close to the slope base did not show the downslope flow of the eddy but agreed well with the profile expected underneath the TBL depression. In addition, the observation of a return flow within a deep BBL over the sodar location supported my conclusion that this field location was comparable to the lower part of the slope in the water tank.

I argued that the TBL depression in the lower part of the slope was caused by upslope flow advection of dense fluid and that it favours a clockwise eddy rotation over the plain adjacent to the slope. The eddy is independent of the length of the plain and not caused by subsidence at the far end of the plain, which corresponds to the centre of a perfectly symmetric valley of double the length of the plain. On the contrary, in a water-tank experiment with an aspect ratio of about three between valley width and ridge height the eddy caused strongly rising motion at the far end of the plain. This suggests that in the atmosphere for valleys with the right aspect ratio, rising motion may occur over the valley centre. In previous field studies only subsidence was reported over valley centres.

Ian Chan (personal communication) found that for plateau lengths exceeding roughly half the ridge height, a plain-plateau flow circulation developed. During the water-tank experiments I observed two regime changes. In the first regime change, the TBL merged with the elevated layer, and the upslope flow formed one large circulation with the plain-plateau flow. In a second regime change, the TBL merged with a new elevated layer formed by the large circulation. The second regime change seems to agree with a discrete change in the TBL development over the plain far from the slope as observed by Chen et al. (1996).

The regime changes in our field observations did not agree with the tank observations. I attributed the discrepancy to an additional governing parameter and the upslope flow circulation being faster in the atmosphere than the water tank. In previous investigations water tanks were designed to reproduce typical atmospheric values. I carried out a detailed scaling analysis by developing mathematical idealisations of the water tank and the field site and tried to achieve similarity between these idealisations. Field and tank observations of non-dimensional (ND) TBL depth agreed within the uncertainty of the field data (20%). Mean specific volume increments in the water tank, however, showed an unexpected linear dependence on time. Furthermore, applying probability theory to the field and water-tank data I demonstrated that ND upslope flow velocities in atmosphere and water tank have significantly different functional dependencies on the governing parameters.

I showed that the tank flows are fluid-dynamically smooth and explained the similarity violation of upslope flow velocity by an fluid-dynamic feedback: in the smooth tank flows, roughness length strongly decreased with increasing upslope flow velocity; by contrast, atmospheric flows were fluid-dynamically rough and the roughness length was approximately independent of upslope flow velocity. Dye experiments indicate that the plain-plateau flow circulation acts as a lid over the upslope flow circulation. This property can explain the linear time dependence of the TBL mean specific volume increment and also supports a tentative upslope flow hypothesis based on the idea of a gravity-current flow into a region of decreasing fluid depth.

In many cases upslope flows in the atmosphere are modified by several external disturbances and exhibit regime changes at multiple scales. Nevertheless, the water tank experiments provide some insight how variations of external conditions affect the transport of air pollutants. I argued that conditions, which likely support the re-entrainment of air pollutants, are symmetric topography, weak stratification and larger-scale flows, strong sensible surface heat flux, low ridge height, short plateau, sensible surface heat flux decrements over the slope, and abrupt slope-angle decrements.

5.2 Recommendations for Future Research

I separate my recommendations for future research according to the schematics of my research approach (Figure 1.4, page 10) into field work, analytical studies, water-tank modeling, and numerical modeling.

Field Work

Of the four methods of scientific investigation used in atmospheric science, field studies require the most effort. However, two research questions that arise from the work in this dissertation can potentially be answered by re-visiting existing data sets. Can we find observational evidence in field data for the existence of the clockwise-rotating eddy? The strongest evidence would be the discovery of the flow in downslope direction over the plain near the slope. Such "downslope" flows during daytime heating would be unexpected from a simple upslope flow model without the eddy. The second question is closely related to the first one: Are there any field observations of strongly rising motion over a valley centre? And if so, does the aspect ratio of valley width to ridge height agree with the value three in the water tank experiments?

Analytical Studies

In the scaling in chapter 3 I made a number of simplifying assumptions. For future research I would recommend trying to improve the scaling by replacing the encroachment model with an entrainment model. Furthermore, subsidence and advection are caused internally by the upslope flow circulation: their inclusion may improve the scaling. Finally, the discussion on the similarity violation of upslope flows (section 4.3.4) suggests that roughness length should be included in the scaling as a governing parameter.

Much further research is required to develop an upslope flow hypothesis, which meets the accuracy requirements I posed and can explain the similarity violation between atmosphere and water tank. Two tentative approaches were presented in section 4.3.4. These need to be studied further. Another promising approach may be to adapt radix layer theory to upslope flows, which has the advantage that it requires less matching at layer interfaces than the approach in Hunt et al. (2003). Further analyses of field and water-tank data using probability theory may provide some guidance in the search for an upslope flow hypothesis.

In Appendix B.6 I study the role of conventional ND governing parameters and conclude that there are exactly five independent parameters, for example Ra, $\Pr$, Fr_i, Re, and Re_{Adrian}, in agreement with Π_1 to Π_5 being independent. The required independence of these five parameters puts constraints on the upslope flow hypothesis that may not be as obvious with the set of Pi groups Π_1 to Π_5. However, to explore this further it is necessary to test in particular the dependence of the maximum upslope flow velocity on the aspect ratio Π_1, for example by building other water tanks with different slope angles.

Water-Tank Modeling

In the atmospheric idealisation I assumed a heated plateau. The field data for July 25 and 26 do not provide enough evidence that this was a good assumption. I recommend for future research to compare the field data with alternative configurations in the water tank, in particular a triangular ridge and a weakly heated plateau.

Because of the multiple benefits I strongly recommend carrying out additional water-tank experiments over a wider range of parameter values and for different plain and plateau lengths. These would permit further investigation of critical parameter values for flow regime changes. They would provide invaluable data for developing an upslope flow hypothesis that can explain the similarity violation. Moreover, these would help clarify the dependence of air-pollution re-entrainment on background stratification, sensible surface heat flux, and ridge height. Finally, more data may help to answer the open questions: Do upslope flows generate shear turbulence in addition to convective turbulence generated by the surface heating? If so, what is the critical Reynolds number? And what is the impact of this additional shear turbulence?

Numerical Modeling

Numerical experiments have more flexibility than field and tank studies. It is for example much easier to test the dependence of upslope flow velocity on the slope angle with a numerical model than a water-tank model. Furthermore, numerical experiments permit access to a wealth of parameters, including the terms in the governing equations, and are therefore an important complement to the other methods of investigation.

Some of the flow details in the water tank occurred at length scales corresponding to several hundred metres in the atmosphere. Meso-scale models are unlikely to capture these details correctly. Large-eddy simulations (LES) with their better spatial resolution are a promising alternative. A challenge will be to adapt existing one-dimensional LES to more realistic two-dimensional topography to reproduce for example the CW rotating eddy over the plain and the adjacent TBL depression over the lower part of the slope. Ideally one would also apply LES to the water tank experiments. LES experiments that can reproduce the similarity violation of upslope flow velocity could provide important data for developing an upslope flow velocity hypothesis that reconciles field with tank observations.

References

Adrian, R. J., Ferreira, R. T. D. S., and Boberg, T., 1986: "Turbulent thermal convection in wide horizontal fluid layers", Experim. in Fluids, 4, 121-141.

Alonso, M., and Finn, E. J., 1980: "Fundamental University Physics, Vol. 1, Mechanics and Thermodynamics", 2nd edition, Addison-Wesley Publishing Company, U.S.A., 538pp.

Atkinson, B. W., 1981: "Meso-scale Atmospheric Circulations", Academic Press, London, U.K., 495pp.

Banta, R. M., 1984: "Daytime boundary layer evolution over mountainous terrain. Part 1: Observations of the dry circulations", Monthly Weather Review, 112(2), 340-356.

Barenblatt, G. I., 2003: "Scaling", Cambridge University Press, Cambridge, U.K., 171pp.

Bastin, S., and Drobinski, P., preprint: "Temperature and wind velocity oscillations along a gentle slope during sea-breeze events", submitted for publication in Bound.-Layer Meteorol.

Blumen, W. (ed.), 1990: "Atmospheric Processes Over Complex Terrain", AMS, Boston, Meteorol. Monogr., 23(45), 323pp.

Brauer, M., and Brook, J. R., 1997: "Ozone personal exposures and health effects for selected groups residing in the Fraser Valley", Atmos. Environ., 31(14), 2113-2121.

Brehm, M., 1986: "Experimentelle und numerische Untersuchungen der Hangwindschicht und ihre Rolle bei der Erwärmung von Tälern". Ph.D. dissertation, Ludwig-Maximilian-Universität München, Germany, 150pp.

Buckingham, E., 1914: "On physically similar systems; illustrations of the use of dimensional equations", Phys. Rev. Lett., Second Series, IV(4), 345-376.

Carson, D. J., 1973: "The development of a dry inversion-capped convectively unstable boundary layer", Quart. J. R. Meteorol. Soc., 99, 450-467.

Chen, R.-R., Berman, N. S., Boyer, D. L., and Fernando, H. J. S., 1996: "Physical model of diurnal heating in the vicinity of a two-dimensional ridge", J. Atmos. Sci., 53(1), 62-85.

Davidson, B., 1963: "Some turbulence and wind variability observations in the lee of mountain ridges", J. Appl. Meteorol., 2, 463-472.

Deardorff, J. W. and Willis, G. E., 1987, "Turbulence within a baroclinic laboratory mixed layer above a sloping surface", J. Atmos. Sci., 44(4), 772-778.

Defant, F., 1949: "Zur Theorie der Hangwinde, nebst Bemerkungen zur Theorie der Berg- und Talwinde", Arch. Met. Geoph. Biokl., Ser. A, 1, 421-450, and in: Whiteman, C. D., and Dreiseitl, E. (1984).

de Wekker, S. F. J., 1997: "The Behaviour of the Convective Boundary Layer Height over Orographically Complex Terrain", Master Thesis, Universität Karlsruhe, Germany, and Wageningen Agricultural University, The Netherlands, 295 pp.

de Wekker, S. F. J., 2002: "Structure and Morphology of the Convective Boundary Layer in Mountainous Terrain", Ph.D. Dissertation, The University of British Columbia, Canada, 191pp.

Egger, J., 1981: "On the linear two-dimensional theory of thermally induced slope winds", Beitr. Phys. freien Atmos., 54, 465-481.

Fortuin, J., 1960: "Theory and application of two supplementary methods of constructing density gradient columns", Journal of Polymer Science, XLIV, 505-515.

Garratt, J. R., 1994: "The Atmospheric Boundary Layer", 1st paperback edition, Cambridge University Press, Melbourne, Australia, 316pp.

Glickman, T. S. (ed.), 2000: "AMS Glossary of Meteorology", CD, 2nd edition, Boston, U.S.A.

Gobrecht, H. (ed.), 1974: "Bergmann-Schaefer, Lehrbuch der Experimentalphysik, Band 1: Mechanik, Akustik, Wärme", 9th edition, Walter de Gruyter, Berlin, Germany, 850pp.

Gregory, P., 2005: "Bayesian Logical Data Analysis for the Physical Sciences", Cambridge University Press, U.K., 488 pp.

Haiden, T., 1990: "Analytische Untersuchungen zur konvektiven Grenzschicht im Gebirge", Ph.D. Dissertation, Universität Wien, Austria, 140pp.

Haiden, T., 2003: "On the pressure field in the slope wind layer", J. Atmos. Sci., 60, 1632-1635.

Hill, D. F., 2002: "General density gradients in general domains: the 'two-tank' method revisited", Experim. in Fluids, 32(4), 434-440.

Hunt, J. C. R., Fernando, H. J. S., and Princevac, M., 2003: "Unsteady thermally driven flows on gentle slopes", J. Atmos. Sci., 60, 2169-2182.

Ingel', L. K., 2000: "Nonlinear theory of slope flows", Izvestiya Atmospheric and Oceanic Physics, 36(3), 384-389.

Jaynes, E. T., (edited by Bretthorst, G. L.), 2003: "Probability Theory. The Logic of Science", Cambridge University Press, U.K., 727pp.

Jelinek, A., 1937: "Beiträge zur Mechanik der periodischen Hangwinde", Beitr. Phys. freien Atmos., 24, 60-84.

Kim, Sunkyoung Annie, 2001: "Discharge of Buoyant Fluid Jets and Particle-laden Jets into Stratified Ambient Fluid", Ph.D. Dissertation, The University of British Columbia, Canada.

Kondo, H., 1984: "The difference of the slope wind between day and night", J. Meteorol. Soc. Japan, 62(2), 224-232.

Koßmann, M., and Fiedler, F., 2000, "Diurnal momentum budget analysis of thermally induced slope winds", Meteorol. Atmos. Phys. 75, 195-215.

Kuchling, H., 1979: "Physik, Formeln und Gesetze", 16th edition, VEB Fachbuchverlag Leibzig, 407pp.

Kuwagata, T., and Kondo, J., 1989: "Observations and modeling of thermally induced upslope flow", Bound.-Layer Meteorol., 49, 265-293.

Li, S.-M., 2004: "A concerted effort to understand the ambient particulate matter in the Lower Fraser Valley: The Pacific 2001 Air Quality Study", Atmos. Environ., 38, 5719-5731.

Lilly, D. K., 1968: "Models of cloud-topped mixed layers under a strong inversion", Quart. J. R. Meteorol. Soc., 94, 292-309.

Mahrt, L., 1982: "Momentum balance of gravity flows", J. Atmos. Sci., 39, 2701-2711.

Mendonca, B., 1969: "Local wind circulation on the slopes of Mauna Loa", J. Appl. Meteorol., 8, 533-541.

Mitsumoto, S., 1989: "A laboratory experiment on the slope wind", J. Meteorol. Soc. Japan, 67 (4), 565-574.

Moody, E. G., King, M. D., Platnick, S., Schaaf, C. B., and Gao, F., 2005: "Spatially complete global surface albedos: Value-added datasets derived from Terra MODIS land products", IEEE Trans. Geosci. Remote Sens., 43, 144-158.

Neff, W. D., 1990, "Remote sensing of atmospheric processes over complex terrain", in: Blumen, W., 173-228.

Orville, H. D., 1964: "On mountain upslope winds", J. Atmos. Sci., 21, 622-633.

Patel, V. C., and Head, M. R., 1969: "Some observations on skin friction and velocity profiles in fully developed pipe and channel flows", J. Fluid Mech., 38(1), 181-201.

Petkovšek, Z., 1982: "Ein einfaches Modell des Tages-Hangwindes", Zeitschrift f. Meteorologie, 32, 31-41.

Plate, E. J., 1998: "Convective boundary layer: a historical introduction", pages 1-22, in: Plate, E. J., et al. (ed.), "Buoyant Convection in Geophysical Flows", Kluwer Acad. Publ., Dordrecht, The Netherlands, 504pp.

PME, 1997: "MicroScale Conductivity Temperature Instrument, Model 125, Operators Manual (Rev. 1, 01-AUG-97)".

Prandtl, L., 1942: "Führer durch die Strömungslehre", Vieweg, Braunschweig, Germany. *English:* 1952: "Essentials of Fluid Dynamics", Blackie, London, U.K., 452pp.

Reuten, C., Steyn, D. G., Strawbridge, K. B., and Bovis, P., 2002a: "The relation between slope flow systems and convective boundary layers in steep terrain", 10th Conf. on Mount. Meteor., 17-21 June 2002, Park City, Utah, AMS, Boston, Massachusetts, 22-25.

Reuten, C., Steyn, D. G., Strawbridge, K. B., and Bovis, P., 2002b: "Air pollutants trapped in slope flow systems", Bull. Amer. Meteor. Soc., 83, 966.

Reuten, C., Steyn, D. G., Strawbridge, K. B., and Bovis, P., 2005: "Observations of the relation between upslope flows and the convective boundary layer in steep terrain", Bound.-Layer Meteorol., 116(1), 37-61.

Riley, K. F., Hobson, M. P., and Bence, S. J., 2002: "Mathematical Methods for Physics and Engineering", 2nd edition, Cambridge University Press, U.K., 1232pp.

Santoso, E., and Stull, R., 1998: "Wind and temperature profiles in the radix layer: the bottom fifth of the convective boundary layer", J. Atmos. Sci., 37, 545-558.

Santoso, E., and Stull, R., 2001: "Similarity equations for wind and temperature profiles in the radix layer, at the bottom the convective boundary layer", J. Atmos. Sci., 58, 1446-1464.

Schumann, U., 1990: "Large-eddy simulation of the upslope boundary layer", Quart. J. R. Meteorol. Soc., 116, 637-670.

Segal, M., Y. Ookouchi, and R. A. Pielke, 1987: "On the effect of steep slope orientation on the intensity of daytime upslope flow", J. Atmos. Sci., 44(23), 3587-3592.

Selkirk, 2004a: "SRS 6929:130", April 2, 2004. Scale 1:20,000. Selkirk Remote Sensing Ltd., Richmond, BC, Canada.

Selkirk, 2004b: "SRS 6929:83", April 2, 2004. Scale 1:20,000. Selkirk Remote Sensing Ltd., Richmond, BC, Canada.

Serway, R. A., and Beichner, R. J., 2000: "Physics for Scientists and Engineers", 5th edition, Saunders College Publishing, Orlando, U.S.A., 1288pp.

Simpson, J. E., 1997: Gravity Currents in the Environment and the Laboratory", 2nd edition, Cambridge University Press, Cambridge, U.K., 244pp.

Sivia, D. S., 1996: "Data Analysis. A Bayesian Tutorial", Oxford University Press, U.K., 189pp.

Snyder, W. H., Lawson, R. E. Jr., Shipman, M. S., and Lu, J., 2002: "Fluid modelling of atmospheric dispersion in the convective boundary layer", Bound.-Layer Meteorol., 102, 335-366.

Steyn, D. G., and Faulkner, D. A., 1986: "The climatology of sea-breezes in the Lower Fraser Valley, B.C.", Climatol. Bull., 20, 21-39.

Steyn, D. G., Bottenheim, J. W., and Thomson, R.B., 1997: "Overview of tropospheric ozone in the Lower Fraser Valley, and the Pacific '93 field study", Atmos. Environ., 31(14), 2025-2035

Steyn, D. G., 1998: "Scaling the vertical structure of sea breezes", Bound.-Layer Meteorol., 86, 505-524.

Steyn, D. G., 2003: "Scaling the vertical structure of sea breezes revisited", Bound.-Layer Meteorol., 107, 177-188.

Strawbridge, K. B., and Snyder, B. J., 2004: "Planetary boundary layer height determination during Pacific 2001 using the advantage of a scanning lidar instrument", Atmos. Environ., 38, 5861-5871.

Stull, R. B., 1988: "An Introduction to Boundary Layer Meteorology", Kluwer Acad. Publ., Dordrecht, The Netherlands, 666pp.

Stull, R. B., 2000: "Meteorology for Scientists and Engineers", 2nd edition, Brooks/Cole, Pacific Grove, U.S.A., 502pp.

Tolman, R. C., 1914: "The principle of similitude", Phys. Rev. Lett., Second Series, III(4), 244-255.

Turner, J. S., 1973: "Buoyancy Effects in Fluids", Cambridge University Press, Cambridge, U.K., 368pp.

van Dop, H., van As, D., van Herwijnen, A., Hibberd, M. F., and Jonker, H., 2005: "Length scales of scalar diffusion in the convective boundary layer: laboratory observations", Bound.-Layer Meteorol., 116(1), 1-35.

Vergeiner, I., 1982: "Eine energetische Theorie der Hangwinde", 17. Int. Tag. Alpine Meteorol., Berchtesgaden 1982. Ann. Meteorol. NF 19, 189-191.

Vergeiner, I., 1991: "Comments on 'Large-eddy simulation of the up-slope boundary layer' by Ulrich Schumann (April 1990, 116, 637-670)", Quart. J. R. Meteorol. Soc., 117, 1371-1372.

Vergeiner, I., and Dreiseitl, E., 1987: "Valley winds and slope winds – observations and elementary thoughts", Meteorol. Atmos. Phys., 36, 264-286.

Vogel, B., Adrian, G., and Fiedler, F., 1987: "MESOKLIP - Analysen der Meteorologischen Beobachtungen von Mesoskaligen Phänomenen im Oberrheingraben", Inst. für Meteorologie & Klimaforschung der Univ. Karlsruhe, Germany, 369 pp.

Weast R. C. (ed.), 1978-79: "CRC Handbook of Chemistry and Physics", 59th edition, CRC Press, Boca Raton, U.S.A., approximately 2400pp.

Wenger, R., 1923: "Zur Theorie der Berg- und Talwinde", Meteorol. Zeits., 40, 193-204.

Whiteman, C. D., 1990: "Observations of thermally developed wind systems in mountainous terrain", 5-42, in: Blumen, W. (ed.): "Atmospheric Processes Over Complex Terrain", AMS, Boston, Meteorol. Monogr., 23(45), 323pp.

Whiteman, C. D., 2000: "Mountain Meteorology. Fundamentals and Applications", Oxford University Press, New York, 376pp.

Whiteman, C. D., and Dreiseitl, E., 1984: "Alpine Meteorology. Translations of Classic Contributions by A. Wagner, E. Ekhart and F. Defant", PNL-5141 / ASCOT-84-3, Pacific Northwest Laboratory, Richland, Washington, 121pp.

Willis, G. E., and Deardorff, J. W., 1975: "Laboratory simulation of the convective planetary boundary layer", Atmos. Tech., 7, 80-86.

Wooldridge, G. L., and McIntyre, E. L., 1986: "The dynamics of the planetary boundary layer over a heated mountain slope", Geofizika, 3, 3-21.

Ye, Z. J., Segal, M., and Pielke, R. A., 1987: "Effects of atmospheric thermal stability and slope steepness on the development of daytime thermally induced upslope flow", J. Atmos. Sci., 44, 3341-3354.

Appendix A: Rigorous Derivation of the Prandtl Model

In 1942, Prandtl developed, with intuitive arguments, and solved analytically a one-dimensional model of slope flows. A rigorous derivation of the Prandtl model from a general form of the Navier-Stokes and heat equations, however, was never published. The reason for this negligence is unlikely to be simplicity or irrelevance of the derivation. It is still being debated if the Prandtl model contains a pressure gradient term (Hayden, 2003), which clearly shows that the derivation is neither trivial nor unimportant. Investigators often developed more complex models as an extension of the Prandtl model, without knowing which terms of the Navier-Stokes equations are maintained in the Prandtl model. In this appendix I will fill the gap.

Momentum Equations

Starting point for the momentum equations is Newton's Second Law applied to a rotating fluid (Stull, 1988)

$$\frac{\partial U_i}{\partial t} + U_j \frac{\partial U_i}{\partial x_j} = -\delta_{i3} g - 2\varepsilon_{ijk}\Omega_j U_k - \frac{1}{\rho}\frac{\partial P}{\partial x_i} + \frac{1}{\rho}\frac{\partial \tau_{ij}}{\partial x_j} \tag{A.1}$$

where I made use of the Einstein summation convention, i.e. in each term equal indices are a shorthand notation for summation over this index. Furthermore, indices 1, 2, and 3 stand for the x, y, and z components, for example $(x_1, x_2, x_3) = (x, y, z)$ and $(U_1, U_2, U_3) = (U, V, W)$. The terms in (A.1) are from left to right: inertia or time change, advection, gravity, Coriolis, pressure-gradient, and viscous stress.

Assuming a Newtonian fluid, homogeneity of viscosity, and incompressibility, the viscous stress term simplifies to

$$\frac{1}{\rho}\frac{\partial \tau_{ij}}{\partial x_j} = \nu \frac{\partial^2 U_i}{\partial x_j^{\,2}} \tag{A.2}$$

where $\nu = \mu/\rho$ is the kinematic viscosity. Furthermore, Prandtl neglected the Coriolis force,

$$2\varepsilon_{ijk}\Omega_j U_k \approx 0 \tag{A.3}$$

for $i = 1,2,3$. After applying these changes and multiplying (A.1) by ρ we get

$$\rho\frac{\partial U_i}{\partial t} + \rho U_j\frac{\partial U_i}{\partial x_j} = -\delta_{i3}\rho g - \frac{\partial P}{\partial x_i} + \rho\nu\frac{\partial^2 U_i}{\partial x_j{}^2} \tag{A.4}$$

Prandtl assumed no mean background wind and prescribed a stationary perturbation of the background potential temperature so that the instantaneous quantities can be separated as

$$U_i = \Delta U_i + u_i' \tag{A.5}$$

$$\rho = \rho_0 + \Delta\rho + \rho' \tag{A.6}$$

$$P = P_0 + \Delta P + p' \tag{A.7}$$

where subscript 0 denotes mean background values, prefix Δ denotes the mean perturbation of the background state due to the prescribed surface heating, and primed quantities are turbulent perturbations. The turbulent perturbations are 0 when Reynolds averaged. Substituting (A.5) to (A.7) into (A.4) gives

$$\begin{aligned}&\left(\rho_0 + \Delta\rho + \rho'\right)\frac{\partial\left(\Delta U_i + u_i'\right)}{\partial t} + \left(\rho_0 + \Delta\rho + \rho'\right)\left(\Delta U_i + u_i'\right)\frac{\partial\left(\Delta U_i + u_i'\right)_i}{\partial x_j} = \\ &-\delta_{i3}\left(\rho_0 + \Delta\rho + \rho'\right)g - \frac{\partial\left(P_0 + \Delta P + p'\right)}{\partial x_i} + \left(\rho_0 + \Delta\rho + \rho'\right)\nu\frac{\partial^2\left(\Delta U_i + u_i'\right)}{\partial x_j{}^2}\end{aligned} \tag{A.8}$$

Multiplying out some of the parentheses and reordering terms,

$$\begin{aligned}&\left(\rho_0 + \Delta\rho + \rho'\right)\frac{\partial\left(\Delta U_i + u_i'\right)}{\partial t} + \left(\rho_0 + \Delta\rho + \rho'\right)\left(\Delta U_i + u_i'\right)\frac{\partial\left(\Delta U_i + u_i'\right)_i}{\partial x_j} = \\ &-\delta_{i3}\rho_0 g - \frac{\partial P_0}{\partial x_i} - \delta_{i3}\left(\Delta\rho + \rho'\right)g - \frac{\partial\left(\Delta P + p'\right)}{\partial x_i} + \left(\rho_0 + \Delta\rho + \rho'\right)\nu\frac{\partial^2\left(\Delta U_i + u_i'\right)}{\partial x_j{}^2}\end{aligned} \tag{A.9}$$

and noting that the background state is in hydrostatic equilibrium, i.e. $-\rho_0 g - \frac{\partial P_0}{\partial z} = 0$, and has no horizontal pressure gradient, $\frac{\partial P_0}{\partial x} = \frac{\partial P_0}{\partial y} = 0$, the equation becomes

$$\begin{aligned}
&\left(\rho_0 + \Delta\rho + \rho'\right)\frac{\partial\left(\Delta U_i + u_i'\right)}{\partial t} + \left(\rho_0 + \Delta\rho + \rho'\right)\left(\Delta U_i + u_i'\right)\frac{\partial\left(\Delta U_i + u_i'\right)_i}{\partial x_j} = \\
&-\delta_{i3}\left(\Delta\rho + \rho'\right)g - \frac{\partial\left(\Delta P + p'\right)}{\partial x_i} + \left(\rho_0 + \Delta\rho + \rho'\right)\nu\frac{\partial^2\left(\Delta U_i + u_i'\right)}{\partial x_j^{\,2}}
\end{aligned} \tag{A.10}$$

At this point we apply the Boussinesq approximation, noting that $\Delta\rho$ and ρ' are small compared to ρ_0,

$$\begin{aligned}
&\rho_0\frac{\partial\left(\Delta U_i + u_i'\right)}{\partial t} + \rho_0\left(\Delta U_j + u_j'\right)\frac{\partial\left(\Delta U_i + u_i'\right)_i}{\partial x_j} = \\
&-\delta_{i3}\left(\Delta\rho + \rho'\right)g - \frac{\partial\left(\Delta P + p'\right)}{\partial x_i} + \rho_0\nu\frac{\partial^2\left(\Delta U_i + u_i'\right)}{\partial x_j^{\,2}}
\end{aligned} \tag{A.11}$$

We now divide the equation by ρ_0 and take the Reynolds average, skipping the detailed steps of the common procedure, but being aware that quantities with prefix Δ are mean perturbations,

$$\frac{\partial\Delta U_i}{\partial t} + \Delta U_j\frac{\partial\Delta U_i}{\partial x_j} + \overline{u_j'\frac{\partial u_i'}{\partial x_j}} = -\delta_{i3}\frac{\Delta\rho}{\rho_0}g - \frac{1}{\rho_0}\frac{\partial\Delta P}{\partial x_i} + \nu\frac{\partial^2\Delta U_i}{\partial x_j^{\,2}}. \tag{A.12}$$

With the assumption of incompressibility the continuity equation is

$$\frac{\partial U_j}{\partial x_j} = 0 \text{ and } \frac{\partial\Delta U_j}{\partial x_j} = 0 \tag{A.13}$$

which implies

$$\frac{\partial u_j'}{\partial x_j} = 0. \tag{A.14}$$

Applying the latter equation and the product rule of calculus to the third term in (A.12) and bringing the term to the right-hand side, (A.12) becomes.

$$\frac{\partial \Delta U_i}{\partial t} + \Delta U_j \frac{\partial \Delta U_i}{\partial x_j} = -\delta_{i3} \frac{\Delta\rho}{\rho_0} g - \frac{1}{\rho_0} \frac{\partial \Delta P}{\partial x_i} - \frac{\partial \overline{u_i' u_j'}}{\partial x_j} + \nu \frac{\partial^2 \Delta U_i}{\partial x_j^{\ 2}}. \tag{A.15}$$

In the atmosphere, molecular viscosity (last term) is negligible except for the bottom few centimetres above the Earth's surface. The resulting equation,

$$\frac{\partial \Delta U_i}{\partial t} + \Delta U_j \frac{\partial \Delta U_i}{\partial x_j} = -\delta_{i3} \frac{\Delta\rho}{\rho_0} g - \frac{1}{\rho_0} \frac{\partial \Delta P}{\partial x_i} - \frac{\partial \overline{u_i' u_j'}}{\partial x_j} \tag{A.16}$$

is applicable to a wide variety of atmospheric situations where the Earth's rotation is negligible. The following assumptions are particular to slope flows and Prandtl's model.

Assuming that the flow is stationary,

$$\frac{\partial \Delta U_i}{\partial t} = 0. \tag{A.17}$$

The last term in (A.16) is approximated by a K-theory approach,

$$\overline{u_j' u_i'} = -K_m \frac{\partial \Delta U_i}{\partial x_j}, \tag{A.18}$$

and further assuming that the eddy viscosity $K_m = const.$,

$$\frac{\partial \left(\overline{u_j' u_i'} \right)}{\partial x_j} = -K_m \frac{\partial^2 \Delta U_i}{\partial x_j^{\ 2}}. \tag{A.19}$$

Note that the K-theory approach, even more so with constant eddy viscosity and for the daytime case, is a bad assumption (Stull, 1988).

With this the equations of motion in vector notation are

$$\begin{aligned} &\Delta U_j \frac{\partial}{\partial x_j} (\Delta U, \Delta V, \Delta W) = \\ &-\frac{\Delta\rho}{\rho_0} g(0,0,1) - \frac{1}{\rho_0} \left(\frac{\partial}{\partial x}, \frac{\partial}{\partial y}, \frac{\partial}{\partial z} \right) \Delta P + K_m \frac{\partial^2}{\partial x_j^{\ 2}} (\Delta U, \Delta V, \Delta W). \end{aligned} \tag{A.20}$$

Prandtl assumed an infinitely long and infinitely wide homogeneous slope with constant slope angle α. This suggests rotating the coordinate system by an angle α about the y-coordinate. The transformation matrix is

$$\begin{pmatrix} \cos\alpha & 0 & \sin\alpha \\ 0 & 1 & 0 \\ -\sin\alpha & 0 & \cos\alpha \end{pmatrix}. \tag{A.21}$$

The metric terms are 1 and the transformations are

$$(x, y, z) \to (s, y, n) \tag{A.22}$$

$$\left(\frac{\partial}{\partial x}, \frac{\partial}{\partial y}, \frac{\partial}{\partial z}\right) \to \left(\frac{\partial}{\partial s}, \frac{\partial}{\partial y}, \frac{\partial}{\partial n}\right) \tag{A.23}$$

$$\left(\frac{\partial^2}{\partial x^2}, \frac{\partial^2}{\partial y^2}, \frac{\partial^2}{\partial z^2}\right) \to \left(\frac{\partial^2}{\partial s^2}, \frac{\partial^2}{\partial y^2}, \frac{\partial^2}{\partial n^2}\right) \tag{A.24}$$

$$(\Delta U, \Delta V, \Delta W) \to (U_s, \Delta V, W_n) \tag{A.25}$$

$$(0,0,1) \to (\sin\alpha, 0, \cos\alpha) \tag{A.26}$$

where s, n are the along-slope and slope-normal components of location and likewise U_s, W_n the respective components of wind velocity. With this coordinate transformation, (A.20) becomes

$$\begin{aligned} &\left(U_s \frac{\partial}{\partial s} + \Delta V \frac{\partial}{\partial y} + W_n \frac{\partial}{\partial n}\right)(U_s, \Delta V, W_n) = \\ &-\frac{\Delta\rho}{\rho_0} g(\sin\alpha, 0, \cos\alpha) - \frac{1}{\rho_0}\left(\frac{\partial}{\partial s}, \frac{\partial}{\partial y}, \frac{\partial}{\partial n}\right)\Delta P + K_m\left(\frac{\partial^2}{\partial s^2} + \frac{\partial^2}{\partial y^2} + \frac{\partial^2}{\partial n^2}\right)(U_s, \Delta V, W_n) \end{aligned} \tag{A.27}$$

In the Prandtl model there are no cross-slope flows and no variations in the y-direction, so $\Delta V = 0$ and symbolically $\frac{\partial}{\partial y} = 0$ and $\frac{\partial^2}{\partial y^2} = 0$, so for the second component in (A.27) both sides of the equation are identically 0. Furthermore, the assumption of an infinitely long homogeneous slope implies that there are no along-slope variations, symbolically $\frac{\partial}{\partial s} = 0$ and

$\frac{\partial^2}{\partial s^2} = 0$; together with mass continuity this also means that there can be no flow normal to the surface, $W_n = 0$. Equation (A.27) then reduces to the following two equations:

$$0 = -\frac{\Delta\rho}{\rho_0} g \sin\alpha + K_m \frac{\partial^2 U_s}{\partial n^2} \tag{A.28}$$

and

$$0 = -\frac{\Delta\rho}{\rho_0} g \cos\alpha - \frac{1}{\rho_0}\frac{\partial \Delta P}{\partial n}. \tag{A.29}$$

In the last equation, the first term on the RHS is the component of reduced gravity in the slope-normal direction. The second term is the gradient of the perturbation pressure field in the slope-normal direction. So (A.29) represents a kind of hydrostatic balance of the perturbation pressure field in the slope-normal direction, called quasi-hydrostatic balance by Mahrt (1982). It is important to notice that quasi-hydrostatic is different from vertically hydrostatic and that the assumption of the latter will lead to errors (Hayden, 2003).

Using the ideal gas law and assuming dry conditions, it is straightforward to show (Stull, 2000) that

$$-\frac{\Delta\rho}{\rho_0} \approx \frac{\Delta\theta}{T_0}. \tag{A.30}$$

Substitution of (A.30) into (A.28) recovers Prandtl's momentum equation

$$0 = g\sin\alpha \cdot \frac{\Delta\theta}{T_0} + K_m \frac{\partial^2 U_s}{\partial n^2}. \tag{A.31}$$

if $\frac{1}{T_0}$ is identified with the coefficient of thermal expansion.

Heat Budget Equation

Next I derive the heat budget equation for the Prandtl model. Starting point is the First Law of Thermodynamics (Stull, 1988):

$$\frac{\partial \theta}{\partial t}+U_j\frac{\partial \theta}{\partial x_j}=\nu_\theta\frac{\partial^2\theta}{\partial {x_j}^2}-\frac{1}{\rho C_p}\frac{\partial \widetilde{Q}^*_j}{\partial x_j}-\frac{L_p E}{\rho C_p}, \tag{A.32}$$

where C_p is the specific heat of dry air at constant pressure, $\widetilde{Q}^*_j$ is the j-component of net radiation, L_p is the latent heat associated with a phase change expressed by E, the mass of water vapour per unit volume and unit time created by a phase change from water or ice to water vapour. The five terms in (A.32) from left to right are storage, advection, molecular diffusion, radiation divergence, and latent heat.

The Prandtl model neglects net radiation and latent heat, so the last two terms can be neglected immediately. I apply the following decompositions

$$U_j=\Delta U_j+u_j' \tag{A.33}$$

$$\theta=\theta_0+\Delta\theta+\theta', \tag{A.34}$$

where again subscript 0 denotes the mean background values, prefix Δ denotes the mean perturbation of the background state due to the prescribed surface heating, and primed quantities are turbulent perturbations. Equation (A.32) becomes

$$\frac{\partial(\theta_0+\Delta\theta+\theta')}{\partial t}+\left(\Delta U_j+u_j'\right)\frac{\partial(\theta_0+\Delta\theta+\theta')}{\partial x_j}=\nu_\theta\frac{\partial^2(\theta_0+\Delta\theta+\theta')}{\partial {x_j}^2}. \tag{A.35}$$

Reynolds averaging the last equation gives

$$\frac{\partial(\theta_0+\Delta\theta)}{\partial t}+\Delta U_j\frac{\partial(\theta_0+\Delta\theta)}{\partial x_j}+\overline{u_j'\frac{\partial\theta'}{\partial x_j}}=\nu_\theta\frac{\partial^2(\theta_0+\Delta\theta)}{\partial {x_j}^2}. \tag{A.36}$$

Making use of incompressibility, the continuity equation, and the product rule of calculus, we can bring the third term into flux form again,

$$\frac{\partial(\theta_0+\Delta\theta)}{\partial t}+\Delta U_j\frac{\partial(\theta_0+\Delta\theta)}{\partial x_j}=\nu_\theta\frac{\partial^2(\theta_0+\Delta\theta)}{\partial {x_j}^2}-\frac{\partial\overline{\left(u_j'\theta'\right)}}{\partial x_j} \tag{A.37}$$

Applying K-theory with constant eddy diffusivity K_H to the last term,

$$\frac{\partial(\theta_0+\Delta\theta)}{\partial t}+\Delta U_j\frac{\partial(\theta_0+\Delta\theta)}{\partial x_j}=\nu_\theta\frac{\partial^2(\theta_0+\Delta\theta)}{\partial x_j^{\,2}}+K_H\frac{\partial^2\Delta\theta}{\partial x_j^{\,2}}. \tag{A.38}$$

Assuming stationary conditions and neglecting molecular diffusion of heat, the first and third term drop out. Writing out the summations over equal indices,

$$\begin{aligned}&\left(\Delta U\frac{\partial\theta_0}{\partial x}+\Delta V\frac{\partial\theta_0}{\partial y}+\Delta W\frac{\partial\theta_0}{\partial z}\right)+\left(\Delta U\frac{\partial\Delta\theta}{\partial x}+\Delta V\frac{\partial\Delta\theta}{\partial y}+\Delta W\frac{\partial\Delta\theta}{\partial z}\right)=\\&K_H\left(\frac{\partial^2\Delta\theta}{\partial x^2}+\frac{\partial^2\Delta\theta}{\partial y^2}+\frac{\partial^2\Delta\theta}{\partial z^2}\right)\end{aligned} \tag{A.39}$$

Prandtl assumed that the background potential temperature profile is linear

$$\theta_0=\theta_S+\gamma\cdot z \tag{A.40}$$

with lapse rate γ, so that

$$\Delta W\cdot\gamma+\left(\Delta U\frac{\partial\Delta\theta}{\partial x}+\Delta V\frac{\partial\Delta\theta}{\partial y}+\Delta W\frac{\partial\Delta\theta}{\partial z}\right)=K_H\left(\frac{\partial^2\Delta\theta}{\partial x^2}+\frac{\partial^2\Delta\theta}{\partial y^2}+\frac{\partial^2\Delta\theta}{\partial z^2}\right) \tag{A.41}$$

Rewriting the equation in vector format,

$$\begin{aligned}&\gamma(\Delta U,\Delta V,\Delta W)\cdot(0,0,1)+(\Delta U,\Delta V,\Delta W)\cdot\left(\frac{\partial}{\partial x},\frac{\partial}{\partial y},\frac{\partial}{\partial z}\right)\Delta\theta=\\&K_H\left(\frac{\partial^2}{\partial x^2}+\frac{\partial^2}{\partial y^2}+\frac{\partial^2}{\partial z^2}\right)\Delta\theta\end{aligned} \tag{A.42}$$

and applying the same coordinate transformation as in (A.22) to (A.26), the last equation becomes

$$\begin{aligned}&\gamma(U_s,\Delta V,W_n)\cdot(\sin\alpha,0,\cos\alpha)+(U_s,\Delta V,W_n)\cdot\left(\frac{\partial}{\partial s},\frac{\partial}{\partial y},\frac{\partial}{\partial n}\right)\Delta\theta=\\&K_H\left(\frac{\partial^2}{\partial s^2}+\frac{\partial^2}{\partial y^2}+\frac{\partial^2}{\partial n^2}\right)\Delta\theta.\end{aligned} \tag{A.43}$$

Following the same arguments as above assuming one-dimensionality and mass continuity, $\Delta V=0$, $W_n=0$, $\frac{\partial}{\partial s}=0$, $\frac{\partial}{\partial y}=0$, $\frac{\partial^2}{\partial s^2}=0$, and $\frac{\partial^2}{\partial y^2}=0$, and we are left with Prandtl's heat budget equation,

$$\gamma \cdot U_s \cdot \sin\alpha = K_H \frac{\partial^2 \Delta\theta}{\partial n^2}. \tag{A.44}$$

The pair of differential equations (A.31) and (A.44) can be decoupled by differentiating (A.44) twice with respect to n and then substituting into (A.31). The resulting differential equations in $\Delta\theta$ and U_s have one physically reasonable solution:

$$\Delta\theta = \Delta\theta_s \cdot \exp\left(-n/l\right) \cdot \cos\left(n/l\right) \text{ and} \tag{A.45}$$

$$U_s = \Delta\theta_s \cdot \frac{g\beta}{N}\left(\frac{K_H}{K_m}\right)^{1/2} \cdot \exp\left(-n/l\right) \cdot \sin\left(n/l\right), \tag{A.46}$$

where

$$l \equiv \left(\frac{4K_m K_H}{N^2 \sin^2\varphi}\right)^{1/4} \tag{A.47}$$

is a mixing length and $\Delta\theta_s$ is the near surface potential temperature increase from the initial background value (Prandtl, 1942).

Alternatively, from the definition of eddy diffusivity of heat follows the boundary condition

$$-K_H \left.\frac{\partial\theta_s}{\partial n}\right|_{n=0} = \overline{w'\theta'_s} = Q_H, \tag{A.48}$$

where Q_H is the sensible surface heat flux. With this the solution to (A.31) and (A.44) can be expressed in terms of sensible surface heat flux Q_H,

$$\Delta\theta = \frac{Q_H l}{K_H} \cdot \exp\left(-n/l\right) \cdot \cos\left(n/l\right) \text{ and} \tag{A.49}$$

$$U_s = \frac{Q_H l}{K_H} \cdot \frac{g\beta}{N}\left(\frac{K_H}{K_m}\right)^{1/2} \cdot \exp\left(-n/l\right) \cdot \sin\left(n/l\right). \tag{A.50}$$

Summary of Assumptions and Approximations

To derive Prandtl's momentum and heat budget equation I applied the following sequence of assumptions and approximations:

1. Newtonian fluid, homogeneity of viscosity (both superseded by point 6 below), and incompressibility
2. Coriolis force negligible
3. Hydrostatic equilibrium of background state, no mean background wind
4. Stationarity
5. Boussinesq approximation
6. Molecular viscosity and diffusivity negligible
7. K-theory with constant K_m and K_H
8. Infinitely long and infinitely wide homogeneous slope with constant slope angle α
9. Dry conditions, no phase changes
10. Net radiation negligible
11. Linear background potential temperature profile

Remark on Horizontal Pressure Gradient

In the derivation of (A.28) and (A.29) I did not neglect the horizontal pressure gradient force. The two equations show that the pressure gradient force acts in the slope-normal direction because I assumed that there are no pressure variations in the along-slope direction. This implies that the pressure gradient force is composed of a vertical and a horizontal component. Much of the confusion over the inclusion of a horizontal pressure gradient force in the governing equations as discussed by Hayden (2003) can be avoided by a rigorous derivation from first principles as demonstrated here for the Prandtl model.

Appendix B: Scaling

B.1 Derivation and Discussion of Upslope Flow Velocity Hypotheses

In this section I will shed light on a few hypotheses on upslope flow velocity extracted from the literature. By combining governing parameters in such a way that the resulting units are length per time, velocity scales can be produced in many different ways. Here, however, I will mostly focus on hypotheses, which are derived by considering the underlying physical processes. It turns out that these hypotheses still require the fitting of parameters. I therefore modify the hypotheses but name them after the author, who developed the original hypothesis.

In the following discussions I will use as a particular case of interest our conditions at Minnekhada Park at 1200 PDT on July 25, 2001:

$$\varphi = 19° \text{ (slope angle)}, \tag{B.1}$$

$$h_a = 720\,m \text{ (CBL depth from (3.51))}, \tag{B.2}$$

$$\theta_{s,a} = 4.5\,K \text{ (CBL mean potential temperature increment from (3.52))}, \tag{B.3}$$

$$Q_{H,a} = 0.21\,K\,m\,s^{-1} \text{ (instantaneous sensible surface heat flux)}, \tag{B.4}$$

$$N_a = 0.015\,s^{-1} \text{ (background stratification)}, \tag{B.5}$$

$$H_a = 760\,m \text{ (ridge height)}. \tag{B.6}$$

The observed maximum upslope flow velocity averaged over the time interval from 1140-1220 PDT with standard error of estimate was

$$U_{obs,a} \approx (3.8 \pm 0.3)\,m\,s^{-1}. \tag{B.7}$$

Upslope Flow Velocity Hypothesis by Hunt et al. (2003)

Hunt et al. (2003) allowed for different dynamics in the surface, mixed, and inversion layers by applying a zonal analysis to the atmosphere. They derived simplified forms of the Navier-Stokes equations for the different layers and matched unknown parameters at the interfaces. For the mean upslope flow velocity they derived

$$U_{M,a} \approx \Gamma_a (\sin\varphi)^{1/3} w_{*a} = \Gamma_a (\sin\varphi \cdot g\beta_a h_a Q_{H,a})^{1/3}, \tag{B.8}$$

where I did *not* make the small-angle approximation $\sin\varphi \approx \varphi$ that the authors made.

$$w_{*a} \equiv (g\beta_a h_a Q_{H,a})^{1/3} \tag{B.9}$$

is the convective (or Deardorff) velocity scale. The constant of proportionality,

$$\Gamma_a \sim \frac{1}{k}\ln\left(\frac{-L_{*,a}}{z_{0,a}}\right)\left[\frac{h_{s,a}}{h_a}\frac{1}{k}\ln\left(\frac{-L_{*,a}}{z_{0T,a}}\right)\right]^{1/3} \sim 10, \tag{B.10}$$

is a function of momentum roughness length $z_{0,a}$ and "thermal" roughness length $z_{0T,a}$, Monin-Obukhov length $L_{*,a}$ (negative for unstable conditions), surface layer depth $h_{s,a}$, and CBL depth h_a. $k \approx 0.4$ is the von Kármán constant. The rough estimate $\Gamma_a \sim 10$ was suggested by Hunt et al. (2003). I will now discuss some characteristics of (B.8).

1. Hunt et al. (2003) derived their hypothesis for small slope angles, but they argued that the assumption that buoyancy drives the flow and determines the turbulence in the CBL holds for $\varphi \le 20°$ so that the slope at Minnekhada Park falls within the range of validity. I am not aware of any other assumptions in Hunt's et al. derivation that would exclude the 19° slope angle at Minnekhada Park.

2. In the derivation of (B.8), Hunt et al. (2003) assumed that CBL depth and upslope flow layer depth are identical. Our field observations on July 25, by contrast, show that the upslope flow filled only the bottom half of the CBL (Figure 2.9, page 24).

3. Hunt et al. (2003) assumed that the environmental stratification above the upslope flow layer is undisturbed, which is unrealistic because the return flow advects nearly neutral fluid over the upslope flow layer.

4. The latter problem is related to the assumption that a return flow underneath the ridge top will only occur underneath an inversion (scenario 1 in Hunt et al., 2003). In the absence of an inversion and an opposing synoptic flow (scenario 3 in Hunt et al., 2003), Figure 2 in Hunt et al. (2003) suggests that the authors assumed a deep unidirectional flow extending from the plain over the slope to the plateau without a return flow.

5. In the hypothesis by Hunt et al. (2003), the upslope flow velocity is assumed independent of height within the mixed layer and is essentially equal to (only slightly smaller than) the maximum upslope flow velocity, which occurs in the surface layer. In contrast, our observations in Figure 2.7 (page 22) and Figure 2.8 (page 23) show that the vertical profile of upslope flow velocity, following a Prandtl profile, decreases from its maximum value at a height approximately one quarter of the upslope flow depth to zero at the top of the upslope flow layer.

6. The dependence of the constant of proportionality, Γ_a, on its arguments is only known to an order of magnitude. Furthermore, none of the arguments is known better than an order of magnitude; this includes the CBL depth, because Hunt et al. (2003) did not considered that the CBL is much shallower over the upper part of the slope than the lower part.

7. The dependence of Γ_a on surface roughness for momentum and heat challenges the assumption that non-dimensional (ND) maximum upslope flow velocity depends only on Π_1, $\Pi_{2,a}$, and $\Pi_{3,a}$, (3.68), because surface roughness was neglected in the scaling. Moreover, it may be impossible to achieve the same ratio of momentum and "thermal" roughness length in atmospheric idealisation (AI) and water-tank idealisation (WTI) because of the different fluid properties.

8. Monin-Obukhov theory was derived from field observations over flat terrain. It may not be valid over sloping terrain at all or require different empirical constants. Even if valid, Monin-Obukhov length and surface layer depth could be functions of upslope flow characteristics like speed and depth so that Γ_a would not be a constant. All these cases could violate the assumption $\Gamma_a \sim 10$.

9. Proportionality between upslope flow velocity and convective velocity scale is physically reasonable, because the convective heating of the CBL seems to drive the upslope motion. It is instructive at this point to have a closer look at a water-tank experiment[5]. Figure Appendix I clearly shows that in the water-tank upslope flows were fully developed before the onset of turbulent convection. It may well be that a change of the driving mechanism occurs in the water tank when convection begins, but the problem of explaining the upslope flow without the presence of convection remains. Figure Appendix I also provides strong arguments against Hunt's et al. (2003) assumption that the upslope flow layer is identical to the heated layer: the heating over the slope has at most reached a depth of a few millimetres above the surface (through molecular diffusion of heat) whereas the upslope flow layer is about 4 cm deep. More information on this experiment is provided in chapter 4.

[5] Background information on the water tank can be found in section 4.2.

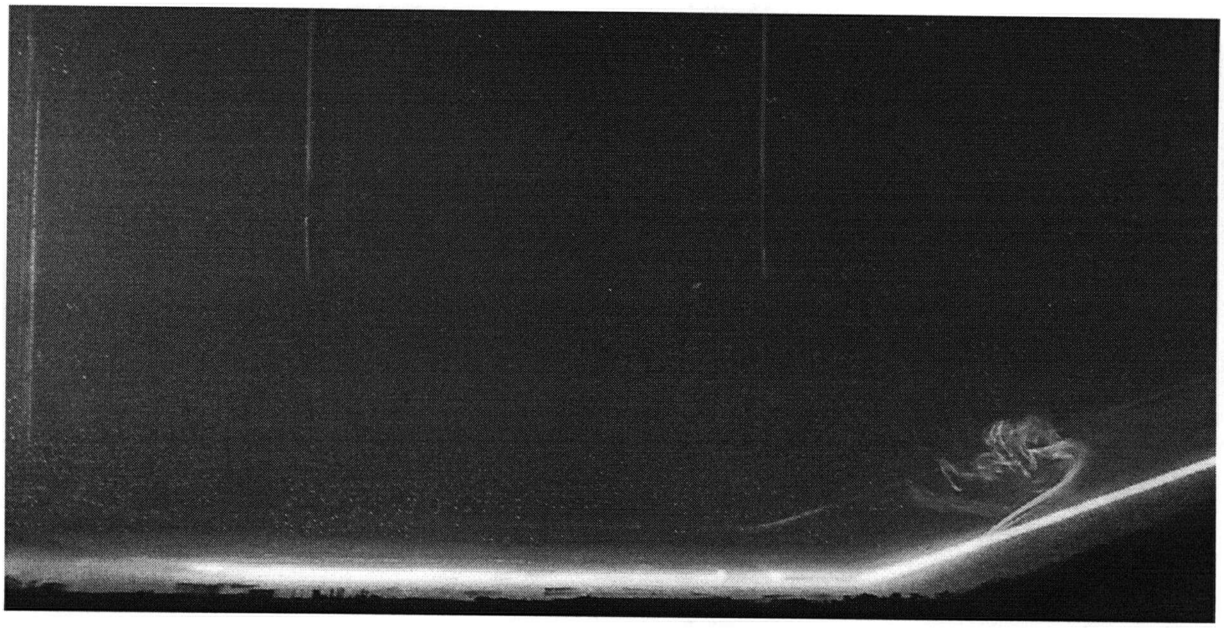

Figure Appendix I: Upslope flow without convective turbulence.
This photograph of a dye experiment shows almost the entire plain and the bottom third of the slope, a total width of about 60 cm. Horizontal and vertical lengths are shown to scale. The photograph was taken 30-40 s after the heating was turned on. Convection is about to begin as can be seen by a few white bulges over the plain near the slope. The upslope flow is already fully developed, well visualised by the dye carried along the slope. The dye was originally injected as a thin layer (<<1 mm) over the plain. The stream of dye also roughly outlines the vertical profile of the upslope flow velocity. The upslope flow layer has a depth of about 4 cm.

Because mean and maximum upslope flow velocity are essentially equal in Hunt's et al. (2003) hypothesis, the predicted maximum upslope flow velocity (B.8)-(B.10) is

$$U_{\max,a} = 10\left(\sin\varphi \cdot g\beta_a h_a Q_{H,a}\right)^{1/3} \approx 12.1\, m\, s^{-1} \tag{B.11}$$

where the value holds for 1200 PDT on July 25, (B.1)-(B.6). Because of the logarithm and cubed root in (B.10), Γ_a depends only weakly on its parameters. Therefore, substantial modifications to the parameters of Γ_a in (B.10) are required to fit $U_{\max,a}$ to the observed velocity $U_{obs,a} \approx (3.8 \pm 0.3)\, m\, s^{-1}$. Despite the attempts by Hunt et al. (2003) to derive the coefficient Γ_a from first principles it remains essentially an unknown parameter, which needs to be determined by fitting the hypothesis to the data. I therefore define the 'Hunt hypothesis' of maximum upslope flow velocity for atmosphere and water tank by

$$U_{Hunt} \equiv c_{Hunt}\left(g\beta h Q_H\right)^{1/3}. \tag{B.12}$$

Upslope Flow Velocity Hypotheses by Chen et al. (1996)

Chen et al. (1996) derived an upslope flow velocity "scale" for atmosphere and water tank from a balance between horizontal advection and pressure gradient term. I present a modified derivation here, applicable for atmosphere and water tank, in which I retain a factor of 2, which Chen et al. (1996) dropped in their derivation.

The hydrostatic pressure difference can be determined from the Navier-Stokes equation for vertical acceleration, i.e. from (A.16)

$$\cancel{\frac{\partial \Delta U_i}{\partial t}} + \cancel{\Delta U_j \frac{\partial \Delta U_i}{\partial x_j}} = -\delta_{i3}\frac{\Delta\rho}{\rho_0}g - \frac{1}{\rho_0}\frac{\partial \Delta P}{\partial x_i} - \cancel{\frac{\partial \overline{u_i' u_j'}}{\partial x_j}} \Rightarrow \tag{B.13}$$

$$\frac{\partial \Delta P}{\partial z} = -g\cdot\Delta\rho\,, \tag{B.14}$$

where Δ denotes departures from the hydrostatic background values. Denoting background values with subscript 'b',

$$\Delta P = P - P_b \tag{B.15}$$

and

$$\Delta\rho = \rho - \rho_b\,. \tag{B.16}$$

Substitution of the last two equations into (B.14), noting that the background is in hydrostatic balance, and using the definition of specific volume, (3.12), gives

$$\frac{\partial P}{\partial z} + \frac{\partial P_b}{\partial z} = -g\cdot\rho - g\cdot\rho_b \quad\Rightarrow\quad \frac{\partial P}{\partial z} = -g\cdot\rho = -g\cdot\frac{1}{\alpha} \tag{B.17}$$

Let $z \in \left[0, z_{top}\right]$, where $z_{top} = D_w$ for the water tank and $z_{top} = \infty$ for the atmosphere. Notice that I assume here that z_{top} is constant, which is reasonable because any lifting of this height due to thermal expansion occurs equally over plain and slope[6]. Integrating both sides of (B.17) vertically and noting that the pressure is zero at z_{top}, we get

[6] This is in contrast to Atkinson's (1981) explanation of *sea breezes:* over the land the air is heated and lifted above a reference height, but not over the water. This horizontal difference in lifting is essential for the sea-

$$P(z)=P(z)-P(z_{top})=-g\cdot\int_{z_{top}}^{z}\frac{1}{\alpha(\tilde{z})}d\tilde{z}=g\cdot\int_{z}^{z_{top}}\frac{1}{\alpha(\tilde{z})}d\tilde{z}. \qquad (B.18)$$

I restrict myself here to the case where the CBL height is smaller than the ridge height, which is true for the atmospheric observations that I consider in this dissertation (until about 1230 PDT). Without advection, the maximum pressure difference would be achieved between a point A over the plain far from the slope and the ridge top B (Figure Appendix II, left).

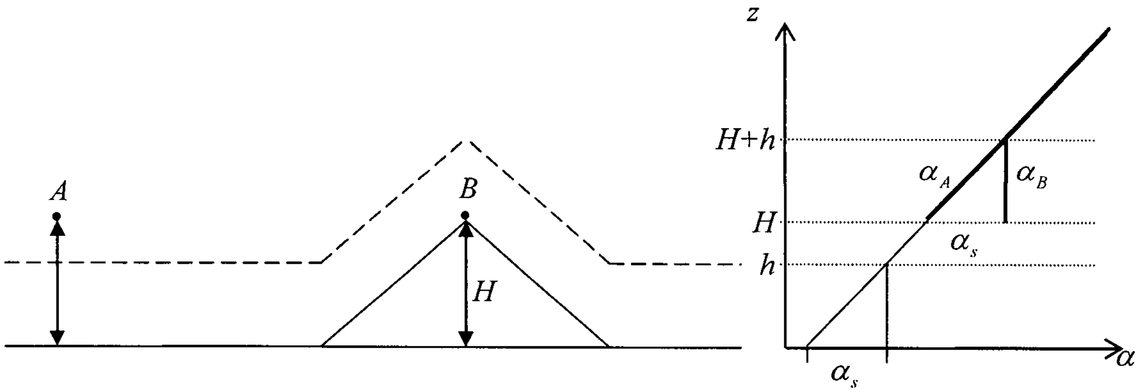

Figure Appendix II: Schemata for derivation of horizontal pressure gradient.
Left: Outline of topography (solid line) with ridge height H, terrain-following CBL top (dashed line) of depth h, and the two reference points A and B. Right: Vertical specific volume profiles at points A and B (bold lines labelled α_A and α_B); the CBL mean specific volume increment is denoted by α_s.

The horizontal pressure difference between A and B from the last equation is

$$\delta P(H)\equiv P_B(H)-P_A(H)=g\cdot\int_{H}^{z_{top}}\left[\frac{1}{\alpha_B(z)}-\frac{1}{\alpha_A(z)}\right]dz. \qquad (B.19)$$

Without compensating advection, the CBL depth h is constant everywhere in the tank and the vertical specific-volume profiles at A and B are identical above $H+h$ (Figure Appendix II, right). Approximating $\alpha_A\cdot\alpha_B=\alpha_0^2$, where α_0 is an average value, the last equation becomes,

breeze initiation but is absent in upslope flows. This implies that sea breezes and upslope flows are fundamentally different processes.

$$\delta P(H) = g \cdot \int_{H}^{H+h} \left[\frac{\alpha_A(z) - \alpha_B(z)}{\alpha_B(z) \cdot \alpha_A(z)} \right] dz \approx \frac{g}{\alpha_0^2} \cdot \int_{H}^{H+h} \left[\alpha_A(z) - \alpha_B(z) \right] dz . \tag{B.20}$$

From the geometry in the right diagram of Figure Appendix II, between H and $H+h$,

$$\alpha_B = const. \tag{B.21}$$

and

$$\alpha_A(z) = \alpha_B - \alpha_s \frac{H-h-z}{h} . \tag{B.22}$$

Substituting the last two equations into (B.20) gives

$$\delta P(H) \approx \frac{g}{\alpha_0^2} \cdot \int_{H}^{H+h} \left[\alpha_B - \alpha_s \frac{H-h-z}{h} - \alpha_B \right] dz \Rightarrow$$

$$\delta P(H) \approx \frac{-g}{\alpha_0^2} \cdot \frac{\alpha_s}{h} \frac{[H-h-z]^2}{-2} \Bigg|_{z=H}^{z=H+h} = -\frac{g}{\alpha_0^2} \cdot \frac{\alpha_s}{2} h \tag{B.23}$$

Next, assume a balance of horizontal pressure gradient and advection; the horizontal component of (A.16) gives,

$$\cancel{\frac{\partial \Delta U_i}{\partial t}} + \Delta U \frac{\partial \Delta U_i}{\partial x} + \cancel{\Delta V \frac{\partial \Delta U_i}{\partial y}} + \cancel{\Delta W \frac{\partial \Delta U_i}{\partial z}} = -\cancel{\delta_{i3} \frac{\Delta \rho}{\rho_0} g} - \frac{1}{\rho_0} \frac{\partial \Delta P}{\partial x_i} - \cancel{\frac{\partial \overline{u_i' u_j'}}{\partial x_j}} \Rightarrow \tag{B.24}$$

$$\Delta U \frac{\partial \Delta U}{\partial x} = -\frac{1}{\rho_0} \frac{\partial \Delta P}{\partial x} , \tag{B.25}$$

The background is assumed at rest and in hydrostatic balance, which gives, together with the definition of specific volume, (3.12),

$$U \frac{\partial U}{\partial x} = -\alpha_0 \frac{\partial P}{\partial x} \quad \Rightarrow \quad U \cdot \delta U = \frac{\delta(U^2)}{2} = -\alpha_0 \cdot \delta P . \tag{B.26}$$

Chen et al. (1996) dropped the factor 2, which I will retain. At point A, $U_A = 0$, so that (B.26) becomes, after replacing δP from (B.23),

$$U_B^2(H) = \frac{g}{\alpha_0} \cdot \alpha_s h . \tag{B.27}$$

Finally, substituting (3.92) into the last equation gives

$$U_B(H) = N\,h, \tag{B.28}$$

which holds for atmosphere and water tank. In the derivation friction was not included, which is likely to reduce the velocity substantially. I therefore define the 'Chen hypothesis' based on (B.28) for atmosphere and water tank:

$$U_{Chen} \equiv c_{Chen} N\,h, \tag{B.29}$$

where the coefficient c_{Chen} includes the contribution of friction.

Chen et al. (1996) derived a velocity scale for atmosphere and water tank,

$$U_0 = \left(\frac{\Im(h,H)}{2}\right)^{1/2} N\,h, \tag{B.30}$$

where

$$\Im(h,H) \equiv \begin{cases} 1 & \text{for } h \le H \\ \dfrac{H}{h}\left(2 - \dfrac{H}{h}\right) & \text{for } h > H. \end{cases} \tag{B.31}$$

The more complicated case for $h > H$ is not of concern for our field observations in the mornings of July 25 and 26, so that

$$\left(\frac{\Im(h_a,H_a)}{2}\right)^{1/2} = \left(\frac{1}{2}\right)^{1/2}, \tag{B.32}$$

and

$$U_0 = \left(\frac{1}{2}\right)^{1/2} N\,h. \tag{B.33}$$

Remarks:

1. In the derivation of (B.29) and (B.33) it is assumed that CBL depth is equal over plain and slope, which is an increasingly worse assumption for the field data as the day progresses (Figure 2.3, page 18).

2. It is also assumed that the environmental stratification above the upslope flow layer is undisturbed; as I pointed out for the approach by Hunt et al. (2003) this is not a good assumption.

3. In this hypothesis, the maximum velocity U_{Chen} was estimated at the ridge top. Assuming a flow of constant depth along the slope, continuity implies that the upslope flow velocity must be equal along the slope. In particular, the derivation implies that the maximum occurs at the surface. Applying the no-slip condition, the true maximum velocity in the atmosphere, $U_{\max,a}$, occurs above the surface, where the pressure gradient is weaker and therefore $U_{\max,a} < N_a h_a$. Essentially this is one way of quantifying the friction coefficient $c_{Chen,a}$ in (B.29). The Prandtl model (1942) includes the boundary condition $U_a(z=0)=0$. Although Prandtl made some very crude assumptions (Appendix A), our field observations of upslope flow velocities on the morning of July 25 agree reasonably well with the vertical profile of upslope flow velocity in the Prandtl model,

$$U_a(z) = N_a h_a \exp(-z_a / l_a) \sin(z_a / l_a), \tag{B.34}$$

where l_a is a measure of the CBL depth (Figure Appendix III).

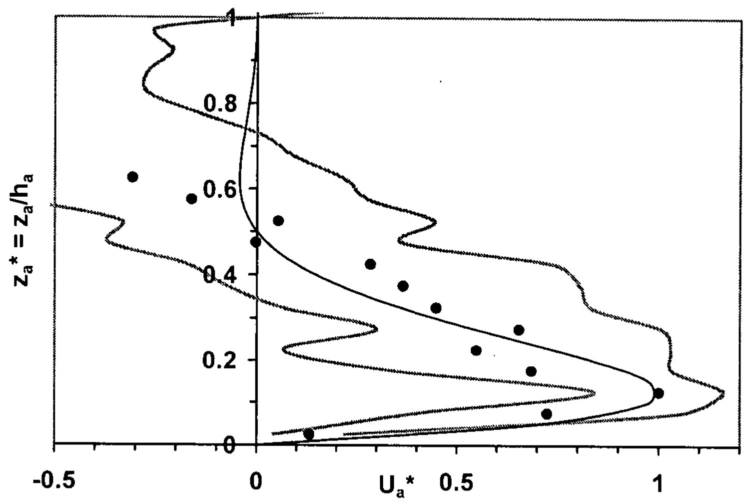

Figure Appendix III: Vertical profile of normalized time average of normalised upslope flow velocity and fitted Prandtl profile for July 25, 2001, 0850-1230 PDT.

Data points represent upslope flow velocity as measured by the sodar over the plain near the foot of the slope, and the grey lines denote one standard deviation. The solid line is a fitted Prandtl profile. I normalised twelve individual vertical profiles of upslope flow velocities by dividing heights by backscatter boundary layer depth and velocities by the maximum velocity for each profile. Then I binned the velocities in $\Delta z_a^* = 0.05$ *thick horizontal layers and calculated their time average and standard deviation for each layer. Finally I rescaled data and standard deviations by setting the maximum of the resulting time-averaged profile to one. The Prandtl profile is uniquely defined by settings its maximum velocity to 1 and the depth of the upslope flow to 0.5. The good agreement between observations and Prandtl profile for the height of the maximum velocity was not imposed.*

In the Prandtl profile, the maximum velocity $U_{\max,a}$ occurs at height $z_a = \pi l_a/4$, so that

$$U_{\max,a} = N_a h_a \exp\left(-\frac{\pi}{4}\right)\sin\left(\frac{\pi}{4}\right) \approx 0.322\ N_a h_a . \tag{B.35}$$

I call this special case of the Chen hypothesis, which includes the no-slip condition at the surface, the 'friction hypothesis',

$$U_{fric} \equiv 0.322\ N h . \tag{B.36}$$

I assume that this hypothesis applies to atmosphere and water tank.

4. Comparing (B.34) with (A.50) gives,

$$N_a h_a = \frac{Q_{H,a} l_a}{K_{H,a}} \cdot \frac{g\beta_a}{N_a} \left(\frac{K_{H,a}}{K_{m,a}} \right)^{1/2} . \tag{B.37}$$

The Prandtl model (A.50) is not very useful practically because the eddy diffusivities $K_{H,a}$ and $K_{m,a}$ are not known – besides being questionable concepts for convective conditions. Furthermore, the Prandtl model assumes steady state, not a good assumption as I will discuss further for the Schumann hypothesis below. From (B.37) I could compute the eddy diffusivities, without obvious benefit, however.

5. In their water-tank experiments, Chen et al. (1996) were not able to measure the maximum upslope flow velocity near the tank bottom surface. The authors conjectured that the maximum upslope flow velocity was about 1.3 times as strong as the maximum velocity of the upper part of the slope flow vortex, i.e. the return flow. Their tank observations, however, do not agree with their velocity scale (B.30); instead, the authors determined a best fit function at the time of maximum heating

$$U_{fit,w} = 1.3 \left(0.18 + \frac{0.15}{h_w *} \right) U_{0,w} , \tag{B.38}$$

where $U_{0,w}$ is the velocity scale (B.30) for the water tank, and

$$h_w * \equiv \frac{h_w}{H_w} \tag{B.39}$$

is the ND CBL height. The best fit is valid in the range $1.1 < h_w * < 3$. Chen et al. (1996) argued that $h_w *$ is the dominant similarity parameter so that the best fit should also apply to the atmosphere for $1.1 < h_a * < 3$, which is slightly higher than our observed values, for example $h_a * \approx 0.9$ at 1200 PDT on July 25.

6. The Chen hypothesis is a gravity-current hypothesis of form

$$U = c \left(g_s d \right)^{1/2} , \tag{B.40}$$

where $c \sim 1$,

$$g_s \equiv \begin{cases} g\beta_a\theta_{s,a} & \text{for atmosphere} \\ \dfrac{g}{\alpha_{0,w}}\alpha_{s,w} & \text{for water tank,} \end{cases} \tag{B.41}$$

is the reduced buoyancy scale, and d is a measure of fluid depth. With $U \equiv U_{Chen}$ and $d \equiv h$,

$$U_{Chen} = c_{Chen}\left(g_s h\right)^{1/2} = c_{Chen} \cdot Nh \tag{B.42}$$

where I used (3.50) and (3.20) for the atmosphere and (3.92) and (3.21) for the water tank.

7. In the Chen and friction hypotheses,

$$c_{Chen} = \frac{U_{Chen}}{\left(g_s h\right)^{1/2}} = Fr_i \text{ and} \tag{B.43}$$

$$0.322 = \frac{U_{fric}}{\left(g_s h\right)^{1/2}} = Fr_i \tag{B.44}$$

are internal Froude numbers (see also Appendix B.6).

For the observations at 1200 PDT on July 25, i.e. (B.1)-(B.6), equations (B.29), (B.35), and (B.38) give,

$$U_{Chen,a} \equiv c_{Chen,a} N_a \cdot h_a \approx c_{Chen,a} \times 10.3\, m\, s^{-1}, \tag{B.45}$$

$$U_{fric,a} = 0.322\, N_a\, h_a \approx 3.5\, m\, s^{-1}, \tag{B.46}$$

$$U_{fit,a} = 1.3\left(0.18 + \frac{0.15}{h_a*}\right) U_{0,a} \approx 3.3\, m\, s^{-1}. \tag{B.47}$$

Notice that $h_a* \approx 0.9$ is slightly outside the range $1.1 < h_a* < 3$ for which Chen et al. (1996) computed the best fit. The friction hypothesis is just within the range of one standard error of the observed value of $U_{obs,a} \approx (3.8 \pm 0.3)\, m\, s^{-1}$, and the best fit by Chen et al. (1996) is not far outside the range.

An Alternative "Gravity-Current" Hypothesis

Using (3.50) and (3.20), the Chen and friction hypotheses (B.45) and (B.46) can be written in gravity current form $U = c\left(g\beta\theta_s h\right)^{1/2} = c\,Nh$. I demonstrate in section 4.4 for the water tank that the upslope flow depth decreases over the slope towards the ridge height and resembles a gravity current flowing into fluid of steadily decreasing depth. A plain-plateau flow at ridge height seems to act as a lid. In section 4.3.2 I used this characteristic to explain the unexpected linear dependence of CBL mean specific volume increment on time. In such a scenario,

$$U = 0.45\left(g_s H_f\right)^{1/2}, \tag{B.48}$$

where H_f is the total height of the fluid right above the gravity-current front (Simpson, 1997). For upslope flows, background stratification is important, but not considered in (B.48), and the factor 0.45 requires an unknown correction. At the foot of the slope, assuming a lid at ridge height, $H_f = H$. An alternative hypothesis can then be defined for atmosphere and water tank, which I call 'gravity-current hypothesis:

$$U_{Grav} \equiv c_{grav}\left(g\beta\theta_s H\right)^{1/2} = c_{grav}\,N\left(hH\right)^{1/2}. \tag{B.49}$$

Remarks:

1. There is no compelling reason to prefer the ridge height over the CBL depth in (B.48) and to assume that the plain-plateau flow acts as a lid. The depth of the upslope flow, for example, increases in time like the CBL depth, while the gravity-current flow should be approximately half the depth of the ridge height at all times. I included this model in the discussion mainly because, as I will show below, it is the only model that includes ridge height or slope length.
2. The maximum upslope flow velocity in (B.49) only depends on constants and does not change in time. In gravity currents there are different flow regimes; equation (B.40) applies to a quasi-steady regime that can persist for long periods of time (Simpson, 1997). It is possible that such a flow regime also exists in upslope

flows, but our field observations show a strong increase of maximum upslope flow velocity during the morning.

3. As with the other two hypotheses, the assumption of constant background stratification on top of the gravity current is not well supported by observations.

To gain a rough estimate of the expected velocities for 1200 PDT on July 25 in such an alternative gravity-current hypothesis, I use $c_{grav} = 0.45$ for neutral background in (B.49) to get a front velocity of

$$U_{Grav,a} = 0.45\left(g\beta_a\theta_{s,a}H_a\right)^{1/2} = 0.45\,N_a\left(h_aH_a\right)^{1/2} = 5.0\,m\,s^{-1}. \qquad \text{(B.50)}$$

The flow speed behind the front should be a little bit larger, but with the inclusion of background stratification the true velocity should be smaller than in (B.50).

Upslope Flow Velocity Hypothesis by Schumann (1990)

Schumann (1990) ran a large-eddy simulation (LES) of the atmosphere above an unbounded, inclined, rough plane. He prescribed a constant and uniform heat flux and a linearly stratified background at rest. In his scaling, Schumann identified as his independent parameters: environmental lapse rate γ_a, coefficient of thermal expansion β_a, gravitational acceleration g, heat flux $Q_{H,a}$, and roughness length $z_{0,a}$. From these he defined a characteristic velocity scale by

$$U_{S,a} = \left(g\beta_a\frac{Q_{H,a}}{N_a}\right)^{1/2}. \qquad \text{(B.51)}$$

A few remarks follow.

1. Schumann did not apply scaling as a rigorous dimensional analysis. As I have argued above (section 3.2), if the Boussinesq approximation applies, $g\beta_a$ is the relevant parameter, not g alone. Replacing γ_a by the buoyancy frequency N_a, the set of independent parameters becomes

$$g\beta_a\left[m\,s^{-2}\,K^{-1}\right],\ N_a\left[s^{-1}\right],\ Q_{H,a}\left[K\,m\,s^{-1}\right],\ \text{and}\ z_{0,a}\left[m\right]. \qquad \text{(B.52)}$$

With this set of independent parameters, definition (B.51) is more obvious because certainly one would need to include $Q_{H,a}$ in the definition, at which point correct multiplication by $g\beta_a$ is necessary to eliminate units of temperature, K, and division by N_a to get the correct ratio of m and s. Notice, however, that in addition to these parameters, the characteristic velocity could also dependent on $N_a z_{0,a}$, which has units of velocity.

2. The characteristic velocity scale is not a velocity particular to the upslope flow. It can be used to non-dimensionalise any velocities. Therefore, Schumann had to determine empirically the relationship between characteristic velocity scale and maximum upslope flow velocities observed in the LES. The relationship is strongly dependent on the slope angle but only weakly dependent on roughness length. For a slope angle of 19° and a reasonable wide range of roughness lengths from 0.1-1.0 m, Schumann's results give

$$U_{\max,a} \approx 2.1 U_{S,a} = 2.1\left(g\beta_a \frac{Q_{H,a}}{N_a} \right)^{1/2} . \tag{B.53}$$

The coefficient is fairly constant at a minimum value of about 2 for slope angles in the range 20-35° but increases approximately linearly to 4-4.5 above and below the range.

3. Schumann's scaling applies to an atmospheric idealisation with constant heat flux. It is not directly transferable to atmospheric observations, because Schumann did not consider the time dependence of heat flux in the atmosphere. Without including total supplied energy density in the scaling, it is not possible to define the time, at which atmospheric observations and LES are comparable. Applying (B.53) to (B.51), using the definitions of the Pi groups in Table 3.2 on page 47, and comparing with (3.68),

$$\frac{U_{\max,a}}{H_a N_a} = 2.1\left(\frac{g\beta_a Q_{H,a}}{H_a^{\,2} N_a^{\,3}} \right)^{1/2} = 2.1\left(\Pi_{3,a}\right)^{1/2} = f_U\left(\Pi_1, \Pi_{2,a}, \Pi_{3,a}\right), \tag{B.54}$$

which means that the factor 2.1 potentially not only contains a dependence on the aspect ratio Π_1 but also on the ND energy density Π_2.

4. The length of the slope or the ridge height is not a parameter in Schumann's scaling, because the slope is infinitely long. For upslope flow velocities in the atmosphere to be comparable with those in Schumann's LES, I speculate that the ridge height would have to be much greater than the upslope flow depth. In the water tank, even before the onset of convection, the upslope flow depth is already more than one quarter of the ridge height (Figure Appendix I on page 176). Maximum upslope flow velocities observed in the field, $U_{obs,a} \approx (3.8 \pm 0.3)\, m\, s^{-1}$, exceed the steady state value predicted by Schumann's model by more than a factor of 2:

$$U_{\max,a} = 2.1 \times \left(g \beta_a \frac{Q_{H,a}}{N_a} \right)^{1/2} \approx 1.5\, m\, s^{-1} \tag{B.55}$$

   This suggests that the flow over the relatively short slope at Minnekhada Park never remained in a steady state, which Schumann observed for at least 4.5 hours for an infinite slope with a 10° angle.

Reconciling the hypothesis with the observations within the desired accuracy of 20% seems impossible for a number of reasons. Very soon after the beginning of positive net sensible surface heat flux the observed maximum upslope flow velocity is much larger than predicted. Moreover, if the real slope were longer, so that the infinite slope in Schumann's LES would be a more appropriate approximation, the observed maximum upslope flow velocity should be even greater. Finally, one would expect an even stronger upslope flow over the central region of the slope than at our measurement site over the plain near the foot of the slope. Replacing the inaccurate coefficient 2.1 in (B.55) by an unknown coefficient c_{Schu}, I define the 'Schumann hypothesis' for atmosphere and water tank by

$$U_{Schu} \equiv c_{Schu} \left(g \beta \frac{Q_H}{N} \right)^{1/2}. \tag{B.56}$$

B.2 Empirical Analysis

In section 3.4 I use simplifying assumptions and physical arguments to derive expressions for h_a and $\theta_{s,a}$. For the upslope flow velocity U_a, however, different models make different predictions. To decide which model is best supported by the data I want to fit monomials to the observations. Quantity and quality of the measurements needed to find a good fit with low uncertainty depend on the complexity of the relationship to be established and are not known a priori. Dimensional analysis can be of substantial help in determining the relationships by reducing the number of governing parameters.

The general procedure is outlined in Barenblatt (2003). I drop the subscripts 'a' and 'w' for those quantities that apply to atmospheric idealisation (AI) and water-tank idealisation (WTI). The maximum upslope flow velocity $U_{\max}$, which has units of length over time, $m\,s^{-1}$, can be non-dimensionalised by dividing by two key parameters, ridge height H and background buoyancy frequency N. The non-dimensional (ND) maximum upslope flow velocity $U_{\max}{}^* = U_{\max}/HN$ must then be a function of the core Pi groups in Table 3.2 (page 47),

$$\Pi_1 = \frac{L}{H},$$

$$\Pi_2 = E \cdot \frac{N}{Q_H}, \text{ and}$$

$$\Pi_3 = g\beta \cdot \frac{Q_H}{H^2 N^3}.$$

Hence,

$$U_{\max} = HN\, f_U\left(\Pi_1, \Pi_2, \Pi_3\right). \tag{B.57}$$

If the governing equations are the same for AI and WTI, the forcing must follow the same underlying mechanism, and the function $f_U\left(\Pi_1, \Pi_2, \Pi_3\right)$ must be identical for both idealisations. Furthermore, because of the similarity requirements (3.30), (3.43), and (3.44), the arguments Π_1, Π_2, and Π_3 of f_U are equal for AI and WTI. Hence, the similarity relationship between AI and WTI becomes

$$U_a^* \equiv \frac{U_a}{H_a N_a} = f_U\left(\Pi_1, \Pi_2, \Pi_3\right) = \frac{U_w}{H_w N_w} \equiv U_w^*. \tag{B.58}$$

Remarks:

1. f_U can be any function of Π_1, Π_2, and Π_3, not necessarily a simple monomial. For example, the upslope flow velocity could depend on $\sin\varphi$ rather than $\Pi_1 = \cot\varphi$. In such a case, the monomial is an approximation to the more complex relationship.
2. Without the Buckingham Pi analysis, finding a best fit involves fitting a function of seven variables (H, Q_H, N, L, E, $g\beta$, and g/α_0) (Table 3.1, page 44). Assume that $O(10)$ measurements per variable are needed to determine a fit with sufficient accuracy, which is a typical value for relatively simple functional relationships and reasonably small errors. Therefore fitting without the Buckingham Pi analysis would require a total of $O(10^7)$ measurements, which is practically impossible. With (B.57), the problem reduces to fitting a function of three non-dimensional parameters, Π_1 to Π_3. Since the aspect ratio $\Pi_1 = L/H$ is fixed, only the dependence on Π_2 and Π_3 can be investigated so that $O(10^2)$ measurements are needed to find a reasonable fit. The field observations of chapter 2 provide only few data and these with large uncertainties; tank observations, by contrast, can be made more easily with smaller uncertainties.
3. A best fit will rarely lead to relationships that can be justified physically, unless many data of extremely good quality are available and the relationships are simple. However, the relationships can be of physical value, for example when showing a regime change at particular parameter values. A well-known example is the pipe flow where the transition from laminar to turbulent flow leads to a rapid increase in the pressure drop along the pipe at a critical value of the Reynolds number (e.g. Barenblatt, 2003).

The five hypotheses (B.12), (B.29), (B.36), (B.49), and (B.56) can be written in the form (B.58). The algebra is straightforward using (3.20), (3.31), (3.32), (3.49), and (3.50). The main steps are:

$$U_{Hunt,a}{}^{*} = \frac{U_{Hunt,a}}{H_a N_a} = c_{Hunt} \left(\frac{g\beta_a Q_{H,a}}{H_a{}^2 N_a{}^3} \frac{h_a}{H_a} \right)^{1/3} = c_{Hunt} \cdot \Pi_{2,a}{}^{1/6} \cdot \Pi_{3,a}{}^{1/2}, \tag{B.59}$$

$$U_{Chen,a}{}^{*} = \frac{U_{Chen,a}}{H_a N_a} \equiv c_{Chen} \frac{\cancel{N_a}\, h_a}{H_a \cancel{N_a}} = c_{Chen} \cdot 2^{1/2} \cdot \Pi_{2,a}{}^{1/2} \cdot \Pi_{3,a}{}^{1/2}, \tag{B.60}$$

$$U_{fric,a}{}^{*} = \frac{U_{fric,a}}{H_a N_a} \equiv 0.322 \frac{\cancel{N_a}\, h_a}{H_a \cancel{N_a}} = 0.322 \cdot 2^{1/2} \cdot \Pi_{2,a}{}^{1/2} \cdot \Pi_{3,a}{}^{1/2}, \tag{B.61}$$

$$U_{Grav,a}{}^{*} = \frac{U_{Grav,a}}{H_a N_a} = c_{Grav} \frac{N_a \left(h_a H_a\right)^{1/2}}{H_a N_a} = c_{Grav} \left(\frac{h_a}{H_a} \right)^{1/2} = c_{Grav} \cdot \Pi_{2,a}{}^{1/4} \cdot \Pi_{3,a}{}^{1/4}, \tag{B.62}$$

$$U_{Schu,a}{}^{*} = \frac{U_{Schu,a}}{H_a N_a} \equiv c_{Schu} \left(g\beta_a \frac{Q_{H,a}}{H_a{}^2 N_a{}^3} \right)^{1/2} = c_{Schu} \cdot \Pi_{3,a}{}^{1/2}. \tag{B.63}$$

Notice that all but the alternative gravity-current hypothesis are proportional to $\Pi_{3,a}{}^{1/2} = \left[g\beta_a Q_{H,a} / \left(H_a{}^2 N_a{}^3 \right) \right]^{1/2} = \left[g\beta_a Q_{H,a} / \left(N_a{}^3 \right) \right]^{1/2} / H_a$, and after multiplication with $H_a N_a$ are not dependent on the ridge height nor the length of the slope. All five hypotheses are of form

$$U_{\max,a}{}^{*} \equiv \frac{U_{\max,a}}{H_a N_a} = f_U \left(\Pi_{2,a}, \Pi_{3,a} \right) = c \cdot \Pi_{2,a}{}^{m_1} \cdot \Pi_{3,a}{}^{m_2}, \tag{B.64}$$

where

$$\Pi_{2,a} = E_a \cdot \frac{N_a}{Q_{H,a}},$$

$$\Pi_{3,a} = g\beta_a \cdot \frac{Q_{H,a}}{H_a{}^2 N_a{}^3}.$$

Nonlinear regression of the field data of July 25 and 26 until 1230 PDT for model (B.64) gives mean values and standard errors of estimate such that

$$U_{\max,a}^* = (5 \pm 17) \cdot \Pi_{2,a}^{\pm 0.3} \cdot \Pi_{3,a}^{(0.6 \pm 0.3)}. \tag{B.65}$$

Alternatively, applying the base-10 logarithm, $\lg \equiv \log_{10}$, to both sides of (B.64) results in[7]

$$\lg\left(U_{\max,a}^*\right) = \lg c + m_1 \cdot \lg \Pi_{2,a} + m_2 \cdot \lg \Pi_{3,a}, \tag{B.66}$$

and multiple linear regression for the same data gives,

$$\lg\left(U_{\max,a}^*\right) = (\pm 2) + (0.1 \pm 0.4) \cdot \lg \Pi_{2,a} + (0.4 \pm 0.4) \cdot \lg \Pi_{3,a}. \tag{B.67}$$

or, substituting the coefficients from (B.67) into (B.64),

$$U_{\max,a}^* = 10^{(\pm 2)} \Pi_{2,a}^{(0.1 \pm 0.4)} \Pi_{3,a}^{(0.4 \pm 0.4)}. \tag{B.68}$$

The (adjusted) multiple regression coefficient R^2 is 0.57. Notice that this result differs from (B.65), because application of the base-10 logarithm to (B.64) introduces weights to the residuals and therefore alters the values of c, m_1, and m_2 for which the sum of the variances is minimal. Both results, however, give such large coefficients that (B.68) is practically useless as an empirical formula for maximum upslope flow velocity. I will investigate this further now using the slightly inaccurate linear representation (B.67), which is visually more intuitive.

Figure Appendix IV shows $\lg U_{\max,a}^*$ separately as a function of $\lg \Pi_{2,a}$ and $\lg \Pi_{3,a}$. The large errors can partly be attributed to measurement uncertainties. For example, in some cases values near the surface, in particular within the bottom 100 m, were missing or the signal-to-noise ratio was very small. Furthermore, the upslope flow velocity in Schumann's (1990) LES showed strong oscillations on the order of 30 minutes. The sodar requires 20-minutes integrations for the velocity signal to stand out from the turbulent background noise. If such oscillations were also present at the field site they will have introduced substantial unsteadiness during the integration period.

[7] See section 4.2 in Jaynes (2003) for an interesting digression on the Weber-Fechner law in human perception and the more intuitive character of the base 10 logarithm.

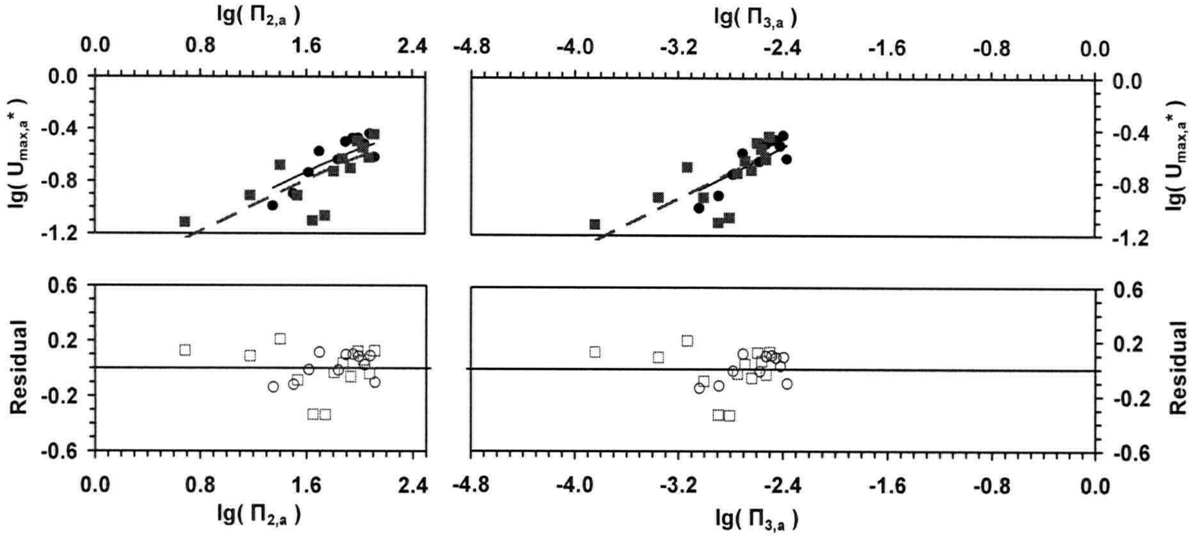

Figure Appendix IV: Multiple regression of ND maximum upslope flow velocity $U_{\max,a}{}^*$ *as function of* $\Pi_{2,a}$ *and* $\Pi_{3,a}$.

Top: Base-10 logarithm of ND maximum upslope flow velocity $U_{\max,a}{}^* = U_{\max,a} / H_a N_a$ *of field observations on July 25 (black filled circles) and 26 (red filled squares) as a function of the base-10 logarithm of* $\Pi_{2,a} = E_a N_a / Q_{H,a}$ *(top left) and* $\Pi_{3,a} = g\beta_a Q_{H,a} / H_a{}^2 N_a{}^3$ *(top right). The lines in the top panels show the predicted values of* $U_{\max,a}{}^* = U_{\max,a} / H_a N_a$ *from the multiple regression for July 25 (black solid line) and 26 (red dashed line). Bottom: The markers show the residual (observed minus predicted) as a function of* $\lg \Pi_{2,a} = \log_{10} \Pi_{2,a}$ *(bottom left) and* $\lg \Pi_{3,a}$ *(bottom right) for July 25 (black open circles) and 26 (red open squares). Vertical and horizontal scales are identical in all four graphs.*

Despite these sources of uncertainties it appears counter-intuitive, given the data distribution in Figure Appendix IV, that the slopes m_1 and m_2 could be negative for both Pi groups. The underlying reason for the large errors is that the two Pi groups are correlated for the atmosphere, with a coefficient of correlation between $\lg \Pi_2$ and $\lg \Pi_3$ of 0.98. Substituting (3.22) and (3.25) into (3.31) and (3.32) gives

$$\Pi_{2,a} = N_a t_{d,a} \cdot \frac{2}{\pi} \cdot \frac{1 - \cos\left(\dfrac{\pi}{2} \dfrac{t_a}{t_{d,a}}\right)}{\sin\left(\dfrac{\pi}{2} \dfrac{t_a}{t_{d,a}}\right)} \tag{B.69}$$

and

$$\Pi_{3,a} = \frac{g\beta_a Q_{\max,a}}{H_a^{\ 2} N_a^{\ 3}} \cdot \sin\left(\frac{\pi}{2}\frac{t_a}{t_{d,a}}\right). \tag{B.70}$$

Therefore, the two Pi groups $\Pi_{2,a}$ and $\Pi_{3,a}$ are coupled via atmospheric reference time t_a. It is possible to form two new, exactly decoupled Pi groups, but these would have a complicated non-monomial relationship to the old Pi groups. It is more instructive to decouple the Pi groups approximately. Let

$$\Pi_{3,a}' \equiv \frac{\Pi_{3,a}}{\Pi_{2,a}} = \frac{\pi}{2}\frac{g\beta_a Q_{\max,a}}{H_a^{\ 2} N_a^{\ 4} t_{d,a}} \frac{\sin^2\left(\frac{\pi}{2}\frac{t_a}{t_{d,a}}\right)}{1-\cos\left(\frac{\pi}{2}\frac{t_a}{t_{d,a}}\right)}. \tag{B.71}$$

Data are only considered for the first 4.5 hours of the 7.75 hours from zero to maximum heat flux; so I replace the trigonometric functions in (B.71) by third-order Taylor approximations,

$$\sin\left(\frac{\pi}{2}\frac{t_a}{t_{d,a}}\right) \approx \left(\frac{\pi}{2}\frac{t_a}{t_{d,a}}\right) - \frac{1}{6}\left(\frac{\pi}{2}\frac{t_a}{t_{d,a}}\right)^3 \tag{B.72}$$

and

$$\cos\left(\frac{\pi}{2}\frac{t_a}{t_{d,a}}\right) \approx 1 - \frac{1}{2}\left(\frac{\pi}{2}\frac{t_a}{t_{d,a}}\right)^2 \tag{B.73}$$

to get

$$\Pi_{3,a}' \approx \frac{\pi g\beta_a Q_{\max,a}}{H_a^{\ 2} N_a^{\ 4} t_{d,a}}\left[1 - \frac{1}{6}\left(\frac{\pi}{2}\frac{t_a}{t_{d,a}}\right)^2\right]^2 \approx \frac{\pi g\beta_a Q_{\max,a}}{H_a^{\ 2} N_a^{\ 4} t_{d,a}}. \tag{B.74}$$

The last approximation holds within about 25% for atmospheric observations until 1230 PDT. The new set of Pi groups, $\Pi_{2,a}$ and $\Pi_{3,a}'$, is now mostly decoupled because $\Pi_{3,a}'$ only weakly depends on atmospheric reference time t_a (correlation coefficient is 0.29). I now look for a monomial relationship of form,

$$U_{\max,a}{}^* = c \cdot \Pi_{2,a}{}^{m_1} \cdot \left(\Pi_{3,a}'\right)^{m_2}. \tag{B.75}$$

Nonlinear regression of the field data of July 25 and 26 until 1230 PDT for model (B.75) gives mean values and standard errors of estimate such that

$$U_{\max,a}{}^{*} = (5 \pm 17) \cdot \Pi_{2,a}{}^{(0.6\pm0.1)} \cdot \left(\Pi_{3,a}{}'\right)^{(0.6\pm0.3)}. \tag{B.76}$$

Alternatively, applying the base-10 logarithm to (B.75),

$$\lg\left(U_{\max,a}{}^{*}\right) = \lg c + m_1 \cdot \lg \Pi_{2,a} + m_2 \cdot \lg \Pi_{3,a}{}', \tag{B.77}$$

I can now carry out a multiple linear regression to get

$$\lg\left(U_{\max,a}{}^{*}\right) = (\pm 2) + (0.5 \pm 0.1) \cdot \lg \Pi_{2,a} + (0.4 \pm 0.4) \cdot \lg \Pi_{3,a}{}' \tag{B.78}$$

or

$$U_{\max,a}{}^{*} = 10^{(\pm 2)} \Pi_{2,a}{}^{(0.5\pm0.1)} \left(\Pi_{3,a}{}'\right)^{(0.4\pm0.4)} \tag{B.79}$$

with the same regression coefficient $R^2 = 0.57$, but a much smaller uncertainty in $\Pi_{2,a}$ as before in (B.68).

This new result is more intuitive than the previous. Plotting again $\lg U_{\max,a}{}^{*}$ separately as a function of $\lg \Pi_{2,a}$ and $\lg \Pi_{3,a}{}'$, it can be seen that the field observations cover only a very narrow range of $\lg \Pi_{3,a}{}'$ far from the origin (Figure Appendix V, top right). Because $\Pi_{2,a}$ and $\Pi_{3,a}{}'$ are only weakly coupled, $\Pi_{2,a}$ is not much affected by the large error in $\Pi_{3,a}{}'$.

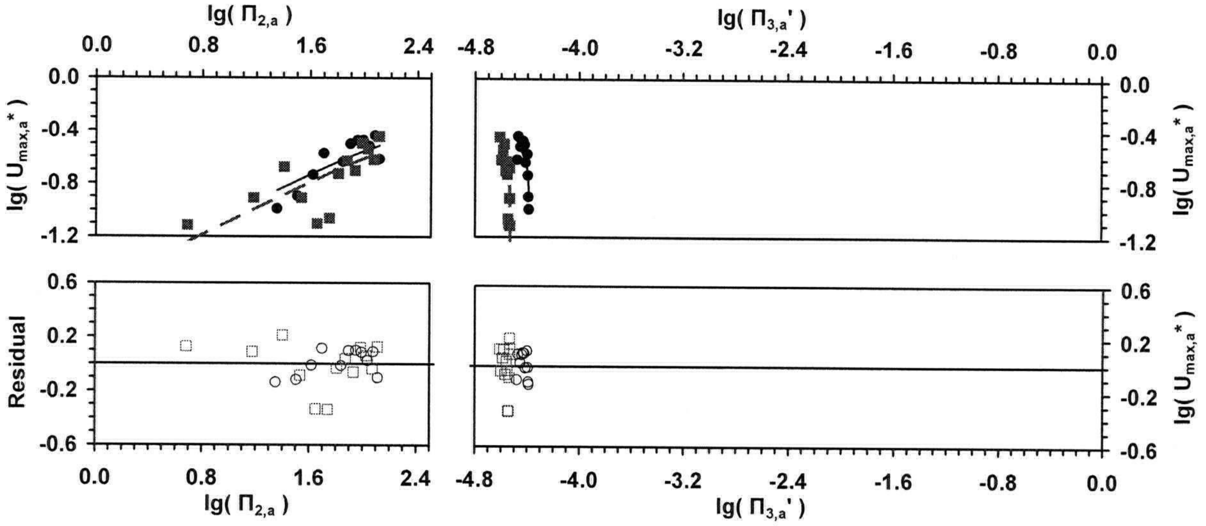

Figure Appendix V: Multiple regression of ND maximum upslope flow velocity $U_{\max,a}*$ as function of $\Pi_{2,a}$ and $\Pi_{3,a}' = \Pi_{3,a}/\Pi_{2,a}$.

Same as Figure Appendix IV, but with $\Pi_{3,a}$ replaced by $\Pi_{3,a}' = \Pi_{3,a}/\Pi_{2,a}$.

In conclusion, it is impossible with the field data from Minnekhada Park to establish a reliable empirical relationship between $\lg U_{\max,a}*$ and $\lg \Pi_{3,a}'$. Is it possible, however, to reject or confirm any of the upslope flow velocity hypotheses discussed above? Using (B.71), hypotheses (B.59)-(B.63) can be re-written in terms of $\Pi_{2,a}$ and $\Pi_{3,a}'$:

$$U_{Hunt,a}* = c_{Hunt} \cdot \Pi_{2,a}^{1/6} \cdot \Pi_{3,a}^{1/2} = c_{Hunt} \cdot \Pi_{2,a}^{2/3} \cdot (\Pi_{3,a}')^{1/2} \text{ (Hunt),} \qquad \text{(B.80)}$$

$$U_{Chen,a}* = c_{Chen} \cdot 2^{1/2} \cdot \Pi_{2,a}^{1/2} \cdot \Pi_{3,a}^{1/2} = c_{Chen} \cdot 2^{1/2} \cdot \Pi_{2,a} \cdot (\Pi_{3,a}')^{1/2} \text{ (Chen),} \qquad \text{(B.81)}$$

$$U_{fric,a}* = 0.322 \cdot 2^{1/2} \cdot \Pi_{2,a}^{1/2} \cdot \Pi_{3,a}^{1/2} = 0.322 \cdot 2^{1/2} \cdot \Pi_{2,a} \cdot (\Pi_{3,a}')^{1/2} \text{ (friction),} \qquad \text{(B.82)}$$

$$U_{Grav}* = c_{Grav} \cdot \Pi_{2,a}^{1/4} \cdot \Pi_{3,a}^{1/4} = c_{Grav} \cdot \Pi_{2,a}^{1/2} \cdot (\Pi_{3,a}')^{1/4} \text{ (gravity current),} \qquad \text{(B.83)}$$

$$U_{Schu,a}* = c_{Schu} \cdot \Pi_{3,a}^{1/2} = c_{Schu} \cdot \Pi_{2,a}^{1/2} \cdot (\Pi_{3,a}')^{1/2} \text{ (Schumann),} \qquad \text{(B.84)}$$

where the factors c_{Hunt}, c_{Chen}, c_{Grav}, and c_{Schu} contain constants and for Hunt and Schumann a dependence on Π_1. Notice that the friction hypothesis is a special case of the Chen hypothesis. It is not possible to reject any of the hypotheses based on (B.68) because of the large uncertainties. However, a comparison with (B.76) suggests rejecting the Chen and friction hypotheses. To explore this further, I apply hypotheses (B.80), (B.81), (B.83), and (B.84) to the field observations and carry out linear regressions to determine the unknown coefficients:

$$c_{Hunt} = 2.4 \pm 0.1 \text{ with } r^2 = 0.91, \tag{B.85}$$

$$c_{Chen} = 0.37 \pm 0.02 \text{ with } r^2 = 0.89, \tag{B.86}$$

$$c_{Grav} = 0.37 \pm 0.02 \text{ with } r^2 = 0.91,^{8} \tag{B.87}$$

$$c_{Schu} = 5.0 \pm 0.2 \text{ with } r^2 = 0.91. \tag{B.88}$$

Based on (B.86) I should reject the friction hypothesis because its coefficient 0.322 is in the tail outside the lower 95 percentile (0.327) of c_{Chen}. Substitution of the latter equations into (B.80), (B.81), (B.83), and (B.84) gives

$$U_{Hunt,a}* = 2.4\Pi_2^{1/6} \cdot \Pi_3^{1/2}, \tag{B.89}$$

$$U_{Chen,a}* = 0.37 \cdot 2^{1/2}\Pi_2^{1/2} \cdot \Pi_3^{1/2}, \tag{B.90}$$

$$U_{Grav}* = 0.37\Pi_2^{1/4} \cdot \Pi_3^{1/4}, \tag{B.91}$$

$$U_{Schu,a}* = 5.0\Pi_3^{1/2}. \tag{B.92}$$

A comparison of these hypotheses with the observations is shown in Figure Appendix VI, which is a common way of representation (e.g. Steyn, 2003). For all four hypotheses the agreement is reasonably good and surprisingly similar. This form of representation masks differences between hypotheses, probably because two dimensions ($\Pi_{2,a}$ and $\Pi_{3,a}$) are merged into one dimension (e.g. $2.4\Pi_{2,a}^{1/6}\,\Pi_{3,a}^{1/2}$ in Hunt's et al. hypothesis).

---

[8] It is not a copy-and-paste error that c_{Chen} and c_{Grav} are equal.

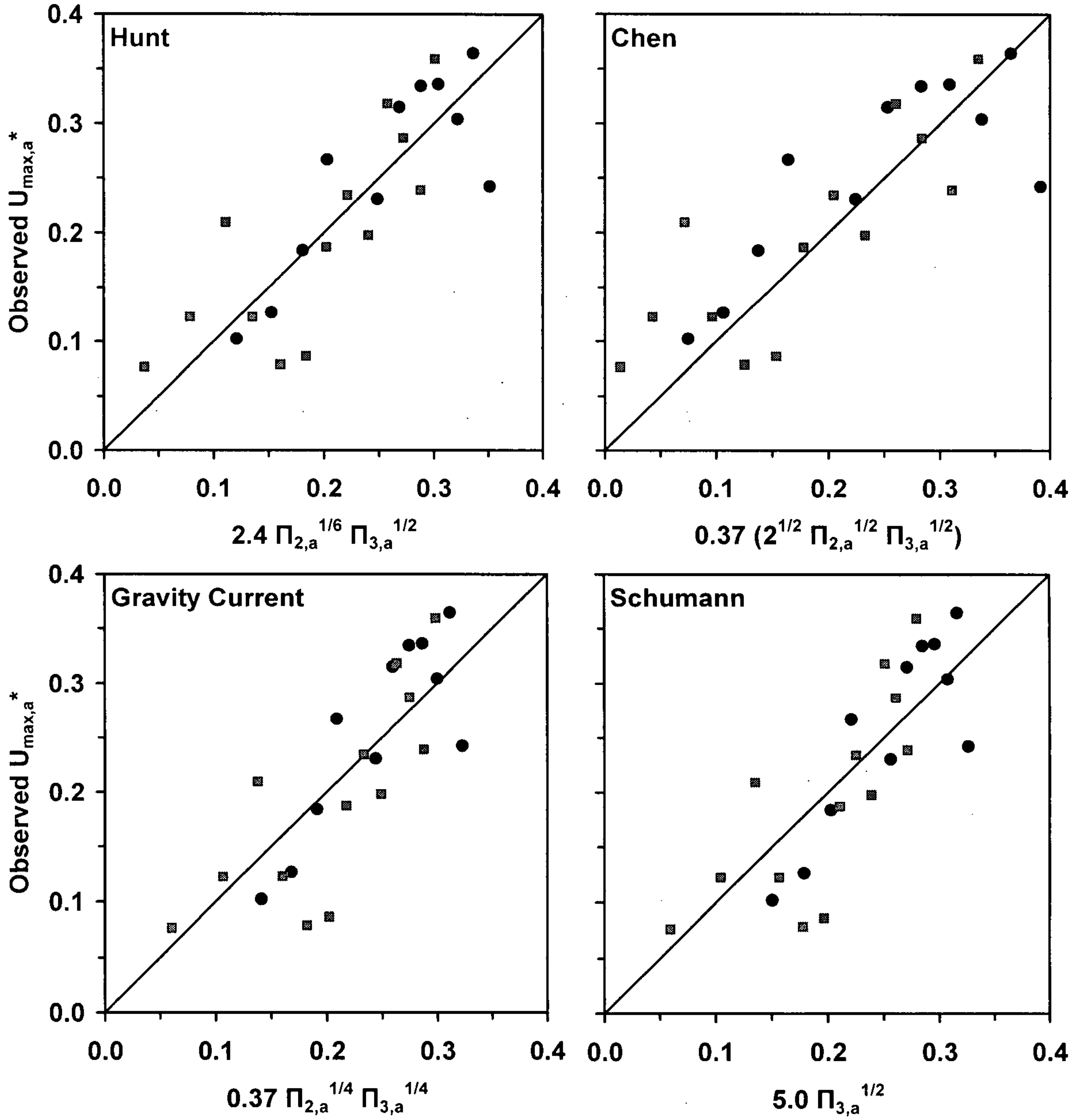

Figure Appendix VI: Comparison of fitted upslope flow velocity hypotheses with field observations in ND form. ND maximum upslope flow velocities (ordinates) are shown for field observations on July 25 (black circles) and July 26 (red squares), only until 1230 PDT, against four different hypotheses of ND maximum upslope flow velocity (abscissae), where the constant factors were fitted. Ordinates and abscissae are of equal scale.

A better way of highlighting the differences between the hypotheses is a dimensional representation separated by the two days of the field study (Figure Appendix VII). Clearly the fitted Hunt, gravity-current, and Schumann hypotheses provide a better fit to the data than the friction and fitted Chen hypotheses (remembering that all curves have to pass through zero velocity at 0800 PTD).

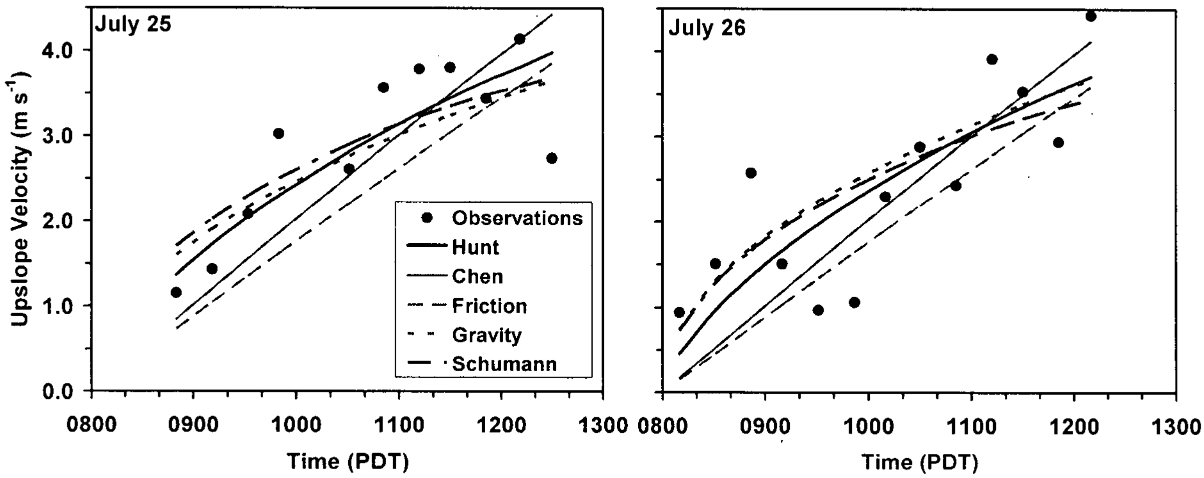

Figure Appendix VII: Comparison of fitted upslope flow velocity hypotheses with field observations in dimensional form.

Data points are field observations of the maximum value in vertical profiles of upslope flow velocity measured by Doppler sodar over the plain near the foot of the slope at Minnekhada Park as a function of time of day on July 25, 2001 (left) and July 26 (right). The curves are predictions derived from different upslope flow velocity hypotheses as shown in the legend in the left graph.

One could proceed by carrying out a formal statistical hypothesis test. Concerns have been raised by researchers, who use probability theory as extended logic, against statistical hypothesis tests with regards to the assumption of a null hypothesis and the optional stopping problem (Jaynes, 2003, and Gregory, 2005). These problems can be avoided and additional insight into the data can be gained by applying probability theory as extended logic to the data. I introduce the methodology in Appendix B.3 and present the results in section 3.4.2.

B.3 Hypothesis Comparison and Parameter Estimation Using Probability Theory

Probability theory as extended logic provides a common and simple framework to explore data. What I will briefly demonstrate here is what is typically called 'Bayesian model comparison' (e.g. Sivia, 1996). Jaynes (2003) avoided the term 'Bayesian analysis' and argued that statistics of random variables and Bayesian analysis are both special cases of probability theory, with the latter being more general than the former. Furthermore, in line with my earlier arguments I avoid the term 'model' and use 'hypothesis' instead. In this section I will derive the equations used in section 3.5 for comparing the four hypotheses for the maximum upslope flow velocity and the joint probability distribution for the two exponents of the Pi groups in a simple monomial model of non-dimensional (ND) maximum upslope flow velocity. One only needs a basic understanding of probability theory to follow my arguments; the interested reader can find more details and explanations in Gregory (2005).

The basic question I asked from the data in section 3.5 was: What are the relative probabilities of the four hypotheses (B.80)-(B.84) for the upslope flow velocity given the field observations of maximum upslope flow velocities at Minnekhada Park on the morning of July 25 and 26, 2001?

I repeat here the propositions formulated in section 3.5.

- I = "The maximum value in the vertical profile of upslope flow velocity at the foot of Minnekhada Park was measured every 20 minutes from 0850-1230 PDT on July 25 and 0810-1210 PDT on July 26, 2001. Maximum upslope flow velocity was non-dimensionalised by dividing by ridge height $H_a = 760\,m$ and buoyancy frequency $N_a = 0.0149\,s^{-1}$ on July 25 and $N_a = 0.0162\,s^{-1}$ on July 26. It is assumed that the ND maximum upslope flow velocity can be expressed as a monomial plus independent, identically distributed Gaussian background noise of unknown but equal variance." (Background information)

- D = "The observed $n = 23$ data were $d_i = \ldots$, where $i = 1,\ldots,n$" (Statement on the data)

- $H^{(1)}$ = "The ideal data are described by $f^{(1)}{}_i = U_{Hunt,a}{}^* = c^{(1)} \cdot \Pi_{2,i}{}^{1/6} \cdot \Pi_{3,i}{}^{1/2}$, $i = 1,\ldots,n$." (Hypothesis by Hunt et al.)

- $H^{(2)}$ = "The ideal data are described by $f^{(2)}{}_i = U_{Chen,a}{}^* = c^{(2)} \cdot \Pi_{2,i}{}^{1/2} \cdot \Pi_{3,i}{}^{1/2}$, $i = 1,\ldots,n$." (Hypothesis by Chen et al.)

- $H^{(3)}$ = "The ideal data are described by $f^{(3)}{}_i = U_{Grav}{}^* = c^{(3)} \cdot \Pi_{2,i}{}^{1/4} \cdot \Pi_{3,i}{}^{1/4}$, $i = 1,\ldots,n$." (Gravity-current hypothesis)

- $H^{(4)}$ = "The ideal data are described by $f^{(4)}{}_i = U_{Schu,a}{}^* = c^{(4)} \cdot \Pi_{3,i}{}^{1/2}$, $i = 1,\ldots,n$." (Hypothesis by Schumann)

I will assume that the constant factors $c^{(1)}$ to $c^{(4)}$ are unknown within set limits. Let $p\left(D, H^{(j)} \middle| I\right)$ denote the conditional probability that both D and $H^{(j)}$ are true[9], given that I is true. This expression can be re-written using the product rule of probability theory,

$$p\left(D, H^{(j)} \middle| I\right) = p\left(D \middle| H^{(j)}, I\right) p\left(H^{(j)} \middle| I\right) \tag{B.93}$$

Likewise,

$$p\left(H^{(j)}, D \middle| I\right) = p\left(H^{(j)} \middle| D, I\right) p\left(D \middle| I\right). \tag{B.94}$$

Because

$$p\left(D, H^{(j)} \middle| I\right) = p\left(H^{(j)}, D \middle| I\right), \tag{B.95}$$

(B.93) and (B.94) can be combined to give Bayes' theorem

$$p\left(H^{(j)} \middle| D, I\right) = \frac{p\left(H^{(j)} \middle| I\right) p\left(D \middle| H^{(j)}, I\right)}{p\left(D \middle| I\right)}. \tag{B.96}$$

The LHS of the last equation, $p\left(H^{(j)} \middle| D, I\right)$, is the quantity I seek in section 3.5, i.e. the conditional probability of the hypothesis $H^{(j)}$ given the data D and the background information I. Bayes' theorem is always the starting point for any Bayesian data analysis problem; the difficulty in this consistent approach lies in determining the RHS of (B.96). $p\left(H^{(j)} \middle| I\right)$ is the prior probability of hypothesis $H^{(j)}$ before the data were considered. $p\left(D \middle| H^{(j)}, I\right)$ is the likelihood of the data, given hypothesis $H^{(j)}$, or simply the sampling distribution. Finally,

---

[9] I follow the common practice to use ',' as a short-hand notation for the conjunction or logical 'AND'.

$p(D|I)$ is the global likelihood, 'global' across the hypothesis space $\{H^{(1)}, H^{(2)}, H^{(3)}, H^{(4)}\}$. I will now treat each of the three factors separately.

Beginning with the prior probabilities, before considering the data I do not prefer any hypothesis over the others, i.e.

$$p\left(H^{(j)}\middle|I\right) = \frac{1}{4} \quad \text{for all } j = 1, \ldots, 4. \tag{B.97}$$

Next I consider the global likelihood. The probability of the entire hypothesis space $\{H^{(1)}, H^{(2)}, H^{(3)}, H^{(4)}\}$ must be equal to one, i.e.

$$\sum_{j=1}^{4} p\left(H^{(j)}\middle|D, I\right) = \sum_{j=1}^{4} \frac{p\left(H^{(j)}\middle|I\right) p\left(D\middle|H^{(j)}, I\right)}{p(D|I)} = 1, \tag{B.98}$$

from which I get, using (B.97),

$$p(D|I) = \sum_{j=1}^{4} p\left(H^{(j)}\middle|I\right) p\left(D\middle|H^{(j)}, I\right) = \frac{1}{4} \sum_{j=1}^{4} p\left(D\middle|H^{(j)}, I\right). \tag{B.99}$$

The global likelihood is therefore a normalisation constant.

Finally, I will investigate the likelihood $p(D|H, I)$. In the background information it was assumed that the data d_i are contaminated with Gaussian noise e_i of unknown variance σ^2. In the j$^{\text{th}}$ hypothesis, each datum can therefore be expressed as

$$d_i = f^{(j)}{}_i + e_i. \tag{B.100}$$

It is customary to use the same symbol p to denote both probabilities of propositions and numerical values. Let D_i denote the proposition that the i$^{\text{th}}$ datum is d_i, so that $D = D_1, \ldots, D_n$, where ',' is a shorthand notation for 'and'. Similarly define $E = E_1, \ldots, E_n$ for the errors. The sampling distribution of the noise is Gaussian,

$$p\left(E_i\middle|\sigma^{(j)}, H^{(j)}, I\right) = \frac{1}{\sqrt{2\pi}\,\sigma^{(j)}} \exp\left(-\frac{e_i^2}{2\left(\sigma^{(j)}\right)^2}\right), \tag{B.101}$$

for given standard deviation $\sigma^{(j)}$. Substituting e_i from (B.100) gives the sampling distribution of the data

$$p\left(D_i \middle| c^{(j)}, \sigma^{(j)}, H^{(j)}, I\right) = \frac{1}{\sqrt{2\pi}\,\sigma^{(j)}} \exp\left[-\frac{\left(d_i - f^{(j)}{}_i\right)^2}{2\left(\sigma^{(j)}\right)^2}\right], \tag{B.102}$$

for given standard deviation $\sigma^{(j)}$ and constant coefficient $c^{(j)}$. Now recall from the background information that we can assume the individual data to be independent of each other and that the noise is independent and identically distributed. From the product rule,

$$p\left(D_1, D_2 \middle| I\right) = p\left(D_1 \middle| D_2, I\right) p\left(D_2 \middle| I\right) = p\left(D_1 \middle| I\right) p\left(D_2 \middle| I\right) \tag{B.103}$$

because the conditional probability of D_1 is independent of the truth of D_2. This can be generalised to

$$p\left(D_1, \ldots, D_n \middle| c^{(j)}, \sigma^{(j)}, H, I\right) = p\left(D_1 \middle| c^{(j)}, \sigma^{(j)}, H, I\right) \cdots p\left(D_n \middle| c^{(j)}, \sigma^{(j)}, H, I\right). \tag{B.104}$$

Applying (B.102) to (B.104) gives

$$\begin{aligned} p\left(D \middle| c^{(j)}, \sigma^{(j)}, H^{(j)}, I\right) &= \prod_{i=1}^{n} \frac{1}{\sqrt{2\pi}\,\sigma^{(j)}} \exp\left[-\frac{\left(d_i - f^{(j)}{}_i\right)^2}{2\left(\sigma^{(j)}\right)^2}\right] \\ &= \frac{1}{\left(2\pi\right)^{n/2}\left(\sigma^{(j)}\right)^n} \exp\left[-\frac{1}{2\left(\sigma^{(j)}\right)^2} \sum_{i=1}^{n} \left(d_i - f^{(j)}{}_i\right)^2\right]. \end{aligned} \tag{B.105}$$

One more step, marginalisation, is required to get an expression for the likelihood $p\left(D \middle| H^{(j)}, I\right)$. Applying equation (3.8) in Gregory (2005) to the proposition used here gives,

$$p\left(D \middle| \sigma^{(j)}, H^{(j)}, I\right) = \int_{c^{(j)}{}_L}^{c^{(j)}{}_H} dc^{(j)}\, p\left(c^{(j)} \middle| \sigma^{(j)}, H^{(j)}, I\right) p\left(D \middle| c^{(j)}, \sigma^{(j)}, H^{(j)}, I\right), \tag{B.106}$$

where the integral is over a prior range of $c^{(j)}$ that is wide enough to neglect the tails of the probability distributions in the integrand. Marginalisation therefore integrates out 'nuisance' parameters, which are not of interest in the particular step of the analysis. Repeating the same step for $\sigma^{(j)}$ gives

$$p\left(D \middle| H^{(j)}, I\right) = \int_{\sigma^{(j)}_L}^{\sigma^{(j)}_H} d\sigma^{(j)} p\left(\sigma^{(j)} \middle| H^{(j)}, I\right) p\left(D \middle| \sigma^{(j)}, H^{(j)}, I\right). \tag{B.107}$$

Substituting (B.106) into (B.107) and noticing that $p\left(c^{(j)} \middle| \sigma^{(j)}, H^{(j)}, I\right) = p\left(c^{(j)} \middle| H^{(j)}, I\right)$, because the constant factors $c^{(j)}$ are independent of $\sigma^{(j)}$,

$$p\left(D \middle| H^{(j)}, I\right) = \int_{\sigma^{(j)}_L}^{\sigma^{(j)}_H} d\sigma^{(j)} p\left(\sigma^{(j)} \middle| H^{(j)}, I\right) \int_{c^{(j)}_L}^{c^{(j)}_H} dc^{(j)} p\left(c^{(j)} \middle| H^{(j)}, I\right) p\left(D \middle| c^{(j)}, \sigma^{(j)}, H^{(j)}, I\right). \tag{B.108}$$

Ignorance about the prior values of $\sigma^{(j)}$ and $c^{(j)}$ within a lower and upper boundary can be accounted for in two fundamentally different ways (Gregory, 2005). 'Location' parameters can be either positive or negative and usually have a relatively narrow prior range. 'Scale parameters' are always positive and the lower and upper boundaries often span several orders of magnitude. The standard deviation by definition can only be positive and is usually treated as a scale parameter. Also the constant factors $c^{(j)}$ can only be positive, because we do not expect negative velocities. Therefore I will treat both $\sigma^{(j)}$ and $c^{(j)}$ as scale parameters. Now assume that the standard deviation spans several orders of magnitude, for example from $\sigma_L = 0.01$ to $\sigma_H = 10$. Total ignorance about the value within the entire range requires that the probability of finding the true value within 0.01-0.1 is equal to the probability of finding the true value within 0.1-1 or 1-10. This is achieved with a Jeffreys prior:

$$p\left(\sigma^{(j)} \middle| H^{(j)}, I\right) = \frac{1}{\sigma^{(j)} \ln\left(\sigma_H / \sigma_L\right)}, \tag{B.109}$$

and likewise

$$p\left(c^{(j)} \middle| H^{(j)}, I\right) = \frac{1}{c^{(j)} \ln\left(c_H / c_L\right)}, \tag{B.110}$$

where I choose the prior ranges to be equal for all four hypotheses. Substitution of (B.105), (B.109), and (B.110) into (B.108) gives

$$p\left(D \middle| H^{(j)}, I\right) = \frac{1}{\ln\left(\sigma_H / \sigma_L\right) \ln\left(c_H / c_L\right) \left(2\pi\right)^{n/2}} \int_{c_L}^{c_L} dc \int_{\sigma_L}^{\sigma_H} d\sigma \frac{1}{c\,\sigma^{n+1}} \exp\left[- \frac{\sum_{i=1}^{n} \left(d_i - f^{(j)}{}_i\right)^2}{2\sigma^2} \right], \tag{B.111}$$

where I dropped the superscript '(j)' in c and σ since the integration is now over the same range.

Both integrals can be manipulated and solved in terms of the error function and the incomplete gamma function. Here, however, it is more beneficial to approximate the integrals by sums, because the integrand is proportional to the joint probability distribution $p\left(c^{(j)},\sigma^{(j)}\middle|D,H^{(j)},I\right)$ of the two unknown parameters $\sigma^{(j)}$ and $c^{(j)}$. To see this, apply Bayes' theorem (B.96) to $p\left(c^{(j)},\sigma^{(j)}\middle|D,H^{(j)},I\right)$,

$$p\left(c^{(j)},\sigma^{(j)}\middle|D,H^{(j)},I\right)=\frac{p\left(c^{(j)},\sigma^{(j)}\middle|H^{(j)},I\right)p\left(D\middle|c^{(j)},\sigma^{(j)},H^{(j)},I\right)}{p\left(D\middle|H^{(j)},I\right)} \tag{B.112}$$

and the product rule (B.93) to $p\left(c^{(j)},\sigma^{(j)}\middle|H^{(j)},I\right)$,

$$p\left(c^{(j)},\sigma^{(j)}\middle|H^{(j)},I\right)=p\left(c^{(j)}\middle|H^{(j)},I\right)p\left(\sigma^{(j)}\middle|H^{(j)},I\right) \tag{B.113}$$

where I made use of the independence of $\sigma^{(j)}$ and $c^{(j)}$. Substituting (B.113) into (B.112) gives

$$\begin{aligned} p\left(c^{(j)},\sigma^{(j)}\middle|D,H^{(j)},I\right) &\propto p\left(c^{(j)}\middle|H^{(j)},I\right)p\left(\sigma^{(j)}\middle|H^{(j)},I\right)p\left(D\middle|c^{(j)},\sigma^{(j)},H^{(j)},I\right) \\ &\propto \frac{1}{c^{(j)}\left(\sigma^{(j)}\right)^{n+1}}\exp\left[-\frac{1}{2\left(\sigma^{(j)}\right)^{2}}\sum_{i=1}^{n}\left(d_i-f^{(j)}{}_i\right)^2\right], \end{aligned} \tag{B.114}$$

where the RHS of (B.114) is the integrand in (B.108) and (B.111). The last equation permits independent tests of the algorithm for solving (B.111) and shows if the range of integration in (B.111) is wide enough to neglect the tails and if the steps in the numerical approximation of the integrals of (B.111) are small enough.

I now have all the information together to calculate the probability of each of the four models given the field data. Substituting (B.97), (B.99), and (B.111) into (B.96) and dropping all constants of proportionality,

$$p\left(H^{(j)}\middle|D,I\right) \propto \int_{c_L}^{c_L} dc \int_{\sigma_L}^{\sigma_H} d\sigma \frac{1}{c\,\sigma^{n+1}} \exp\left[-\frac{1}{2\sigma^2}\sum_{i=1}^{n}\left(d_i - f^{(j)}{}_i\right)^2\right]$$

$$\propto \sum_{c_k=c_L}^{c_H} \sum_{\sigma_l=\sigma_L}^{\sigma_H} \frac{1}{c_k\,\sigma_l^{\,n+1}} \exp\left[-\frac{\sum_{i=1}^{n}\left(d_i - c_k \cdot \Pi_{2,i}{}^{m_1^{(j)}} \cdot \Pi_{3,i}{}^{m_2^{(j)}}\right)^2}{2\sigma_l^2}\right], \tag{B.115}$$

where I approximated the integrals in the first line by sums in the second line and substituted the general form of the four models for $f^{(j)}{}_i$; $m_1^{(j)}$ and $m_2^{(j)}$ have to be replaced by the respective exponents of the four hypotheses.

Figure Appendix VII demonstrates that the friction hypothesis performs worse than the other hypotheses. However, all but the friction hypothesis had an unknown parameter that was fitted to the data, and in most cases the agreement with data improves when more unknown parameters are introduced into a hypothesis. Probability theory (quantitatively) penalises hypotheses for each unknown parameter and thus allows one to decide what degree of complexity is justified by the data. I demonstrate this now by adding the friction hypothesis to the hypothesis space. Again, I only outline the changes to the derivation above and refer the reader to the literature (e.g. Gregory, 2005) for more detailed examples:

- $H^{(5)}$ = "The ideal data are described by $f^{(2)}{}_i = U_{fric,a}{}^* = 0.322 \cdot 2^{1/2} \cdot \Pi_{2,i}{}^{1/2} \cdot \Pi_{3,i}{}^{1/2}$, $i = 1,\ldots,n$." (Friction hypothesis)

Bayes' theorem and most other equations remain unchanged; (B.97) and (B.99) become

$$p\left(H^{(j)}\middle|I\right) = \frac{1}{5} \quad \text{for all } j = 1,\ldots,5, \tag{B.116}$$

$$p\left(D\middle|I\right) = \sum_{j=1}^{5} p\left(H^{(j)}\middle|I\right) p\left(D\middle|H^{(j)},I\right) = \frac{1}{5}\sum_{j=1}^{5} p\left(D\middle|H^{(j)},I\right). \tag{B.117}$$

Only marginalisation over $\sigma^{(5)}$, (B.107), but not over the coefficient, (B.106), is necessary for the friction hypothesis:

$$p\left(D\middle|H^{(j)},I\right) = \int_{\sigma_L}^{\sigma_H} d\sigma^{(j)} p\left(\sigma^{(j)}\middle|H^{(j)},I\right) p\left(D\middle|\sigma^{(j)},H^{(j)},I\right). \tag{B.118}$$

The prior is again given by (B.109),

$$p\left(\sigma^{(5)}\middle|H^{(5)},I\right)=\frac{1}{\sigma^{(5)}\ln\left(\sigma_H/\sigma_L\right)},\tag{B.119}$$

and the sampling distribution follows from (B.105),

$$p\left(D\middle|\sigma^{(5)},H^{(5)},I\right)=\frac{1}{\left(2\pi\right)^{n/2}\left(\sigma^{(5)}\right)^n}\exp\left[-\frac{1}{2\left(\sigma^{(5)}\right)^2}\sum_{i=1}^{n}\left(d_i-f^{(5)}{}_i\right)^2\right].\tag{B.120}$$

Substituting (B.116)-(B.120) into Bayes' theorem (B.96) gives,

$$p\left(H^{(5)}\middle|D,I\right)=\frac{\frac{1}{5}\int\limits_{\sigma_L}^{\sigma_H}d\sigma\frac{1}{\sigma\ln\left(\sigma_H/\sigma_L\right)}\frac{1}{\left(2\pi\right)^{n/2}\sigma^n}\exp\left[-\frac{\sum_{i=1}^{n}\left(d_i-f^{(5)}{}_i\right)^2}{2\sigma^2}\right]}{\frac{1}{5}\sum_{j=1}^{5}p\left(D\middle|H^{(j)},I\right)}\tag{B.121}$$

Notice that only those constants can be dropped in (B.121) and in the derivation of (B.115) that are common to all hypotheses. Revisiting the steps leading to (B.115),

$$p\left(H^{(j)}\middle|D,I\right)\propto\frac{\Delta c}{\ln\left(c_H/c_L\right)}\sum_{c_k=c_L}^{c_H}\sum_{\sigma_l=\sigma_L}^{\sigma_H}\frac{1}{c_k\sigma_l^{\,n+1}}\exp\left[-\frac{\sum_{i=1}^{n}\left(d_i-c_k\cdot\Pi_{2,i}{}^{m_1^{(j)}}\cdot\Pi_{3,i}{}^{m_2^{(j)}}\right)^2}{2\sigma_l^{\,2}}\right],\tag{B.122}$$

and (B.121) becomes

$$p\left(H^{(5)}\middle|D,I\right)\propto\sum_{\sigma_l=\sigma_L}^{\sigma_H}\frac{1}{\sigma_l^{\,n+1}}\exp\left[-\frac{\sum_{i=1}^{n}\left(d_i-0.322\cdot2^{1/2}\cdot\Pi_{2,i}{}^{1/2}\cdot\Pi_{3,i}{}^{1/2}\right)^2}{2\sigma_l^{\,2}}\right].\tag{B.123}$$

The step length Δc in the summation over c in (B.122) is not any longer a common factor. The factor $1/\ln\left(c_H/c_L\right)$ in (B.122) is the penalty, which hypotheses $H^{(1)}$ to $H^{(4)}$ receive for having one more unknown parameter than $H^{(5)}$. Obviously, the penalty depends on the prior range of the constants and the choice of a Jeffreys versus a constant prior. More information is available in the literature (e.g. Gregory, 2005; Sivia, 1996).

The arguments leading to (B.114) demonstrate the close relationship between parameter estimation and hypothesis comparison in probability theory. After the foregoing derivations it is straightforward to find the joint probability distribution $p(m_1, m_2 | D, I)$ for the hypothesis

- H = "The ideal data are described by $f_i = U_a{}^* = c \cdot \Pi_{2,i}{}^{m_1} \cdot \Pi_{3,i}{}^{m_2}$, $i = 1,\dots,n$."

With the same data and background information as before, marginalisation in the most basic form (equation (3.11) in Gregory, 2005) gives

$$p(m_1, m_2 | D, I) = \int_{\sigma_L}^{\sigma_H} \int_{c_L}^{c_H} dc\, d\sigma\, p(m_1, m_2, c, \sigma | D, I). \tag{B.124}$$

Applying Bayes' theorem to the integrand gives

$$p(m_1, m_2, c, \sigma | D, I) \propto p(m_1, m_2, c, \sigma | I)\, p(D | m_1, m_2, c, \sigma, I). \tag{B.125}$$

The first factor on the RHS can be split up using the product rule and assuming that all four parameters m_1, m_2, c, and σ are *a priori* independent of each other,

$$p(m_1, m_2, c, \sigma | I) = p(m_1 | I)\, p(m_2 | I)\, p(c | I)\, p(\sigma | I), \tag{B.126}$$

while the second factor is the sampling distribution

$$p(D | m_1, m_2, c, \sigma, I) = \frac{1}{(2\pi)^{n/2}} \frac{1}{\sigma^n} \exp\left[-\frac{\sum_{i=1}^{n} \left(d_i - c \cdot \Pi_{2,i}{}^{m_1} \cdot \Pi_{3,i}{}^{m_2} \right)^2}{2\sigma^2} \right]. \tag{B.127}$$

Substituting (B.125), (B.126), and (B.127) into (B.124) yields

$$\begin{aligned} p(m_1, m_2 | D, I) \propto & \int_{\sigma_L}^{\sigma_H} \int_{c_L}^{c_H} dc\, d\sigma \cdot p(m_1 | I)\, p(m_2 | I)\, p(c | I)\, p(\sigma | I) \\ & \cdot \frac{1}{(2\pi)^{n/2}} \frac{1}{\sigma^n} \exp\left[-\frac{1}{2\sigma^2} \sum_{i=1}^{n} \left(d_i - c \cdot \Pi_{2,i}{}^{m_1} \cdot \Pi_{3,i}{}^{m_2} \right)^2 \right]. \end{aligned} \tag{B.128}$$

Following the same rationale that led to (B.109) and (B.110), the prior probabilities $p(c | I)$ and $p(\sigma | I)$ can be determined as

$$p(\sigma|I)=\frac{1}{\sigma\ln(\sigma_H/\sigma_L)} \quad \text{and} \quad p(c|I)=\frac{1}{c\ln(c_H/c_L)}. \tag{B.129}$$

By contrast, m_1 and m_2 can be negative and are location parameters, for which a constant prior is the correct choice, i.e.

$$p(m_1|I)=\frac{1}{m_{1,H}-m_{1,L}} \quad \text{and} \quad p(m_2|I)=\frac{1}{m_{2,H}-m_{2,L}}. \tag{B.130}$$

Substituting the last two results into (B.128) gives

$$p(m_1,m_2|D,I)\propto \int_{c_L}^{c_H} dc\frac{1}{c}\int_{\sigma_L}^{\sigma_H} d\sigma\cdot\frac{1}{\sigma^{n+1}}\exp\left[-\frac{1}{2\sigma^2}\sum_{i=1}^{n}\left(d_i-c\cdot\Pi_{2,i}^{\ m_1}\cdot\Pi_{3,i}^{\ m_2}\right)^2\right]. \tag{B.131}$$

Determining the joint probability distribution requires running through five loops, the inner sum over the $n=23$ data points, two for the integrals, and two for establishing the contour plot of $p(m_1,m_2|D,I)$ as a function of m_1 and m_2. On a standard PC that is not feasible, but two substantial simplifications can be applied. Firstly, I require the limits of integration over σ to be so wide that practically $\sigma_L\to 0$ and $\sigma_H\to\infty$. Following the same derivation as those leading to equation (C.17) in Gregory (2005), the inner integral of (B.131) substantially simplifies and I get,

$$\begin{aligned} p(m_1,m_2|D,I) &\propto \int_{c_L}^{c_H} dc\frac{1}{c}\left[\sum_{i=1}^{n}\left(d_i-c\cdot\Pi_{2,i}^{\ m_1}\cdot\Pi_{3,i}^{\ m_2}\right)^2\right]^{-n/2} \\ &\propto \sum_{c_k=c_L}^{c_H}\Delta c_k\frac{1}{c_k}\left[\sum_{i=1}^{n}\left(d_i-c_k\cdot\Pi_{2,i}^{\ m_1}\cdot\Pi_{3,i}^{\ m_2}\right)^2\right]^{-n/2}, \end{aligned} \tag{B.132}$$

where the gamma function that results from the integration is absorbed in the proportionality.

A second simplification is necessary because the lower and upper boundaries of integration must cover a range of approximately eight orders of magnitude in order to gain a fairly complete picture of the joint probability distribution. The integral is replaced by a sum in which both c_k and the step length Δc_k increase exponentially with index k. Let n_s denote the number of steps per order of magnitude, then

$$c_k=c_L\cdot 10^{k/n_s} \quad \Rightarrow \tag{B.133}$$

$$\Delta c_k = c_{k+1} - c_k = c_L \cdot 10^{(k+1)/n_s} - c_L \cdot 10^{k/n_s} = c_L \cdot 10^{k/n_s} \cdot \left(10^{1/n_s} - 1\right), \tag{B.134}$$

so that

$$\frac{\Delta c_k}{c_k} = \frac{c_L \cdot 10^{k/n_s} \cdot \left(10^{1/n_s} - 1\right)}{c_L \cdot 10^{k/n_s}} = 10^{1/n_s} - 1 = const\,. \tag{B.135}$$

The final result for the joint probability distribution therefore becomes

$$p\left(m_1, m_2 \middle| D, I\right) \propto \sum_{k=0}^{k_H} \left[\sum_{i=1}^{n} \left(d_i - c_L \cdot 10^{k/n_s} \cdot \Pi_{2,i}{}^{m_1} \cdot \Pi_{3,i}{}^{m_2} \right)^2 \right]^{-n/2}, \tag{B.136}$$

with $k_H = n_s \cdot \log_{10} \frac{c_H}{c_L}$ and n_s the number of steps per order of magnitude in c. In this form the joint probability distribution can be computed with very good resolution on a standard PC in about one hour.

Contour plots of the joint probability distributions (B.114) and (B.136) for the field data are shown in section 3.4.2.

B.4 Two Atmospheric Test Cases and Their Corresponding Water-Tank Experiments

Given the independent water-tank parameters in Table 3.3 on page 50, is it technically feasible to model the field observations of July 25 and 26, 2001? For example, in section 3.6 an atmospheric reference time of 1200 PDT corresponded to a water-tank reference time of 5 minutes. This is long enough to be able to measure many vertical profiles of specific volume at a fine resolution. Table Appendix I below shows part of a spreadsheet, which I used during my trial and error of the scaling.

The quantities of particular interest are: the water-tank reference time t_w; the buoyancy frequency N_w, which determines the required amount of salt; the CBL mean temperature increment T_w and specific volume increment $\alpha_{s,w}$; and the maximum upslope flow velocity

$U_{\max,w}$. The values in the spreadsheet are all technically achievable, and measurements are feasible.

The non-dimensional (ND) vertical convection time t_v* and the ND horizontal advection time t_h* in the lower part of Table Appendix I have the same values for atmospheric idealisation (AI) and water-tank idealisation (WTI), a consequence of the matching of Π_1 to Π_3. The ND quantities in the last six lines, which are often used in fluid dynamics, will be discussed in the section B.6.

Table Appendix I (next two pages): Two test cases extracted from a spreadsheet to facilitate Buckingham Pi analysis.
Quantities in the upper third above the horizontal line are constant; potential governing parameters are in ***bold, italic serif font****; the three critical non-dimensional (ND) parameters are in* **bold sans serif font***; dependent quantities are in* normal font *including ND parameters that are dependent on the critical ND parameters* Π_1 *to* Π_3. *The columns under 'Atmospheric Idealisation' on the next page contain two test cases corresponding to field observations on July 25 and 26, 2001, both at 1200 PDT. The only difference between the governing parameters of the two cases is the stronger background stratification on July 26. The columns under 'Water-Tank Idealisation' one the page following the next page contain the water-tank values that meet the similarity constraints, according to the formulae in chapter 3, for the cases on July 25 and 26.*

Parameter	Atmospheric Idealisation Formula	July 25	July 26
Gravitational Acceleration	$g =$	$9.8\ m/s^2$	$9.8\ m/s^2$
Kinematic Viscosity	$\nu_a =$	$1.51E\text{-}05\ m^2/s$	$1.51E\text{-}05\ m^2/s$
Molecular Diffusivity of Heat	$\kappa_a =$	$2.11E\text{-}05\ m^2/s$	$2.11E\text{-}05\ m^2/s$
Width of Tank		- -	- -
Length of Plain and Plateau	$L_{t,a} = L_{b,a} =$	$2396\ m$	$2396\ m$
Aspect Ratio	**$\Pi_1 = L_a/H_a =$**	**2.90**	**2.90**
Ridge Height	$H_a =$	$760\ m$	$760\ m$
Horizontal Length of Slope	$L_a =$	$2207\ m$	$2207\ m$
Diagonal Length of Slope	$L_{D,a} = (H_a^2+L_a^2)^{1/2} =$	2334 m	2334 m
Tank bottom surface area		- -	- -
Depth of Water above Plain		- -	- -
Coefficient of Thermal Expansion	$\beta_a =$	$0.00367\ K^{-1}$	$0.00367\ K^{-1}$
Specific Volume at Water Surface		- -	- -
Diurnal Heating Time Scale	$t_{d,a} =$	$27900\ s$	$27900\ s$
Reference Time	$t_a =$	$14400\ s$	$14400\ s$
Backgr. Environ. Lapse Rate	$\gamma_a = d\theta_a/dz =$	$6.20E\text{-}03\ K/m$	$7.30E\text{-}03\ K/m$
Backgr. Buoyancy Frequency	$N_a = (g\beta_a\gamma_a)^{1/2} =$	$0.0149\ s^{-1}$	$0.0162\ s^{-1}$
Maximum Heat Flux	$Q_{max,a} =$	$0.289\ Km/s$	$0.289\ Km/s$
Instantaneous Heat Flux	$Q_{H,a} = Q_{max,a} \sin(\pi/2\ t_a/t_{d,a}) =$	0.209 Km/s	0.209 Km/s
Energy Density	$E_a = Q_{max,a} t_{d,a}\ 2/\pi\ [1-\cos(\pi/2\ t_a/t_{d,a})] =$	1597 Km	1597 Km
CBL Depth	$h_a = (2g\beta_a E_a)^{1/2} / N_a =$	718 m	661 m
CBL Pot. Temp. Increment	$\theta_{s,a} = N_a (E_a / 2g\beta_a)^{1/2} =$	4.45 K	4.83 K
CBL Specific Volume Increment		- -	- -
ND Energy Density	**$\Pi_{2,a} = E_a N_a/Q_{H,a} =$**	**114**	**124**
ND Buoyancy Parameter	**$\Pi_{3,a} = g\beta_a Q_{H,a}/ H_a^2 N_a^3 =$**	**0.00391**	**0.00306**
ND Viscosity	$\Pi_{4,a} = \nu_a / H_a^2 N_a =$	1.75E-09	1.61E-09
ND Thermal Diffusivity	$\Pi_{5,a} = \kappa_a / H_a^2 N_a =$	2.44E-09	2.25E-09
ND Half Length of Plain	$\Pi_{6,a} = L_{b,a} / H_a =$	3.15	3.15
ND Half Length of Plateau	$\Pi_{7,a} = L_{t,a} / H_a =$	3.15	3.15
Convective Velocity Scale	$w_{*a} = (g\beta_a h_a Q_{H,a})^{1/3} =$	1.76 m/s	1.71 m/s
Vertical Convective Time	$t_{v,a} = h_a/w_{*a} =$	409 s	387 s
Maximum Horizontal Velocity	$U_{max,a} = 4.9\ (g\beta_a Q_{H,a}/N_a)^{1/2} =$	3.5 m/s	3.3 m/s
Horizontal Advection Time	$t_{h,a} = L_a/U_{max,a} =$	634 s	660 s
ND Vertical Convection Time	$t_{v,a}^* = t_{v,a} N_a =$	6.11	6.28
ND Horizontal Advection Time	$t_{h,a}^* = t_{h,a} N_a =$	9.47	10.71
Internal Froude Number	$Fr_{i,a} = 4.9\ (2\Pi_{2,a})^{-1/2} =$	0.147	0.141
Overall Richardson Number	$Ri_{0,a} = 1/Fr_{i,a}^2 =$	46.5	50.4
Channel Flow Reynolds Number	$Re_a = 0.175\ h_a U_{max,a}/\nu_a =$	2.90E+07	2.56E+07
Rayleigh Number	$Ra_a = g\beta_a\theta_{s,a}h_a^3/ \kappa_a\nu_a =$	1.86E+17	1.58E+17
Prandtl Number	$Pr_a = \nu_a/\kappa_a =$	0.716	0.716
Grashof Number	$Gr_a = Ra_a/Pr_a =$	2.60E+17	2.21E+17

Parameter	Formula	Water-Tank Idealisation July 25	July 26
Gravitational Acceleration	$g =$	$9.8\ m/s^2$	$9.8\ m/s^2$
Kinematic Viscosity	$\nu_w =$	$8.90E-07\ m^2/s$	$8.90E-07\ m^2/s$
Molecular Diffusivity of Heat	$\kappa_w =$	$1.45E-07\ m^2/s$	$1.45E-07\ m^2/s$
Width of Tank	$W_w =$	$0.431\ m$	$0.431\ m$
Length of Plain and Plateau	$L_{t,w} = L_{b,w} =$	$0.470\ m$	$0.470\ m$
Aspect ratio	$\Pi_1 = L_w/H_w =$	**2.90**	**2.90**
Ridge Height	$H_w =$	$0.149\ m$	$0.149\ m$
Horizontal Length of Slope	$L_w =$	$0.433\ m$	$0.433\ m$
Diagonal Length of Slope	$L_{D,w} = (H_w^2+L_w^2)^{1/2} =$	0.458 m	0.458 m
Tank bottom surface area	$A_w = W_w(2L_{t,w}+L_{D,w}) =$	0.6022 m^2	0.6022 m^2
Depth of Water above Plain	$D_w =$	$0.58\ m$	$0.58\ m$
Coefficient of Thermal Expansion	$\beta_w =$	$2.60E-04\ K^{-1}$	$2.60E-04\ K^{-1}$
Specific Volume at Water Surface	$\alpha_{0,w} =$	$1.00E-03\ m^3/kg$	$1.00E-03\ m^3/kg$
Diurnal Heating Time Scale		- -	- -
Reference Time	$t_w = \Pi_2(g\beta_w Q_{H,w}/H_w^2\Pi_3)^{-1/3} =$	301 s	301 s
Backgr. Environ. Lapse Rate	$\gamma_w = \alpha_{0,w}/g\,(g\beta_w Q_{H,w}/H_w^2\Pi_3)^{2/3} =$	1.46E-05 m^2/kg	1.72E-05 m^2/kg
Backgr. Buoyancy Frequency	$N_w = (g\beta_w Q_{H,w}/H_w^2\Pi_3)^{1/3} =$	0.3785 s^{-1}	0.411 s^{-1}
Maximum Heat Flux			
Instantaneous Heat Flux	$Q_{H,w} =$	$1.85E-03\ Km/s$	$1.85E-03\ Km/s$
Energy Density	$E_w = Q_{H,w}t_w =$	0.557 Km	0.557 Km
CBL Depth	$h_w = (2g\beta_w E_w)^{1/2}/N_w =$	0.141 m	0.130 m
CBL Temperature Increment	$T_{s,a} = N_w(E_w/2g\beta_w)^{1/2} =$	3.96 K	4.29 K
CBL Specific Volume Increment	$\alpha_{s,w} = \gamma_w h_w =$	2.06E-06 m^3/kg	2.24E-06 m^3/kg
ND Energy Density	$\Pi_{2,w} = \Pi_{2,a} =$	**114**	**124**
ND Buoyancy Parameter	$\Pi_{3,w} = \Pi_{3,a} =$	**0.00391**	**0.00306**
ND Viscosity	$\Pi_{4,w} = \nu_w/H_w^2N_w =$	1.06E-04	9.76E-05
ND Thermal Diffusivity	$\Pi_{5,w} = \kappa_w/H_w^2N_w =$	1.73E-05	1.59E-05
ND Half Length of Plain	$\Pi_{6,w} = L_{b,w}/H_w =$	3.15	3.15
ND Half Length of Plateau	$\Pi_{7,w} = L_{t,w}/H_w =$	3.15	3.15
Convective Velocity Scale	$w_{*w} = (g\beta_w h_w Q_{H,w})^{1/3} =$	0.0087 m/s	0.0085 m/s
Vertical Convective Time	$t_{v,w} = h_w/w_{*w} =$	16.1 s	15.3 s
Maximum Horizontal Velocity	$U_{max,w} = 4.9(g\beta_w Q_{H,w}/N_w)^{1/2} =$	0.0173 m/s	0.0166 m/s
Horizontal Advection Time	$t_{h,w} = L_w/U_{max,w} =$	25.0 s	26.1 s
ND Vertical Convection Time	$t_{v,w}^* = t_{v,w}N_w =$	6.11	6.28
ND Horizontal Advection Time	$t_{h,w}^* = t_{h,w}N_w =$	9.48	10.71
Internal Froude Number	$Fr_{i,w} = 4.9\,(2\Pi_{2,w})^{-1/2} =$	0.325	0.141
Overall Richardson Number	$Ri_{0,w} = 1/Fr_{i,w}^2 =$	9.49	50.4
Channel Flow Reynolds Number	$Re_w = 0.175\,h_w U_{max,w}/\nu_w =$	478	423
Rayleigh Number	$Ra_w = g\,(\alpha_{s,w}/\alpha_{0,w})\,h_w^3/\kappa_w\nu_w =$	4.35E+08	3.70E+08
Prandtl Number	$Pr_w = \nu_w/\kappa_w =$	6.14	6.14
Grashof Number	$Gr_w = Ra_w/Pr_w =$	7.09E+07	6.02E+07

B.5 A Strategy for Scaling

In Buckingham Pi analysis, choosing the governing parameters is often not straightforward but rather a complex interplay between intuition and science. I owe to Barenblatt (2003) the reference to Maurice Maeterlinck's 'Blue Bird': Two children in search for the Blue Bird, "the great secret of things and of happiness", draw upon a myriad of animals, trees, things, and phenomena, i.e. 'governing parameters'; the reader learns about the complicated interactions of the different 'governing parameters' while being walked through several cycles of trial and error.

The scaling in chapter 3 is far less ambitious; nevertheless the development was a many-step process with a confusingly complex set of possible governing parameters. 'Blue Bird' teaches the same lesson I learnt: choosing more parameters than necessary will not automatically result in unimportant Pi groups in the Buckingham Pi analysis. For examples, the choice of the buoyancy parameter $g\beta$ as an independent quantity rather than its individual components g and β may seem obvious after the fact; it was not in early scaling attempts. It turned out that the individual components never occurred separately; this provided the clue that g and β should be grouped as $g\beta$ (see for example Barenblatt, 2003).

The choice of the energy density, E, was even less obvious. One can always form the energy density from time t and instantaneous surface heat flux Q_H. Unlike g and β, which always occur together as the product $g\beta$, t and Q_H can occur separately – but only in dimensional quantities. In non-dimensional (ND) quantities, time t is always paired up with heat flux Q_H such as to form the energy density E.

In both examples I found the correct choice primarily by tediously untangling the algebraic dependences in a spreadsheet application before applying the Buckingham Pi analysis (Table Appendix I on page 211 is an extract of the spreadsheet). Correct grouping of the independent quantities was not necessary in the spreadsheet. From the spreadsheet I knew that, to achieve perfect similarity between atmospheric and water-tank idealisation, I had to match $m = 7$ ND quantities, which later became Π_1 to Π_7 in the Buckingham Pi analysis; by contrast, $t_{h,w}$* and $t_{v,w}$* for example, were automatically matched (Table Appendix I, page 211). Having $k = 3$ fundamental units, the Buckingham Pi theorem implied $n = m + k = 7 + 3 = 10$ governing parameters. Because I had originally identified more than 10 potentially governing parameters I knew that I had to group some of them. The steps that led to the scaling between the two systems, in my case atmospheric idealisation (AI) and water-tank idealisation (WTI), may serve as a useful general recipe:

1. List the first guess of governing parameters of the two systems.
2. Derive the dependent quantities. Notice that the algebraic relationships can be turned around to swap independent and dependent variables.
3. Form a first set of quantities that may be mutually physically-independent.
4. From the quantities in this set form ND quantities by appropriate multiplications and divisions. Many of the ND quantities thus formed will depend on each other. For some the dependence is obvious, for the others it will become obvious in the next two steps.
5. Enter the algebra into a spreadsheet (Table Appendix I).
6. Tune the independent parameters of one system to equalise the ND quantities of both systems. Some ND quantities automatically become equal. For example, assume that seven ND quantities match after tuning only three of them; then the four ND quantities that matched automatically are algebraically dependent on the three tuned quantities. The number of independent ND parameters, in this example three, is the number of Pi groups in the Buckingham Pi analysis.
7. The dependences revealed in the last step serve as a guide to find the algebraic relationships missed in step 4.
8. With the number of fundamental units, and expected Pi groups given, the Buckingham Pi theorem implies the number of independent parameters. Use this as a guide to group the independent parameters.
9. Carry out the final Buckingham Pi analysis (section 3.3).
10. Derive measurable quantities for both systems to test the scaling (section 3.4).

11. Correct the spreadsheet with the final grouping of the independent parameters.

B.6 Scaling of other Non-dimensional Quantities

Do non-dimensional (ND) quantities that are often identified as governing parameters, like the Reynolds number, play a role in addition to the Pi groups identified in chapter 3 or how do they relate to those Pi groups? In this section I will discuss some of most common ND parameters.

The values shown in this section are taken from the first test case, July 25, 2001, 1200 PDT, in Table Appendix I on page 211 above. For most of this section a distinction between atmospheric idealisation (AI) and water-tank idealisation (WTI) will not be necessary. I will drop the subscripts 'a' and 'w' when a formula applies equally to AI and WTI.

Froude Number and Richardson Number

Defining the reduced buoyancy scale by

$$g_s \equiv \begin{cases} g\beta_a\theta_{s,a} & \text{for atmosphere} \\ \dfrac{g}{\alpha_{0,w}}\alpha_{s,w} & \text{for water tank,} \end{cases} \tag{B.137}$$

the internal Froude number (Turner, 1973) is given by

$$Fr_i \equiv \frac{U_{\max}}{\sqrt{g_s h}} = \frac{U_{\max}}{Nh}, \tag{B.138}$$

where I used (3.50) and (3.20) in the atmospheric case, and (3.92) and (3.21) in the water-tank case. The overall Richardson number follows directly from the internal Froude number:

$$Ri_o \equiv \frac{g_s h}{U_{\max}^{\;2}} = Fr_i^{-2}. \tag{B.139}$$

For our field observations at 1200 PDT on July 25, from (B.2), (B.5), and (B.7) follows the observed internal Froude number

$$Fr_{i,a} = \frac{U_{obs,a}}{N_a h_a} \approx 0.35. \tag{B.140}$$

The internal Froude number can also be predicted from the hypotheses by using the predicted maximum upslope flow velocities in (B.138). Table Appendix I on page 211 shows the case for the Schumann hypothesis where Fr_i is a function of Π_2 only. For all hypotheses, Fr_i can be expressed in terms of Π_1, Π_2, and Π_3 and therefore does not contain any new physics beyond the scaling. The internal Froude number is a ND quantity frequently used in the study of hydraulic effects in fluid dynamics, in particular for flows over obstacles or for gravity currents. In the scaling I developed, the governing parameters specify topography and heating and therefore flow velocity and Fr_i.

Rayleigh Number and Prandtl Number

I will now turn to those ND quantities that involve the two molecular governing parameters, kinematic viscosity $\nu\left[m^2 s^{-1}\right]$ and thermal diffusivity $\kappa\left[m^2 s^{-1}\right]$. In the Buckingham Pi analysis of convection between two very wide horizontal plates kept at constant temperatures, where the lower plate is warmer than the upper plate, there are two Pi groups governing the flow in the fluid between the plates, commonly chosen to be the Rayleigh and the Prandtl numbers (Barenblatt, 2003). Intuitively, the onset and characteristics of vertical motions should depend on the ratio between the buoyancy forcing and the inhibition by molecular viscosity and the degree to which thermal diffusion can equalise vertical temperature differences, i.e.

$$Ra \equiv \frac{g_s h^3}{\nu\kappa} = \frac{(2\Pi_2\Pi_3)^2}{\Pi_4\Pi_5} \approx \begin{cases} 1.86\times10^{17} & \text{for atmosphere} \\ 4.35\times10^{8} & \text{for water tank,} \end{cases} \tag{B.141}$$

where I made use of (B.137), (3.49), (3.50), (3.20), (3.91), (3.92), and the definition of the Pi groups in Table 3.2. The values are for 1200 PDT on July 25 and the corresponding water-tank experiment (Table Appendix I, page 211). The Prandtl number is defined by

$$\Pr \equiv \frac{\nu}{\kappa} = \frac{\Pi_4}{\Pi_5} \approx \begin{cases} 0.716 & \text{for atmosphere} \\ 6.14 & \text{for water tank.} \end{cases} \tag{B.142}$$

For the purpose of this thesis, this difference in diffusion of momentum versus heat is not important, because diffusion happens at much larger time scales (hours to days) than the duration of an experiment (order of 10 minutes)[10]. The onset of convection occurs at a Rayleigh number of $O(10^3)$ and the transition to turbulent convection at $O(10^5)$ (Turner, 1973). Soon after the beginning of the experiments the upslope flow in the tank is convectively turbulent, exceeding the critical value by orders of magnitude. This strong convective turbulence suggests that it may be possible to achieve similarity between AI and WTI for the bulk properties and that the discrepancy in the Prandtl and Rayleigh number is not critical for the overall flow.

In contrast to upslope flows, night time *downslope* flows are markedly different with respect to the onset of turbulence. For a stable flow down an inclined cooled surface (Turner, 1973) the governing ND parameter is the ratio of Rayleigh and Prandtl number, the Grashof number

$$Gr \equiv Ra/\mathrm{Pr} = \frac{g_s h^3}{\nu^2} = \left(\frac{2\Pi_2\Pi_3}{\Pi_4}\right)^2 \approx \begin{cases} 2.60\times10^{17} & \text{for atmosphere} \\ 7.09\times10^{7} & \text{for water tank.} \end{cases} \tag{B.143}$$

The values are taken from the *convectively driven* upslope flow case at 1200 PDT on July 25 (Table Appendix I, page 211). Downslope flows are typically about one order of magnitude shallower than upslope flows so that for water-tank modeling of downslope flows the Grashof number is many orders of magnitude smaller than the critical value for fully turbulent flow, $O(10^{11})$, and even several orders of magnitude smaller than the critical value for first fluctuations, $O(10^7)$ (from linear extrapolation of Turner's (1973) Fig. 4.18). If fully developed turbulent flow is required to achieve similarity of the bulk properties between atmospheric and water-tank model, these considerations would imply that similarity is technically very difficult, if not impossible, to achieve for *downslope* flows. Notice that a similar argument holds for the return flow part of the flow in the water tank if the return flow is not within the

---

[10] Notice, however, that the use of salt to initially stratify the water leads to sharp interfaces of temperature and salinity during the experiments, for example at the top of the CBL, where temperature diffuses on time scales of $O(10\,s)$ because of the strong gradient. The much faster diffusion of heat than of salt at these interfaces causes double diffusive convection (Appendix C.4).

CBL. In this case, return flow in atmosphere and water tank could be significantly different, although I do not have evidence for such a difference.

Channel Flow Reynolds Number

The Reynolds number is an important ND parameter in many turbulent flows. It is generally defined as the ratio of inertial and viscous forces,

$$\mathrm{Re} \equiv \frac{UL}{\nu}, \tag{B.144}$$

where U and L are appropriate velocity and length scales. When a critical value of the Reynolds number is exceeded the flow becomes turbulent (usually there is a range of Reynolds numbers, in which the flow alternates between turbulent and laminar). The role of the Reynolds number in thermally-driven upslope flows remains an open question. Schumann (1990) and Deardorff and Willis (1987) attributed roughly half of the observed turbulence to shear that is generated by the upslope flow motion. These LES and water-tank results support the importance of the Reynolds number in upslope flows. But how should the Reynolds number be defined for the upslope flow geometry in the tank and what is its expected critical value? I will here try to give a preliminary answer, only. A comprehensive investigation could be a potential topic for further research.

I propose as a measure for the onset of mechanical turbulence a channel flow Reynolds number defined by

$$\mathrm{Re} \equiv \frac{2\overline{U}H_{1/2}}{\nu}, \tag{B.145}$$

where $H_{1/2}$ is the half-height of an infinitely wide channel, and $\overline{U} \equiv \frac{1}{H_{1/2}} \int_0^{H_{1/2}} \langle U \rangle dz$ with $\langle U \rangle$ being the time-averaged flow (Figure Appendix VIII). Transition to turbulence occurs for $1{,}350 < \mathrm{Re} < 1{,}800$ (Patel and Head, 1969). Because there is enough disturbance of the flow by convective turbulence, one can expect shear turbulence to be triggered and maintained when a minimum critical Reynolds number of 1,350 is exceeded.

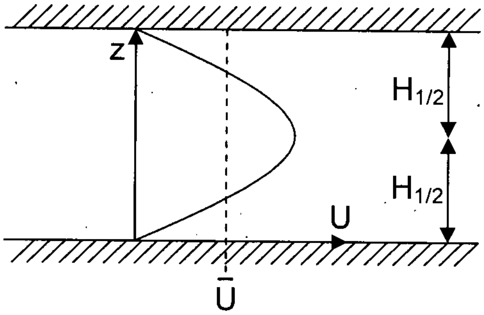

Figure Appendix VIII: Schematics of closed-channel flow.
The solid curve shows the flow speed U as a function of distance z from the bottom plate. The vertical dashed line represents the average speed $\overline{U}$ across the channel height $2H_{1/2}$.

I demonstrated in Appendix B.1 that the field observations are well approximated by a Prandtl profile with, from (B.35),

$$U_0 = 3.1\, U_{\max}, \tag{B.146}$$

assumed to hold for atmosphere and water tank. Here, U_0 is the velocity that would occur at the surface without friction. First I consider generation of mechanical turbulence only at the lower boundary and interpret the upslope flow between the surface and the height of the maximum velocity at $H_{1/2} = \pi l/4$ as the bottom half of the channel flow in Figure Appendix VIII. Then the mean velocity is

$$\overline{U} = \frac{1}{\pi l/4} \int_0^{\pi l/4} U_0 \exp(-z/l) \sin(z/l)\, dz = \frac{3.1 U_{\max}}{\pi l/4}\, l \int_0^{\pi/4} \exp(-z) \sin z\, dz .$$

The integral can be solved by twice integrating by parts to give

$$\overline{U} = \frac{4 \times 3.1 U_{\max}}{\pi} \left[-\frac{1}{2} \exp(-z)(\sin z + \cos z) \right]_{z=0}^{z=\pi/4} \approx 0.70\, U_{\max} . \tag{B.147}$$

The Prandtl profile intercepts the height axis at $z = \pi l$, marking the top of the upslope flow. In our observations for July 25, 2001, this corresponds to half the CBL depth, $z = h/2$. Therefore,

$$l = \frac{h}{2\pi}. \tag{B.148}$$

Equating the height of maximum velocity in the Prandtl profile, $\pi l/4$, with the half-height $H_{1/2}$ in (B.145) and Figure Appendix VIII, gives

$$H_{1/2} = \frac{\pi l}{4} = \frac{\pi\, h/2\pi}{4} = \frac{h}{8}, \tag{B.149}$$

where I substituted l from (B.148). Applying (B.147) and (B.149) to (B.145), finally results in

$$\mathrm{Re} \equiv \frac{2H_{1/2}\overline{U}}{\nu} \approx \frac{2h \times 0.7U_{\max}}{8\nu} = 0.175\frac{hU_{\max}}{\nu} \approx \begin{cases} 2.90\times 10^{7} & \text{for atmosphere} \\ 478 & \text{for water tank.} \end{cases} \tag{B.150}$$

Even for this well developed upslope flow, the Reynolds number for the water-tank model is much smaller than the critical value of 1,350. More accurately I should use the slope-parallel component of the upslope flow velocity, but this would not alter the conclusion that the critical Reynolds number cannot be reached.

So far I have considered shear turbulence generated at the surface, only. At the interface between upslope and return flow, however, the relative velocity is almost twice as large and the length scale several times larger. The Reynolds number is therefore about one order of magnitude larger and most likely exceeds the critical Reynolds number for shear turbulence between upslope and return flow layer. Figure Appendix I (page 176) provides evidence that even early in the water-tank experiments shear turbulence is generated at the upper part of the upslope flow, but not at the bottom.

Making use of (B.138) and (B.143), the Reynolds number can also be expressed as

$$\mathrm{Re} = 0.175 Fr_i\, Gr^{1/2} = 0.175 Fr_i \left(\frac{Ra}{\mathrm{Pr}}\right)^{1/2}. \tag{B.151}$$

Apart from the factor 0.175 this result corresponds to $Gr = \mathrm{Re}^2/Fr_i^2$ in equation (4.2.7) in Turner (1973). Therefore, the Reynolds number does not contain new physics beyond that contained in the internal Froude, Grashof, Rayleigh, and Prandtl number. Note, however, that it should contain an additional weak dependence on the aspect ratio when the slope parallel component of the upslope flow velocity is considered.

I complete this section with a brief discussion on the use of alternative definitions of the Reynolds numbers by other researchers.

The Reynolds Number by Chen et al.

In contrast to the modified channel Reynolds number in (B.150), Chen et al. (1996) defined the Reynolds number by

$$\mathrm{Re}_{Chen} \equiv \frac{LU_0}{\nu} = \frac{\Pi_1 \left(2\Pi_2\Pi_3\right)^{1/2}}{\pi_4} = \begin{cases} 2.37\times\left(10^3-10^5\right) & \text{for atmosphere} \\ 2.59\times10^4 & \text{for water tank,} \end{cases} \tag{B.152}$$

where I used (B.33), (3.90), and the definitions of the Pi groups in Table 3.2 (page 47). $\pi_4 = \Pi_{4,w} = \nu_w / H_w{}^2 N_w$ in the water tank and $\pi_4 = \nu_{e,a} / H_a{}^2 N_a$ in the atmosphere, where $\nu_{e,a} = 0.1 - 10\, m^2 s^{-1}$ is a constant eddy viscosity for the atmosphere. This scaling approach has a number of problems not found in the derivation of (B.150):

- It is not obvious why the authors chose the slope length L as length scale, because representative length scales are usually perpendicular to the flow velocity as a measure of the shear of the mean flow, e.g. in pipe or channel flows. Consequently, the critical value of the pipe flow Reynolds number cannot be used as a criterion for bulk similarity.
- The scaling velocity U_0 is much larger than observed velocities and therefore not a suitable velocity for determining the Reynolds number.
- Eddy viscosity arises from a local turbulence closure of the momentum equations which is inappropriate for the non-local character of convection, and constant eddy viscosities disagree with observations (Stull, 1988).

The Turbulent-Convection Reynolds number

The turbulent-convection Reynolds number used by Snyder et al. (2002) addresses a different question. It is based on Adrian et al. (1986),

$$\mathrm{Re}_{Adrian} \equiv \frac{w_* h}{\nu} = \left(2\Pi_2\right)^{2/3} \frac{\Pi_3}{\Pi_4} = \begin{cases} 8.34\times10^7 & \text{for atmosphere} \\ 1{,}379 & \text{for water tank,} \end{cases} \tag{B.153}$$

where I made use of (B.9), (3.90), and the definition of the Pi groups in Table 3.2 on page 47. The values for AI and WTI exceed the critical value of 550 which guarantees self-similarity of the root-mean-square velocity and temperature statistics (Adrian et al., 1986). Notice that, although the CBL depth h is parallel to the convective velocity scale w_*, it is the only choice for a length scale and is related to the typical width of rising thermals in the CBL, which is perpendicular to w_*. I will argue next that the turbulent convection Reynolds number may be of great importance.

Summary and Conclusions

The Nusselt (Nu) and the Péclet number (Pe) are expressible in terms of the Rayleigh and Prandtl number (see for example Turner, 1973). Therefore they do not add new physics and will not be discussed any further. I am not aware of other ND parameters that could be potentially relevant in upslope flow systems.

In all examples discussed in this section, the ND parameters are expressible in terms of the three core Pi groups Π_1 to Π_3, and the molecular Pi groups Π_4 and Π_5 (Table 3.2, page 47). Regardless of the choice of $U_{\max}{}^*$, the Grashof number is a function of Rayleigh and Prandtl number, $Gr = fct(Ra, \Pr)$, and the overall Richardson number a function of internal Froude number, $Ri_0 = fct(Fr_i)$. The set of potentially relevant ND parameters thus is reduced to an alternative set of Pi groups, Ra, $\Pr$, Fr_i, Re, and Re_{Adrian}. It must be possible to express Π_1 to Π_5 in terms of this new set, which implies that Ra, $\Pr$, Fr_i, Re, and Re_{Adrian} must be independent of each other[11]. This could be an interesting topic for future research, because the independence of these five parameters puts constraints on the upslope flow hypothesis that may not be as obvious with the set of Pi groups Π_1 to Π_5. However, to explore this further it would be necessary to test in particular the dependence of the maximum upslope flow velocity on the aspect ratio Π_1.

---

[11] This is another argument for the Reynolds number to be dependent on the aspect ratio as conjectured after (B.151).

Appendix C: Physical Scale Modelling

In this appendix technical details extending section 4.2 are presented in sections C.1-C.9. The remaining sections provide material complimentary to other sections in chapter 4.

C.1 Technical Design of the Water Tank

Side walls and end walls of the tank are made of ¼-inch (6.4 mm) tempered glass, the tank bottom is a 1/8-inch (3.2 mm) stainless steel sheet bent at the two ends of the slope to give a 19° angle. The glass walls are held together in a frame welded from of 3/16-inch (4.8 mm) L-shaped stainless steel bars. The steel frame has an adjustable bolt under each corner so that the tank can be levelled.

The steel bottom fits within the glass walls and rests on ½-inch (12.7 mm) panels of Micarta cotton fabric phenolic composite which are attached to the glass walls with silicone (Figure Appendix IX). The gap between the steel sheet and the cotton fabric phenolic composite panels as well as the glass wall is sealed with high-temperature silicone (Dow Corning 736 heat-resistant sealant). One side of a 1/16 inch (1.6 mm) thick U-shaped stainless steel bar is spot welded to the bottom of the stainless steel bottom sheet, while the base of the U-shaped bar is bolted to the cotton fabric phenolic composite panels.

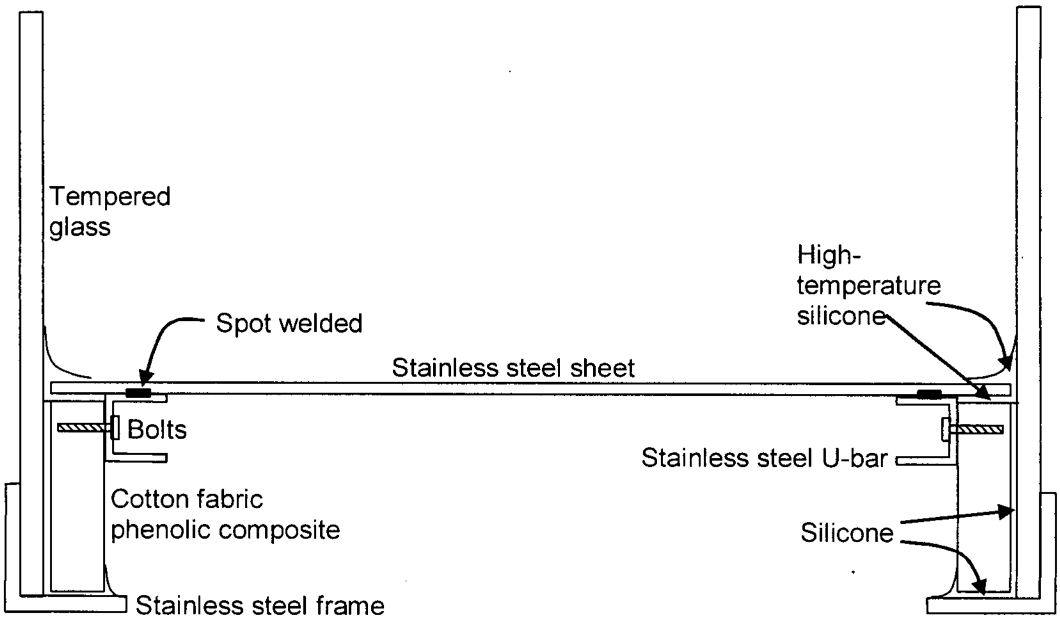

Figure Appendix IX: Schematic side view of tank. (Not to scale.)

C.2 Heating

Convection is triggered in the tank by heating the bottom steel sheet from below with 34 Watlow Mica strip heaters each rated 500 W at 240 V input voltage. Each strip heater is 1½ inch (3.8 cm) wide and 15¼ inch (38.7 cm) long with an effective heating area of approximately 1½ inch by 11½ inch (29.2 cm). The 34 strip heaters are arranged in parallel touching each other, each strip crossing the width of the tank (Figure Appendix X). There are eleven strip heaters (1-11) underneath the plain, twelve underneath the slope (12-23), and eleven underneath the plateau (24-34). As shown by the braces at the bottom of Figure Appendix X, the strip heaters underneath the plain and the plateau can be controlled in groups of five or six heaters and the heaters underneath the slope can be controlled individually. Custom-made controls allow almost continuous variation of the effective electrical input power from approximately 30% to 100% of the maximum value.

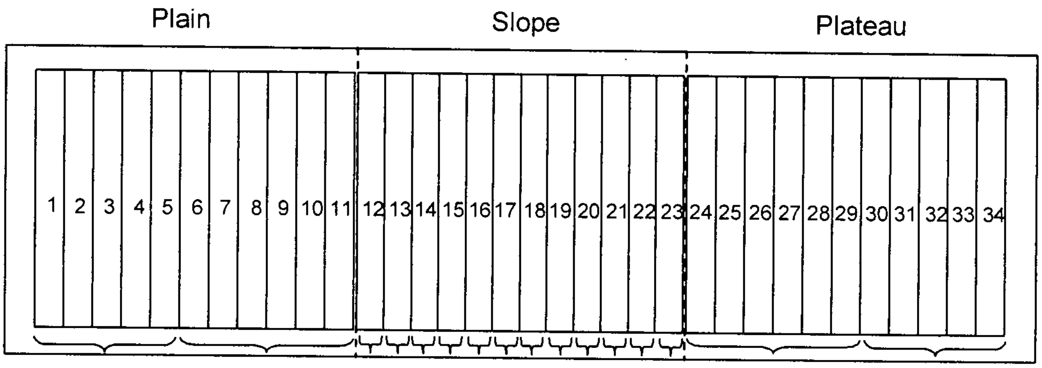

Figure Appendix X: Plan view of strip heater arrangement. (Approximately to scale.)
The braces indicate how the strip heaters can be controlled individually or in groups of five or six heaters.

Originally I tried to use flexible silicone rubber heaters attached underneath the tank with an adhesive, which provided a very intimate contact and homogeneous heating. Because stratified water is a bad heat sink the heating elements exceeded their maximum working temperature of 232°C within one to two minutes. The Watlow Mica strip heaters with stainless steel sheaths are rated up to 650°C. While these heaters stay within their temperature limits, establishing intimate contact and homogeneous heating is much more difficult because of the strip heaters' tendency to bend during thermal expansion.

The strip heaters are installed underneath the tank bottom as shown in Figure Appendix XI. The gap between bottom sheet and strip heaters is filled with another stainless steel sheet. To provide strong contact between the strip heaters and both stainless steel sheets, each strip heater is pressed up against the steel sheets at the two end points and in the centre. At the two end points, small strips of Micarta cotton fabric phenolic composite fill the gap between U-bar and strip heater, held in place with bolts. A stainless steel T-bar stretches along the entire length of the tank underneath the centres of the strip heaters and is bolted to the cotton fabric phenolic composite panels at the two end walls of the tank and reinforced by a cross bar in the middle of the tank (cross bar not shown in Figure Appendix XI). The force between the T-bar and the heaters is applied by simple springs: I bent tempered Copper-Constantan strips into a V-shape so that the two legs of the "V" have to be pressed together to fit into the gap. The opening angle of the V-shaped strips can be changed by hand to adjust the force depending on the gap size.

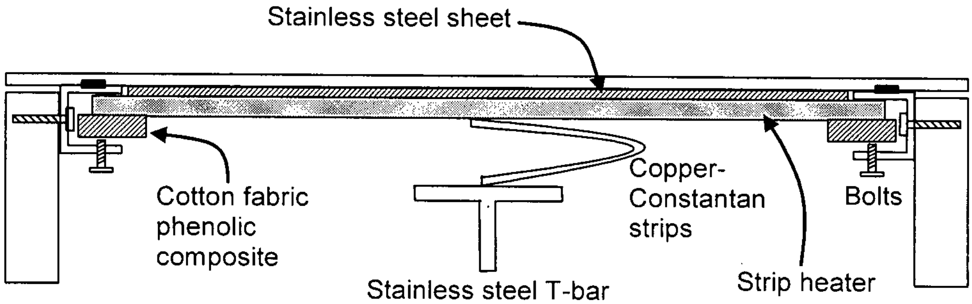

Figure Appendix XI: Side view of strip heater installation underneath the tank bottom.

C.3 Filling the Tank with Salt-Stratified Water

One of two quantities is commonly varied in the vertical to achieve density stratification: temperature or salt concentration. The advantages of temperature over salt stratification are that density measurements and data analysis are easier; the major disadvantages are greater costs and technical effort. Both methods are much harder to apply in tanks with a non-flat bottom, and salt stratification, which I used, may be the only technically feasible solution.

In a tank with a flat bottom and vertical walls, a linear stratification can be achieved easily with the 'two-tank' method (Fortuin, 1960). The experimental tank is filled at the tank bottom through an inlet, which is fed from a freshwater tank. The freshwater tank is connected at the bottom with a saltwater tank of same dimensions so that both tanks always have the same water level when water is draining from the freshwater tank into the experimental tank. The salt concentration of the water draining from the freshwater tank into the experimental tank will increase linearly with height until the last bit has the same salt concentration as the saltwater tank originally had. Since the freshwater is drained first and the saltwater last, the experimental tank is filled from top to bottom. One can reverse the filling order by switching freshwater and saltwater tank and using an inlet floating on the water surface in the experimental tank. The two-tank method works extremely well for flat-bottom tanks.

Hill (2002) developed a method to produce any density gradient for any topography. A computer program numerically solves the associated inverse problem and controls the flow rates between the tanks with peristaltic pumps. An easier and cheaper method for my purpose was to model the filling in a simple spreadsheet, using some clues and trial and error, to find an appropriate modification of the topography in the filling tanks to compensate for the varying plan-form area during the filling of the bottom part of the experimental tank.

Width and height of both filling tanks are equal to width and height of the experimental tank and the sum of the lengths of freshwater and saltwater tank equals the length of the experimental tank (Figure Appendix XII). There are two faucets for draining the freshwater tank. The upper faucet is opened to fill the experimental tank above the level of the plateau. This draining takes roughly three to four hours and can be done unattended. The remaining water is now level with the upper edge of a wedge in the saltwater tank which has the same angle as the slope in the experimental tank. A small amount of salt is dissolved in the saltwater tank before continuing the filling process. Then the bottom faucet is used to drain the reduced volume of the bottom part of the experimental tank. This takes up to one hour and requires some tilting of the tanks to completely drain the tanks.

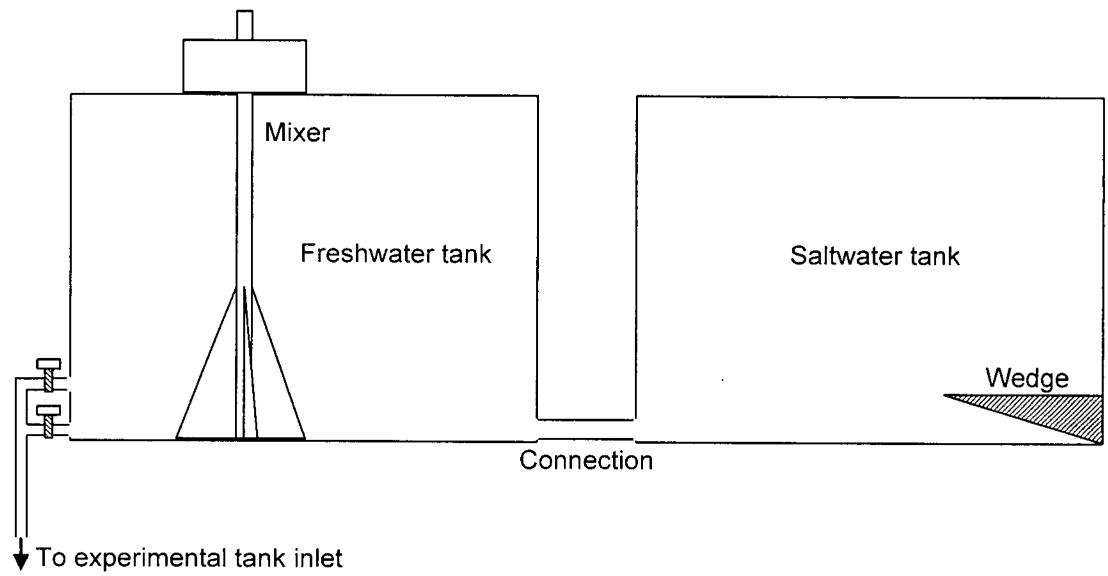

Figure Appendix XII: Schematic of filling tanks.
Side view, approximately to scale. The mixer ensures that the saltwater, which drains into the freshwater tank through the connection, is well mixed with the freshwater. The solid wedge compensates for the volume change due to the slope in the tank.

C.4 Measurement of Specific Volume

Instrumentation and Calibration

One difficulty with using salt to create density stratifications mentioned in the previous section is that measurements are more difficult. The density of heated saltwater is a complex interplay of salt concentration and temperature. The requirements on the measurement instrumentation are demanding. I needed probes which have minimal impact on the water flow, have a fast response time, high accuracy, and high spatial resolution. The only product that meets my requirements is the Conductivity & Temperature (CT) sensor manufactured by Precision Measurement Engineering, Inc. (PME).

PME specifies a temperature accuracy of 0.05°C, a temperature time response of 7×10^{-3} s, and a time response of conductivity measurements of -3 db at approximately 800 Hz. I achieved at best a 1-2% accuracy of salt concentration measurements, as a result of a chain of uncertainties in the complicated calibration, measurement, and conversion procedure. Both the conductivity and the temperature sensor return a voltage that is related to conductivity and temperature via approximate measurement equations. Tables and approximate transcendental equations are provided in the operator's manual to convert conductivity and temperature to salt concentration (PME, 1997). Details of the conversions for calibration and measurements are given in section C.8. In addition to the measurement uncertainty, the filling process causes errors, some apparently systematic (Figure Appendix XIII). The main reason for systematic errors is probably the shape and position of the wedge in the saltwater tank (Figure Appendix XII). Incomplete mixing of saltwater into the freshwater tank is another potential cause for uncertainties. Sometimes it is possible that a slightly damaged probe still operates but with a drift or slower response time. In some cases (Figure Appendix XIII), these errors can be reduces by adjusting the calibration.

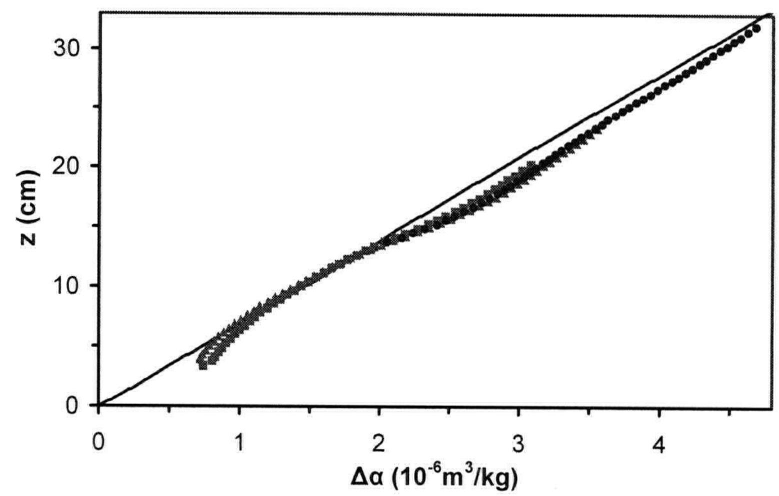

Figure Appendix XIII: Background stratification of test case.

The solid line shows the expected background stratification for the test case with $N_t = 0.374\,s^{-1}$, corresponding to an atmospheric lapse of $\gamma = 6.0 \times 10^{-3}\ K\,m^{-1}$ on July 25, 2001. The data points show vertical profiles taken over the plain 15 cm from the slope (red squares), over the slope 9 cm from the bottom (green triangles), and over the slope 9 cm from the ridge (blue circles). Shown are the raw data without smoothing. The calibration of the vertical profile over the plain (red squares) was adjusted to account for an apparent drift.

Besides the inconvenience of the conversion procedure the major drawback of the CT sensor is its delicateness. Mechanical impact on the CT sensor tip immediately destroys the sensor; vibrations of the sensor shaft can also lead to damage. While it is preferable to avoid handling of the CT probes, every new experiment requires recalibration and reinstallation of the sensor. I followed the calibration procedure described in PME (1997). As calibration solution I kept a 10-litre mineral water container filled with saltwater in the laboratory. This solution provides the low temperature point and the maximum conductivity point so that only one more measurement of hot freshwater is needed to complete the calibration. The calibration solution's conductivity was measured with a highly accurate laboratory salinometer. Every few weeks I verified that there was no significant drift of the salt concentration.

Measurement Procedures

In a typical experiment I used three CT probes simultaneously, which were attached to the beam of a vertical profiler. The profiler was driven up and down by a stepper motor, which was controlled by the same program that also captured the CT sensor voltage output. Measurements were started from a prescribed maximum height above the tank bottom. For some experiments the probes were successively driven down into the water by 3 mm increments; temperature and conductivity voltages of all three probes were captured synchronously eight times, and the mean value was calculated and stored. Capturing the data took about 0.75 s at each height. A very deep vertical profile of 480 mm with a resolution of 3 mm therefore took approximately two minutes to capture. Much time was needed for stopping and restarting the profiler in each step. Therefore, for later experiments the probes were driven downward while continuously acquiring data every 0.25 s at a vertical resolution of 3.5-4.0 mm. For experiments with stationary probes, measuring eight times, averaging, and storing the data required a total of 0.2 s. A typical stationary time series taken over 16 minutes and 40 seconds (1000 s) contains 5000 data points.

When the profiler reached a height of 4 mm above the tank bottom it returned to a new maximum height to start again. During the upward motion the probe shaft dragged water vertically upward by more than 5 cm. This 'selective withdrawal' (Turner, 1973) leads to a hysteresis because during the measurements during ascents show the specific volume of the water withdrawn from lower heights (Figure Appendix XIV). I therefore only took measurements during the descents and usually did not include the upper measurements that were under the influence of the withdrawn water.

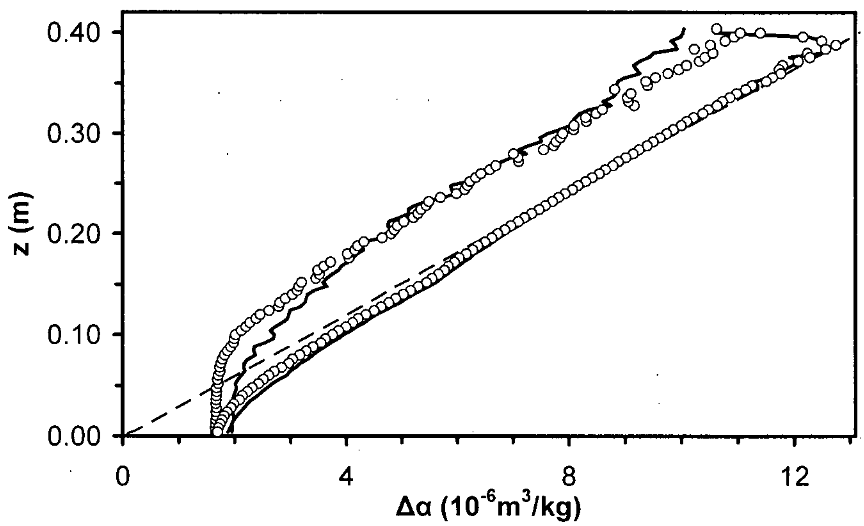

Figure Appendix XIV: Hysteresis caused by selective withdrawal by CT probes.

The solid curve shows the first ascent (upper curve) followed by a descent (lower curve). The open circles show the second ascent (upper circles) followed by a descent (lower circles). There were more than one hour between the two sets of ascent/descent showing a slight drift but overall good reproducibility.

Double-Diffusive Convection

Finally I briefly discuss double-diffusive convection that originally raised some concerns. The vertical profile in Figure Appendix XV shows two mixed layers, one corresponding to the backscatter boundary layer (from 0 to 0.15 m) and one corresponding to a second layer above the ridge height (0.15 to 0.20 m). Both layers are topped by a spike of low specific volume. Such a large difference of specific volume should lead to very strong downward convection at the top of the two mixed layers. The cause of the spikes is the different diffusion of salt ($D_s = 1.5\times10^{-9}\,m^2\,s^{-1}$) and heat ($\kappa_w = 1.45\times10^{-7}\,m^2\,s^{-1}$).

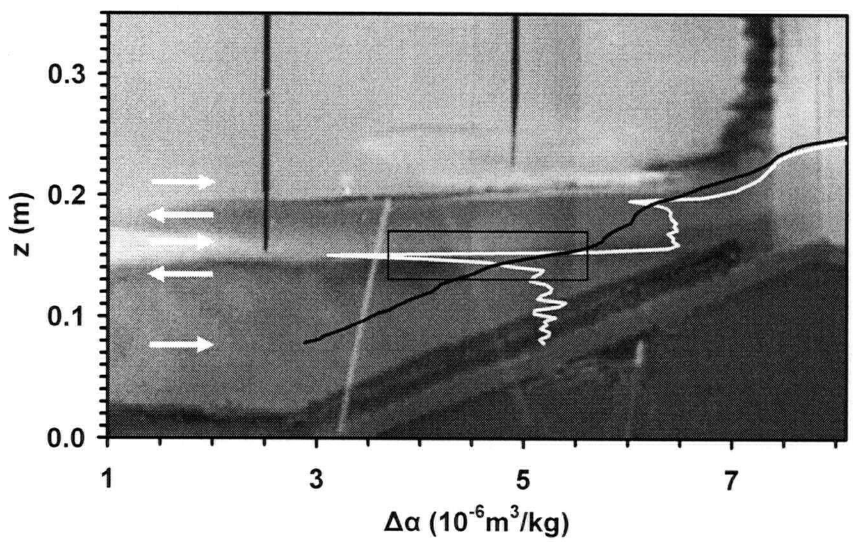

Figure Appendix XV: Double-diffusive convection.
Vertical profile of specific volume (white curve) superimposed on top of the corresponding movie frame of the dye experiment and specific volume profile before the beginning of the experiment (black curve). The movie frame shows two vertical shafts of the conductivity and temperature probes. The vertical profiles in this figure were measured with the right probe over the centre of the slope. The vertical profiles and the movie frame have the same vertical scale. The white arrows show the flow direction of the horizontal layers. The black rectangle encloses the domain that is enlarged in Figure Appendix XVII. A removable end wall was placed at the ridge top. Red dye crystals were originally dropped over the ridge to the left of the end wall and then slid down the slope, leaving behind a red trail. The green dye was originally released to the right of the removable end wall and shows that there was some minor leakage through the removable end wall.

To understand the underlying mechanism that drives double-diffusive convective in this case, it is helpful to first sketch the overall flow during the experiment and second to zoom into the area of the black rectangle in Figure Appendix IX and decompose the specific volume profile into its constituents, temperature and salinity (Figure Appendix XVII).

A close inspection of the movie of the tank experiment reveals many layers of counter-clockwise circulations stacked on top of each other (Figure Appendix XVI). Upslope and return flow form the lowest, primary circulation. A secondary circulation can be seen right on top of the primary circulation.

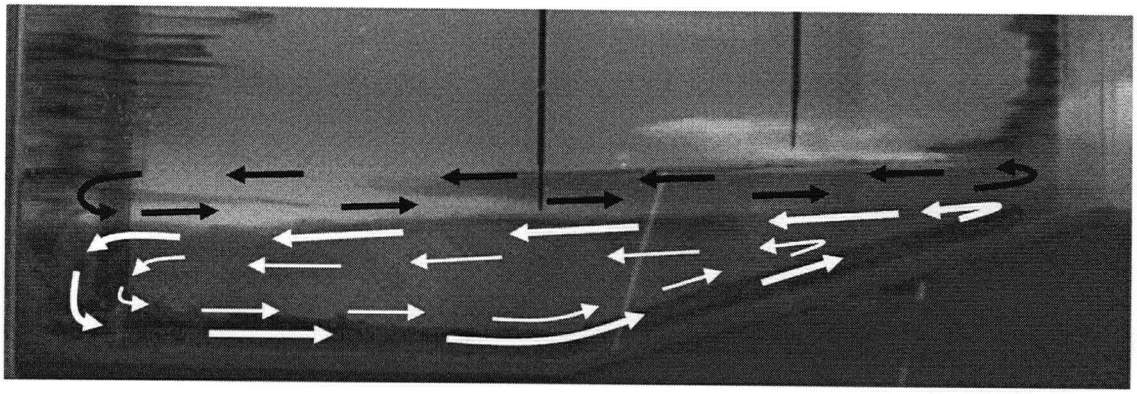

Figure Appendix XVI: Circulations in water tank.

Circulations deduced from movements of dye and vertical profiles of salinity and temperature. White arrows show the primary circulation of upslope and return flow; black arrows show a secondary circulation above the upslope and return flow circulation. More circulations of decreasing depth and slow speed exist above the secondary circulation.

The secondary circulation brings cool water of low salinity from the left end wall into the region of the black rectangle in Figure Appendix XV. In the enlargement in Figure Appendix XVII this is visible as the middle layer, which does not contain red dye. The return part of the secondary circulation is the upper layer in the enlargement, and the return flow of the primary circulation is the lower layer. The salinity of the upper part of the layer is identical to its original salinity, while the lower part has a slightly increased salinity, probably as a result of shear-turbulence mixing with the lower layer. The salinity at top of the lower layer is larger than its original surface value over the centre of the slope. This fluid therefore must have been transported by the upslope flow into this region from the bottom half of the slope, in line with the closed circulation indicated in Figure Appendix XVI.

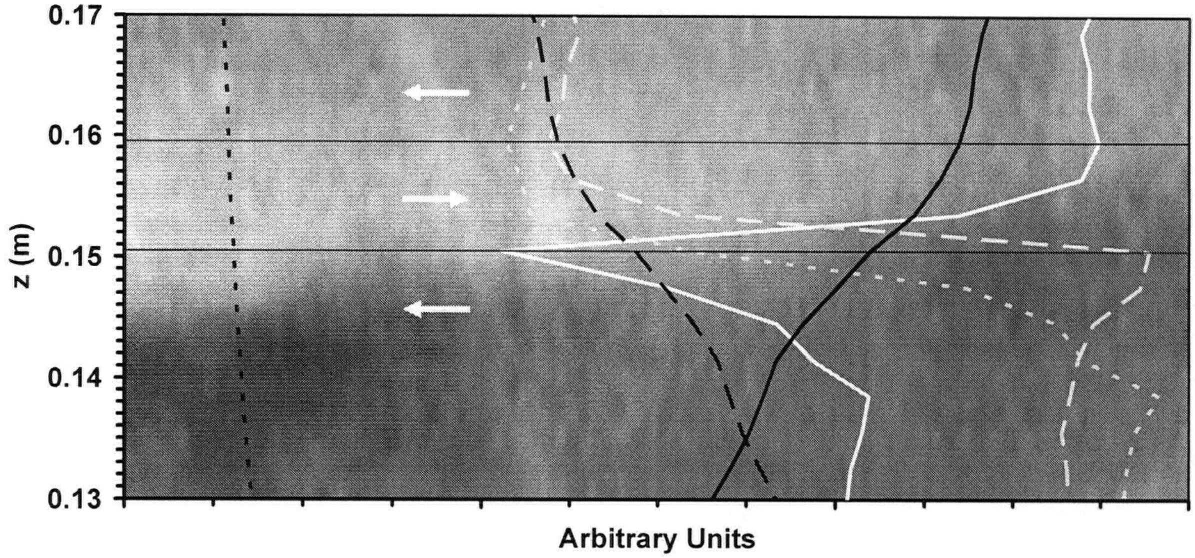

Figure Appendix XVII: Temperature and salinity in double-diffusive convection.
The background is an enhanced-colour view of the rectangular region in Figure Appendix XV. Superimposed are for approximately the same time during the experiment: the vertical profiles of specific volume (white solid curve), temperature (white dotted curve), and salinity (white dashed curve). Shown are also the vertical profiles before the start of the experiment: specific volume (black solid curve), temperature (black dotted curve), and salinity (black dashed curve). The curves are rescaled to arbitrary units for illustrative purposes. Shown are also the approximate layer boundaries (black thin horizontal lines) and the flow direction in the three layers (white arrows).

Salinity is high and fairly constant within the entire lower layer and very rapidly drops within the bottom few millimetres of the middle layer. By contrast, the temperature adjusts over a depth of more than one centimetre and the adjustment occurs across the interface between lower and middle layer. The reason for this difference is that the diffusivity of heat ($\kappa_w = 1.45\times10^{-7} m^2 s^{-1}$) is 100 times as large as that of salt ($D_s = 1.5\times10^{-9} m^2 s^{-1}$). During the time when lower and middle layer shared the common interface, heat diffused much faster across the interface than salt. As a result the specific volume has decreased in the return flow layer near the interface.

In this situation, narrow plumes of high salinity ('salt fingers') drop out of the bottom of the return flow layer as can be seen at an early stage of the same experiment (Figure Appendix XVIII). This image is very similar to Turner's (1973) Fig. 8.8, turned upside down. At this time, the CBL has not reached the return flow layer everywhere, yet. At the position of the CT probe, a rising thermal has penetrated to the return flow layer and destroyed the salt fingers, while near the return flow front the salt fingers have not had enough time to drop out of the region saturated with dye.

Figure Appendix XVIII: Salt fingers caused by double-diffusive convection.
This frame was taken at an earlier time from the same movie as Figure Appendix XV. The red dye visualises salt fingers dropping into the dye-free region underneath the return flow between the protruding return flow front and the black shaft of the conductivity and temperature probe.

Double-diffusive convection in Figure Appendix XV happens in a region of strong convective heating and therefore amplifies the convection. At this stage of the experiment I do not expect this to alter to overall flow structure. At an earlier stage, as in Figure Appendix XVIII, this convection at best improves the comparability with the atmosphere. In the atmosphere the return flow is always turbulent, but in the water tank double-diffusive convection adds turbulence to the return flow that may otherwise be laminar.

C.5 Tracer Dispersion

Injected dyes are a simple and convenient method for getting excellent qualitative and partially quantitative information on the layering and the dynamics of the flow in the tank. They correspond to tracers in the atmosphere. Figure Appendix XVI shows an example of an experiment with three different dyes, which I will explain in detail in the following paragraphs.

$KMnO_4$ is a very rich dye in the form of red-purple crystals with a density much higher than saltwater (red dye in Figure Appendix XVI). When carefully dropped over the water surface, $KMnO_4$ crystals sink to the tank bottom leaving a red-purple vertical trail. The dye helps visualise any residual large eddy motion in the tank. During the experiment the dye crystals on the tank bottom release a constant stream of dye that serves as a tracer for the backscatter boundary layer like PM emitted into the atmosphere. Further away from the tank bottom the vertical column of dye distorts due to horizontally moving fluid layers and permits a clear distinction between laminar and turbulent layers. Experiments with $KMnO_4$ require a white background and a fully illuminated tank for photographing.

Food colouring (blue dye in Figure Appendix XVI) works under the same background and light conditions as $KMnO_4$ providing alternative colours, in particular blue and green. They are liquid and less rich than $KMnO_4$. I diluted food colours with water and injected them with a long syringe at desired locations.

Of particular value for alternative light conditions is Uranine (fluorescein sodium salt, $C_{20}H_{10}Na_2O_5$), a very rich green fluorescent dye (green dye in Figure Appendix XVI). It works best in a dark laboratory, against a black background, and illuminated by a bright sheet of light. The water soluble Uranine powder does not sink in water and must therefore be dissolved and injected into the tank. Uranine proves extremely useful when dissolved in high-density saltwater and injected at the edge of the tank. The dense solution spreads out very evenly over the tank bottom without diluting. When a light sheet illuminates the tank from above, rising thermals in the heated tank can be captured extremely well and the top of the CBL can be determined with good accuracy. If injected in the right concentration Uranine can be used in conjunction with bright particles for particle image velocimetry.

C.6 Measurement of Velocity

Recording Velocity Fields in the Water Tank

Velocities in the water tank were measured using particle image velocimetry (PIV). The flow was visualised with submerged particles (section C.9) illuminated by a bright light source. In the first PIV experiment I stirred two to four spatulas of each of about five density ranges in Kodak Professional Photo-Flo 200 solution. Photo-Flo reduces surface tension but also tends to foam when stirred into saltwater. I carefully poured the slurry of particles into the freshwater tank. The mixer in the freshwater tank kept the particles from settling, which ensured a good yield and distribution of particles over plain and slope. If a high particle density far from the experimental tank inlet is needed it is better to pour the particle slurry into the empty experimental tank at the location, where most particles are needed. Often a combination of adding particles to the freshwater tank and the experimental tank gives the best results. When I drained the tank after completion of the experiment I sieved out the particles for reuse in later experiments. Over the course of several experiments more particles of different densities were added.

The motion of the particles was recorded on a DV magnetic tape with a consumer digital video camera (Canon Optura 10 or Canon ZR 100). I focused the camera manually because in auto-focus mode the video camera tends to frequently re-focus causing repeated flashes of over-exposed and blurred images. The camera operates best in a normal light mode because it is sensitive enough to capture the particles with normal shutter speed while low light or night settings tend to lead to streaks and delayed response.

I transferred the video into an avi file on a computer by connecting the video camera to the computer via a "firewire" cable (IEEE 1394) and then capturing the video in Pinnacle Studio. The captured video file was then time-lapsed by a factor of three and saved as an avi file with Indeo 5.10 compression. The compressed video file is accessible in Matlab. To perform the PIV analyses I used MatPIV, a set of Matlab function developed by J. Kristian Sveen.

PIV Pre-Processing

To prepare the video for MatPIV, I extracted all individual frames of the time-lapsed video (the individual frames are 1/10 seconds apart) as bitmap images, converted the colour images into black and white, and set all grey values below a cut-off (typically 160-180, where 0 is black and 255 white) to 0. This effectively discriminated the very bright white particles in the light beam from background noise, for example particles outside of the light beam, reflections at the glass walls of the tank, bubbles, external stray light, and the CT probes.

MatPIV requires as input the horizontal and vertical scales of the video frames. As part of the MatPIV package, Kristian Sveen developed a Matlab function "definewoco.m" to calculate the conversion from pixels to true length. Before the experiment a white board with equally spaced black "+" symbols was placed into the focal plane of the video camera and recorded for a few seconds[12]. For the PIV analysis, one frame of this short video was extracted and converted into an inverted grey scale bitmap file, so that the image showed light grey "+" symbols on a dark grey background. The conversion function "definewoco.m" is programmed for different symbols either light on dark or reversed. Ian Chan found light "+" signs on a dark background to work best. The conversion function prompts the user to highlight the "+" symbols to be used for the conversion scale calculation and to enter the true coordinates. I typically used 9-15 "+" signs spaced at 10-20 cm. The conversion function generates a length scale conversion data file ("worldco.mat", the "world coordinates") that is used as input to the main PIV function.

To avoid unnecessary PIV calculations and erroneous velocities, areas outside of the water tank and areas right at the surface or end walls, which appears practically white under strong reflection from the light source, need to be masked out. Included in the MatPIV package is a function "mask.m" that prompts the user to define polygons around those areas that should be masked out and generates a "mask.bmp" image that is used by the main MatPIV program.

PIV Main Processing

Besides mask and length scale conversion files, the main MatPIV function requires as input two bitmap images of video frames for particle tracking and a number of custom settings described next.

MatPIV tracks particles inside small interrogation windows within the video frame. It increases quantity and quality of the output but also the computational effort to run MatPIV in several loops with interrogation windows, which overlap and, from one loop to the next, decrease in size and are horizontally and vertically offset. I received good results using the multi-pass method with interrogation window sizes 32 by 32 pixels for the first pass and 16 by 16 pixels for the second and third pass and with a window overlap of 0.25.

I applied MatPIV to adjacent frames. Recall that the videos were time lapsed by a factor of three so that velocities were measured based on frames 0.1 s apart. At typical velocities of 0.5 cm s^{-1}, particles moved by 0.05 cm. On a frame of 720 pixels wide corresponding to 40 cm,

[12] This also facilitates the manual focusing which is difficult with small particles only.

particles moved by approximately 1 pixel. This spacing is appropriate since "matpiv.m" uses all particles in a given interrogation window to calculate velocities with sub-pixel resolution. If the time spacing is too large MatPIV is not able to relate particles between frames.

The core functions within MatPIV contain a global and a local filter with hard coded thresholds and an interpolator. I removed these function calls to reduce CPU time because tests showed that they do not improve data quality substantially for my data sets.

PIV Batch- and Post-Processing

Ian Chan wrote a batch function that carries out the main "matpiv.m" function repeatedly on selected frames. I set the batch function such that MatPIV was repeated every second frame, i.e. every 0.2 s. For a typical video length of about 1000 s the batch function generated about 5000 2-D velocity fields and took roughly 15 hours to compute on a 3 GHz Pentium 4 processor, when only small regions where masked out. This fine time resolution of 0.2 s was needed to calculate for example vertical velocity variances.

In the atmosphere, upslope flow velocities were determined with a Doppler sodar, which averaged over approximately 20 minutes. The relationship between time differences in atmospheric and water-tank idealisation is non-linear (section 3.6). Nevertheless, a suitable averaging time can be determined from noting that four hours of positive heat flux in the atmosphere (0800-1200 PDT) correspond to 300 s in the water tank (see Table Appendix I on page 211), i.e. 20 minutes in the atmosphere correspond to 25 s in the laboratory. I chose to average over 20 s (100 individual 2-D velocity fields), which was sufficiently long to average out turbulent variations. A comparison with averages over 6 s showed very similar velocities, but the 20-s averages produced substantially more data points in higher flow regions where the particle density was typically lower.

The MatPIV package comes with different filters to automate the removal of outliers in the velocity field. The filters, however, require defining thresholds that effectively remove outliers without eliminating important data slow down computations. Instead I removed all filters and in the last step, when calculating the average upslope flow velocity, applied the median rather than the mean, which removed most outliers by assigning them much less weight than in the case of the mean. A comparison with global filter and mean value calculations showed that the median calculations without filtering performed equally well.

C.7 Determining the Heat Flux into the Tank

In chapter 3 I identified the constant heat flux $Q_{H,w}$ into the tank as one of the key parameters. An accurate estimate of $Q_{H,w}$ is of great importance for comparing predictions (section 3.5) with water-tank observations (section 4.3).

There are a number of ways to determine the heat flux into the tank. A direct measurement with a thin film heat flux sensor is fairly inaccurate in my experimental setup: the sensor requires intimate contact with the surface which is difficult to achieve because of the varying roughness and thickness of the paint; moreover, on the scale of a typical heat flux sensor ($\sim 0.01m$), heating with the strip heaters is inhomogeneous, so that one would have to average over measurements at many randomly distributed points.

A more accurate method of determining the net heat flux into the tank is to measure the warming of the water and convert this into the corresponding energy supplied. I filled the tank with freshwater and constantly stirred the water while heating from below. From time series of temperature at different points in the tank volume I could determine the net energy input very accurately.

The downside of this setup is that the heat losses could be different from an experiment with stratified saltwater. However, determining heat input into salt-stratified water requires simultaneous measurements of CBL mean specific volume increment $\alpha_{s,w}$ and CBL depth h_w; this introduces greater uncertainties, roughly 10-20% of the true heat flux, than the expected difference in heat loss, a few percent of the total heat flux. Furthermore, one must account for additional heat flux into the CBL from entrainment at the top. With the underlying assumption that the entrainment model by Carson (1973) is sufficiently accurate this requires simultaneous calculation of the entrainment coefficient A and the net heat flux $Q_{H,w}$. Certainly, this method is not feasible for the entire tank because of the great depth variations and complicated internal structure of the CBL caused by the upslope flow. Restricting oneself to flat convection, e.g. over the plateau, induces additional uncertainties since the ratio between heated surface area and water volume is smaller over plain and plateau than over the slope; the same holds for the ratio between lateral heat loss area (side and end walls) and heated volume.

Given these uncertainties in salt-stratified tank experiments I will now derive the typical value suggested in (3.26), $Q_{H,w} \approx 1.85 \times 10^{-3}\, K\, m\, s^{-1}$, from the freshwater method described above.

To estimate the energy loss, I first determined the total maximum power that was delivered by the strip heaters underneath the tank bottom. The power outlet supplies an effective voltage of $V_{eff} = 199V$ to the strip heaters. After about 30 s of supplying full power to the strip heaters, the effective current through each strip heater is fairly steady with a mean value of $I_{eff} = 1.711\, A$. In a purely Ohmic AC circuit, current is in phase and proportional to voltage so that the total power of all 34 strip heater is

$$P_w = 34 \times V_{eff} \cdot I_{eff} = 11{,}560\, W\,. \tag{C.1}$$

The horizontal cross-sectional area of the tank bottom is

$$A_{h,w} = 0.591\, m^2\,. \tag{C.2}$$

A typical experiment is run at a 50% duty cycle, i.e. 50% of the total power is supplied to the strip heaters. Hence, the maximum power density that could have been supplied by the strip heaters through the tank bottom is

$$\widetilde{Q}_{H,w} = 50\% \times \frac{P_w}{A_{h,w}} = 0.5 \times \frac{11{,}560\, W}{0.6021\, m^2} = 9600\, W\, m^{-2}\,. \tag{C.3}$$

To measure the actual net heat flux into the water, I filled three quarters of the tank volume with freshwater and installed three C&T probes at different locations in the tank and an electrical mixer. During the heating, the probes took 5000 temperature measurements over 1000 s (about 17 minutes). In addition I took manual measurements of the water temperature with a mercury thermometer with a resolution of 0.05°C every 30 s. Between manual measurements I stirred the tank water with a batten. The results are shown in Figure Appendix XIX.

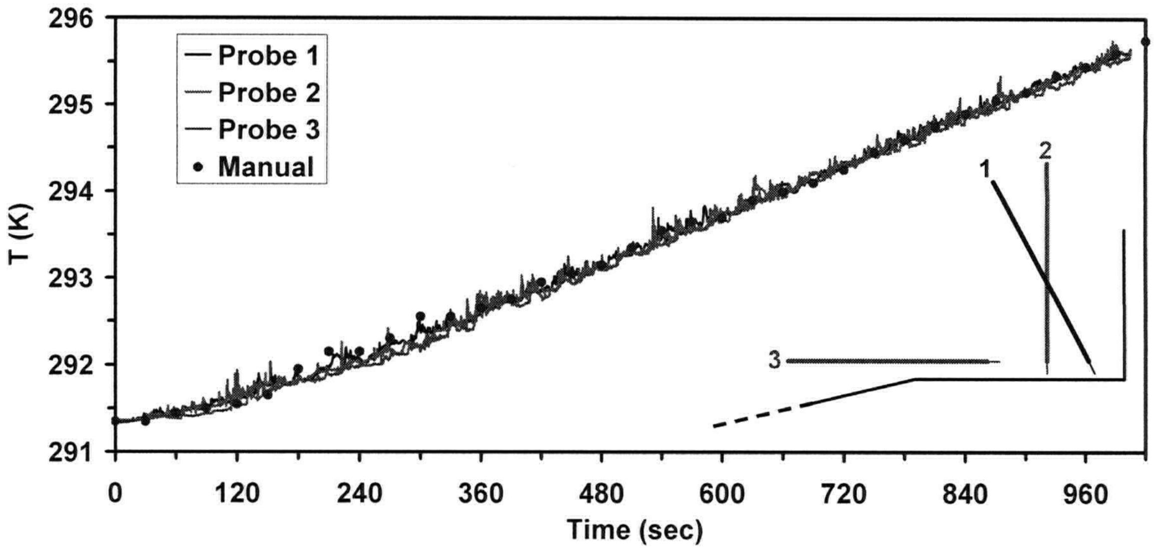

Figure Appendix XIX: Heating of a well-mixed freshwater tank.
The three coloured lines show the time series of temperatures measured with C&T probes every 0.2 s for a total duration of 1000 s. The blue circles show manual reference measurements with a mercury thermometer. The positions and angles of the three probes in the tank are shown to the right underneath the curves.

After an adjustment time of about 300 s all three probes show a linear trend and excellent agreement with the manual temperature measurements. The net heat flux can be calculated from the slope of the trend. To determine the trend one can either use a simple linear regression or an elaborate Bayesian analysis. If one assumes that the perturbations from the trend follow a Gaussian distribution then the Bayesian straight-line fit leads to the same results as a linear least-square regression (Sivia, 1996). Although it is obvious from Figure Appendix XIX that the turbulent perturbations are skewed, two improvements can be applied to justify a simple linear regression.

Firstly, the sets of measurements by the three probes, X_1, X_2, and X_3, are synchronised and independent. Furthermore, the turbulence distributions must have a finite mean and variance, limited for example by the boiling and freezing temperature of water. Therefore the Central Limit Theorem applies, which tells us that the sample average of n probes converges to a Gaussian distribution for $n \to \infty$. This convergence is fast, and a Gaussian is a better estimate for the mean of all three probes, $(X_1 + X_2 + X_3)/3$, than for the individual measurements X_1, X_2, and X_3.

Secondly, in the case of a skewed distribution, the median of the three probes (i.e. the intermediate of the three values) is a more robust measure of the "average" temperature measured by the three probes than the mean (Gregory, 2005).

The median of the three probes and the linear regression result from using MS Excel are shown in Figure Appendix XX. The resulting sampling distribution is well-approximated by a Gaussian (inset). The "Regress" command in Mathematica gives a slope with standard error of

$$\frac{\Delta T_w}{\Delta t_w} = (4.7849 \pm 0.0024) \times 10^{-3}\ \mathrm{K/s} \tag{C.4}$$

and an $r^2 = 0.9990$.

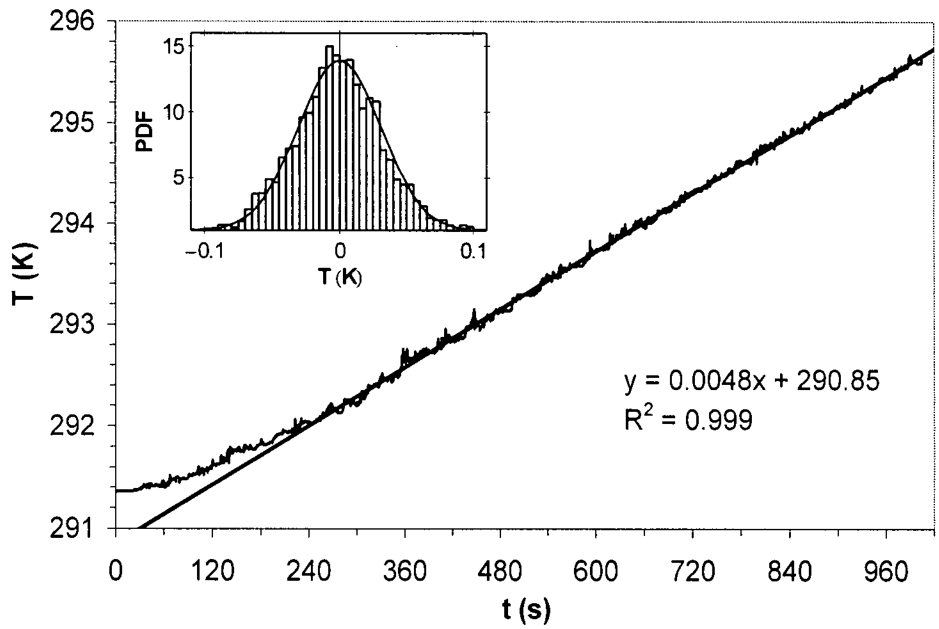

Figure Appendix XX: Time series of the median of the three probes in a heated and well-mixed freshwater tank. The thick straight line is the linear least-square fit to the median of the three coloured curves in Figure Appendix XIX (thin line). For the linear trend line I removed the first 240 s and used the least-square regression functionality in MS Excel. The inset shows the probability density function of the temperature perturbations of the detrended time series and a fitted Gaussian.

According to the First Law of Thermodynamics, the heat energy added to water of volume V_w, density ρ_w, and specific heat C_w heated by ΔT_w is given by $C_w \cdot \rho_w \cdot V_w \cdot \Delta T_w$. The energy supplied to the tank through the horizontal bottom area $A_{h,w}$ of the water tank in any given laboratory time interval Δt_w is then the (dynamic) heat flux

$$\widetilde{Q}_{H,w} = C_w \cdot \rho_w \cdot \frac{V_w}{A_w} \cdot \frac{\Delta T_w}{\Delta t_w} \tag{C.5}$$

and in kinematic units

$$Q_{H,w} = \frac{V_w}{A_w} \cdot \frac{\Delta T_w}{\Delta t_w} = \overline{D_w} \cdot \frac{\Delta T_w}{\Delta t_w}, \tag{C.6}$$

where $\overline{D_w} = (0.463 - 0.313)/2\,m = 0.388\,m$ was the mean water depth in the tank, hence

$$Q_{H,w} \approx 1.85 \times 10^{-3}\,K\,m\,s^{-1}. \tag{C.7}$$

The corresponding power supplied to the water is $P_w = 4650\,W$, which is 81% of the total power delivered by the strip heaters.

This freshwater experiment should provide a good estimate of the heat flux during experiments with stratified saltwater. In both cases, some heat is lost to solid parts of the tank and most is lost to the air underneath the tank. In a stratified tank the water surface temperature remains constant so that no heat is lost there. In the freshwater experiment the net heat exchange at the water surface is also negligible because the difference between water and room temperature increased during the experiment from about -2.5 to 2°C.

C.8 Conversion of Probe Voltages to Specific Volume

The water-tank equivalent of atmospheric potential temperature is specific volume, the inverse of density. Variations of specific volume in the tank are caused by salinity and temperature variations. To produce the equivalent of vertical profiles of potential temperature I used ultra-fast conductivity and temperature (CT) probes which output a conductivity and temperature voltage. A complicated procedure is required to convert this output into specific volume. The manual use of the tables and formulas provided in PME (1997) is not feasible for the large amount of measurements. Therefore, I developed a program in Mathematica that automates the conversion. The program logic is shown below followed by the Mathematica notebook. All formulae are taken from PME (1997) and Kim (2001) and references therein.

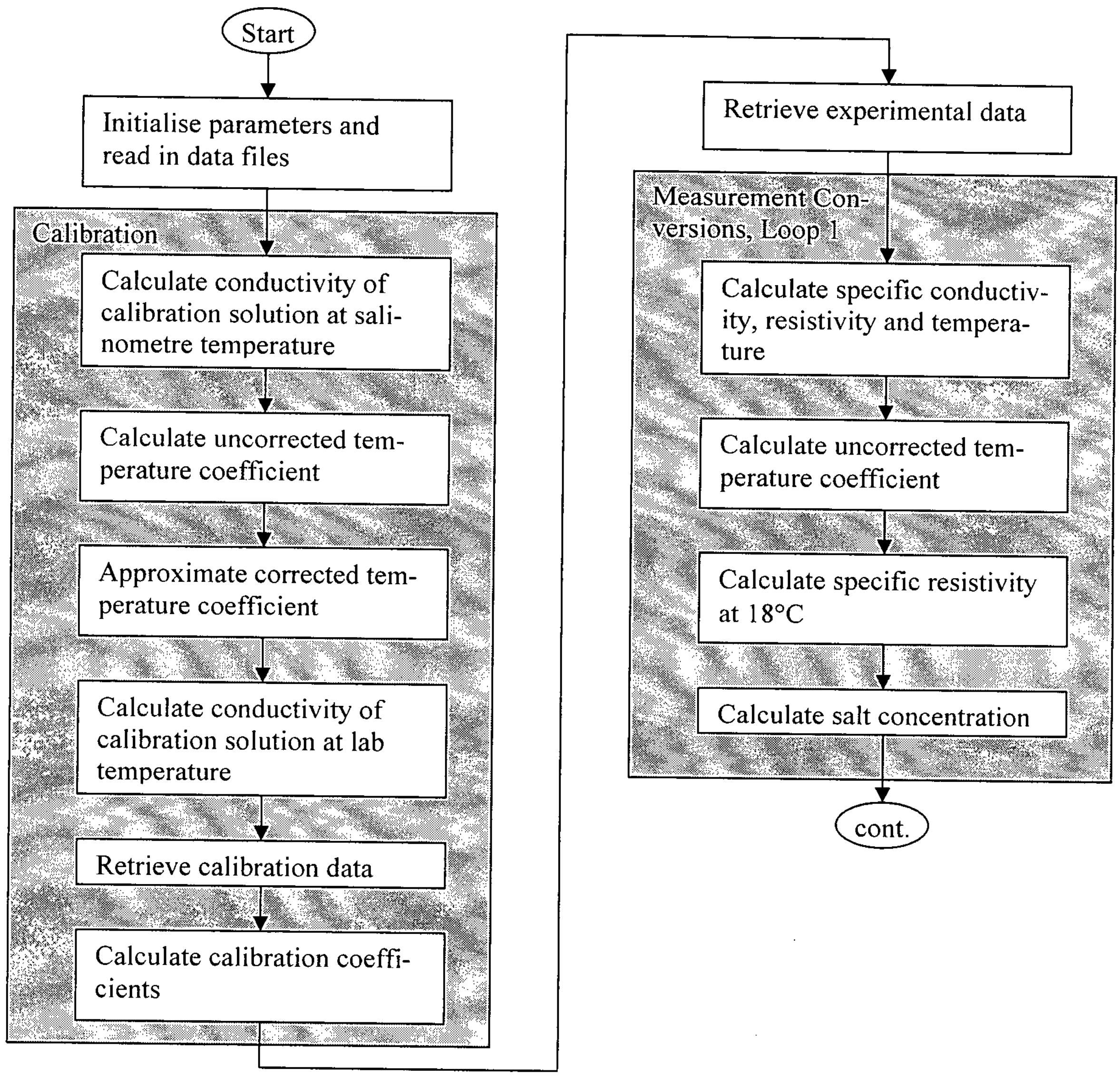

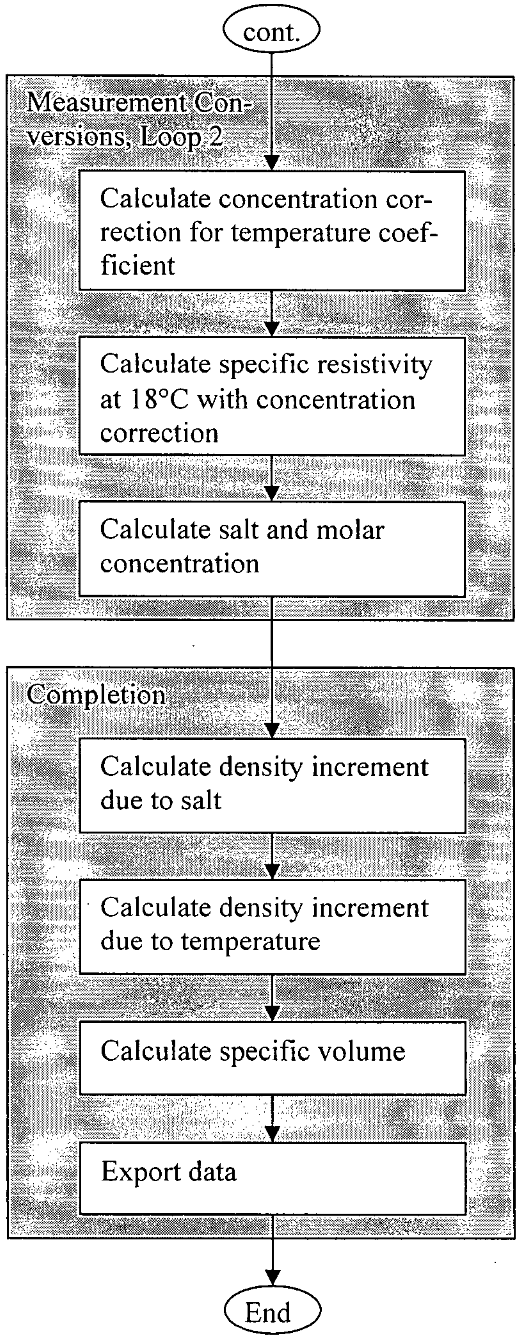
cont.
Measurement Conversions, Loop 2
Calculate concentration correction for temperature coefficient
Calculate specific resistivity at 18°C with concentration correction
Calculate salt and molar concentration
Completion
Calculate density increment due to salt
Calculate density increment due to temperature
Calculate specific volume
Export data
End

CT Calibration and Measurement

CT Probe Calibration and Conversion of CT Probe Voltage to Water Specific Volume

Introduction

This program consists of two parts. In the first part, the CT probe parameters are determined from the calibration values. In the second part, using the parameter values of the first part, the program reads in the output file of the profiler software and converts the pair of voltage measurements into temperature, salt concentration, and finally specific volume. Specific volume will be graphed versus height and the input file amended by these three quantities.

Initial Clean Up

```
Remove["Global`*"];
Off[General::"spell"];
Off[General::"spell1"];
```

Input

V_C is the output voltage of the conductivity channel in V.

V_T is the output voltage of the temperature channel in V.

$V_{off,C}$ is the voltage offset of the conductivity probe in V (known from calibration).

$V_{off,T}$ is the voltage offset of the temperature probe in V (known from calibration).

G_C is the conductivity gain in $\frac{V\,cm}{mS}$ (known from calibration).

$\tilde{A}$ is a non-dimensional parameter, which includes the temperature gain (known from calibration).

B is a parameter in the temperature equation in K (known from calibration).

Specifying Parameters

Have to specify these:

```
dateOfExp = "2004-08-04";
(* This is the folder used in the file path for reading and writing data files *)
dataFilePath =
 "C:\\Documents and Settings\\Christian Reuten\\My Documents\\Study\\Areas\\
   Water Tank Studies\\CT Calibration and Measurement\\" <> dateOfExp;
(* This is the file path that will usually not be changed *)
nProbes = 3              (* number of probes *);
condRatioCalSolData = {1.08898, 1.08896, 1.08904, 1.08903, 1.08905}
(* conductivity ratio of calibration solution (CalSol) determined with salinometre *);
tCalSolC = 30
(* temperature at which conductivity ratio of CalSol was measured in salinometre *);
rowTlow = {11, 11, 11}
(* rows in CAL.DAT from which to calculate low temperature calibration point *);
t1C = {22.9, 22.9, 22.9}  (* low temperature calibration point in °C *);
rowThigh = {7, 7, 7}
(* rows in CAL.DAT from which to calculate high temperature calibration point *);
t2C = {34.5, 34.5, 34.5}  (* high temperature calibration point in °C *);
rowCalSol = {11, 11, 11}
(* rows in CAL.DAT from which to calculate conductivity of CalSol *);
tcC = t1C                 (* temperature of calibration solution in lab *);
```

Reading in the Raw Data Files

Make sure all header lines are deleted since reading them in from a “dat” file does not work properly.

```
rawDataCal = Drop[Import[dataFilePath <> "\\CAL.DAT", "Table"]];
```

```
rawDataExp = Drop[Import[dataFilePath <> "\\EXP.DAT", "Table"]];
```

Preliminary Calculations

Mean conductivity ratio from salinometre measurements:

```
condRatioCalSol = Mean[condRatioCalSolData];
```

Conversions from °C to K:

```
t1K = t1C + 273.15;
t2K = t2C + 273.15;
tcK = tcC + 273.15;
```

Number of sets of scans:

```
nSetsCal = Length[rawDataCal]
nSetsExp = Length[rawDataExp]
```

11

127

Calibration

Conductivity of CalSol

Step 1: Conductivity of solution at salinometre water bath temperature

```
c0 = 6.766097*^-1;
c1 = 2.00564*^-2;
c2 = 1.104259*^-4;
c3 = -6.9698*^-7;
c4 = 1.0031*^-9;
rt[T_] := c0 + T * (c1 + T * (c2 + T * (c3 + c4 * T)));
(* temperature correction coefficient *)
ctCalSolC = condRatioCalSol * (42.9140 * rt[tCalSolC] / rt[15])  (* in mS/cm *)
```

63.5431

Step 2: Calculate uncorrected temperature coefficient as a function of temperature *t* in °C:

```
aBT = {2.1179818 * 10^-2, 7.8601061 * 10^-5, 1.5439826 * 10^-7, -6.2634979 * 10^-9, 2.2794885 * 10^-11};

btCalSolC = Sum[aBT[[i + 1]] tCalSolC^i, {i, 0, 4}]            (* in 1/°C *)
 btcC = Table[Sum[aBT[[i + 1]] tcC[[j]]^i, {i, 0, 4}], {j, 3}]
(* in 1/°C *)
```

0.0235262

```
{0.0229918, 0.0229918, 0.0229918}
```

Step 3: Approximate concentration correction:

```
btildetCalSolC = btCalSolC - 0.0008;     (* in 1/°C *)
btildetcC = btcC - 0.0008;
(* in 1/°C *)
```

Step 4: Calculate conductivity of calibration solution at lab temperature:

```
c = ctCalSolC * (1 + btildetcC * (tcC - 18)) / (1 + btildetCalSolC * (tCalSolC - 18))
```

```
{55.3563, 55.3563, 55.3563}
```

Retrieving Calibration Data from Raw Data Files

In the following command, the Take retrieves a set of scanned data for a given setting or test solution. These data need to be averaged, done with Mean. The i-loop covers all sets of data taken. This has to be done 6 times, V_T and V_C for probes 1, 2, and 3, which are in columns 3-8 of the original data file.

```
calData = Table[{rawDataCal[[i, 3]], rawDataCal[[i, 4]], rawDataCal[[i, 5]],
   rawDataCal[[i, 6]], rawDataCal[[i, 7]], rawDataCal[[i, 8]]}, {i, nSetsCal}]
```

```
{{2.431, 2.56, 2.682, 2.116, 2.459, 2.642},
 {2.431, 2.519, 2.684, 2.09, 2.462, 2.633}, {-0.001, -0.002, -0.001, -0.001, -0.001, -0.001},
 {-0.662, -4.995, -0.527, -5., -0.628, -5.}, {-0.622, -4.995, -0.484, -5., -0.589, -5.},
 {-0.557, -4.993, -0.416, -5., -0.524, -5.}, {-0.38, -4.994, -0.234, -5., -0.349, -5.},
 {2.318, 1.989, 2.567, 2.047, 2.352, 2.167}, {2.304, 2.009, 2.557, 2.081, 2.338, 2.174},
 {2.328, 2.005, 2.583, 2.15, 2.364, 2.159}, {2.25, 2.009, 2.507, 2.1, 2.25, 2.166}}
```

Retrieving Calibration Voltages from Calibration File

Step 1: Temperature Voltage Offset (hard-coded because hardly changes)

```
vtoff = {-4.988, -4.990, -4.999}   (* temperature voltage offset in V *)
```

```
{-4.988, -4.99, -4.999}
```

Step 2: Conductivity Voltage Offset (hard-coded because hardly changes)

```
vcoff = {-5., -5., -5.}          (* temperature voltage offset in V *)
```

```
{-5., -5., -5.}
```

Step 3: Low Temperature Voltage

```
vt1 = {calData[[rowTlow[[1]], 1]], calData[[rowTlow[[2]], 3]], calData[[rowTlow[[3]], 5]]}
  (* voltage (in V) at low temperature t1 *)
```

```
{2.25, 2.507, 2.25}
```

Step 4: High Temperature Voltage

```
vt2 = {calData[[rowThigh[[1]], 1]], calData[[rowThigh[[2]], 3]],
  calData[[rowThigh[[3]], 5]]}    (* voltage (in V) at maximum temperature t2 *)
```

```
{-0.38, -0.234, -0.349}
```

Step 5: High Conductivity Voltage

```
vc = {calData[[rowCalSol[[1]], 2]], calData[[rowCalSol[[2]], 4]],
  calData[[rowCalSol[[3]], 6]]}  (* conductivity voltage (in V) of high cond. solution *)
```

```
{2.009, 2.1, 2.166}
```

Calculation of Calibration Coefficients

$$\texttt{gc} = \texttt{N}\left[\frac{\texttt{vc} - \texttt{vcoff}}{\texttt{c}}\right] \;\; (*\ \texttt{in}\ \frac{\mathrm{V}\times\mathrm{cm}}{\mathrm{mS}}\ *)$$

```
{0.126616, 0.12826, 0.129452}
```

$$\texttt{b} = \texttt{N}\left[\frac{\texttt{t1K} * \texttt{t2K} * \texttt{Log[vt1 - vtoff]} - \texttt{t1K} * \texttt{t2K} * \texttt{Log[vt2 - vtoff]}}{\texttt{t2K} - \texttt{t1K}}\right] \;\; (*\ \texttt{in K}\ *)$$

```
{3545.45, 3573.28, 3486.13}
```

$$\texttt{a} = \texttt{N}\left[\frac{\texttt{t1K} * \texttt{Log[vt1 - vtoff]} - \texttt{t2K} * \texttt{Log[vt2 - vtoff]}}{\texttt{t1K} - \texttt{t2K}}\right] \;\; (*\ \texttt{dimensionless}\ *)$$

```
{-9.99649, -10.0553, -9.79461}
```

Measurements

Retrieving Experiment Data from Raw Data Files

Time and height are in columns 1 and 2 of the original data file, resp., and V_T and V_C for probes 1, 2, and 3 are in columns 3-8 of the original data file.

```
expData = rawDataExp;
```

Retrieving Experiment Voltages from Experiment File

```
vT = {expData[[All, 3]], expData[[All, 5]], expData[[All, 7]]};
vC = {expData[[All, 4]], expData[[All, 6]], expData[[All, 8]]};
```

Processing of Data

We need to find the specific volume.
This is a 2-step process, each of which consists of sub-steps. It is not possible to determine the concentration correction b_{corr} to the temperature coefficient b_t before the concentration is determined. Therefore, the concentration is first calculated based on b_t without concentration correction. That provides a fairly accurate approximation to the final concentration. The concentration is used to determine b_{corr}. Finally, the corrected temperature coefficient $\tilde{b}_t$ is used to calculate a more accurate salt concentration.

1. Specific conductivity C in $\frac{mS}{cm}$ and temperature T in K.

2. Conversion to specific resistivity $R_t = \frac{10^{-3}}{C}$ in Ω cm and temperature $t = (T - 273.16K)\frac{°C}{K}$ in °C.

Note on units: $1\ \Omega cm = 1\ \frac{V}{A} cm = 1\ \frac{cm}{S} = 10^{-3}\ \frac{cm}{mS}$ (S = "Siemens").

3. Temperature coefficient b_t.

I. Loop 1 without concentration correction of temperature coefficient.

4. Specific resistivity at 18 °C, R_{18}.

5. Salt concentration $p = p(R_{18})$ in %.

II. Loop 2 with concentration correction of temperature coefficient.

3. Temperature coefficient $\tilde{b}_t$ from uncorrected coefficient b_t and concentration correction b_{corr}.
4. Specific resistivity at 18 °C, R_{18}.
5. Salt concentration $p = p(R_{18})$ in %.
6. Molar concentration M_0.
7. Density increment due to salt, $\Delta\rho_s$ in $\frac{kg}{m^3}$.
8. Density of pure water ρ_0 in $\frac{kg}{m^3}$ as a function of temperature t in °C.
9. Density $\rho = \Delta\rho_s + \rho_0$ in $\frac{kg}{m^3}$ and specific volume $\alpha = \rho^{-1}$ in $\frac{kg}{m^3}$.

Step 1: Specific conductivity and temperature

```
c = N[(vC - vcoff)/gC]; (* in mS/cm *)
```

```
tK = b/(Log[vT - vtoff] - a);
```

Step 2: Conversion to specific resistivity and temperature in °C

```
rt = 10^3/c ; (* in Ω cm *)
```

```
tC = tK - 273.15;
```

Step 3: Temperature coefficient

Coefficients of polynomial:

```
aBT = {2.1179818 * 10^-2, 7.8601061 * 10^-5, 1.5439826 * 10^-7, -6.2634979 * 10^-9, 2.2794885 * 10^-11};
```

Uncorrected temperature coefficient as a function of temperature t in °C:

```
bt = Sum[aBT[[i + 1]] tC^i, {i, 0, 4}]; (* in 1/°C *);
```

Loop 1: No concentration correction for temperature coefficient

```
btilde = bt; (* in 1/°C *)
```

Step 4: Specific resistivity at 18 °C

```
r18temp = rt * (1 + btilde * (tC - 18));
```

Step 5: Salt concentration p in %

Define the coefficients for the different polynomials:

```
a1 = {53.5590, 24.2130, -138.3184, 745.0609};
a2 = {53.6508, 17.7272, -6.9940, -2.0216, 3.0262};
a3 = {65.3068, 7.0523, -3.1346, 1.4293};
a4 = {-923.8866, 1241.9749, -546.7730, 96.6712, -4.8034};
```

Define polynomials:

```
f1[p_] := Sum[a1[[i + 1]] (√p)^i, {i, 0, 3}];
f2[p_] := Sum[a2[[i + 1]] (√p)^i, {i, 0, 4}];
f3[p_] := Sum[a3[[i + 1]] (Log[p])^i, {i, 0, 3}];
f4[p_] := Sum[a4[[i + 1]] (Log[p])^i, {i, 0, 4}];
```

Dependent on the concentration p, determine the specific resistivity at 18 °C, R_{18}, from x = p*r18 (eqn. 3-6):

```
ptemp = Table[
  Which[
   r18temp[[j, i]] > 5534, Re[p /. Solve[p * r18temp[[j, i]] == f1[p], p][[1]]],
   r18temp[[j, i]] > 65.387, Re[p /. Solve[p * r18temp[[j, i]] == f2[p], p][[1]]],
   r18temp[[j, i]] > 8.237, p /. FindRoot[(p * r18temp[[j, i]] == f3[p]), {p, 1}],
   r18temp[[j, i]] > 4.64, p /. FindRoot[(p * r18temp[[j, i]] == f4[p]), {p, 10}],
   r18temp[[j, i]] == r18temp[[j, i]], 999
  ],
  {j, nProbes},
  {i, nSetsExp}];
```

Loop 2: Concentration correction for temperature coefficient

Define the correction matrix:

```
bcorrMatrix = {{-0.0001, -0.0004, -0.0009, -0.0011},
  {-0.0001, -0.0007, -0.0007, -0.0004},
  {-0.0002, -0.0012, -0.0004, 0.0004}};
```

Values of temperature t (in °C) and concentration p (in %):

```
tVector = {0, 50, 100};
pVector = {0.1, 0.5, 1.0, 5.0};
```

Determine the four adjacent correction values for the input of temperature t (in °C) and concentration p (in %).

```
bcorrtemp = {};
For[j = 1, j ≤ nProbes, j++,
 For[i = 1,
  i ≤ nSetsExp,
  i++,
  t = tC[[j, i]];
  {x1, y1} = Which[
      t ≤ tVector[[2]] &&                         ptemp[[j, i]] <= pVector[[2]], {1, 1},
      t <= tVector[[2]] && pVector[[2]] < ptemp[[j, i]] <= pVector[[3]], {1, 2},
      t <= tVector[[2]] && pVector[[3]] < ptemp[[j, i]]                , {1 , 3},
    50 < t ≤ tVector[[3]] &&                      ptemp[[j, i]] ≤ pVector[[2]] , {2, 1},
    50 < t ≤ tVector[[3]] && pVector[[2]] < ptemp[[j, i]] <= pVector[[3]], {2, 2},
    50 < t ≤ tVector[[3]] && pVector[[3]] < ptemp[[j, i]]                , {2, 3}];
  {x2, y2} = {x1, y1} + {1, 1};
  (* Slopes and y-intercepts: *)
  mt1 = (bcorrMatrix[[x1, y2]] - bcorrMatrix[[x1, y1]]) / (pVector[[y2]] - pVector[[y1]]);
  mt2 = (bcorrMatrix[[x2, y2]] - bcorrMatrix[[x2, y1]]) / (pVector[[y2]] - pVector[[y1]]);
  bt1 = bcorrMatrix[[x1, y1]] - mt1 * pVector[[y1]];
  bt2 = bcorrMatrix[[x2, y1]] - mt2 * pVector[[y1]];
  (* interpolated values for the correction factor at the minimum (t1) and
    maximum (t2) of the temperature interval: *)
  bcorrt1 = mt1 * ptemp[[j, i]] + bt1;
  bcorrt2 = mt2 * ptemp[[j, i]] + bt2;
  (* interpolate for temperature, slope, y-intercept: *)
  mt = (bcorrt2 - bcorrt1) / (tVector[[x2]] - tVector[[x1]]);
  bt12 = bcorrt1 - mt * tVector[[x1]];
  bcorrtemp = Append[bcorrtemp, mt * t + bt12];
 ]
];
```

```
bcorr = Transpose[Table[{bcorrtemp[[i]], bcorrtemp[[i + nSetsExp]], bcorrtemp[[i + 2 nSetsExp]]},
   {i, nSetsExp}]];
```

Corrected temperature coefficient:

```
btilde = bt + bcorr;    (* in 1/°C *)
```

Step 4: Specific resistivity at 18 °C with corrected temperature coefficient

```
r18 = rt * (1 + btilde * (tC - 18));
```

Step 5: Salt concentration p in %

```
psalt = Table[
  Which[
   r18[[j, i]] > 5534, Re[p /. Solve[p * r18[[j, i]] == f1[p], p][[1]]],
   r18[[j, i]] > 65.387, Re[p /. Solve[p * r18[[j, i]] == f2[p], p][[1]]],
   r18[[j, i]] > 8.237, p /. FindRoot[(p * r18[[j, i]] == f3[p]), {p, 1}],
   r18[[j, i]] > 4.64, p /. FindRoot[(p * r18[[j, i]] == f4[p]), {p, 10}],
   r18[[j, i]] == r18[[j, i]], 999
  ],
  {j, nProbes},
  {i, nSetsExp}];
```

Step 6: Molar concentration M_0

$$m0 = \frac{1}{0.058443}\frac{psalt}{100 - psalt};$$

Step 7: Density increment due to salt, Δp_s

$$aa = \{\{-0.2341, 3.4128 * 10^{-3}, -2.7030 * 10^{-5}, 1.4037 * 10^{-7}\}, \{5.3956 * 10^{-2}, -6.2635 * 10^{-4}, 0, 0\}, \{-9.5653 * 10^{-4}, 5.2829 * 10^{-5}, 0, 0\}\};$$

```
bb = {45.5655, -1.8527, -1.6368, 0.2274};
```

$$deltaRhoS[m\_, t\_] := Sum[Sum[aa[[i, j]] * t^{j} * m^{(i+1)/2}, \{j, 4\}], \{i, 3\}] + Sum[bb[[j]] * m^{(j+1)/2}, \{j, 4\}];$$

Step 8: Density of pure water ρ_T as a function of temperature in °C

$$k = \{999.8396, 18.224944, -7.922210 * 10^{-3}, -55.44846 * 10^{-6}, 149.7562 * 10^{-9}, -393.2952 * 10^{-12}\};$$

$$rhoT[t\_] := (1 + 18.159725 * 10^{-3} * t)^{-1} * Sum[k[[i]] * t^{i-1}, \{i, 6\}];$$

Step 9: Density and specific volume

```
rho = Table[rhoT[tC[[j, i]]] + deltaRhoS[m0[[j, i]], tC[[j, i]]], {j, nProbes}, {i, nSetsExp}];

alpha = 1 / rho;
```

Output of Data

```
outputData =
 Table[{expData[[i, 1]], expData[[i, 2]], alpha[[1, i]], alpha[[2, i]], alpha[[3, i]],
   tK[[1, i]], tK[[2, i]], tK[[3, i]], psalt[[1, i]], psalt[[2, i]], psalt[[3, i]]},
  {i, nSetsExp}];

Export[dataFilePath <> "\\Output " <> dateOfExp <> " Exp.dat", outputData]

C:\Documents and Settings\Christian Reuten\My Documents\Study\Areas\Water Tank
  Studies\CT Calibration and Measurement\2004-08-04\Output 2004-08-04 Exp.dat
```

C.9 Production of Neutrally-Buoyant Particles

Velocities in the water tank are measured by tracing the motion of illuminated individual particles in consecutive video frames. The choice and production of particles for PIV is often a major challenge, but is considered a technical issue which is often not shared in publications. The following exposition may be useful for readers for their own PIV requirements since the particles meet stringent requirements and can be used in a broad range of applications. These are the requirements that the particles had to meet:

1. Between the start of the filling of the tank with water and the start of the experiment there is a time lag of at least 18-24 hours to minimise the eddy motion in the tank. Therefore the particles have to be neutrally buoyant to avoid settling.

2. There is a continuous range of densities within the tank, so the particles have to cover a similarly wide range.

3. There are density ranges that are particularly important. It therefore has to be possible to fine tune the density ranges of the particles.

4. The tank is heated very strongly. As a conservative estimate I required the particles to withstand temperatures of up to 100°C. This turned out to be a necessary property during the production process even if the tank was not heated.

5. To stand out against an otherwise dark background the particles have to be light-coloured, preferably white.

6. Distance and brightness of the light source, stray light, and size of the video window vary substantially for different experiments. Therefore it has to be possible to tailor the size of the particles.

The particles I produced to meet all the requirements are a mixture of high-temperature wax and titanium dioxide, TiO_2. Both substances pose minimal health threats. I used pellets of CALWAX 220, which has a congealing point of 220°F (104°C) and a density less than the approximately 1000 kg m^{-3} of freshwater. Calwax Corporation sells wholesale quantities, only. TiO_2 in sufficient purity is available as a dry pigment (e.g. by Gamblin) from art supply stores. The bright white pigment has a density of about 4000 kg m^{-3}, is very heat resistant, and mixes with wax in any ratio. I was advised not to use ZnO pigments since they discolour when mixed with hot wax.

First, two containers are prepared: one with freshwater and one with saltwater of highest salinity to bracket the density range. To reduce surface tension a few tablespoons of Kodak Professional Photo-Flo 200 solution are added to about one litre of water.

In the first process step, the wax pellets are melted in a pan on a kitchen stove. This has to be done very slowly and with sufficient body protection since wax has a flash point above which it will burst into flames. Then some TiO_2 is mixed into the wax. A small amount of wax is removed, and once hard, dropped into the container with freshwater. As long as the wax mixture floats, TiO_2 is repeatedly added.

Once the wax mixture's density exceeds that of freshwater, part of the wax mixture is removed and collected in a container. More TiO_2 is added. Again, a small amount of wax is removed, but this time dropped into the container with saltwater. If the wax mixture floats, part of the wax mixture is removed and collected in another container. Adding TiO_2, testing density, and removing part of the wax is repeated until the wax mixture sinks in the saltwater.

The whole procedure can now be reversed by adding wax to the pan until the wax mixture starts floating in freshwater. Usually going through the complete cycle three to four times and removing 30-40 portions of different density will cover the entire density range with sufficient continuity.

In the next process step the different wax portions have to be measured and binned. I prepare containers with different salt concentrations (again Photo-Flo has to be added) and check in which containers the wax portions sink and float. The portions are then labelled accordingly with the lower and upper salinity limit.

In the final and most time-consuming step, the wax portions are crushed with a mortar to the required size. I use two differently-sized metal meshes. The wax particles have to be small enough to pass through the coarser mesh, but particles that drop through the finer mesh are removed since they will cause stray light in the tank. In this process step, ordinary paraffin wax with a congealing point of approximately 60°C will lump together during the crushing with the mortar because of the heat that develops, which necessitates the use of high-temperature wax even if the expected tank bottom surface temperatures are much lower than the congealing point of wax.

C.10 Entrainment Coefficient over the Heated Plateau

Carson (1973) pointed out that the entrainment at the top of the atmospheric CBL is typically small in the morning under a strong inversion and larger, up to an entrainment coefficient of $A_a \approx 0.5$, in the later stages of convection when the environmental stability is weaker. The same holds in the water tank which I will demonstrate next by comparing two experiments with different background stratification performed over the heated plateau, only, with the rest of the tank separated by a removable end wall (Figure Appendix XXI).

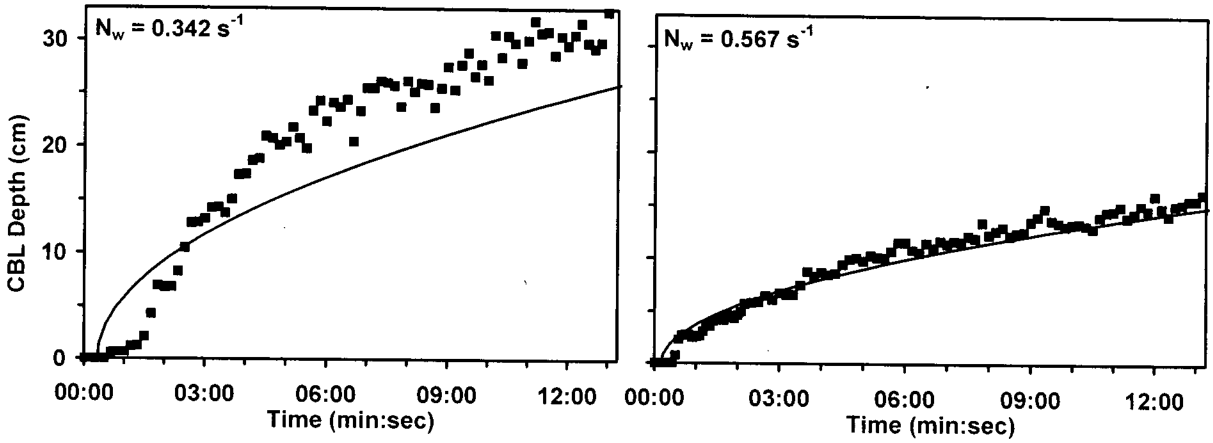

Figure Appendix XXI: Tank observations of the CBL growth over flat terrain for two different stratifications. A thin layer ($\ll 1\,mm$) of fluorescent dye was released over the plain. I identified the CBL top visually as the boundary separating high and low dye concentrations. The CBL depth determined in this way corresponds to the backscatter boundary layer in the atmosphere determined from lidar data. The solid squares are tank observations of CBL depth, and the solid curve shows the prediction for a CBL without entrainment from the top. The Left graph is for a buoyancy frequency of 0.342 s^{-1}, the right graph for 0.567 s^{-1}. Both graphs have the same scales. The start time of convection is chosen as the time when the first thermal was released anywhere from the tank bottom. Because that location did not coincide with the point of CBL depth measurement, the CBL growth begins later than predicted but catches up with the predicted growth within approximately two minutes.

The following applies both to atmosphere and water tank. Let Q_{top} denote the heat flux added to the CBL by entrainment at the CBL top; then the entrainment coefficient is defined as

$$A \equiv -\frac{Q_{top}}{Q_H}, \tag{C.8}$$

the ratio of net sensible heat fluxes at the top (negative) and the bottom (positive) of the CBL. If h_p is the predicted CBL depth for $A = 0$ and h is the observed CBL depth, then (Carson, 1973)

$$A = \frac{1-r}{r-2} \tag{C.9}$$

with

$$r \equiv \frac{h}{h_p}. \tag{C.10}$$

For a buoyancy frequency of $N_w \approx 0.342\,s^{-1}$ in the tank (from (3.95) corresponding to the atmospheric test case but with a lower background stratification of $N_a \approx 0.0135\,s^{-1}$) the entrainment coefficient can be determined from Figure Appendix XXI (left graph) and (C.9)-(C.10) as $A_w \approx 0.4$. For a greater background buoyancy frequency of $N_w \approx 0.567\,s^{-1}$ ($N_a \approx 0.0224\,s^{-1}$ in the atmosphere) the entrainment coefficient was $A_w \approx 0.1$. This agrees with Carson (1973).

Heating enters the tank water initially through molecular diffusion. After roughly 30 seconds, thermals begin rising randomly. When such a thermal rises at the measurement location the CBL depth rapidly increases and briefly overshoots which can be seen in both graphs of Figure Appendix XXI.

C.11 Empirical Analysis of Maximum Upslope Flow Velocity

Following the same rationale as in section 3.4.2 and Appendix B.2, I look for a monomial relationship between ND maximum upslope flow velocity $U_{\max,w}$ and $\Pi_{2,w}$, $\Pi_{3,w}$, i.e.

$$U_{\max,w}{}^* = c \cdot \Pi_{2,w}{}^{m_1} \cdot \Pi_{3,w}{}^{m_2}, \tag{C.11}$$

so that

$$\log\left(U_{\max,w}{}^*\right) = \log c + m_1 \cdot \log \Pi_{2,w} + m_2 \cdot \log \Pi_{3,w}. \tag{C.12}$$

I use the data set in Table 4.1 on page 94, which I repeat here without caption:

Name	$N_w\left(s^{-1}\right)$	$\overline{Q}_{H,w}$ $\left(10^{-3}\,Kms^{-1}\right)$	$\Pi_{3,w}$	$L_{b,w}(m)$	$L_{t,w}(m)$	$Q_{H,w}$ details $\left(10^{-3}\,K\,m\,s^{-1}\right)$ Plain	Slope	Plateau
WT1	0.567	1.85	0.00117	0.470	0.470	1.85	1.85	1.85
WT2	0.379	1.85	0.00406	0.470	0.470	1.85	1.85	1.85
SP	0.379	1.85	0.00406	0.225	0.470	1.85	1.85	1.85
TR1	0.379	2.68	0.00588	0.470	0	1.48	1.67-3.70	-
TR2	0.342	3.15	0.00903	0.470	0	1.48/2.04	2.59-3.70	-
WT3	0.374	2.96	0.00649	0.470	0.470	1.85	2.96	1.85

Nonlinear regression of the data for the model in (C.11) gives

$$U_{max,w}{}^* = (0.64 \pm 0.14) \cdot \Pi_{2,w}{}^{(0.56\pm0.03)} \cdot \Pi_{3,w}{}^{(0.80\pm0.04)}, \tag{C.13}$$

with a weak positive correlation of 0.26 between $\Pi_{2,w}$ and $\Pi_{3,w}$. Multiple (linear) regression of the data for the model in (C.12) gives a significantly different result for c, m_1, and m_2,

$$\log(U_{max,w}{}^*) = (0.29 \pm 0.07) + (0.47 \pm 0.02) \cdot \log \Pi_{2,w} + (0.93 \pm 0.03) \cdot \log \Pi_{3,w}, \tag{C.14}$$

with $R^2 = 0.85$ and a weak negative correlation of -0.15 between $\Pi_{2,w}$ and $\Pi_{3,w}$. The multi-linear fit and the residuals are shown in Figure Appendix XXII.

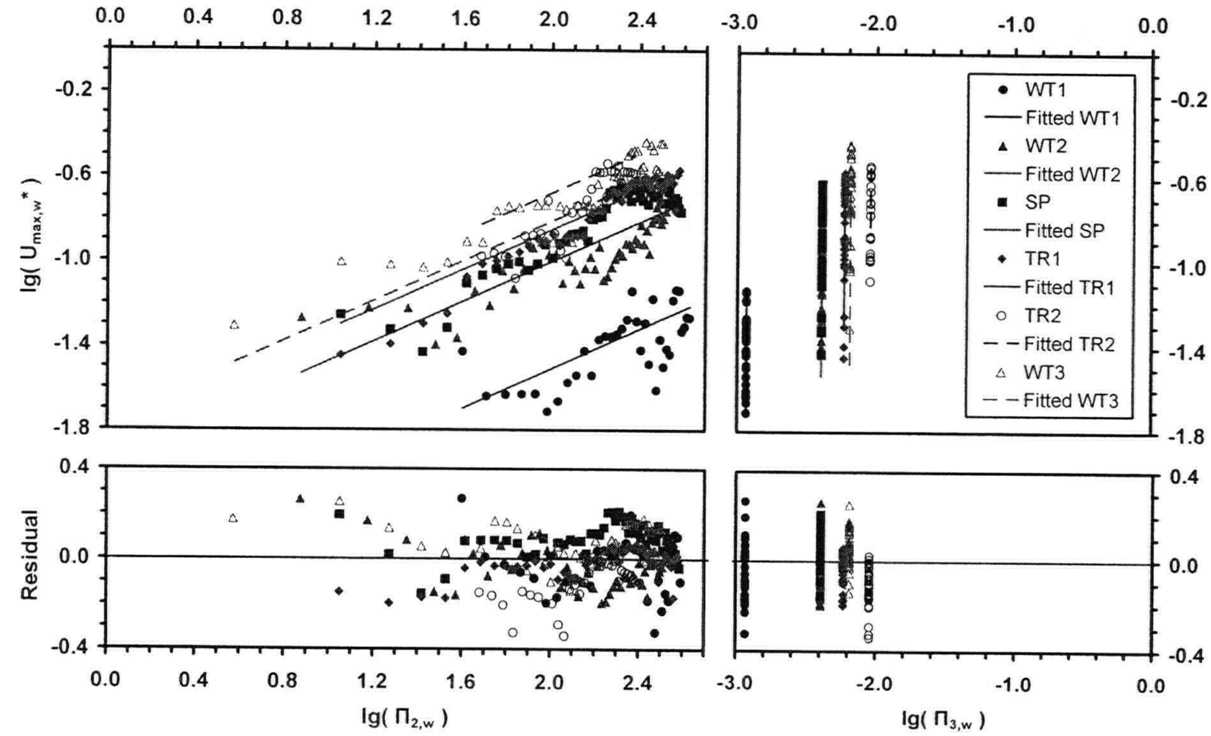

Figure Appendix XXII: Multiple linear regression of ND water-tank maximum upslope flow velocities. Top: Base-10 logarithm ($\lg = \log_{10}$) of ND maximum upslope flow velocity $U_{max,w}{}^* = U_{max,w} / H_w N_w$ from the water-tank experiments in Table 4.1 as a function of lg *of $\Pi_{2,w} = N_w t_w$ (left) and $\Pi_{3,w} = g\beta_w Q_{H,w} / H_w{}^2 N_w{}^3$ (right). The lines show the predicted values from multiple linear regression. The legend in the top right graph applies to all four graphs. Bottom: Residuals (observed minus predicted). Vertical scales are identical in all four graphs.*

The range of data in the water tank (Figure Appendix XXII) is much wider than in the atmosphere (Figure Appendix V, page 196), and I have about ten times as many water-tank data as atmospheric observations. This leads to a substantially lower uncertainty for the water-tank observations than the atmospheric observations, although the quality of individual data is not better. The low quality is the result of many observational constraints and technical limitations, in particular the need to measure at sufficiently small temporal and spatial scales to capture flow details similar to the atmosphere. At the same time the main goal of this dissertation, the investigation of the trapping of air pollutant in upslope flow systems, requires capturing the overall flow characteristics.

Comparing (C.13) with the five hypotheses in (4.14)-(4.18), from $m_1 = 0.56 \pm 0.03$ I can reject all but the Chen and friction hypotheses, for which the exponent $m_1 = 1/2$ of $\Pi_{2,w}$ is just within the 95% confidence interval $[0.50, 0.62]$. All hypotheses, however, predict exponents m_2 of $\Pi_{3,w}$, which are clearly outside of the 95% confidence interval $[0.72, 0.88]$. Clearly, similarity of upslope flow velocities in atmosphere and water tank is violated if Π_1, Π_2, and Π_3 are assumed to be the only governing parameters.